

# The High-Dynamic Double-Crystal Monochromator

***Citation for published version (APA):***

Ramalho Geraldes, R. (2023). *The High-Dynamic Double-Crystal Monochromator: a Mechatronic Paradigm Shift in Synchrotron Beamline Instrumentation*. [Phd Thesis 1 (Research TU/e / Graduation TU/e), Mechanical Engineering]. Eindhoven University of Technology.

***Document status and date:***

Published: 03/07/2023

***Document Version:***

Publisher's PDF, also known as Version of Record (includes final page, issue and volume numbers)

***Please check the document version of this publication:***

- A submitted manuscript is the version of the article upon submission and before peer-review. There can be important differences between the submitted version and the official published version of record. People interested in the research are advised to contact the author for the final version of the publication, or visit the DOI to the publisher's website.
- The final author version and the galley proof are versions of the publication after peer review.
- The final published version features the final layout of the paper including the volume, issue and page numbers.

[Link to publication](#)

***General rights***

Copyright and moral rights for the publications made accessible in the public portal are retained by the authors and/or other copyright owners and it is a condition of accessing publications that users recognise and abide by the legal requirements associated with these rights.

- Users may download and print one copy of any publication from the public portal for the purpose of private study or research.
- You may not further distribute the material or use it for any profit-making activity or commercial gain
- You may freely distribute the URL identifying the publication in the public portal.

If the publication is distributed under the terms of Article 25fa of the Dutch Copyright Act, indicated by the "Taverne" license above, please follow below link for the End User Agreement:

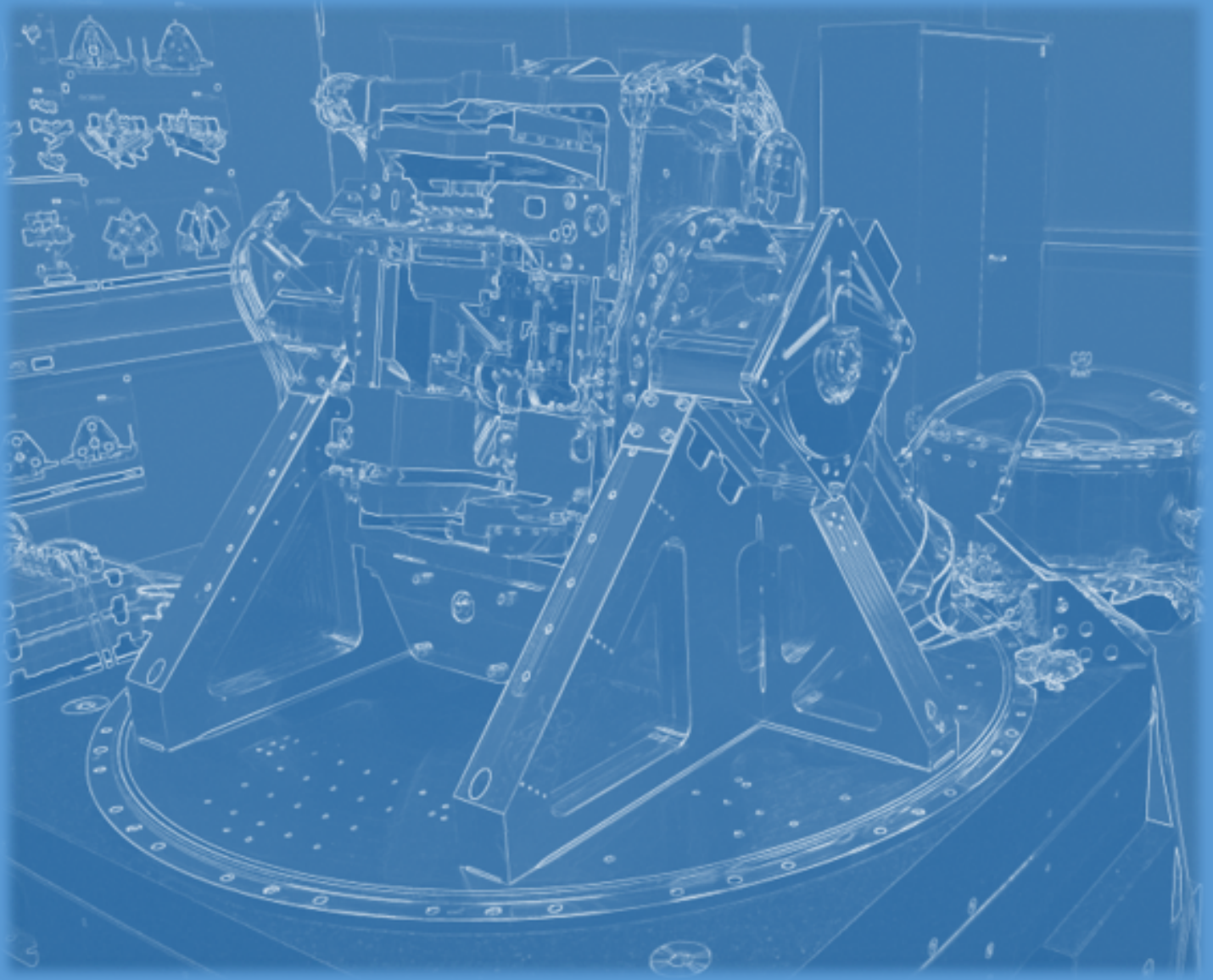
[www.tue.nl/taverne](http://www.tue.nl/taverne)

***Take down policy***

If you believe that this document breaches copyright please contact us at:

[openaccess@tue.nl](mailto:openaccess@tue.nl)

providing details and we will investigate your claim.



# **The High-Dynamic Double-Crystal Monochromator**

a Mechatronic Paradigm Shift in  
Synchrotron Beamline Instrumentation

**Renan R. Geraldles**





**The High-Dynamic Double-Crystal  
Monochromator**  
a Mechatronic Paradigm Shift in Synchrotron  
Beamline Instrumentation

Renan R. Geraldes



**CNPEM**



The research presented in this thesis has been performed within the framework of the Sirius Project at the Brazilian Synchrotron Light Laboratory (LNLS) at the Brazilian Center for Research in Materials and Engineering (CNPEM), being funded by the Brazilian Ministry of Science Technology and Innovation (MCTI).

The High-Dynamic Double-Crystal Monochromator a Mechatronic Paradigm Shift in Synchrotron Beamline Instrumentation by Renan Ramalho Geraldes – Eindhoven: Technische Universiteit Eindhoven, 2023 – Proefschrift.

A catalogue record is available from the Eindhoven University of Technology Library.  
ISBN: 978-90-386-5776-9.

Typeset by the author in pdfL<sup>A</sup>T<sub>E</sub>X.

Reproduction: Ipskamp Printing, Enschede, The Netherlands.

Copyright © 2023 by R.R. Geraldes. All rights reserved.

# **The High-Dynamic Double-Crystal Monochromator**

## **a Mechatronic Paradigm Shift in Synchrotron Beamline Instrumentation**

PROEFSCHRIFT

ter verkrijging van de graad van doctor  
aan de Technische Universiteit Eindhoven,  
op gezag van de rector magnificus, prof.dr. S.K. Lenaerts,  
voor een commissie aangewezen door het College voor Promoties  
in het openbaar te verdedigen  
op maandag 3 juli 2023 om 11.00 uur

door

Renan Ramalho Geraldes

geboren te São Paulo, Brazilië



Dit proefschrift is goedgekeurd door de promotoren en de samenstelling van de promotiecommissie is als volgt:

voorzitter:	prof.dr.ir. P.D. Anderson
1 <sup>e</sup> promotor:	prof.dr.ir. J.P.M.B. Vermeulen
2 <sup>e</sup> promotor:	prof.dr.ir. M. Steinbuch
copromotor:	dr.ir. G. Witvoet
leden:	prof.dr.ir. O.J. Luiten
	prof.dr.ir. D.M. Brouwer (Universiteit Twente)
	prof.dr. D. Trumper (Massachusetts Institute of Technology)
adviseur:	dr.ir. T. Ruijl (MI-Partners)

Het onderzoek of ontwerp dat in dit proefschrift wordt beschreven is uitgevoerd in overeenstemming met de TU/e Gedragscode Wetenschapsbeoefening.

“For the world is in a bad state, but everything will become still worse unless each of us does their best.” (Viktor Frankl)



---

## Societal Considerations

---

Modern societies face great challenges. All over the world, (far too many) human lives continue to be constrained and threatened not only by poverty, famine, diseases and corruption, but also by racism, xenophobia, and gender and religious intolerance, to name a few. Crises in liberal democracies and stronger oligarchical and nationalist movements are in course while coordinated global response seems to be necessary to face global human problems, such as climate change, sanitary and disease control (see the recent/ongoing COVID-19 pandemic), immigration waves, feeding 8 billion people, exhaustion of natural resources, cyber security, and ethical regulations on artificial intelligence and data property, for example. Yet, unfortunately, opposing the astonishing current levels (and trend) of disinformation and denialism, simplifying stories and ideologies will hardly encompass and fulfill the needs of a complex reality. Hence, empathy and widening of perspectives and points of view via liable and reliable education are possibly more urgent than ever.

Regardless personal/group opinions, beliefs and/or interests, Nature has its ways and the scientific method is committed to finding and describing the physical world we live in. Indeed, the way gravity works, the behavior of electrons, or the interaction of light with matter are independent of political views or economical models. Thus, even though science will be always within knowledge boundaries and by itself cannot guide the human decisions, it offers a predictable ground on which discussions can be seriously carried out and decisions can be made. In addition to that, science greatly benefits from sharing and collaborating, such that one can learn and advance based on findings from others, rather than waste limited time, effort and resources on repeated research. Common goals have the power to unify people and build bridges to address real problems, in contrast to Manichean fears that burn bridges and raise walls.

Synchrotron light sources are large facilities that are used by the international scientific community (and by industry) as powerful microscopes to investigate matter under various aspects, covering fields from biology to materials sciences, from energy to cultural heritage, from agronomy to electronics, to name only a few. Thanks to a recent new generation of the so-called storage rings used to produce synchrotron light, spatial resolution of structures, as well as time resolution of processes and/or measure-



ment throughput, can be now potentially increased by a few orders of magnitude to enable unprecedented research opportunities. Nonetheless, to make use of this power, equivalent advances are required at the experimental stations, the so-called beamlines. Considering the increased complexity of the systems, the urgent technological problems and limited financial resources, it has been identified that, as opposed to *trial-and-error* or shy *best-effort* approaches that are often found in beamline instrumentation, alternative project development frameworks may be mandatory from now on — at least for a few critical components.

This thesis describes the High-Dynamic Double-Crystal Monochromator (HD-DCM), developed by the Brazilian Synchrotron Light Laboratory (LNLS) in collaboration with the Dutch mechatronics consultant MI-Partners. The work involved identifying a technological bottleneck, overcoming some conservative views and ways-of-working in the synchrotron community, finding a financial and political strategy to carry the project, integrating expertise from different fields into a multidisciplinary high-end X-ray optical component, training, and deployment to beamlines at Sirius, the fourth-generation synchrotron light source in Brazil. The result is a successful high-precision instrument, exceeding previous state-of-the-art systems by at least a factor five in static operation and making possible unprecedented high-stability spectroscopic scans to the benefit of the scientific community — and the society. Therefore, this thesis aims at being a case study and incentive for how systems engineering, precision engineering and predictive modeling tools can be used in a science-oriented environment for systematic and deterministic problem solving. Finally, beyond the development of a particular machine, it also proves the potential of bringing communities closely together — in this case, the synchrotron and the precision engineering/mechatronics communities — to boost collective knowledge and aid human needs.

---

# Summary

## The High-Dynamic Double-Crystal Monochromator

---

Synchrotron light sources are research facilities with an essential role in academic and industrial global research. Working as special microscopes in experimental stations known as beamlines, a wide range of the electromagnetic radiation spectrum can be covered (from infrared to hard X-rays), with tremendously broad application fields, including materials sciences, energy, health and agronomy, to name a few.

Within this context, there is a particular class of instruments known as Double-Crystal Monochromators (DCMs) that is extensively used at tender and hard X-ray beamlines to select narrower energy bandwidths out of incoming photon beams with broader energy bands for specific experimental techniques. In a nutshell, a DCM consists of an arrangement of two crystals (such as high-purity silicon or germanium pieces) that must be precisely positioned and oriented with respect to the incoming beam and each other, so as to provide the desired energy selection according to Bragg's law of diffraction and a fixed-offset downstream monochromatic photon beam.

This thesis describes the technological breakthrough provided by incorporating precision engineering and mechatronic concepts that have been developed and used in the semiconductors industry over the past few decades to the context of DCMs at synchrotron beamlines. In this sense, it could be argued that the so-called High-Dynamic Double-Crystal Monochromator (HD-DCM) coins a new sub-class of instruments, with a novel conceptual mechatronic architecture that not only achieves superior positioning control in static operational conditions, but also enables unprecedented scanning possibilities to the benefit of research in both the scientific community and the industry.

Indeed, the work presented here aims at starting to at least partly address the call from synchrotron users for better instruments that can comply with requirements of the emerging fourth-generation light sources. As compared to standard DCMs, the HD-DCM now allows for, on the one hand, improvements in spatial resolution of X-ray images and maps, and, on the other hand, higher temporal resolution of processes and throughput, thanks to its high-performance scanning functionality. The first two units of the HD-DCM are installed at Sirius, the new-generation synchrotron at the Brazilian Synchrotron Light Laboratory (LNLS), with applications ranging from

retrieving the structure of SARS-CoV-2 proteins in an X-ray crystallography beamline to investigating samples emulating Earth's inner core in an X-ray beamline dedicated to extreme pressure, temperature and magnetic conditions.

The contributions of this thesis can be split in two main parts. The first part is dedicated to a detailed description of the mechatronic architecture of the HD-DCM and the systematic predictive design approach applied to build an innovative, multidisciplinary and complex high-end machine first-time right. It covers: i) decisions in the selection of motion degrees-of-freedom; ii) changes related to transforming a high-stiffness mechanical design into an isolated mechatronic architecture with high-bandwidth closed-loop control; iii) improvements in mechanical guiding and actuation, as well as in the metrology architecture, for the nanometer-level requirements; iv) thermo-mechanical functionality decoupling of parts for superior accuracy and dynamics; v) reduction of disturbance agents by design; vi) development of mechatronic models of the plant, according to Dynamic Substructuring methods, and of disturbance models, following educated guestimates and experimental measurements; vii) controller design and bandwidth analysis via loopshaping; viii) design convergence according to the Dynamic Error Budgeting framework; and ix) preliminary performance validation.

The second part of this thesis is more synchrotron-oriented and focuses mostly on the engineering challenges in integrating this new type of high-end machine into a beamline environment. It comprises: i) a more high-level overview on the architectural differences between standard DCMs and the HD-DCM, which also highlights how typical choices for experimental flexibility may need to be traded for higher performances; ii) a new positioning problem formulation oriented to scanning, which has a direct impact both in scientific plans and perspective, and in engineering choices, requirements and limitations; iii) emerging performance requirements that are derived to correlated beamline instruments, such as the X-ray source and detectors, spanning over aspects as sensitivity, signal-to-noise ratio, motion and synchronism; and iv) proven performance with X-rays at the beamlines in static and scanning operation, making explicit the achievement of the original goals of the HD-DCM, while fostering advances needed from the beamline side.

Hence, the content of this thesis addresses the rise of a new type of instrument in synchrotron beamlines, with promising perspectives for future research. Naturally, all this research potential is related to at least equally broad research opportunities in interdependent beamline components and science. Finally, it is worth saying that the HD-DCM became an edifying project in terms of beamline instrumentation design at the LNLS. In the last few years, the lessons learned, alongside the developed tools and framework, have far extrapolated the original scope of the HD-DCM, providing already the elements for the construction of innovative X-ray mirror systems and multi-modal microscopes with X-ray nanoprobe at Sirius.

---

# Contents

---

<b>Societal Considerations</b>	<b>VII</b>
<b>Summary</b>	<b>IX</b>
<b>1 Introduction</b>	<b>1</b>
1.1 Beyond the Human Eye . . . . .	1
1.2 The Importance of Synchrotron Light Sources . . . . .	2
1.3 New-Generation Synchrotron Light Sources . . . . .	5
1.4 Next-Generation Beamlines Challenges . . . . .	7
1.5 Difficulties in Beamline Design Optimization . . . . .	8
1.6 Double-Crystal Monochromators . . . . .	11
1.7 The High-Dynamic Double-Crystal Monochromator . . . . .	13
1.8 Thesis Outline . . . . .	16
<b>2 The Mechatronic Architecture and Design of the High-Dynamic Double-Crystal Monochromator for Sirius Light Source</b>	<b>21</b>
2.1 Introduction . . . . .	22
2.2 Background . . . . .	25
2.3 Specifications . . . . .	28
2.4 Architecture and Design . . . . .	32
2.5 Conclusions and Discussions . . . . .	61
2.A List of Abbreviations . . . . .	62
<b>3 Predictive Modeling through Dynamic Error Budgeting applied to the High-Dynamic Double-Crystal Monochromator for Sirius Light Source</b>	<b>67</b>
3.1 Introduction . . . . .	68
3.2 Modeling Methodology . . . . .	70
3.3 HD-DCM Model . . . . .	75
3.4 DEB Results . . . . .	89
3.5 Conclusions . . . . .	95



3.A	List of Abbreviations . . . . .	96
3.B	Mechanical Structure to Model . . . . .	97
<b>4</b>	<b>A Review on the High-Dynamic Double-Crystal Monochromator for Sirius/LNLS</b>	<b>101</b>
4.1	Introduction . . . . .	102
4.2	Mechatronic Architecture . . . . .	103
4.3	Integration Architecture . . . . .	105
4.4	Performance Results . . . . .	107
4.5	Conclusions . . . . .	109
<b>5</b>	<b>Fly-Scan-Oriented Motion Analyses and Upgraded Beamline Integration Architecture for the High-Dynamic Double-Crystal Monochromator at Sirius/LNLS</b>	<b>111</b>
5.1	Introduction . . . . .	112
5.2	DCM Positioning Problem Formulation . . . . .	114
5.3	Undulator Properties and Positioning Analyses . . . . .	122
5.4	HD-DCM Integration and Operation Schemes . . . . .	127
5.5	Experimental Results . . . . .	134
5.6	Conclusions . . . . .	147
5.A	List of Abbreviations . . . . .	149
<b>6</b>	<b>Conclusions and Outlook</b>	<b>153</b>
6.1	Conclusions . . . . .	153
6.2	Outlook . . . . .	154
	<b>Appendices</b>	<b>161</b>
<b>A</b>	<b>Complementary DCM Geometrical Description</b>	<b>161</b>
A.1	Nominal Geometry . . . . .	161
A.2	Alignment Effects . . . . .	162
<b>B</b>	<b>Dynamic Substructuring and Modal State-Space Representation</b>	<b>167</b>
B.1	Dynamic Substructuring . . . . .	167
B.2	Modal Representation of a Complete Model . . . . .	170
B.3	State-Space Representation . . . . .	171
<b>C</b>	<b>Experimental Control Implementation</b>	<b>173</b>
C.1	Position- and Machine-specific Considerations . . . . .	173
C.2	System Identification . . . . .	174
C.3	Controller Design . . . . .	179
	<b>Bibliography</b>	<b>187</b>

List of Publications	199
Acknowledgements	203
Curriculum Vitae	207



# CHAPTER 1

---

## Introduction

---

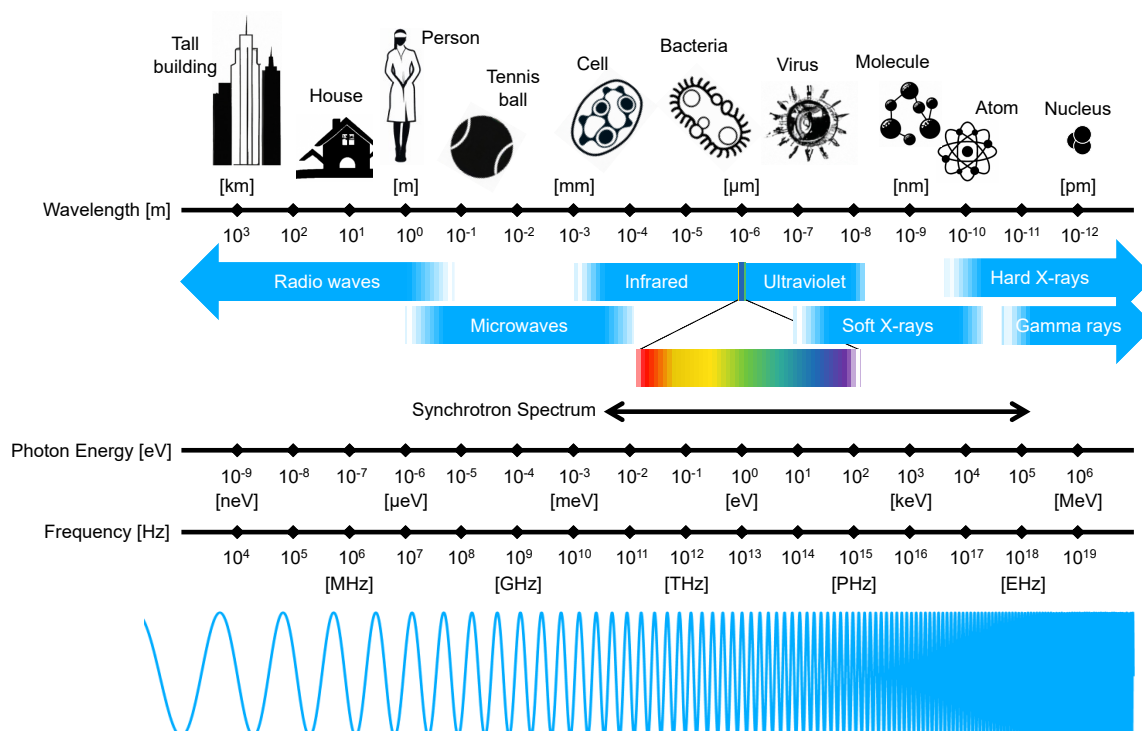
### 1.1 Beyond the Human Eye

At the turn from the 16<sup>th</sup> to the 17<sup>th</sup> centuries, the invention of first optical microscopes and telescopes, together with the rebirth of the scientific method in Europe, has completely changed the human relationship with the natural world — and the societies. From that moment on, humanity started to have access to tools that not only aided daily processes, but widened the sensorial capabilities in many orders of magnitude — the vision in particular. Then, unrevealed worlds started to be explored, for example, from the first studies with bacteria in the 17<sup>th</sup> century in the biological field, to chemical processes in industrial systems in the 18<sup>th</sup> century, passing through the revolutions in Physics. And, until today, knowledge and scientific potential drive individuals, institutions, organizations and governments, via scientific, economical and political interests, toward a permanent expansion of the frontiers.

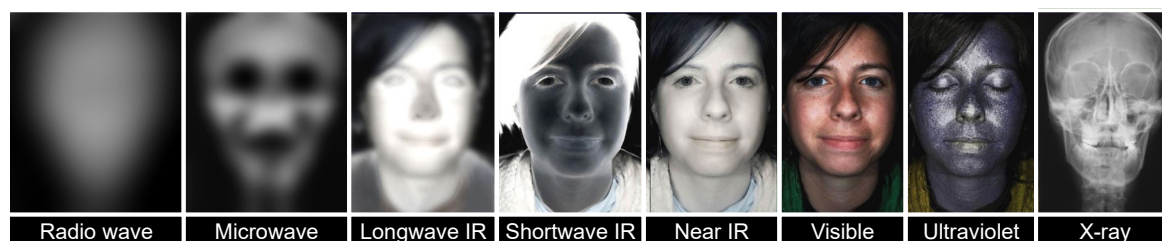
Yet, as depicted in Figure 1.1, it turns out that the visible light in optical microscopes and telescopes corresponds to just a small fraction of the electromagnetic radiation spectrum. Indeed, starting from radio waves — with frequency and wavelength in the order of  $10^4$  Hz and  $10^3$  m, respectively —, it passes by microwaves, infrared (IR), visible light, ultraviolet (UV) and X-rays, finally reaching the so-called gamma rays — with frequency and wavelength in order of  $10^{19}$  Hz and  $10^{-12}$  m, respectively. So, as it might be expected, the visible spectrum that is natural to the humans is related solely to a limited fraction of the information available in the universe, such that much more can be extracted from the remaining portions of the spectrum.

For instance, an ordinary object that provides information about color, transparency and texture with the naked eye, may offer knowledge about temperature and surface molecular properties in the infrared domain. With X-rays, the material chemical composition, its structural atomic organization or radiographic images may be obtained — as an example, a human face seen at different wavelengths is shown in Figure 1.2. Therefore, specific instruments have been built to increase the spectrum that is accessible to us, i.e., to convert radiation waves that are outside the visible light frequency/wavelength range to something that can be seen by the human eye. As such, today a number of astronomical observations are possible only thanks to radiotelescopes, whereas atomic levels can be observed indirectly via X-ray microscopes.





**Figure 1.1:** Electromagnetic radiation spectrum, indicating the ranges of: radio waves, microwaves, infrared, visible light, ultraviolet, soft and hard X-rays, and gamma rays. Scales are provided for the radiation frequency and wavelength, along with objects of comparable sizes for general reference. Also shown is the corresponding photon energy scale, according to the wave-particle duality concept. The synchrotron light is pointed out to cover a broad spectral range from infrared up to hard X-rays.




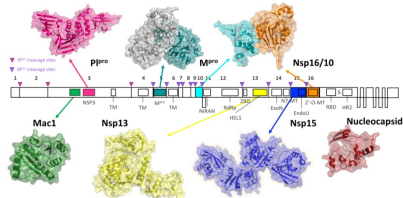

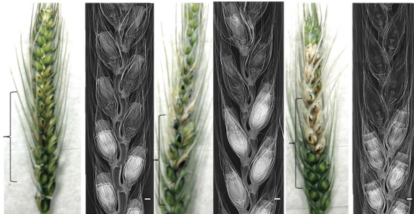
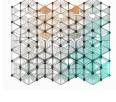
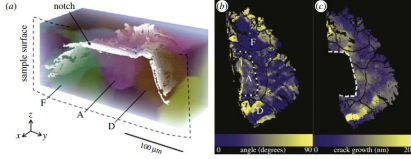

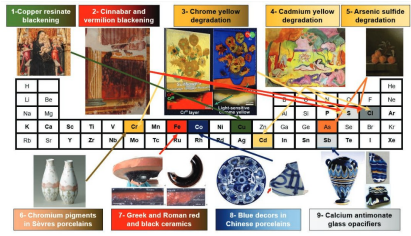

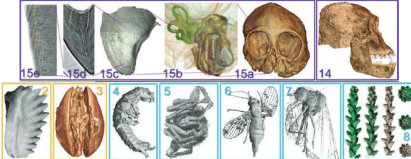
**Figure 1.2:** Human face as seen using different sensors types over the electromagnetic spectrum. From radio waves to X-rays, not only the image resolution and contrast are altered, but also wavelength-specific information can be extracted from the interaction between radiation and matter. (Adapted from <http://www.chemistryland.com/CHM107/Final/FinalWritten.html>).

## 1.2 The Importance of Synchrotron Light Sources

From all the experimental tools ever invented, *synchrotron light sources* are among those with the greatest potential and impact in the knowledge and development of materials [5–7]. This is because they are used as special microscopes, covering the broad range from infrared to X-rays, as also indicated in Figure 1.1. Hence, organic

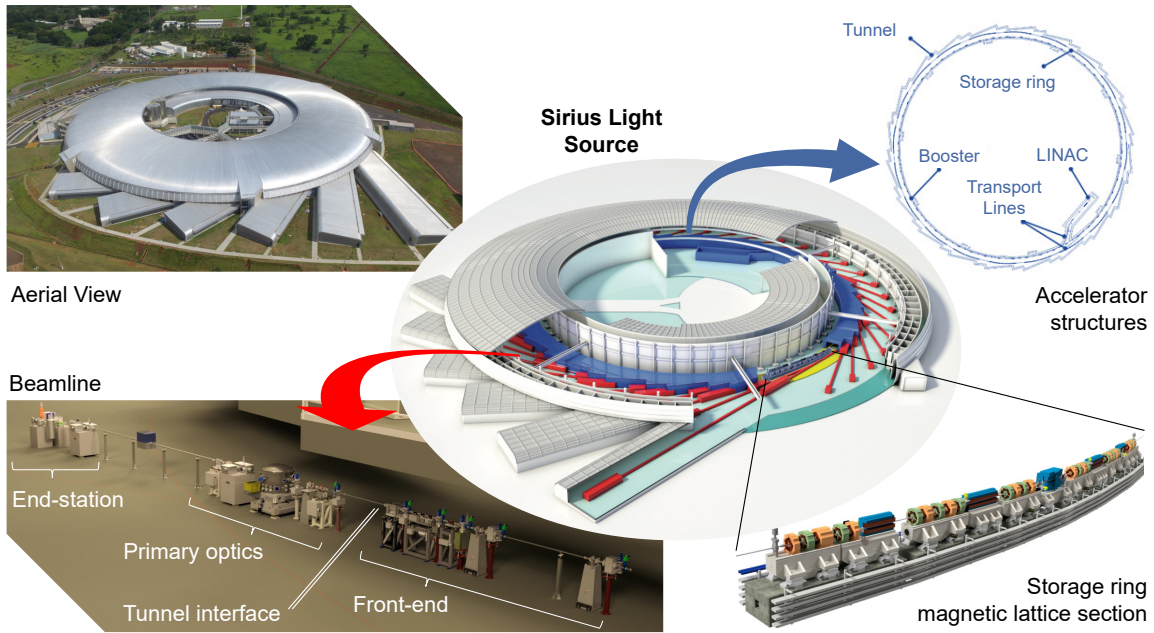
and inorganic materials, in a variety of states of complexity and conditions, may be investigated multidisciplinarily and in multiscale. As such, characteristics and processes that are natural or artificially induced can be understood and developed in favor of the society and its technologies. Indeed, over the past 60 years, synchrotron radiation has revolutionized a wide range of academic and industrial research fields, as demonstrated by countless research papers, academic theses and industrial patents, as well as a number of Nobel Prizes [5,6]. As briefly illustrated in Table 1.1, research fields are virtually unlimited, spanning over medical, pharmaceutical, agronomical, environmental, energy, materials science, structural biology, paleontology, and cultural heritage studies, to name a few. Many of these fields are critical to the well-being of the society and the sustainability of the planet in the coming decades.

**Table 1.1:** Examples within a few research fields covered by synchrotron science.

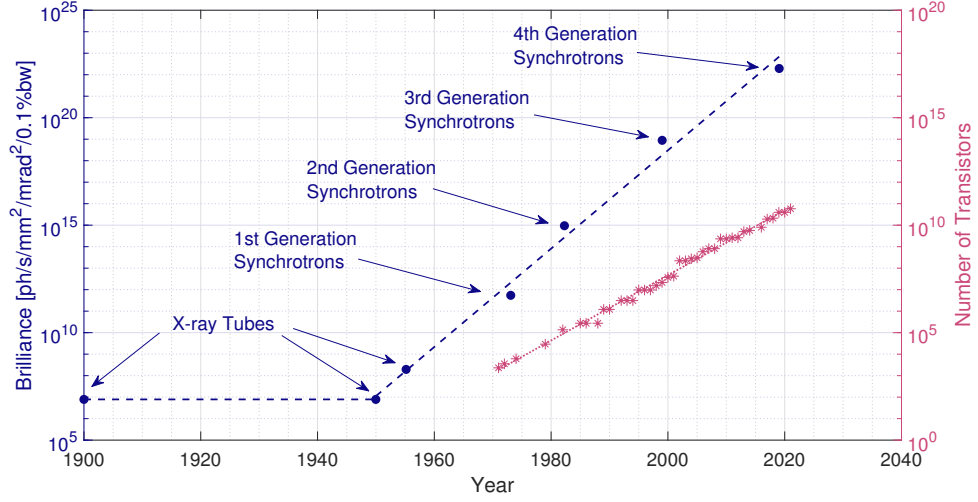
Field	Example	Description
 Health		SARS-CoV-2 genome and proteins screened via X-ray crystallography at the Diamond Light Source (reprinted from [1]).
 Agronomical		Comparison between healthy and diseased wheat florets using phase-contrast X-ray imaging (reprinted from [2]).
 Materials		X-ray tomography and images for a crack growth in Mg (reprinted from [3]).
 Cultural Heritage		Summary of artistic materials analyzed by X-ray absorption at the European Synchrotron Radiation Facility (reprinted and adapted from [4]).
 Paleontology		Samples analyzed via high-resolution computed X-ray tomography at the European Synchrotron Radiation Facility (reprinted and adapted from [4]).

In modern facilities, synchrotron radiation is typically produced in large particle accelerator structures known as *storage rings*, with circular-like geometry and perimeters varying from a few hundred meters to a few kilometers. The emission of photons follows from Maxwell’s equations, with light relativistic particles (generally electrons, but also positrons) being accelerated by different arrangements of magnetic fields — either in *dipoles* of the permanent storage ring magnetic lattice or in complementary components known as *insertion devices*. Then, the so-called *beamlines* are defined by particular sets of components used to transfer the photon beam from the source to the experimental stations, while tailoring the beam properties to the desired specifications — namely, photon energy, beam size, beam divergence, photon flux, temporal and/or spatial coherence, and polarization [8]. An example of such a facility is provided in Figure 1.3 by Sirius, at the Brazilian Synchrotron Light Source (LNLS), in Brazil [9].

This research work addresses a particular class of synchrotron beamline instruments known as *Double-Crystal Monochromators* and the engineering paradigm shift that was necessary to overcome the existing bottlenecks and improve scientific conditions in the hard X-ray domain. The following subsections are dedicated to a contextualization and an overview of this project.



**Figure 1.3:** Sirius synchrotron light source at the LNLS, in Brazil. Center: schematic drawing of the facility. Top left: aerial view. Top right: top view schematic of the electrons accelerator structures, starting with the *linear accelerator* (LINAC) and going through transport lines, first to the *booster ring* for energy ramp-up, and finally to the *storage ring*; the main tunnel around the accelerators for radiation protection is also indicated. Bottom right: CAD drawing of the magnetic lattice of the storage ring. Bottom left: beamline CAD drawing, indicating front-end components inside the tunnel interface, a primary optics set (in an optical hutch, not shown), and end-station elements (in an experimental hutch, not shown). (Adapted from LNLS’ archive.)



**Figure 1.4:** X-ray sources brilliance (or spectral brightness) evolution from the first X-ray tubes to the last generation synchrotron light sources. As an evidence of the scientific and technological drive, its growth rate is seen to exceed even that of the Moore’s law for the number of transistors on a microchip. (Adapted from CNPEM’s database and <https://ourworldindata.org/>.)

### 1.3 New-Generation Synchrotron Light Sources

At the beamlines, intense photon beams from infrared to hard X-rays can be used in a variety of experimental techniques and methods to investigate how matter works at different length scales (see also Figure 1.2), down to the atomic and molecular levels [5–7, 10]. Hence, synchrotron scientists are always after brighter sources, since higher brightness can be advantageous for almost any experiment [5, 10], be it because of smaller probe beam sizes — often related to spatial resolution — or higher fluxes — with influence on signal-to-noise ratio, overall experiment time and/or time-dependent processes. In other words, brighter sources have the potential of enabling unprecedented *spatial* and *temporal resolutions*, as well as increasing scientific *throughput* and beam time *efficiency*.

As depicted in Figure 1.4, this drive is so strong that the rate of synchrotron brightness gain over the years even beats the well-known Moore’s law for the fast improvement rate of semiconductors — with an 1000-fold factor taking roughly 20 years for the number of transistors whereas about 12 years for synchrotron brilliance. From a fundamental aspect, the path toward ultimate synchrotron brightness is related to the pursuit of the so-called *diffraction-limited storage rings* (DLSRs). In this case, the radiation emittance is limited by the diffraction-limited photon emittance while the electron emittance can be significantly smaller<sup>1</sup> [6, 11]. To achieve this, however,

<sup>1</sup>The emittance is a quantity given by the product of the beam size by its angular divergence, being also defined by the convolution between the electron beam parameters and photon properties at a given wavelength.

extreme focusing capabilities for the electron beam in the storage ring is required, posing severe theoretical and engineering challenges. The latest major step in this direction, namely, the emergence of the so-called fourth-generation light sources, took a couple of decades to move from conceptual levels to technically and economically feasible projects (see Figure 1.4).

Compared to the previous generation, one to two orders of magnitude gain in brightness have become possible thanks to technological progress mainly in: small-aperture vacuum systems, precision machining and alignment, and non-linear beam dynamics in accelerator technology<sup>2</sup> [6, 10, 12]. Yet, beyond the technical challenges in the design, development, installation and control strategies of the accelerators per se [14, 15], increasingly more stringent requirements are expanded to special foundations, buildings and infrastructure as well [16–18]. Indeed, over the years, experience has shown that consistent delivery of bright and stable sources to the beamlines are strictly dependent on aspects such as: i) ground motion and vibrations, resulting from settling, water-content effects and earthquakes to other natural and cultural sources; and ii) thermal effects in the accelerators [19–22].

As new green-field facilities, the MAX IV, in Sweden, started operation in 2015, whereas Sirius/LNLS, in Brazil, had its first experiments in 2020. In parallel, many other facilities are at different phases of upgrade from existing third-generation storage rings, including: the ESRF (European Synchrotron Radiation Facility) and Soleil, in France; the DLS (Diamond Light Source), in the UK; the ALS (Advanced Light Source) and the APS (Advanced Photon Source), in the USA; and the SPring-8, in Japan [6, 12]. The ESRF took the lead, already resuming user operations in 2020 after a relatively short shut-down time.

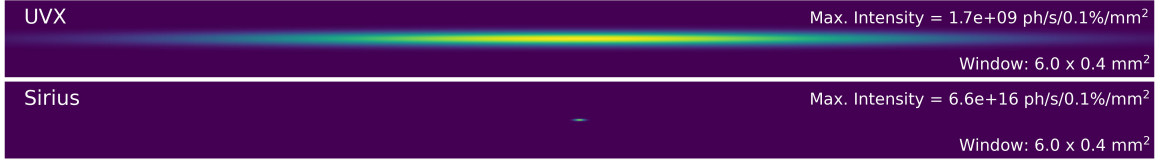
In a nutshell, this last step in the reduction of the emittance and the gain in brightness comes from a corresponding reduction in the horizontal emittance of the electron beam in the storage ring — once third-generation storage rings already operate with vertical emittances near the diffraction limit [12]. Now, the largely asymmetric beams that were typical from previous generations become much more symmetrical. Figure 1.5 shows an example through section-view intensity simulation results of 10 keV photon beams at the source position. Parameters of a second-generation (UVX/LNLS) and a fourth-generation (Sirius/LNLS) light sources are used: in addition to a maximum intensity increase by more than seven orders of magnitude in this particular case, the beam in the bottom graph is tiny and far more symmetrical than in the top one.

These changes also promote an increase in the transversal coherence of the light, particularly at higher energies (i.e., smaller wavelengths), which allows for unprecedented scientific opportunities thanks to: higher illumination uniformity for imaging experiments, broadened options for coherence-based characterization methods, higher resolution possibilities in some spectroscopy (i.e., analysis as a function of energy) methods, and extreme nanofocusing limits [6, 7, 10, 12].

---

<sup>2</sup>A detailed description of accelerators physics and technologies go beyond the scope of here, but a comprehensive discussion can be found in [5, 6, 10–13] and the references therein.





**Figure 1.5:** Photon source size comparison between the UVX storage ring, the former second-generation light source at the Brazilian Synchrotron (LNLS), and Sirius, its new fourth-generation light source. The intensity-plot simulations show the photon flux in a window of 0.4 mm in vertical by 6 mm in horizontal considering an undulator source (insertion device) and the photon energy of 10 keV. The wide aspect ratio required for the windows provides a sense of the large asymmetry of the photon sources of earlier-generation synchrotrons, whereas the direct comparison between plots highlights the significant beam size (and asymmetry) reduction. The caption indicates the tremendous increase in intensity/flux. [Courtesy of Sergio Lordano from LNLS' Optics Group]

## 1.4 Next-Generation Beamlines Challenges

Naturally, with the new generation of storage rings, the quality of the new science will be limited by the performance of the weakest component in this chain [10], such that a parallel effort has been, and will continue to be, necessary in the development of beamline instrumentation to completely explore the potential offered by photon beams with higher brightness and coherence level. Indeed, similarly to the progress achieved in the accelerators domain, enabling technologies are needed at the beamline side to make the foreseen scientific opportunities possible [8].

For instance, in X-ray optics, improvements in windows, absorbers, mirrors and monochromators are required to reach optimal transfer of transversal coherence from the source to the sample [8]. As a reference number, X-ray mirrors may be specified with sub-Angstrom surface quality, and slope errors in the order of tens of nrad RMS (root mean square) for wavefront preservation [8, 23], which needs to be accomplished including manufacturing and metrology limitations, fixation and thermal management. Regarding detectors, clear demands include reaching shorter timescales, down to the milli- and microsecond range, and extending operation toward higher photon energies ( $> 20$  keV) [8, 24, 25]. Furthermore, data management is a crucial aspect, since many beamlines already today easily generate multiple terabytes of data per experiment [8]. This places serious charges in terms of data acquisition, storage, transfer and analysis, with the likelihood of increase by orders of magnitude in the near future, given the ever pushing tendency of increase in spatial and temporal resolutions.

At this point, it is worth noting that fulfilling nominal optical layouts and detection schemes for beamline designs in reality carries many other very specific needs. First of all, regarding radiation safety in terms of X-rays and gamma rays, shielding hutches and access protocols must be present, along with dedicated safety components that include collimators, shutters and beam stops, as well as local shielding around specific optical components [26, 27]. These not only narrow down design freedom, but also

consume significant design effort and financial resources, which might otherwise be redirected to other performance-related ends.

Next, managing photon beams that may exceed 10 kW in total power and reach hundreds of W/mm<sup>2</sup> in power density is one of the main challenges in beamline components — whether in complementary masks, slits and shutters, or the extremely sensitive mirrors and monochromators [27–30] —, which require water and cryogenic cooling solutions that go beyond the technology available from similar fields, such as high energy lasers [31]. Another ubiquitous part of beamline design is vacuum technology, often ultra-high vacuum (UHV), which is required not only to prevent/reduce photon absorption and scattering in the beam path but also to physically preserve sensitive optical elements and samples (see [32] for an example). Lastly, just as experienced at the storage ring domain, an increase in the sophistication and sensitivity of the experiments — with smaller photon beam sizes reaching a few tens of nanometers in the new X-ray microscopes, and the rise of longer beamlines reaching hundreds of meters — has been pushing special foundations, buildings and infrastructure requirements also in beamline designs [16, 33–36].

To the purposes of this thesis, particular interest concerns two correlated themes that are well-established in other industries (such as semiconductors) but have emerged only very recently (virtually along with and as part of this research project) in the beamline instrumentation scope, namely: i) positioning control in the order of single-digit nanometers and nanoradians; and ii) high-performance continuous motion scans. The first is related to improved spatial resolution, whereas the latter span from reduced radiation damage to samples and higher throughput to time-resolved studies and new experimental approaches [34, 35, 37–40]. In that sense, elements defining the photon probe as well as sample systems must be considered, while unprecedented challenging transient thermal effects may arise and need to be dealt with. This trend, however, leans toward design and optimization charges that are in contrast with standard beamline development workflows.

## 1.5 Difficulties in Beamline Design Optimization

A beamline is composed of tens to hundreds (or thousands) of sub-components. Some of them, such as masks and shutters, may face mainly challenging thermo-mechanical stresses due to up to multi-kW power loads, for instance. Some photon detectors, in turn, may be quite expensive and require radiation hardness, large dynamic ranges, and sufficient spatial and temporal resolutions. Yet, for being more case-specific and multidisciplinary, sample environments and optical components tend to be the most critically affected by a number of practical challenges in beamline design for optimization and ultimate performance, as discussed below.

### 1.5.1 Physical Boundaries and Application Match

First of all, the very same physics that allows for the investigation of different materials properties using different photon wavelengths creates fundamental absolute boundaries for beamline instrumentation. This means that the realization of reflective, refractive or diffractive optics, as well as the sensitivity and efficiency of photon beam sensors and experimental detectors, may be very specific — and not only considering the wide range from the infrared to the X-ray domain, but even within relatively narrow wavelength ranges, due to, for example, absorption and critical angle effects.

Hence, just as constructing an ideal and universal X-ray detector has thus far proved impossible, with a diversity of detection technologies and concepts being developed for families of applications [8], also absorbers, mirrors and monochromators have been developed with specific technologies, which can be roughly organized in generic groups or classes. Furthermore, each beamline optical design tends to be tailored to the particular properties of each storage ring, source type, experimental method and main scientific cases. As such, it turns out that every beamline optical component in the world is subject to essentially a unique condition, creating hurdles in achieving (or evolving toward) ultimate design optimization, as compared to other high-end industrial systems with serial production. Indeed, given the costs and timescales involved, developing completely new beamline systems for each individual application is often seen as a not viable approach [8].

### 1.5.2 Financial and Personnel Constraints

Another fact is that synchrotron facilities are generally associated to national or international research centers which rely on governmental funding, being subject to dynamic political scenarios. Thus, managers have already a limited amount of financial resources to handle priorities of many stakeholders in accelerator, beamline and infrastructure projects inside the institutes — since: i) the storage rings are under continuous evolution; ii) synchrotron facilities typically host a few tens of beamlines with various demands and scientific programmes; and iii) multiple complementary systems are needed, including power, water and cryogenic plants, preparation labs and computer centers, to name a few. And, on top of that, there is also the continuous competition with other governmental plans and a large uncertainty in terms of cash flow, which, in terms of dedicated long-term development projects, face completely different challenges than those found in private businesses and relatively stable/predictable markets.

In many cases, heavier instrumentation research programmes find their way via collaborative projects established among a few facilities, sharing costs and mitigating the sensitivity to local fluctuations, but at the same time increasing the complexity of these programmes due to, for instance, broadened scopes, larger numbers of stakeholders, increased communication and documentation needs, and different cultures and policies. Also related to the financial boundaries and collaboration needs is the fact the institutes are capable of keeping only a limited number of people in their staff, which



must share: i) scientific and technical demands; ii) development and operational needs; and iii) a wide range of technical fields and applications. This makes the development of tens to hundreds of instruments with ultimate performances distributed over the many beamlines an unfeasible target.

### 1.5.3 Suppliers Constraints

So, another fundamental pool of actors in synchrotron beamline technology is the companies with business in scientific instruments and beamline instrumentation. Indeed, with different backgrounds, from university and/or synchrotron spin-offs to market diversification in larger groups, these companies are able to complement synchrotron in-house technical capabilities, boost the development of common synchrotron needs, and eventually reach higher expertise levels. However, many of these companies work on narrow profit margins and/or have constrained infrastructure resources, which may limit their capacity of taking risks or realizing innovative designs. Added to that, are the facts that: i) standardization for commercial purposes may be difficult for different beamline customers, while also going against application-specific optimization, particularly concerning optical components; ii) the companies are oftentimes assigned with a limited scope of a given beamline component/project, so that globally optimized solutions may be out of reach; and iii) from the outside, it can be difficult to raise an exhausting set of specifications, and/or to react to higher-level project changes, which certainly impairs ultimate operation.

### 1.5.4 Culture and Way of Working

All these points, together with the exploratory nature of a research environment — which is prone to continuous changes — and the dynamic aspect of the cases of interest in the scientific community, have historically promoted a pragmatic *best-effort* approach in beamline instrumentation design. Surely, for several decades, most of the times it has been reasonable and advantageous to design and install instruments that, even if not ideal, would be able to work to some extent and allow sufficient operational levels to quickly provide meaningful scientific output. Later, incremental upgrades might be proposed, after experimentally finding that actually a different cooling strategy might be needed, or a different set of crystals would be preferable, or a different combination of motion axes for the sample would offer extended capabilities.

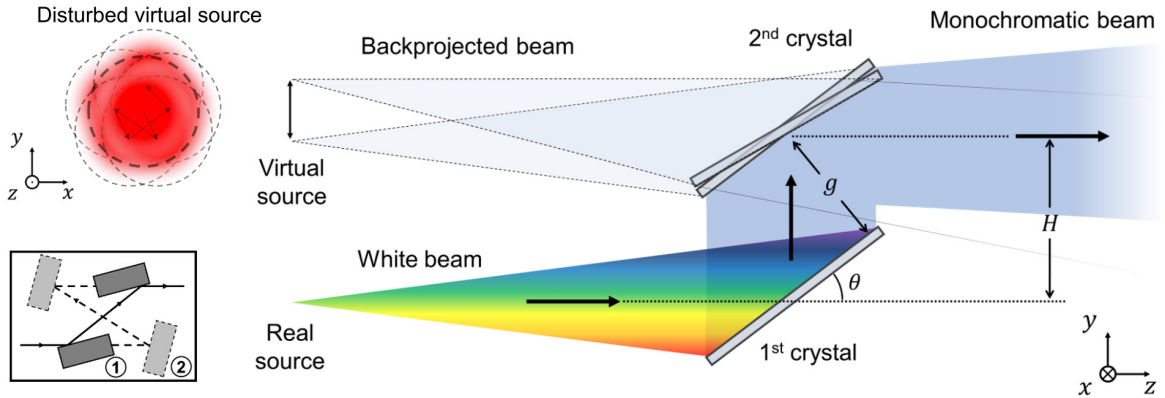
Still, the effectiveness of this approach partly relies on *forgiveness factors* associated to the experimental analyses being carried out, whether in terms of time, spatial and/or spectral resolutions. Then, some of the questions that started to be raised in some of the third-generation light source beamlines and are now strongly reinforced for the fourth-generation ones are about: i) the sufficiency of this way of working, or the “radius of convergence” for this solution; and ii) what alternatives there are to the extreme cases, when needed.

## 1.6 Double-Crystal Monochromators

Monochromators are beamline instruments used in experiments or processes that require specific energy and/or angular distributions — i.e., photons limited within a narrow band of energy and/or beams with controlled divergence — to achieve the desired sensitivity, focusing capacity and/or signal-to-noise ratio (see also Section 1.1). Thus, energy and divergence can be filtered from the incoming synchrotron photon beam according to each beamline optical layout, which may be performed by different elements in different types of embodiment.

For instance, various arrangements with diffraction gratings and slit systems can be used for visible, ultraviolet, or extreme ultraviolet light, whereas multiple solutions and designs based on monocrystalline crystals or multi-layered structures are typically found for X-rays. Hence, each beamline may choose from none to more than one monochromator (used alternatively or in series) in its layout, depending on its particular experimental methods and scientific cases. When present, they are commonly part of the primary optics set, in an optical hutch close to storage ring tunnel (see Figure 1.3), but many examples can be found at other positions as well. And then, they are often considered the “heart” of the beamline, because many of the properties of the experimental beam will only be as good as the monochromator makes them.

Among the different types, a Double-Crystal Monochromator (DCM), represented in Figure 1.6, is defined by an arrangement of two crystals in which: i) the desired photon energy/wavelength is selected by the incidence angle  $\theta$  of the beam with respect



**Figure 1.6:** Double-Crystal Monochromator (DCM) conceptual representation. Right: Side-view showing the two crystals used to filter the desired energy/wavelength from the incoming so-called white beam as a function of the incidence angle  $\theta$ , with a nominal fixed offset  $H$  for the monochromatic beam given by the distance between crystals  $g$ . The geometrical effect of small angular variations between the crystals compromises the nominal parallelism between the beams and moves the virtual source around, disturbing the nominal beam size and position. Top left: Front-view depicting a disturbed virtual source due to mechanical instabilities in the crystals. Bottom left: Example of the varying distance  $g$  for two different working angles.

to the surfaces of the crystals according to Bragg’s law of diffraction [41]; and ii) the monochromatic beam is kept at a fixed offset  $H$  with respect to the incoming beam by adjusting the distance  $g$  between the crystals as a function of  $\theta$  [42, 43]. With crystals typically made of pure blocks of silicon or germanium, this configuration is suitable for beamlines working in the range of tender to hard X-rays, i.e., from about 2 to 100 keV. And the main interest on DCMs, making them one of the most popular choices, is truly its fixed-exit characteristic, ideally creating a “perfect source” that would spare complementary beamline realignment regardless the selected operational energy.

The high complexity related to the design and operation of monochromators is derived from the many topics discussed in the previous sections. Indeed, severe operational conditions in UHV environment, high power loads and densities, high radiation levels, and high-precision positioning accuracies (for different objects with respect to the beam and each other) are frequently combined in a single instrument. Besides that, it is impossible for designers to address unique sets of parameters and requirements in absolute long-lasting solutions, which becomes a serious issue toward ultimate performances. And yet, the recent advances in accelerators technology and experimental techniques started to place unprecedented pressure on monochromators operations.

### 1.6.1 The Need for a Breakthrough

In 2014, the European synchrotron, the ESRF, in Grenoble, hosted the Workshop on X-ray Double-Crystal Monochromators [44], gathering most of the worldwide experts in the field. The conclusion was that, notwithstanding significant dedicated design and upgrading efforts in the previous years, many DCMs had become bottlenecks to their beamline performances and, in addition to that, no existing DCM would be able to meet some of the requirements of the new-generation beamlines and storage rings.

Specifically, apart from challenging thermal effects resulting from the interaction of the X-rays with the crystals, the main and ubiquitous issue consisted in mechanical vibration levels. This is because errors/changes in the angle between the crystals, may: i) violate the diffraction tolerance limits and harm the outgoing monochromatic beam intensity, if the mismatch is sufficiently large; or ii) even if the angle difference is small, shift the monochromatic beam and its virtual source, as also illustrated in Figure 1.6. Hence, vibrations caused by environmental and operational disturbances may move the probe with respect to the point of interest in the sample and/or increase the apparent beam size, depending on the acquisition rate (or integration time) of the experimental detectors. How critical these effects are in practice is something that is case-specific, depending on the overall optical design of the beamline, the particular experimental method being used, the sample setup and, naturally, the nominal beam sizes and achievable vibration levels in the DCM. Yet, a common understanding of existing limitations was clear.

At the time, it was agreed that for most cases vibration levels in the order of 10 to 20 nrad RMS (root mean square) would be required to preserve the quality of the sources of third and fourth-generation synchrotrons — for source sizes of about 5  $\mu\text{m}$ .

Preferably, this should consider the frequency range between 1 Hz and 2.5 kHz, that covers most of beamline experiments acquisition rates. Nonetheless, after many years of incremental upgrades of traditional DCM designs, the state-of-the-art performance in fixed-energy operation was still limited at 20 and 50 nrad RMS [45, 46], for horizontal- and vertical-offset DMCs, respectively<sup>3</sup>. But yet, during motion, due to additional disturbances introduced by stepper motors and mechanical bearings, angular variations easily exceeded the  $\mu$ rad levels. Hence, if stand-still operation of DCMs already tended to negatively affect the beam delivery, their scanning perspectives were orders of magnitude far from realizing the potential of spectroscopy experiments that would become available with the unprecedented brightness of the new-generation light sources.

## 1.7 The High-Dynamic Double-Crystal Monochromator

With a tradition in in-house development, and the technical and financial opportunity created by the construction of Sirius, the LNLS therefore decided for a novel approach to face the DCM challenge. The outcome of this endeavor is the so-called High-Dynamic Double-Crystal Monochromator (HD-DCM), which gives rise to a new sub-class of instruments within the DCM universe.

This thesis addresses technical aspects related both to the machine with its unique architecture and to the emerging implications regarding its integration in a beamline environment. In that sense, the main research questions under consideration were:

- Given an apparent saturation from the beamline instrumentation technology for DCMs, what kind of architecture would be necessary to overcome the existing limitations? How deep would the changes need to be to enable both stand-still operation with higher stability and equivalent scanning capabilities?
- How to manage the risks of a significantly different design considering the technical challenges, the required investment and the timeline, with the need of the first units already in the early commissioning phase of the first beamlines of Sirius? Would the potential performance gains be truly worth it?
- How a different technology would propagate in the beamline environment? What differences would be found in interfacing/integrating the new instrument with other beamline components for an optimized operation?

The following subsections present how this thesis answers each of the questions posed above.

---

<sup>3</sup>In fixed-energy operation, horizontal-offset DCMs, i.e., those in which the beam is deflected in the horizontal plane and a horizontal offset is created between the incoming beam and the exit monochromatic beam, historically tended to achieve better levels than their vertical-bounce counterparts. This was due to different mechanical arrangements and static disturbance effects. Yet, the choice for one type or another in a beamline is not completely free, since it may depend, for example, on the polarization properties of the photon beam.

### 1.7.1 Mechatronic Architecture

Mapping the DCM technological scenario and studying the standard designs, one would find machines characterized by a *high-stiffness mechanical design concept*, operating either in open-loop or low-bandwidth closed-loop control [45–53]. Moreover, the main design rules might be roughly defined by: i) handling the beam power via water or liquid nitrogen cooling, as needed; ii) being careful about crystal clamping and beam-related thermal deformations; iii) providing a generous set of stacked moving stages covering the degrees of freedom required for positioning and aligning the crystals with respect to the beam and each other; iv) keeping, whenever possible, design flexibility to add/remove crystal sets or change operation parameters for different scientific purposes; v) keeping control dependence to a minimum, preferably relying on “simple, easy to use and reliable” motion options based on stepper motors and piezo-steppers, proven for maintainability and little risk to beamline routine operation; vi) applying standard best-effort practices for mechanical stiffness and attenuation of flow-induced vibrations; and vii) minding vacuum levels and radiation damage.

Yet motion-wise, a closer look would reveal that the fine-positioning and scanning requirements for a next-generation DCM would be actually more closely related to those of modern lithography machines in the semiconductors industry. Indeed, using mature technologies, miniaturization and efficient throughput in chip manufacturing relies on multiple relatively large masses being accurately positioned and/or moved at high speeds and accelerations with resolutions reaching sub-nanometer levels [54, 55]. Hence, the HD-DCM design documented in this thesis proposes an answer to the DCM technological problem by respecting the synchrotron-specific boundary conditions while implementing an entirely different mechatronic architecture according to a *high-bandwidth closed-loop control concept*.

First of all, this means embracing a control-based solution, with extended capabilities at the expense of a higher complexity in design and operation. Next, a compromise between *desirable* science-driven design flexibility and the *required* high-performance levels must be found. This is related to converging and committing to a finite and pragmatic set of specifications via scientific-engineering iterations during the conceptual phase of the project. Then, a systemic approach is absolutely essential, with mechanical, thermal and control aspects being simultaneously and continuously considered and optimized for the machine as a whole since the very beginning.

The desired performance for the HD-DCM is achieved with a DCM embodiment reinvented from scratch, following strict precision engineering principles and high-performance mechatronics design rules [56, 57]. A *high-dynamic* module is implemented in the so-called *crystal cage*, allowing an inter-crystal closed-loop control bandwidth in the order of 200 Hz for superior *disturbance-rejection* and *setpoint-tracking* capabilities. It adopts an *isolated mechatronic architecture*, based on a *minimal set of degrees of freedom* in a *parallel-kinematic arrangement*, using *flexural guiding* and *force actuators*, and including a *reaction mass* that works as a dynamic filter. Sufficiently fine and fast feedback is provided by a *short metrology loop* using embedded optical

interferometers. High-bandwidth control can be reached thanks to a mechanical design with *high-frequency internal modes* and a *control rate* of 20 kHz implemented in a digital controller using FPGA (field-programmable gate array) and a real-time operating system. Simplifying control strategies result from a *collocated design* and *loop shaping technique* [57–59]. Lastly, a decoupled thermal management solution allows for the cryogenic operation of the crystals while preventing thermal expansion issues, preserving the system dynamics, and minimizing flow-induced vibration effects. In addition, a *long-stroke stage* for the crystal cage and a *main rotary system* for the Bragg angle complement the in-vacuum portion of the HD-DCM, whereas an integrated *granite bench* can be used for the primary alignment of the instrument with respect to the synchrotron beam (see Figure 1.7 for a basic impression) — all respecting the global dynamic needs.

### 1.7.2 Development Framework

Beyond certain levels of complexity, design approaches based on trial-and-error and/or best-effort may prove to be upsetting and unrewarding, perhaps never meeting the end goals. Thus, once again benefiting from the experience and know-how from the semiconductor industry, the development of the HD-DCM relies on fundamental predictive modeling and management tools toward a *first-time-right* result. Regarding project management, systems engineering disciplines, including methodical requirements engineering, project phasing, risk assessments, and documentation [60], are key assets. Concerning modeling, besides hand calculations and more common finite-element multiphysics simulations, Dynamic Error Budgeting is a crucial tool in iteratively guiding the mechatronic design and converging to a solution with a predictable performance that fulfills the specifications [61].

Complying with these techniques, satellite experimental setups are carried out along with the design work to mitigate risks and extract data for the models. Some of the relevant themes for the HD-DCM are: i) vacuum compatibility, radiation hardness and disturbance characterization of actuators and sensors; ii) flow-induced vibrations caused by the liquid nitrogen cooling of the crystals; and iii) floor vibration measurement campaigns. Therefore, all considered, even though an entirely new architecture for the HD-DCM is proposed, the predictive design approach presented in this thesis is arguably capable of minimizing development risks to levels that are close to zero when compared to the unpredictable traditional best-effort way. By systematically reducing the uncertainties and increasing the confidence in the instrument under development, there can be not only technical assertiveness but also clearer budgetary estimates and delivery milestones.

### 1.7.3 Integration to the Beamline Environment

In static operation, related to experiments realized with fixed-energy, the HD-DCM can be seen in practice as a stand-alone unit in the beamline environment. This is

approximately the case in asynchronous energy-varying step-scan spectroscopy experiments as well, in which parameters in the beamline X-ray source, mirrors and detectors may need to be correlated to the DCM at every data point but independently set in between, i.e., without any control cross-talk or interdependence. In this case, it suffices to have a consistent network communication and enough settling time for the instruments for each scan step. The fixed-offset high-performance continuous-scan (fly-scan) capabilities introduced by the HD-DCM, however, motivates a large review in the beamline integration architecture, in the optical and performance requirements of related instruments, and in the operation strategies.

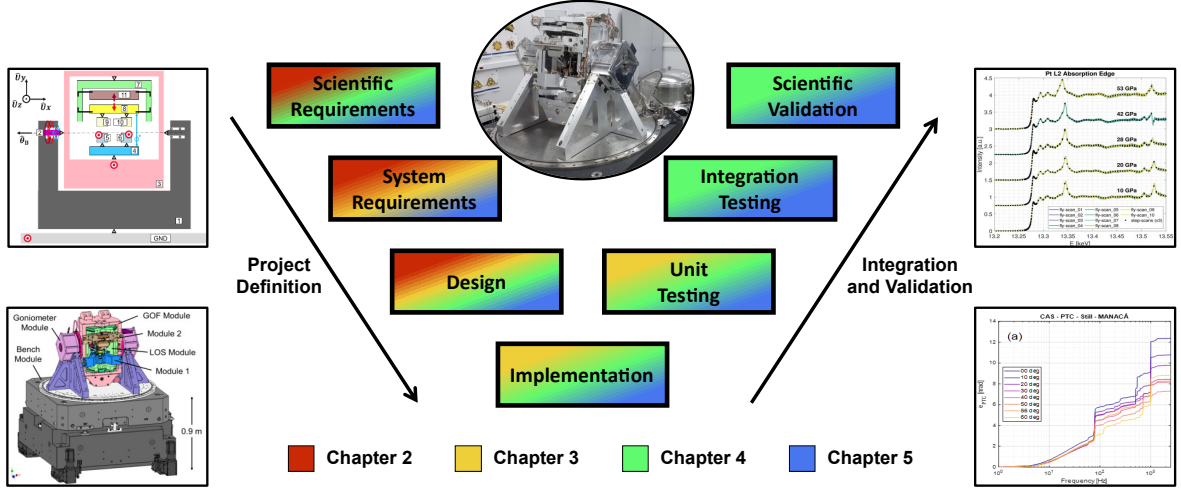
For one thing, probably as a significant difference with respect to the operating scenario of lithography machines, the X-ray emission in tunable beamline sources and the diffraction in the DCM are highly non-linear physical phenomena. As such, an otherwise presumably straightforward energy scan for a given range (say 1 keV) at a given rate (say 0.1 keV/s) may actually require displacement, velocity and acceleration setpoints that differ by several orders of magnitude, depending on the absolute energy values. Besides motion, severe transient thermal effects may also take place and require unprecedented solutions. Hence, scientific interests must be case-specific planned, while scanning optimization strategies must respect energy-tuning tolerances, occasional optical correction needs, and engineering boundaries in the whole beamline optical chain. Furthermore, communication, triggering and synchronization needs between different beamline elements are taken to a completely new level, since very heterogeneous pieces of hardware and software begin to be required to work together as a single and much broader macrosystem that must be managed by a central orchestrator.

These aspects combined foster complex research fields in beamline instrumentation performance and optimization, which claim for dedicated efforts before many of the promising scientific opportunities can be ultimately explored to their full extent. In this thesis, initial steps involving the HD-DCM are reported, having been proven at the MANACÁ (Macromolecular Micro and Nano Crystallography) and the EMA (Extreme Methods of Analysis) beamlines, two of the beamlines that are already regularly open for users at Sirius.

## 1.8 Thesis Outline

The distribution of the content of this thesis reflects one of the goals of this work, namely, bridging and bringing closer the precision mechatronics and the synchrotron engineering communities. As demonstrated by the HD-DCM, it truly seems that the first could be of greater assistance in aiding solving part of the many engineering challenges faced by the latter, which, in turn, has a direct impact on the global scientific output and societal advances.

The four main chapters of the thesis consist of peer-reviewed publications, which are self-contained but intimately interconnected, as schematically outlined within a V-model systems development representation in Figure 1.7. Chapter 2 and Chapter 3



**Figure 1.7:** Schematic overview of the thesis chapters distributed in a V-model representation, with scientific and system requirements, design, implementation, testing and validation that have the HD-DCM as the central character but expand over correlated instruments at the beamline. The insets show a picture of the HD-DCM under assembly in a clean room and representative illustrations of each chapter.

are presented as published in *Precision Engineering*. The first provides an introduction to the DCM problem, the requirements that were elaborated to the HD-DCM, and a comprehensive description of its innovative mechanical design and mechatronic architecture. The latter explores the predictive modeling framework and compares predictions with experimental results. Within the Dynamic Error Budgeting evaluation, *plant* and *disturbance models* are discussed and used in a *bandwidth optimization analysis*, according to a *decentralized control* approach for single-input-single-output controller design via *loop shaping*.

Moving on to the synchrotron domain, Chapter 4 was published in the *Journal of Physics: Conference Series* (JPCS) after the 14<sup>th</sup> *International Conference on Synchrotron Radiation Instrumentation* (SRI2021). It proposes a short review with a didactic examination on the fundamental conceptual differences between the HD-DCM and standard DCM mechanical architectures. Furthermore, an early global beamline integration architecture including other beamline instruments is considered, and stand-still and preliminary scanning performances at the beamline are displayed. Chapter 5, published in the *Journal of Synchrotron Radiation*, provides the latest status of HD-DCM at Sirius beamlines, overcoming some of the initial beamline integration issues and already enabling unprecedented high-performance fixed-exit scanning spectroscopy experiments — with time reductions of up to two or three orders of magnitude as compared to conventional step-scan standards. A dedicated motion analysis for the positioning problem in scanning operation, a tuning/synchronization tolerance evaluation method, and noise-related challenges in achieving X-ray-based performance measurements for the HD-DCM are addressed as well.

Conclusions and recommendations are summarized in Chapter 6. Finally, to close



the thesis, a complementary set of sections is presented as appendices, extending the discussion of a few topics beyond the scope of the publications presented in chapters 2, 3, 4 and 5. Firstly, Appendix A adds to Chapter 2 in what concerns geometrical parameters that guided the specifications and design choices for the HD-DCM. Then, Appendix B expands the mathematical description regarding the Dynamic Substructuring modeling work and the chosen modal state-space representation within the Dynamic Error Budgeting methodology. Its main purpose is to provide to the less experienced reader a more comprehensive step-by-step modeling summary guide than what is explicitly shown in Chapter 3. Lastly, Appendix C provides additional information on the experimental control implementation aspects of the HD-DCM, by addressing position- and machine-specific considerations, as well as plant identification and controller design details.

## References

- [1] Fearon D. *et al.* 2021 *Acta Cryst. A* vol. 77 C196
- [2] Lahlali R. *et al.* 2015 *BMC Plant Biol.* **15**(1) 1
- [3] Withers P.J. 2015 *Philos. Trans. R. Soc. A* **373**(2036) 20130157
- [4] Cotte M. *et al.* 2019 *Synchrotron Radiat. News* **32**(6) 34
- [5] Robinson A.L. 2015 *Synchrotron Rad. News* **28**(4) 4
- [6] Tavares P.F. *et al.* 2018 *J. Electron Spectros. Relat. Phenomena* **224** 8
- [7] Mino L. *et al.* 2018 *Rev. Mod. Phys.* **90**(2) 025007
- [8] Susini J. *et al.* 2014 *J. Synchrotron Rad.* **21**(5) 986
- [9] Liu L. *et al.* 2014 *J. Synchrotron Rad.* **21**(5) 904
- [10] Eriksson M. *et al.* 2014 *J. Synchrotron Rad.* **21**(5) 837
- [11] Willmott P. 2019 *An Introduction to Synchrotron Radiation: Techniques and Applications* (John Wiley & Sons)
- [12] Hettel R. 2014 *J. Synchrotron Rad.* **21**(5) 843
- [13] Hwu Y. and Margaritondo G. 2021 *J. Synchrotron Rad.* **28**(3) 1014
- [14] Tavares P.F. *et al.* 2018 *J. Synchrotron Rad.* **25**(5) 1291
- [15] Liu L. *et al.* 2021 *Proc. 12th Int. Particle Acc. Conf. (IPAC'21)* (JACoW Publishing) 13–18
- [16] Simos N. 2019 *Synchrotron Facilities: Vibration and Stability Challenge*
- [17] Rodrigues F. *et al.* 2019 *Synchrotron Rad. News* **32**(5) 20
- [18] Chen J. *et al.* 2019 *Synchrotron Radiat. News* **32**(5) 27
- [19] Krebs G.F. 1997 *Proc. 1997 Particle Acc. Conf.* vol. 1 (IEEE) 793–795
- [20] Cheng H. *et al.* 1999 *Proc. 1999 Particle Acc. Conf.* vol. 2 (IEEE) 1150–1152
- [21] Simos N. *et al.* 2019 *Synchrotron Radit. News* **32**(5) 4
- [22] Marques S.R. *et al.* 2022 *Proc. 13th Int. Particle Acc. Conf. (IPAC'22)* (JACoW) 226–229
- [23] Siewert F. *et al.* 2014 *J. Synchrotron Rad.* **21**(5) 968
- [24] Denes P. and Schmitt B. 2014 *J. Synchrotron Rad.* **21**(5) 1006
- [25] Hatsui T. and Graafsma H. 2015 *IUCrJ* **2**(3) 371
- [26] Liu J.C. *et al.* 2006 *Rad. Meas.* **41** S156

- [27] Volpe L.M. *et al.* 2017 *Proc. 9th Mech. Eng. Des. of Synchrotron Radiat. Equip. and Instrum. (MEDSI'16)* (JACoW Publishing) 324–326
- [28] Mochizuki T. *et al.* 1998 *J. Synchrotron Rad.* **5**(4) 1199
- [29] Mills D.M. 1993 *High Heat Flux Engineering* vol. 1739 (SPIE) 456–463
- [30] Bilderback D.H. *et al.* 2000 *J. Synchrotron Rad.* **7**(2) 53
- [31] Anthony F.M. 1995 *Opt. Eng.* **34**(2) 313
- [32] Nicklin C. *et al.* 2016 *J. Synchrotron Rad.* **23**(5) 1245
- [33] Kearney S.P. *et al.* 2019 *Synchrotron Radiat. News* **32**(5) 13
- [34] Nazaretski E. *et al.* 2017 *J. Synchrotron Rad.* **24**(6) 1113
- [35] Villar F. *et al.* 2018 *Synchrotron Radiat. News* **31**(5) 9
- [36] Cacho-Nerin F. *et al.* 2020 *J. Synchrotron Rad.* **27**(4) 912
- [37] Hidas D. *et al.* 2022 *Nucl. Instrum. Methods Phys. Res. A* **1031** 166505
- [38] Deng J. *et al.* 2019 *Rev. Sci. Instrum.* **90**(8) 083701
- [39] Schropp A. *et al.* 2020 *J. Appl. Cryst.* **53** 957
- [40] Bornmann B. *et al.* 2019 vol. 2054 (AIP Publishing) 040008
- [41] Ashcroft N.W. 2003 *Solid State Physics* (Thomson Press (India) Ltd)
- [42] Hastings J.B. 1977 *J. Appl. Phys.* **48**(4) 1576
- [43] Lemonnier M. *et al.* 1978 *Nucl. Instrum. Methods* **152**(1) 109
- [44] European Synchrotron Radiation Facility (ESRF) 2014 *Double Crystal Monochromator Workshop* <http://www.esrf.eu/home/events/conferences/2014/double-crystal-monochromator-workshop.html>, accessed: Oct. 1st, 2021
- [45] Kristiansen P. *et al.* 2015 *J. Synchrotron Rad.* **22**(4) 879
- [46] Kristiansen P. *et al.* 2016 *J. Synchrotron Rad.* **23**(5) 1076
- [47] Kelly J. *et al.* 2013 *J. Phys. Conf. Ser.* **425**(5) 052009
- [48] Waterstradt T. *et al.* 2018 *Sub-20-nrad Stability of an LN<sub>2</sub>-Cooled Vertical-Offset Double-Crystal Monochromator*. Presented at MEDSI'18 in Paris, France, unpublished
- [49] Baker R. *et al.* 2018 *Proc. 10th Mech. Eng. Des. of Synchrotron Radiat. Equip. and Instrum. (MEDSI'18)* (JACoW Publishing) 440–444
- [50] Dolbnya I.P. *et al.* 2018 *J. Synchrotron Rad.* **26**(1) 253
- [51] Fan Y. *et al.* 2020 *Nucl. Instrum. Methods Phys. Res. A* **983** 164636
- [52] Wu J. *et al.* 2021 *Nucl. Instrum. Methods Phys. Res. A* **988** 164872
- [53] Baker R. *et al.* 2021 *ESRF Double Crystal Monochromator - Design and Working Modes*. Presented at MEDSI'20 in Chicago, USA, unpublished
- [54] Butler H. 2011 *IEEE Control Syst. Mag.* **31**(5) 28
- [55] Heertjes M.F. *et al.* 2020 *Proc. 2020 Am. Control Conf. (ACC)* (IEEE) 3686–3703
- [56] Soemers H. 2011 *Design Principles for Precision Mechanisms* (T-Pointprint)
- [57] Schmidt R. *et al.* 2011 *The Design of High Performance Mechatronics: High-Tech Functionality by Multidisciplinary System Integration* 2nd edn. (IOS Press)
- [58] Skogestad S. and Postlethwaite I. 2007 *Multivariable Feedback Control: Analysis and Design* vol. 2 (John Wiley & Sons)
- [59] Witvoet G. *et al.* 2017 *Proc. 2017 IEEE Conf. on Control Tech. and Appl. (CCTA)* (IEEE) 726–731
- [60] Faulconbridge I. and Ryan M. 2015 *Introduction to Systems Engineering* (Argos Press)
- [61] Jabben L. 2007 *Mechatronic Design of a Magnetically Suspended Rotating Platform* Ph.D. thesis Delft University of Technology



---

## The Mechatronic Architecture and Design of the High-Dynamic Double-Crystal Monochromator for Sirius Light Source

---

### Abstract

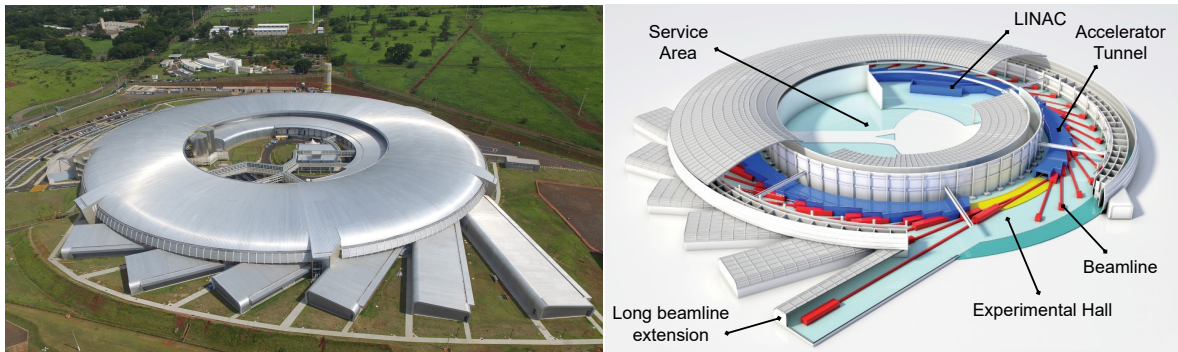
The High-Dynamic Double-Crystal Monochromator (HD-DCM) has been in development since 2015 for X-ray beamlines of Sirius, the 4th-generation light source at the Brazilian Synchrotron Light Laboratory (LNLS). Being the first DCM to implement an isolated mechatronic architecture with high closed-loop performance, its development was based on predictive design via the Dynamic Error Budgeting (DEB) workflow to deliver positioning performance improvements by factors of 5 and 100 with respect to state-of-the-art DCMs, in fixed and scanning modes, respectively — which not only increases beam stability in conventional operation, but also enables unprecedented high-stability spectroscopy perspectives. After introducing the role of the instrument within the scope of X-ray beamlines, this paper discusses its innovative architecture through its detailed mechanical design. The achieved inter-crystal parallelism of 10 nrad RMS (1Hz-2.5kHz) results from a systems approach, following strategic control-oriented design, thermo-mechanical decoupling, the minimization of moving degrees-of-freedom, disturbance management, including flow optimization and the selection of smooth force actuators, and the implementation of embedded short-loop high-accuracy metrology.

## 2.1 Introduction

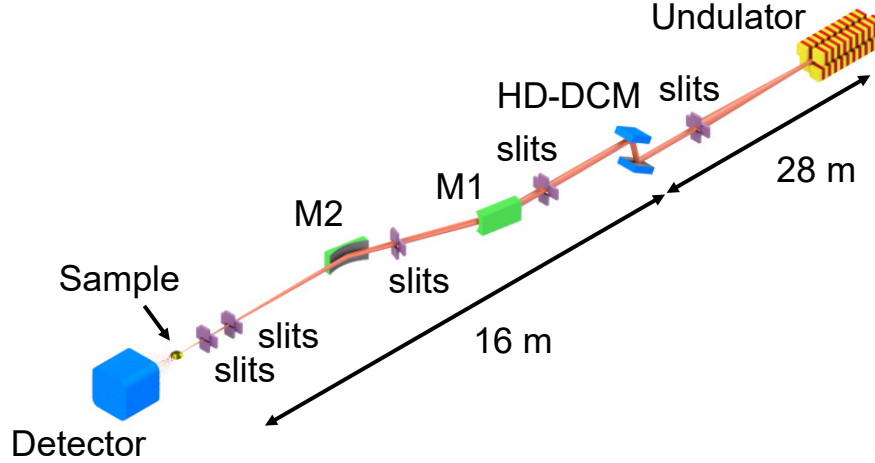
Synchrotron light sources are broad-band-spectrum photon sources, producing small and highly collimated beams of photons from infrared up to hard X-rays, which allow for broad-band scientific research and industrial applications, with so-called samples in fields ranging from biology, chemistry and medicine, to earth, energy and materials sciences. Since a few years, a 4<sup>th</sup> generation of storage ring light sources have been emerging to push the X-rays brightness and coherence fraction to unprecedented levels in the field, so that a breakthrough has been expected in science opportunities in terms of temporal and spatial resolutions [1, 2]. Sirius, shown in Figure 2.1, is a 4<sup>th</sup> generation 3 GeV low-emittance electron storage ring, at the Brazilian Synchrotron Light Laboratory (LNLS), at the Brazilian Center for Research in Energy and Materials (CNPEM), in Campinas, Brazil [3]. By the end of 2021, 5 beamlines were already open for external users and around 10 more in different stages of design, assembly and commissioning.

Beamlines are the beam transport lines, i.e. arrangements of: optical elements, used to collect, monochromatize and focus the beam to the sample; sample manipulators, to position the sample with respect to the beam, and sample setups, with special sample environments for gases, temperature, pressure and magnetic fields, for example; and detectors, that finally capture the outcome of the interaction of the photons with the sample, generating the data to be analyzed. With absorption, scattering, diffraction, fluorescence and imaging techniques, among others, matter properties and processes can be investigated in unmatched ways [4]. As an example, Figure 2.2 shows the optical layout of the MANACÁ (MAcromolecular Micro and NAno CrystAllography) diffraction beamline, the first to start operating in Sirius and to use the monochromator presented here.

The so-called monochromators are beamline instruments used in experiments or



**Figure 2.1:** Sirius 4th-generation 3 GeV low-emittance synchrotron light source at the LNLS/CNPEM, Campinas, Brasil. Left: Aerial view. Right: Schematic orthographical view, highlighting: the linear accelerator (LINAC); the accelerator tunnel; the beamlines; the experimental hall and the beamline extensions; and the inner service area. [Source: CNPEM archive]



**Figure 2.2:** Optical layout of the MANACÁ crystallography beamline at Sirius, with: the undulator, as the photon source; slits; the monochromator (HD-DCM); the focalizing mirrors (M1 and M2); the sample; and the detector. The distances between the monochromator and the source and the sample are shown out of scale for reference. [Source: Sirius MANACÁ Group]

processes that require specific energy and/or angular distributions (i.e. photons limited within a narrow band of energy and/or beams with controlled divergence) to achieve the desired sensitivity, focusing capacity and/or signal-to-noise ratio (SNR). Thus, energy and divergence are filtered from an incoming beam depending on the beamline requirements, which may be performed by different elements in very different types of monochromators. For example, various arrangements with diffraction gratings and slit systems can be used for visible, ultraviolet (UV), or extreme ultraviolet (EUV) light, whereas multiple solutions and designs based on monocrystalline crystals or multilayered structures are typically found for X-rays.

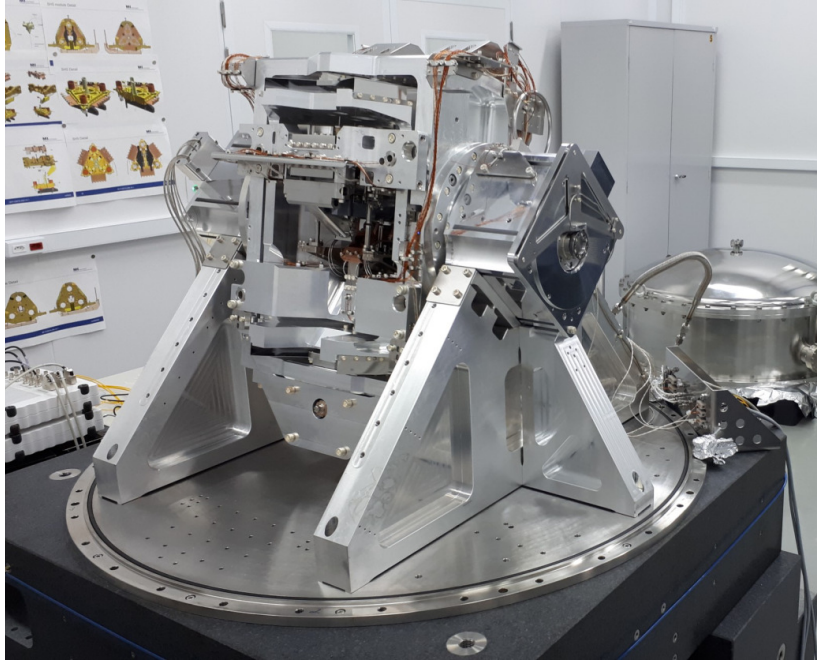
The high complexity related to the design and operation of monochromators starts with the typical combination of severe operational conditions, such as: ultra-high vacuum (UHV) environment, to prevent contamination of the optical elements and dispersion of the beam from interaction with gas molecules; high power loads and densities, that may reach the kW range and hundreds of  $\text{W}/\text{mm}^2$ , respectively, leading to high thermal stresses and deformations and requiring sophisticated water and cryogenic cooling schemes; high radiation levels; and high-precision positioning accuracies for different objects with respect to the beam and to each other. On top of that, beamlines typically have a unique set of parameters and requirements, making it impossible for monochromator designers to reach absolute long-lasting solutions. Nevertheless, to allow the experiments to profit from the progress of the new-generation storage rings, the beamline instruments must perform accordingly.

The instrument described in this paper belongs to a particular class of monochromators, namely, the so-called fixed-exit X-ray Double-Crystal Monochromators (DCMs). Since the first instruments developed in the late 1970s and early 1980s [5–9], incremental upgrades have been gradually implemented over these four decades to adapt

to more stringent requirements of synchrotrons over time [10–17]. In general, this evolutionary approach has remained in the synchrotron community even after the Workshop on X-ray Double-Crystal Monochromators (DCM), held in 2014 by the European Synchrotron Radiation Facility (ESRF) in Grenoble [18], in which a great number of worldwide experts in the field concluded that no existing DCM would be able to meet some of the requirements of the new-generation beamlines.

Taking the challenge with a different approach, the LNLS started the development of a new type of DCM in 2015, with strong paradigm changes. Indeed, in its core, the so-called High-Dynamic DCM (HD-DCM) [19–21], which is depicted in Figure 2.3, replaces the existing open-loop or low-bandwidth high-stiffness mechanical designs by an isolated mechatronic architecture with high-bandwidth closed-loop control. This allows it improving some key performance indicators by up to two orders of magnitude with respect to corresponding vertical-bounce state-of-the-art DCMs, not only meeting clearly stricter requirements of new-generation beamlines, but also eventually creating new scientific opportunities with *enabling technology*. By the end of 2020, two units of the HD-DCM were already available for the commissioning and early operation of the MANACÁ and the EMA (Extreme condition x-ray Methods of Analysis) beamlines at Sirius. Next, by 2022-2023, two more beamlines will receive a new member of the HD-DCM family, the so-called HD-DCM Lite, which is currently under development for slightly different specifications.

This article presents in details the innovative mechatronic design of the HD-DCM.



**Figure 2.3:** The HD-DCM, developed by the LNLS for Sirius X-ray beamlines, according to an innovative isolated mechatronic architecture for improved positioning performance. For visibility of the in-vacuum mechanics, the system is shown in the assembly clean-room before the vacuum vessel is mounted.

First, a background about DCMs is introduced in Section 2.2; next, the engineering specifications are described in Section 2.3; then, the architecture of the HD-DCM and its mechatronic design, reached via the predictive modeling approach using the Dynamic Error Budgeting (DEB) [22], is detailed in Section 2.4; after that, conclusions and discussions are elaborated in Section 2.5; lastly, a list of abbreviations is provided in Section 2.A. The associated DEB, including the detailed predictive modeling workflow, and comparisons between predictions and experimental results at the MANACÁ beamline are presented in [23]. A further elaborated discussion on geometry aspects, together with calibration strategies and commissioning results with the synchrotron beam, is given in [24].

## 2.2 Background

Before presenting the specifications and diving into the details of the design of the HD-DCM, it is necessary to start by explaining the nominal DCM geometrical concept and the associated limitations that have been recently found in traditional DCM designs, so that the architectural alternatives proposed by the HD-DCM can be properly understood.

A DCM in an X-ray beamline is defined by an arrangement of two crystals (typically, pure blocks of silicon or germanium) according to two basic requirements. Firstly, the desired photon wavelength or energy is defined by the incidence angle of the beams with respect to the surfaces of the two subsequent crystals according to Bragg’s law of diffraction [25]

$$2d \cdot \sin(\theta_B) = n \cdot \lambda, \quad (2.1)$$

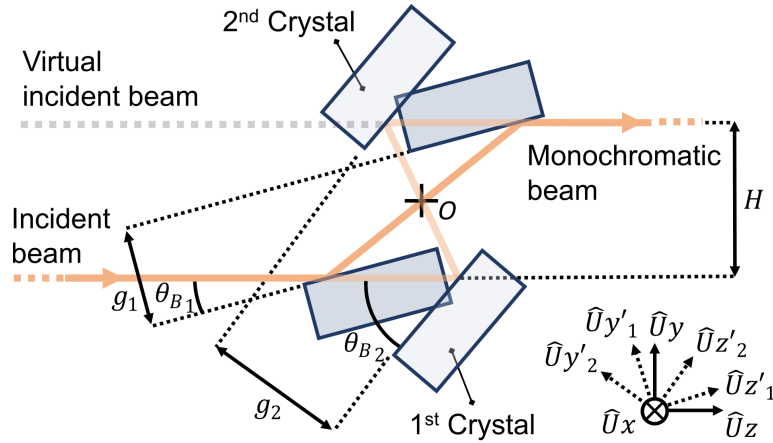
where  $d$  is the lattice parameter (also known as d-spacing) of the given crystal,  $\theta_B$  is the so-called Bragg angle,  $n$  is a positive integer that defines the diffraction order<sup>1</sup>, and  $\lambda$  is the photon wavelength (simply related to energy  $E$  via Planck’s constant  $h$  and the speed of light  $c$  as  $E = hc/\lambda$ ). Secondly, the monochromatic beam has to be kept at a fixed offset  $H$  with respect to the incoming beam, which is achieved by geometrically adjusting the gap  $g$  between the two crystals.

This concept is depicted in Figure 2.4 for Bragg angles  $\theta_{B_1}$  and  $\theta_{B_2}$ , and gaps  $g_1$  and  $g_2$ , where it can be seen that the position and pointing vector of the outgoing beam and, consequently, its projection as a virtual source, directly depend on the positioning of the crystals, with respect to each other and to the beam. Thus, in addition to the appropriate matching between  $g$  and  $\theta_B$ , the alignment and dynamic angular errors between crystals, i.e. of relative tip-tilt rotations  $Rx'$  and  $Rz'$ , around the  $Ux'$  and  $Uz'$  axes, respectively, in the rotated coordinate system (CS), are critical. After navigation naming conventions,  $Rx'$  and  $Rz'$  are typically referred to as pitch and roll angles.

As exemplified in [10–17], traditional DCM designs have always been based on a *high-stiffness concept*, the most commonly used designing approach in precision engi-

<sup>1</sup>For the sake of simplicity, without compromising generality, only the first harmonics will be considered hereafter, i.e.,  $n = 1$ .





**Figure 2.4:** DCM concept with a geometrically-symmetric arrangement of crystals at two incidence angles with respect to the rotation point  $O$ , showing that the offset  $H$  between the monochromatic and incident beams is preserved in the two Bragg angles  $\theta_{B_1}$  and  $\theta_{B_2}$  if the gaps  $g_1$  and  $g_2$  are adjusted. The coordinate systems are represented out of  $O$  for readability, with rotating coordinate systems in prime notations. The incident beam axis is aligned with the  $Uz$ -axis and the main rotation axis is the negative  $Ux$ -axis.

neering, in which the position of the parts is determined by a high mechanical stiffness between them [26]. Motion axes, for general alignment or actual positioning during experiments, are typically based on stepper motors and piezo stepper actuators operating in open-loop, even when iteratively following some sort of feedback signal. Therefore, traditional DCMs might be seen as high-resolution automated instruments, rather than high-performance mechatronics systems, here understood as closed-loop control systems in which the controlled quantity is constantly measured, compared with a reference value, and actuated in case of discrepancies between them.

In former light sources, with the larger photon source sizes, and experiment times limited either by photon flux statistics for sufficient SNR and/or detector architecture, DCMs have been generally used in one of the two operational modes: *fixed-energy* mode, the most basic operational condition, in which a given energy is preselected during setup and maintained over the whole experiment; and *step-scan* mode, which is the classical approach in standard spectroscopy experiments, based on subsequent data acquisitions steps for a discrete number of energy values over a determined energy range.

Regarding disturbance agents, here understood as undesired variables in the system that tend to adversely affect the variables of interest [22], in fixed-energy mode the positioning errors between crystals over time is mostly affected by floor and cooling disturbances, and by thermal drift. This is essentially the case also in step-scan mode, provided that sufficient settling time is allowed for every step, but with two additional remarks: corrective realignment, either from look-up tables or iterative feed-

back<sup>2</sup>, might be necessary between steps to compensate parasitic motion errors; and thermal loads and scattering effects might vary over the scanning range. Thus, active control and motion disturbances, as well as setpoint limitations, have never played a significant role in the specifications of these machines.

As the experiments have gradually become more sensitive to positioning errors in the DCMs over the years, synchrotron engineering teams and suppliers have responded with incremental design improvements. However, with limited capacity for reducing masses and inertias of the assemblies with the crystal, the main alternatives to decrease dynamic positioning errors of the crystals within this high-mechanical-stiffness design concept are either increasing the stiffness of the mechanical links and interfaces, or decreasing the levels of the disturbances. It had been with work in these two threads over a few decades that by 2015 the short-term pitch vibration amplitude between the crystals of state-of-the-art vertical-offset DCMs reached about 50 nrad RMS (root mean square) for the frequency range between 1 and 2.5 kHz in stand-still fixed-energy condition [11].

Now, the smaller beam sizes and higher fluxes provided by 4th-generation synchrotrons bring stricter positioning error budgets at the same time that, together with recent developments in the field of detectors, start to push experiment times to be reduced by one or two orders of magnitude. In particular, a third DCM operational mode, the so-called *fly-scan* mode may be more generally explored. In this case, experimental data of the sample is continuously recorded during beam energy variation over the desired energy range, i.e. as the Bragg angle and the gap between crystal change on the fly. Consequently, pitch errors around 10 nrad RMS over kHz bandwidth for fast detectors has become an ideal requirement in all operation modes. By 2015, this value was already 5 times smaller than what had been seen as stand-still performance in the best systems. Moreover, as hard motion disturbances act on traditional DCMs during fly-scans — mostly due to the high-bandwidth energy content of stepping actuators —, pitch errors often exceed 1  $\mu$ rad RMS [11], which exceed the new requirements by two orders of magnitude.

Considering that high-mechanical-stiffness designs and mitigation of disturbances would be close to practical limits [18], and believing that no existing solution would handle fly-scan needs, the LNLS, in collaboration with the consultant in mechatronics MI-Partners, started in 2015 the project of the HD-DCM for Sirius [19–21], with this target of 10 nrad RMS in pitch errors up to 2.5 kHz for all operation modes. It has been the first DCM to implement an isolated mechatronic architecture capable of reaching 250Hz-bandwidth closed-loop mechatronic performance [26], based on predictive-modeling design and DEB to realize it “first time right”.

By 2018, independent parallel further results in high-stiffness DCMs were reported

---

<sup>2</sup>Iterative feedback is here understood as the simple correction method in which a motion reference is commanded in open-loop for stepper motors or piezo steppers and only after the given trajectory is finished the result is compared with the reading of some sort of external signal of interest, with a few iterations being possibly required until convergence within a given error band.

by a synchrotron instrumentation vendor and by the ESRF. The first claimed remarkable 15 nrad RMS (up to 2 kHz) in fixed-energy mode at factory tests (still to be proven at the beamline), but no perspectives for scanning were envisioned [12]. The latter presented the revisited design concepts of their ongoing project [13], but no practical results. More recently, in 2021, a project update has been given in [17], unfortunately still without dynamic position stability performance numbers. In 2020, the Shanghai synchrotron (SSRF) has reported measurements of existing DCMs with fixed-energy pitch errors above 150 nrad RMS up to 1 kHz [15]. Then, in 2021, upgrades in the SSRF system were presented, but pitch errors above 75 nrad RMS are shown even in a low measurement bandwidth of only 30 Hz [16].

Thus, the HD-DCM, with its control-based enabling technology, is, to the best of our knowledge, the only one to have proven angular errors between crystals below 15 nrad RMS up to 2.5 kHz also during energy scans [20]. The overall specifications and the design of the HD-DCM are detailed in the following sections.

### 2.3 Specifications

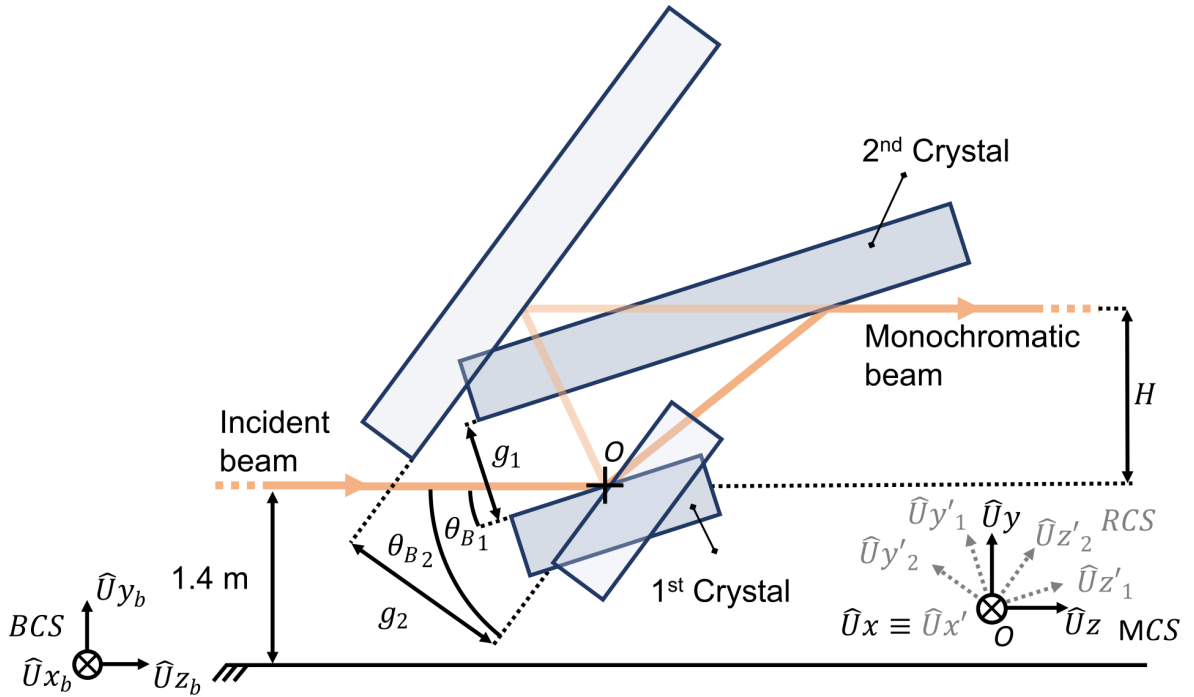
The engineering choices and specifications in beamline X-ray DCMs result from a large number of factors. Firstly, they depend on the accelerator parameters, such as electron beam current and energy, and electron bunch (or package) sizes. Next, the type of photon source, i.e. if it is a bending magnet or one among different types of the so-called insertion devices, plays an important role. Then, the beamline optical layout, placing the monochromator as a first optical element or after filters or mirrors, for example, leads to different requirements. Finally, the type of crystal and the specific operational energy range of the beamline may drive completely different specifications. As every beamline in the world is essentially unique with respect to the combination of all of these parameters, every DCM might be unique as well.

Moreover, from Bragg's law of diffraction (see Equation (2.1)), the conversions of variables from the photon energy domain, which is the quantity of interest to experiments, to distances, projections and motion, which are needed for engineering, follow trigonometric equations. As a result, not only does the whole beamline arrangement affect the design choices of a DCM, but even within the same instrument, the operational variables and sensitivities may vary by several orders of magnitude. As an example, relevant variable parameters at low and high-energy limits in the specific case of the HD-DCM project are given in Table 2.1, highlighting: source sizes; power loads in the crystals; power densities in the 1<sup>st</sup> crystal (since in the 2<sup>nd</sup> crystal it happens to be negligible); and power load variations, angular strokes and gap strokes for energy ranges of 1 keV, which would be typical for energy scans.

The engineering requirements of the HD-DCM are summarized in Table 2.2, whereas their derivation from the scientific requirements goes beyond the purpose of this article and will be discussed in a future work. The HD-DCM geometry is specified as depicted in Figure 2.5. At the beamline, the inertial beam coordinate system (BCS) is leveled at

**Table 2.1:** Set of relevant variable parameters in the HD-DCM at its low and high-energy limits for a general gist of the non-linear relation between photon energy and engineering parameters.

Parameter	Low Energy	High Energy
Vert. source (FWHM) [ $\mu\text{m}$ ]:	20	6
Hor. source (FWHM) [ $\mu\text{m}$ ]:	55	45
Max. beam power 1 <sup>st</sup> cr. [W]:	150	150
Min. beam power 1 <sup>st</sup> cr. [W]:	40	130
Power dens. 1 <sup>st</sup> cr. [ $\text{W}/\text{mm}^2$ ]:	$\leq 50$	$\geq 2.8$
Max. beam power 2 <sup>st</sup> cr. [W]:	0.2	1.5
Min. beam power 2 <sup>st</sup> cr. [W]:	$\approx 0$	0.1
Power variation for 1 keV [W]:	$\leq 40$	$\leq 2$
Angular stroke for 1 keV [ $^\circ$ ]:	$\leq 23$	$\geq 0.1$
Gap stroke for 1 keV [mm]:	$\leq 6$	$\geq 0.001$



**Figure 2.5:** HD-DCM geometry according to the fixed beam impact point concept at the rotation axis  $O$ , showing two Bragg angles  $\theta_{B1}$  and  $\theta_{B2}$ , and the corresponding gaps  $g_1$  and  $g_2$ . The coordinate systems are represented out of  $O$  for readability. The main coordinate system (MCS) in the HD-DCM has positioning degrees of freedom (DoFs) with respect to the inertial beam coordinate system (BCS) for pre-operational alignment, whereas the rotating coordinate system (RCS), in prime notations, has one controlled DoF with respect to the MCS in the  $Rx$ -axis (rotation around the  $Ux$ -axis) for energy-selection operation. The incident beam axis is aligned with the  $Uz$ -axis, the main rotation axis  $\theta_B$  is the negative  $Rx$ -axis, and the  $Uy$ -axis is parallel to gravity for upwards vertical offset.

**Table 2.2:** HD-DCM specifications.

Parameter	Description
Geometry:	<ul style="list-style-type: none"> <li>· Upwards vertical-offset</li> <li>· Fixed beam impact point</li> </ul>
Crystal sets:	<ul style="list-style-type: none"> <li>· Si(111) and Si(311)</li> </ul>
Set selection ( $U_{BCS}$ ):	<ul style="list-style-type: none"> <li>· range: <math>\pm 35</math> mm</li> <li>· accuracy: <math>&lt; 0.1</math> mm</li> </ul>
MCS height ( $U_{yBCS}$ ):	<ul style="list-style-type: none"> <li>· range: <math>\pm 2.5</math> mm</li> <li>· accuracy: <math>&lt; 50</math> <math>\mu\text{m}</math></li> </ul>
MCS align. ( $R_{yBCS}$ ):	<ul style="list-style-type: none"> <li>· range: <math>\pm 2</math> mrad</li> <li>· accuracy: <math>&lt; 0.14</math> mrad</li> </ul>
MCS align. ( $R_{zBCS}$ ):	<ul style="list-style-type: none"> <li>· range: <math>\pm 2</math> mrad</li> <li>· accuracy: <math>&lt; 0.25</math> mrad</li> </ul>
1 <sup>st</sup> cr. align. accuracy:	<ul style="list-style-type: none"> <li>· <math>U_{y'_1} &lt; 50</math> <math>\mu\text{m}</math></li> <li>· <math>R_{x'_1}, R_{y'_1}, R_{z'_1} &lt; 0.25</math> mrad</li> </ul>
Main rotation ( $\theta_B$ )	<ul style="list-style-type: none"> <li>· range: 3 to 60°</li> <li>· accuracy: <math>&lt; 0.15</math> <math>\mu\text{rad}</math></li> <li>· error: <math>&lt; 0.15</math> <math>\mu\text{rad}^a</math></li> <li>· max. speed: 1 °/s</li> </ul>
Nominal offset (H):	<ul style="list-style-type: none"> <li>· 18 mm</li> </ul>
Gap ( $U_{y'}$ )	<ul style="list-style-type: none"> <li>· range: 9 to 18 mm</li> <li>· accuracy: <math>&lt; 0.3</math> <math>\mu\text{m}</math></li> <li>· error: <math>&lt; 0.3</math> <math>\mu\text{m}^a</math></li> <li>· max. speed: 0.5 mm/s</li> </ul>
Pitch ( $R_{x'}$ )	<ul style="list-style-type: none"> <li>· range: <math>\pm 1</math> mrad</li> <li>· accuracy: <math>&lt; 150</math> nrad</li> <li>· error: <math>&lt; 10</math> nrad<sup>a</sup></li> </ul>
Roll ( $R_{z'}$ )	<ul style="list-style-type: none"> <li>· range: <math>\pm 1</math> mrad</li> <li>· accuracy: <math>&lt; 90</math> nrad</li> <li>· error: <math>&lt; 90</math> nrad<sup>a</sup></li> </ul>
Crystal temperature:	<ul style="list-style-type: none"> <li>· 1<sup>st</sup>: 78 K (indirect LN<sub>2</sub>)</li> <li>· 2<sup>nd</sup>: 155 K (braids)</li> </ul>
Vacuum level:	<ul style="list-style-type: none"> <li>· <math>&lt; 5 \times 10^{-8}</math> mbar</li> </ul>

<sup>a</sup>RMS in frequency range between 1 Hz and 2.5 kHz.

the nominal floor height, with the  $U_{y_b}$ -axis aligned with the gravity vector but pointing upwards and the  $U_{z_b}$ -axis defined by the nominal beam direction. Then, the nominal incoming beam travels 1.4 m above the floor, parallel to the  $U_{z_b}$ -axis, in  $U_{y_b}U_{z_b}$ -plane of the BCS.

Next, being specified with a non-translating 1<sup>st</sup> crystal and upwards vertical offset, the main coordinate system (MCS) of the HD-DCM can be defined by having the main

rotation axis in the negative  $Ux$ -axis and the  $UxUz$ -plane coincident with the nominal diffraction surface of the 1<sup>st</sup> crystal at  $\theta_B = 0$ . Finally, a rotating coordinate system (RCS) (using prime notation) for the crystals can be defined with coincident MCS origin  $O$  and  $Ux$ -axis.

Having a non-translating 1<sup>st</sup> crystal is related to cooling boundary conditions (see Section 2.4.2.1), whereas having the diffraction surface nominally through the  $Ux$ -axis allows for a fixed-beam-impact-point concept, keeping the 1<sup>st</sup> crystal as short as possible and minimizing detrimental transient thermal effects related to the high-power incoming beam walking over the diffraction surface. Still, to provide more flexibility regarding energy ranges and different filtering bandwidths, two sets of silicon crystals should be alternatively selectable<sup>3</sup>. Thus, keeping a plane of symmetry in the core of the HD-DCM, the  $UyUz$ -plane (also  $Uy'Uz'$ -plane) is actually a mirror plane, with one set of crystals in the right half-plane at  $-35$  mm and the other set mirrored in the left half-plane at  $+35$  mm along the  $Ux$ -axis.

So, the nominal positions  $(x_{MCS}, y_{MCS})_{BCS}$  of the MCS at the beamline in millimeters are either  $(-35, 1400)_{BCS}$ , for the operation with of the rightmost set of crystals, or  $(35, 1400)_{BCS}$ , for the operation of the leftmost set of crystals, with the MCS orthogonal to the BCS. Yet, in the overall alignment of HD-DCM with respect to the beam there are two forgiving degrees of freedom (DoFs). Firstly,  $z_{MCS}$ , i.e. the position of the HD-DCM along the beamline, is indeed a free parameter, with no strong requirement or impact in performance. Secondly, the orthogonality between the MCS and the BCS in  $Rx$ , i.e. the level of the HD-DCM bench with respect to gravity in  $Rx$ , can be quite forgiving if the residual remaining angle can be simply compensated for the crystals with the RCS.

Regarding the MCS, except for the selection between sets of crystals, with the longer required motion range of at least 70 mm, the remaining positioning range requirements are limited to a few millimeters and milliradians, mostly to overcome: manufacturing tolerances, floor unevenness and positioning limitations and uncertainties during installation at the beamline. The accuracy requirements, in turn, are within a few tens or hundreds of micrometers and microradians. Yet, these are relatively soft requirements, since they are meant mainly to an ideal minimization of parasitic effects over different Bragg angles, which, in practice, are of second-order importance and can be still partly compensated with other DoFs.

The 1<sup>st</sup> crystals of the two sets, which are by design fixed to the RCS, should comply with similar accuracy alignment budgets, including:  $Uy'_1$ , which affects the fixed-beam-impact-point concept; and small-angle orthogonality errors for  $Rx'_1$ ,  $Ry'_1$  and  $Rz'_1$  because of similar parasitic effects over different Bragg angles. In this case, also as relatively soft accuracy requirements, the ultimate condition is that residual alignment errors (and their indirect effects) can be properly compensated either with the main rotation or the 2<sup>nd</sup> crystals.

---

<sup>3</sup>The two sets have Si(111) and Si(311) crystallographic orientations, following the standard *Miller indices* notation [25].

The main operational angular range is  $3^\circ \leq \theta_B \leq 60^\circ$  and the nominal vertical beam offset is  $H = 18$  mm. Thus, the 2<sup>nd</sup> crystals operational gap  $9 \text{ mm} \leq g \leq 18 \text{ mm}$  is required over the  $Uy'$ -axis. In addition to that, positioning of the 2<sup>nd</sup> crystals must comply with the range of  $\pm 1$  mrad for pitch  $Rx'$  and roll  $Rz'$ , such that angular offsets from manufacturing and assembly with the crystals can be compensated. Maximum speeds for these motion DoFs are given according to expected fly-scan experiments at the most stringent energy limits. In operation, either at fixed-energy mode or during scans, the maximum positioning RMS errors in the frequency range between 1 Hz and 2.5 kHz are specified as: 0.15  $\mu$ rad for the main rotation; 300 nm for the gap; 10 nrad for pitch; and 90 nrad for roll. Again, it was this pitch strict requirement that motivated the conceptual innovation in the HD-DCM. Regarding positioning accuracy, it must be reached via internal metrology and calibration, or by means of external feedback.

To conclude, in order to handle the power loads up to 150 W and the power densities up to 50 W/mm<sup>2</sup>, the 1<sup>st</sup> crystals are cryocooled to 78 K with liquid nitrogen (LN<sub>2</sub>) via indirect flow through copper heat exchangers. As for the 2<sup>nd</sup> crystals the power loads are at least two orders of magnitude lower, i.e. below 1.5 W, the power densities are negligible, and the temperature setpoint is higher at 155 K<sup>4</sup>, a simpler solution of indirect cooling via copper braids is possible. Finally, the vacuum level should be kept ideally below  $5 \times 10^{-8}$  mbar, so that the crystals are preserved in their interaction with the X-rays, and heat exchange is limited primarily to predictive conduction and to radiation.

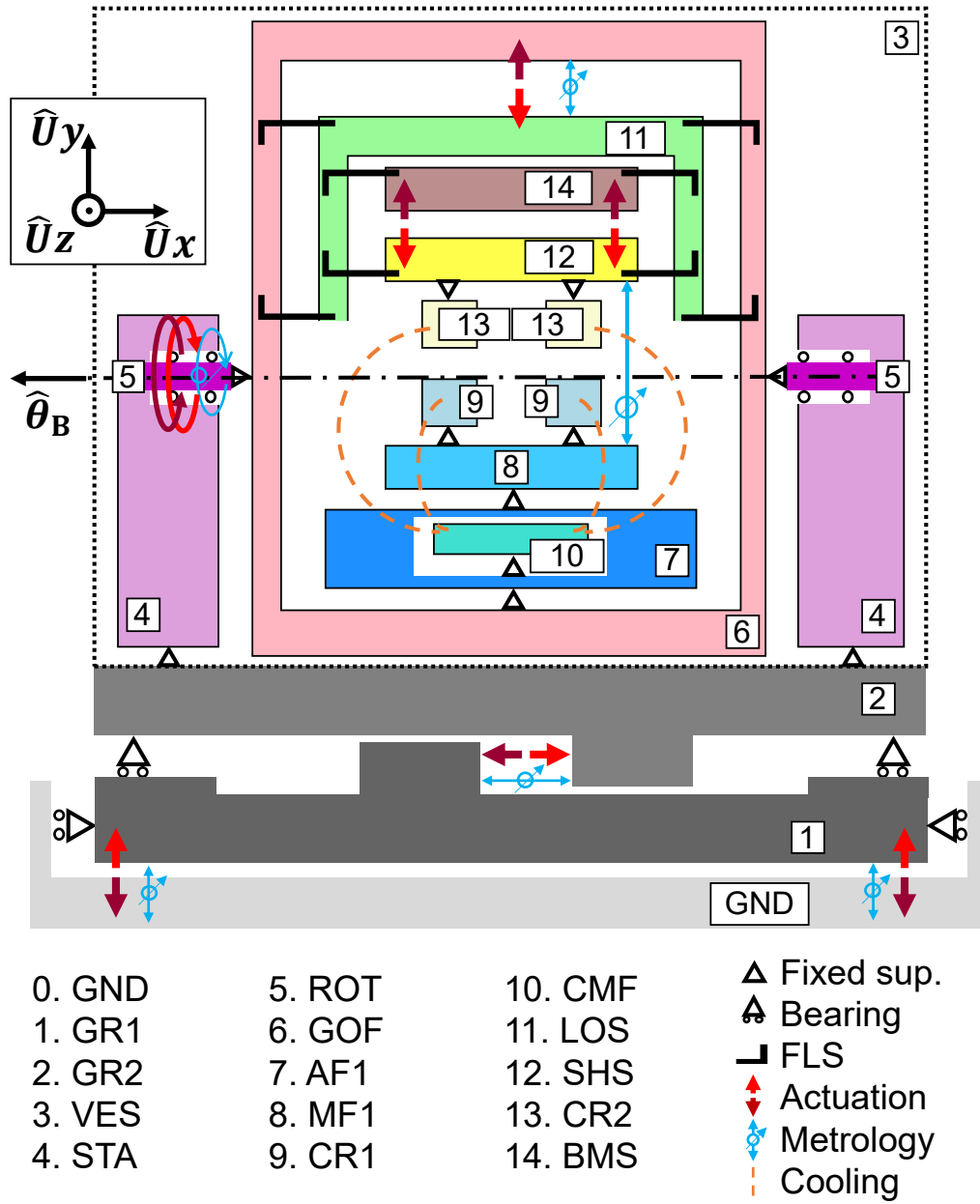
In the following section, the architecture, the essential design concepts and the embodiment of the HD-DCM, developed within the DEB methodology to meet these specifications, are described in details. The DEB workflow itself is presented in [23], whereas some complementary information on thermal management is available in [28].

## 2.4 Architecture and Design

The architecture of the HD-DCM can be summarized in the schematic mechanical model shown in Figure 2.6. The alignment of the MCS with respect to the beam is achieved outside vacuum by means of a two-level granite bench GR1 and GR2. At the interface with the floor GND, a system with levelers allows for the alignment of the height  $Uy_{BSC}$ , tip  $Rx_{BSC}$  (which is redundant with the main rotation axis, but results from the solution with independent levelers) and tilt  $Rz_{BSC}$ . Then, between granite blocks, air-bearings are used for the remaining set selection  $Ux_{BSC}$  and orthogonality  $Ry_{BSC}$ . The main rotation function  $Rx$  is implemented already inside the vacuum vessel VES by means of a so-called goniometer, which, in this case, consists of two symmetrically-arranged commercial rotary stages with mechanical bearings and direct drive, with their stators STA and the rotors ROT.

---

<sup>4</sup>Silicon has a negative thermal expansion coefficient below 125 K, such that equivalent diffraction conditions due to equal lattice parameters are met at 78 and 155 K. Yet, the first are set to 78 K for superior thermal conductivity. For more information on silicon cryogenic thermal properties, see [27].



**Figure 2.6:** HD-DCM schematic mechanical model, consisting of: ground (GND); bottom and top granite blocks (GR1 and GR2); vacuum vessel (VES); stators (STAs) and rotors (ROT) of the two direct-drive rotary stages; main rotating frame (GOF); auxiliary frame 1 (AF1); 1<sup>st</sup> crystals (CR1s) and their metrology frame (MF1); cooling manifold (CMF); long-stroke structure (LOS); 2<sup>nd</sup> crystals (CR2s) and the short-stroke frame (SHS), as their metrology frame; and balance mass (BMS). Fixed and moving connections are represented by their standard symbols, folded leafsprings (FLSs) by L-shaped forms. The rotation axis is represented by the horizontal center line. The cooling connections between the CMF and the CR1s and CR2s are represented by the dashed lines. Action and reaction forces of the actuators are represented by arrows, and metrology between parts by dials.



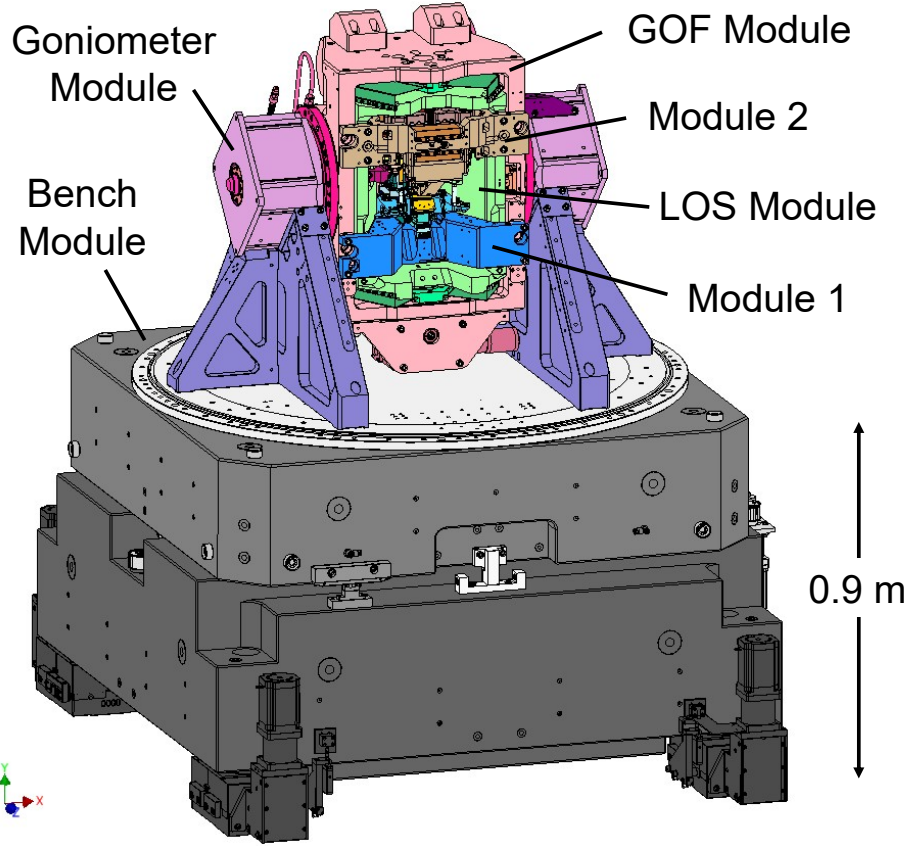
The 1<sup>st</sup> crystals CR1s are mounted to a common metrology frame MF1, which, in turn, is fixed to the main rotating goniometer frame GOF via the auxiliary frame AF1. This auxiliary frame also holds the cooling manifold CMF, from where a LN<sub>2</sub> circuit is derived for cooling of the CR1s and where braids are connected for cooling of the 2<sup>nd</sup> crystals CR2s. For the CR2s, three voice-coil (VC) actuators and three laser interferometers are used to control the position of the short-stroke frame SHS (also known as metrology frame 2, MF2) in  $Uy'$ ,  $Rx'$  and  $Rz'$  over a tangential arrangement of three folded leafsprings (FLSs). Then, to avoid the excitation of reaction dynamics in controlling the SHS, a balance mass BMS is used with an equivalent arrangement of FLSs. Finally, both the SHS and the BMS are actually connected to an additional low-bandwidth long-stroke structure LOS, which complements the required  $Uy'$  stroke of the CR2s. Guided by an arrangement of six FLSs, the LOS is driven by a stepper motor and measured by an absolute optical encoder.

Functionally, these parts may be organized in modules and submodules. In the so-called *Core Module* there are four submodules: the *Module 1*, containing the CR1s, the MF1, the AF1 and the CMF; the *Module 2*, containing the CR2s, the SHS and the BMS; the *LOS Module*, containing the LOS; and the *GOF Module* containing the GOF. Then, there are the *Goniometer Module*, containing the STA and the ROT, and the *Bench Module*, containing the GR1, the GR2 and the VES. The embodiment of the HD-DCM, according to this classification, is made clear in the mechanical design shown Figure 2.7.

In the following subsections, the main conceptual choices are firstly introduced, to set the appropriate technical background, then, the mechanical design of each module, including their parts and accessories, is presented in details.

### 2.4.1 Design Concepts

The most fundamental idea in this project was turning the traditionally passive or slow positioning of gap  $Uy'$ , pitch  $Rx'$  and roll  $Rz'$  DoFs into servo error specifications of a high-bandwidth closed-loop control system. First of all, for a crystal-to-crystal control bandwidth in the range of 200 to 250 Hz — for sufficient noise suppression and trajectory following capacity during scans (see also [23]) —, the mechanical eigenfrequencies related to the crystal mounts, which are typically found at most around a few hundred Hz in traditional DCMs, needed to be taken to the kHz range. Next to that, innovative actuation, metrology and cooling schemes needed to be developed. The key conceptual choices that distinguish the HD-DCM from traditional DCMs are: minimal positioning DoFs; long-stroke and short-stroke arrangement; smooth motion guiding; smooth actuation; inter-crystal metrology; crystal mounting; and decoupled cooling. These building blocks are individually addressed here before the mechanical design of each module is presented in section 2.4.2.



**Figure 2.7:** The HD-DCM mechanical design, according to the color code in Figure 2.6 and to the modular classification: Module 1, Module 2, LOS Module and GOF Module, building the macro Core Module; the Goniometer Module; and the Bench Module. The vacuum vessel is hidden for visualization purposes.

#### 2.4.1.1 Minimal Positioning DoFs

Given the demanding dynamic requirements, a mechanical design concept with only the essential positioning DoFs was envisioned, i.e.: wherever possible, the assembly is carefully constrained and statically determined by design. This can be understood as an effort to reduce as much as possible the number of positioning stages that are typically found in the core of DCMs, such that the number of parts and components, interfaces, guiding elements, actuators and sensors can be minimized — which not only may help in cutting costs, simplifying maintenance and reducing outgassing in vacuum, but also supports the predictive modeling approach and the pursuit of performance optimization.

Concerning the core, from the fixed-beam-impact-point requirement, the CR1s can be directly mounted to the MF1 and aligned with respect to the main rotation axis by construction. Then, for the CR2s on the SHS, only the three essential  $Uy'$ ,  $Rx'$  and  $Rz'$  DoFs between crystals are made active. In this case, the cost of intentionally not having translational freedom in  $Uz'$  for the CR2s, as often found in DCM designs, is twofold: larger CR2s are needed to handle beam-walk at different angles

(see Figure 2.5); and additional design effort is required in terms of concepts, material selection, manufacturing tolerances, and assembly alignment strategies. Regarding the bench, preventing stacks of several positioning stages, the positioning DoFs for the alignment of MCS with respect to the BCS share only two interface layers, namely: the levelers interface between the floor and the GR2 for  $Uy_{BSC}$ ,  $Rx_{BSC}$ , and  $Rz_{BSC}$ ; and the air-bearings interface between the GR2 and the GR1 for  $Ux_{BSC}$  and  $Ry_{BSC}$  (see Section 2.4.2.3).

#### 2.4.1.2 Long-Stroke and Short-Stroke Arrangement

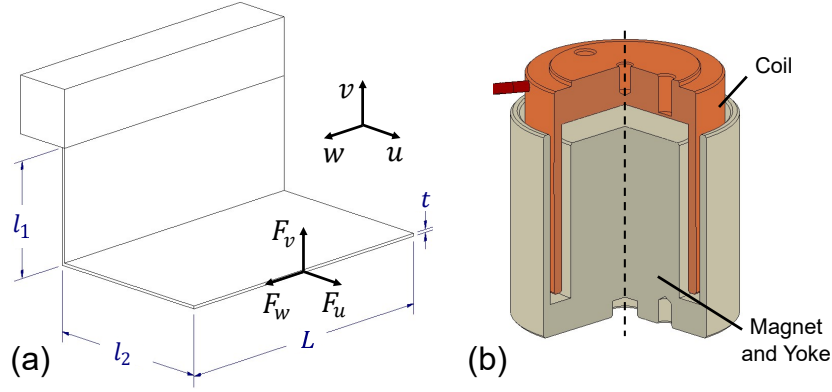
The cascade arrangement of a coarse long-stroke stage and a fine short-stroke stage is a well-known concept that is extensively used in high-performance mechatronics systems in which motion resolution and range have a span of several orders of magnitude, typically above  $10^5$  or  $10^6$  [29,30]. In the HD-DCM, the SHS, which is responsible for the high-dynamic performance with nanometer-level control error for  $Uy'$ ,  $Rx'$  and  $Rz'$ , would not be able to cover the 9 mm required gap stroke. Thus, the LOS is introduced for complementary  $Uy'$  stroke, with independent actuation and feedback.

#### 2.4.1.3 Smooth Motion Guiding

Appropriate guiding mechanisms and interfaces in the core are essential to achieve the desired dynamics, nanometer-level control error and repeatability in the so-called crystal cage (CCG). Therefore, all positioning DoFs in the core are guided by means of elastic (or flexural) elements, with much better modeling and calibration perspectives than rolling elements alternatives, that would have lubrication issues and friction effects, in addition to the risk of mechanical noise from the very rolling elements during motion. Indeed, when properly designed, such elastic systems benefit from an infinite lifetime and no maintenance, whereas the intrinsic high-repeatability concept allows for superior calibration schemes of non-linearities and parasitic errors.

A *parallel-kinematic* approach is adopted to provide the three positioning DoFs of the SHS in a single motion layer, as opposed to the more conventional concept of stacking stages for complementary functions. Fortunately,  $Uy'$ ,  $Rx'$  and  $Rz'$  form the classic *piston-tip-tilt* configuration, which is a convenient parallel-kinematic combination that was even extended to the linear motion of the LOS. This is achieved via arrangements of FLSs (see Section 2.4.2.1.2), generically illustrated in Figure 2.8a, which individually act as single-DoF constraints (*w-axis*) with translational and rotational stiffnesses that can be easily modeled from the material properties and the geometry [31].

Rolling bearings did eventually remain in the HD-DCM in locations where the impact on the overall performance was less critical. This is the case in the actuator mechanism of the LOS, still within the *Core Module*, and the commercial rotary stages of the *Goniometer Module*. In both cases, more convenient solutions can be modularly replaced in future upgrades if necessary, without significant impact in the general architecture.



**Figure 2.8:** Motion-related design concepts used in the HD-DCM: (a) folded leafspring (FLS) elastic mechanism as a single-DoF constraint (w-axis), with translational and rotational stiffnesses resulting from the material properties and the geometry: arm lengths  $l_1$  and  $l_2$ , bending length  $L$  and thickness  $t$ ; and (b) voice-coil (VC) actuator, for contactless axial force between the coil and the magnet with the yoke.

Finally, although less relevant to motion errors because of its basic alignment nature, rolling bearings have also been eliminated from the design of the bench. The major benefit is in dynamics, as a stack of bearings is replaced by the intermittent air-bearing layer between the GR1 and the GR2. Indeed, the combination of embedded air-bearings with commercial items can be turned-off during operation, virtually creating a monolithic structure for the system (see Section 2.4.2.3).

#### 2.4.1.4 Smooth Actuation

Concerning actuation, an essential step for performance was partly replacing well-established designs based on stepper motors, which have always been extensively used at beamline instrumentation as cost-effective and reliable options. Indeed, steppers are still conveniently used for the bench and the actuator of the LOS<sup>5</sup>, but for the SHS they would severely limit the control bandwidth and also become an internal disturbance source due to its nature of motion in discrete steps.

Next, in principle, the nanometer-level resolution necessary for the SHS could be realized by means of position-based or force-based actuators. The first, represented by piezo stacks or piezo walkers, are historically far more common in synchrotron instrumentation, being the typical choice in existing DCMs. The latter, idealized with voice-coils (also known as Lorentz actuators), depicted in Figure 2.8b, on the other hand, open rather interesting possibilities<sup>6</sup>.

Indeed, piezo actuators are inherently stiff, so that the final dynamics would be limited both by the masses and mass moments of inertia of parts to be controlled, and

<sup>5</sup>In future upgrades of the LOS actuator, the stepper may be replaced together with the rolling bearings.

<sup>6</sup>Linear motors would have the same working principle of VCs, but are geometrically less favorable in such a compact arrangement as the core of the HD-DCM.

by the stiffness of the actuators and their decoupling elements. As a result, the control strategies and achievable closed-loop bandwidth would also become limited to the range of 20 Hz for the SHS. Moreover, piezo stacks alone would have insufficient range for this application, whereas piezo walkers had three major disadvantages: friction effects, such as gripping, stick-slip or wear, which are particularly critical in vacuum; stepping high-frequency disturbance injection, much like the steppers, during fly-scans; and speed limitations. Both friction and stepping disturbances are difficult to be characterized and modeled, complicating or impairing the predictive modeling approach.

In turn, being a contactless type of actuator, VCs are free of friction and nearly free of stiffness (seen as position dependence of force) between the actuator parts (coil and magnet), so that different dynamic concepts may be envisioned. The chosen one has the SHS and the BMS decoupled from the LOS between 6 and 10 Hz, and the BMS as a low-pass filter for the control of the SHS, suppressing observable high-frequency resonances and allowing for a control bandwidth in the range of 200 to 250 Hz (see [23]). In addition, VCs can be made with convenient displacement and force ranges, and can be very accurately characterized and modeled.

#### 2.4.1.5 Inter-Crystal Metrology

In the core of standard DCMs, optical encoders or capacitive sensors have been typically used as stand-alone signals for open-loop iterative feedback in stacked stages driven by stepper motors or piezo steppers. Eventually, external feedback from beam position monitors (BPMs) might be also be available. Yet, in neither case inter-crystal metrology was absolutely essential within these high-stiffness instruments.

In the HD-DCM, on the other hand, aiming at ultimate active positioning control between crystals, an appropriate choice for inter-crystal feedback is crucial. The three basic conditions to be simultaneously fulfilled are: nanometer-level resolution, already considering sensor noise over the large control bandwidth; compatibility with the operational gap stroke of 9 mm and the pitch and roll ranges of 1 mrad; and update rate between 10 and 20 kHz, for sufficient phase margin at the desired closed-loop bandwidth.

Three alternatives have been considered, namely: external beam feedback, embedded autocollimator and embedded distance measurement instruments. The first was ruled out because of beamline optics dependence and sensor technology limitations regarding sensitivity and rate. The second was disproved as well because of technological limitations regarding sensitivity and rate. Thus, although unable to rigorously provide absolute inter-crystal metrology, as the first two options might do — but, rather, indirect metrology between metrology frames —, the latter alternative, relying on mature technologies with sufficiently high update rates and resolutions, has been selected.

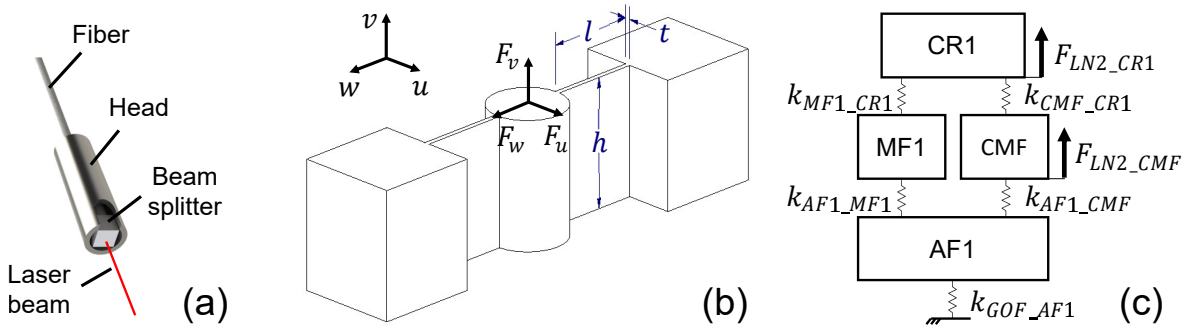
From the long list of commercially available measurement options, including optical encoders, capacitive probes, inductive sensors and confocal sensors, among others, the only one that, to the best of our knowledge, simultaneously complied with all requirements was the laser interferometer. This choice became even more attractive thanks

to the fortuitous timing of the commercial release of a few innovative compact optical-fiber-based Michelson and Fabry-Perot interferometers, illustrated in Figure 2.9a, which perfectly suited the integration to the MF1 and the SHS in this application.

#### 2.4.1.6 Crystal Mounting

A robust mechanical design for a 200 to 250 Hz closed-loop control bandwidth in the crystal cage pushes the so-called *suspension frequencies* of the crystals on the MF1 and the SHS towards the kHz range. With limited options regarding the mass and inertia of the crystals, the subject of their mounting stiffness to the frames becomes a critical point. Moreover, in addition to control issues, the highest mounting stiffness is desired because of the indirect-metrology limitations. Indeed, the feedback is blind not only to the actual position of the crystals beyond their resonances, but also to the displacements between the crystals and their frames due to direct forces acting on them, such as those resulting from the cooling scheme (see Section 2.4.1.7).

To fulfill the high-stiffness mounting requirements with acceptable thermal stresses and deformation in the crystals, resulting from different temperatures and thermal expansion coefficients between the crystals and their frames, a semi-kinematic mounting design concept is used. It consists in fixing the crystals to the frames at three pads with specifically compliant design. Indeed, the symmetric embedded flexural structure (EFS) shown in Figure 2.9b can be made compliant in one translational and two rotational DoFs ( $u$ -axis,  $Rv$ -axis and  $Rw$ -axis), and stiff in the remaining DoFs, with all translational and rotational stiffnesses easily modeled from the material properties and the geometry. Thus, this mounting concept works as a flexural alternative to the classical *Maxwell Kinematic Coupling*, here creating a quasi-exactly-constrained as-



**Figure 2.9:** Metrology-related design concepts used in the HD-DCM: (a) SmarAct’s Picoscale fiber-optics Michelson laser interferometer head (IFH) [32]; (b) embedded flexural structure (EFS), with translational and rotational stiffnesses resulting from the material properties and the geometry: length  $l$ , height  $h$  and thickness  $t$ ; and (c) simplified 1D dynamic model for the decoupled cooling concept with respect to one of the 1<sup>st</sup> crystals (CR1s), including: the main cooling manifold (CMF), the metrology frame 1 (MF1) and the auxiliary frame 1 (AF1), with stiffness links  $k$  between parts, and liquid nitrogen flow-induced force disturbances  $F_{LN2}$  acting on the CR1 and the CMF.

sembly<sup>7</sup> with a thermal center (TC) for the crystals that is, in principle, less sensitive to non-deterministic friction effects.

Moreover, on top of predictable mechanical performance, these flexures allow for predictable thermal properties. Indeed, by selecting the appropriate material with the desired Young's modulus and low thermal conductivity, the thickness  $t$ , height  $h$  and length  $l$  parameters can be tuned for the desired mechanical stiffness and high thermal resistance for cryogenic isolation<sup>8</sup>. In fact, because of the convenient combination of mechanical and thermal performances, this solution with EFSs was applied in the HD-DCM not only with the crystals, but also for thermal isolation in the MF1, the VCs and the cooling braids.

#### 2.4.1.7 Decoupled Cooling

Decoupled cooling can be understood both as different cooling solutions for the CR1s and the CR2s, and, especially, as decoupled cooling and positioning functionalities within the design. Indeed, the indirect inter-crystal metrology concept requires that the position of the crystals be defined by the MF1 the and SHS, respectively, not by parallel cooling structures.

This concept can be discussed via the simplified 1D dynamic model for the CR1s presented in Figure 2.9c, in which the parts are coupled by their respective stiffness links  $k$  and there are force disturbances  $F_{LN2}$ , caused by the so-called flow-induced vibrations (FIV), acting on the CR1 and the CMF. For a proper correlation between the CR1 and the MF1,  $k_{MF1\_CR1}$  must be as high as possible, so that their relative displacement, caused either by  $F_{LN2\_CR1}$  or elastic forces resulting from a relative displacement between the CR1 and the CMF, can be minimized. Indeed, displacements of the CMF with respect to the CR1 and the MF1 are inevitable due to thermal expansion (mainly during cooldown) or reaction to  $F_{LN2\_CMF}$ . Then, minimizing these parasitic elastic forces on the CR1 requires that  $k_{CMF\_CR1}$  be as low as possible, while providing LN<sub>2</sub> to the CR1 and preserving dynamics. As detailed in Section 2.4.2.1.1, this could only be achieved with a design based on multiple thin pipes, replacing the typical thick pipes found in most water-cooled or cryocooled DCMs. Finally, minimizing the relative displacement between the CR1 and the CMF requires that both  $k_{AF1\_MF1}$  and  $k_{AF1\_CMF}$  be high-stiffness links.

Similar reasoning applies to the CR2s, except that the position of the SHS is actively controlled and the complex LN<sub>2</sub> pipes of  $k_{CMF\_CR1}$  can be replaced by compliant copper

<sup>7</sup>The three pads, constraining three DoFs each, result in an overdetermined design. Additional elastic hinges could be used to reach an exactly-constrained mounting in six DoFs, but at the cost of lower mounting stiffnesses. As a compromise, the embedded flexural structures, the internal stiffness of the crystals and the manufacturing specs were designed to allow for tolerable crystal deformations with optimized mounting stiffnesses.

<sup>8</sup>Simple analytical calculations for stiffness were found to be systematically within at least 80% of agreement with more sophisticated *finite element* (FE) simulations. For thermal resistances, however, a simple formulation was used as a first estimate, but needed to be refined via FE simulations, so that the strong gradients and non-linear effects would be included.

braids  $k_{CMF,CR2}$  (see Section 2.3), which is essential for the long gap stroke and the angular stroke of the SHS.

### 2.4.2 Detailed Mechanical Design

Once the specifications have been presented and that the architecture and the main design concepts have been introduced, the mechanical design of the HD-DCM can be thoroughly explained according to the aforementioned modular classification.

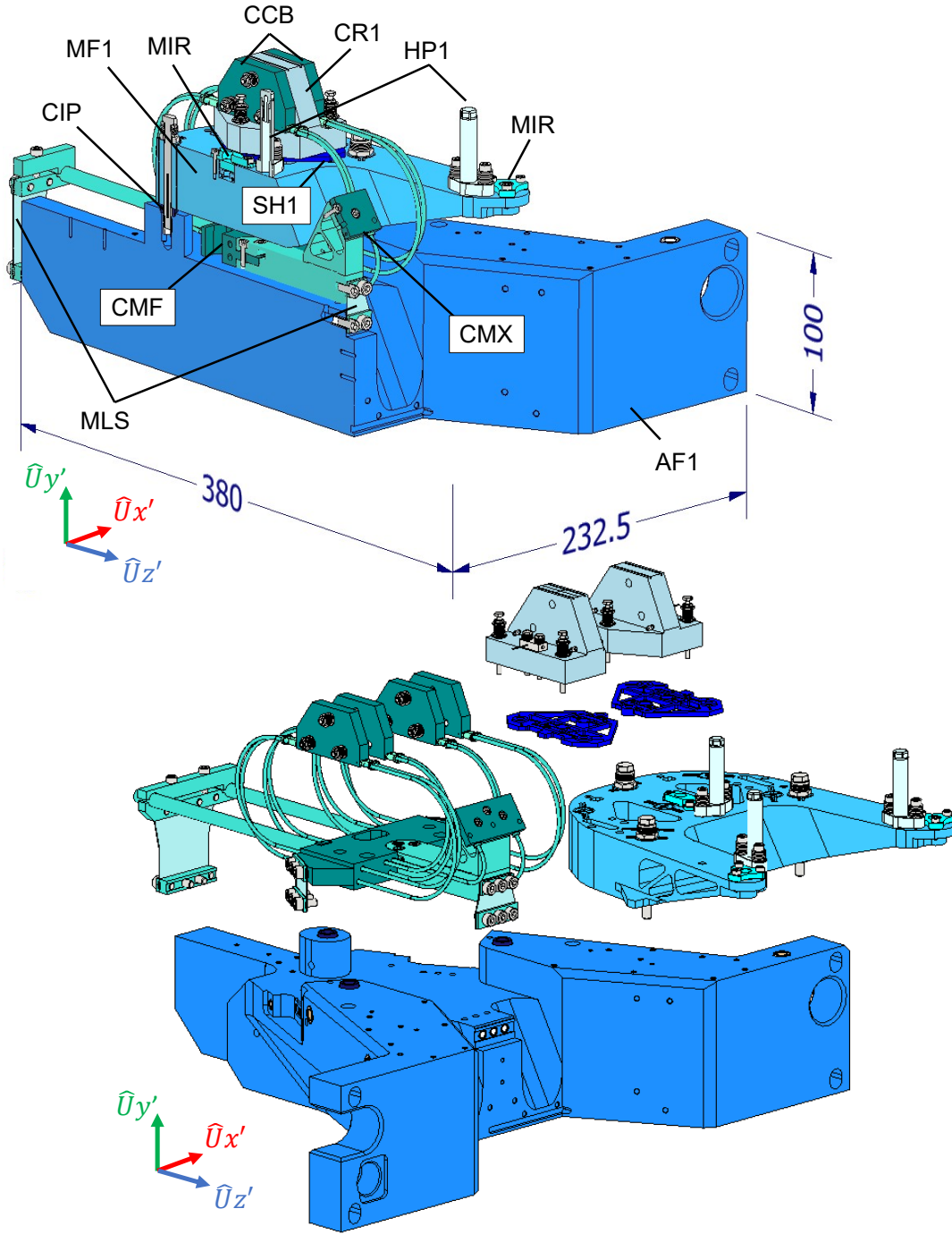
#### 2.4.2.1 Core Module:

**2.4.2.1.1 Module 1** It is the sub-assembly with the 1<sup>st</sup> crystals. As shown in Figure 2.10, it essentially consists of: the two crystals CR1s and their calibrated shims SH1s; the metrology frame MF1, holding the crystals, three plane mirror MIRs as the interferometer targets and the so-called homing pins HP1s; the cooling manifold assembly, with the main cooling manifold CMF, the cooling manifold extension CMX and the crystal cooling blocks CCBs; and the auxiliary frame AF1, which makes the interface with the main rotating frame GOF (see Figure 2.6 and Figure 2.7), holds the MF1 via complementary isolation pads CIPs, and supports the manifold assembly via leafsprings MLSS.

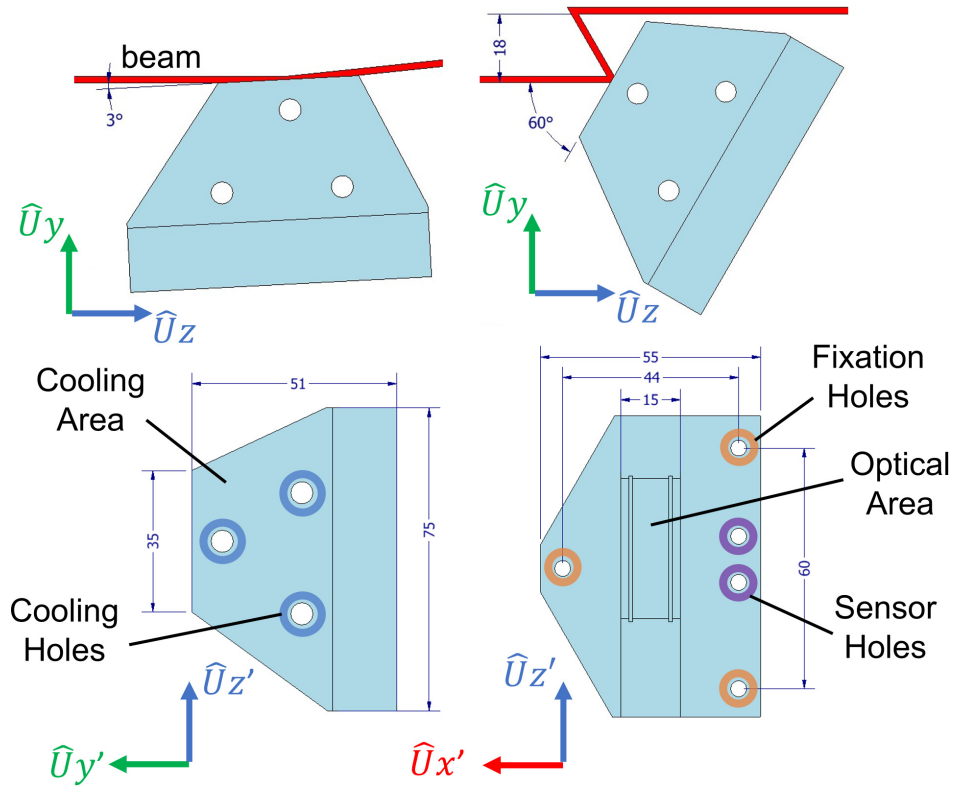
**2.4.2.1.1.1 First Crystals (CR1s)** The CR1s are made of high-purity silicon ingots and their design, shown in Figure 2.11, results from simultaneous beam acceptance, mechanical, dynamic, thermal and manufacturing boundary conditions. The unusual shape, as compared to DCM crystal standards, allows for deterministic fixation to the MF1 at three points – with optimized  $Rx'$  rotational stiffness, for dynamic performance, and high  $Rx'$  bending stiffness, to minimize mechanically-induced deformations of the diffraction planes – and efficient symmetric lateral cooling over a total area of about 3600 mm<sup>2</sup>, which is essential to minimize the detrimental effects of the thermal gradient imposed by the X-ray beam.

Manufacturing limitations result in crystal height deviations of a few tenths of millimeters with respect to the nominal value and, more critically, of parallelism deviations of up to 0.2° (or 3.5 mrad) between the diffraction planes and the bottom mounting surfaces. With the calibrated SH1s the height difference between CR1s can be reduced to about 0.01 mm and the deviations in parallelism, to 0.002° (or 0.035 mrad). Thus, both crystals can be simultaneously aligned to the rotation axis, and the operational angular tolerances in the interferometers of approximately 0.05° (or 1 mrad) are preserved. Grade 5 titanium is used for the SH1s to make their flexural design with EFSs — which is necessary for thermal expansion, since they are in parallel with the CR1s and with the EFSs in the MF1 in the  $Ux'Uz'$ -plane — more robust and to increase thermal resistance to the MF1. Additionally, flexural extensions in the SH1s have threaded holes and serve as joint nuts to facilitate the mechanical fixation of temperature sensors to the CR1s.





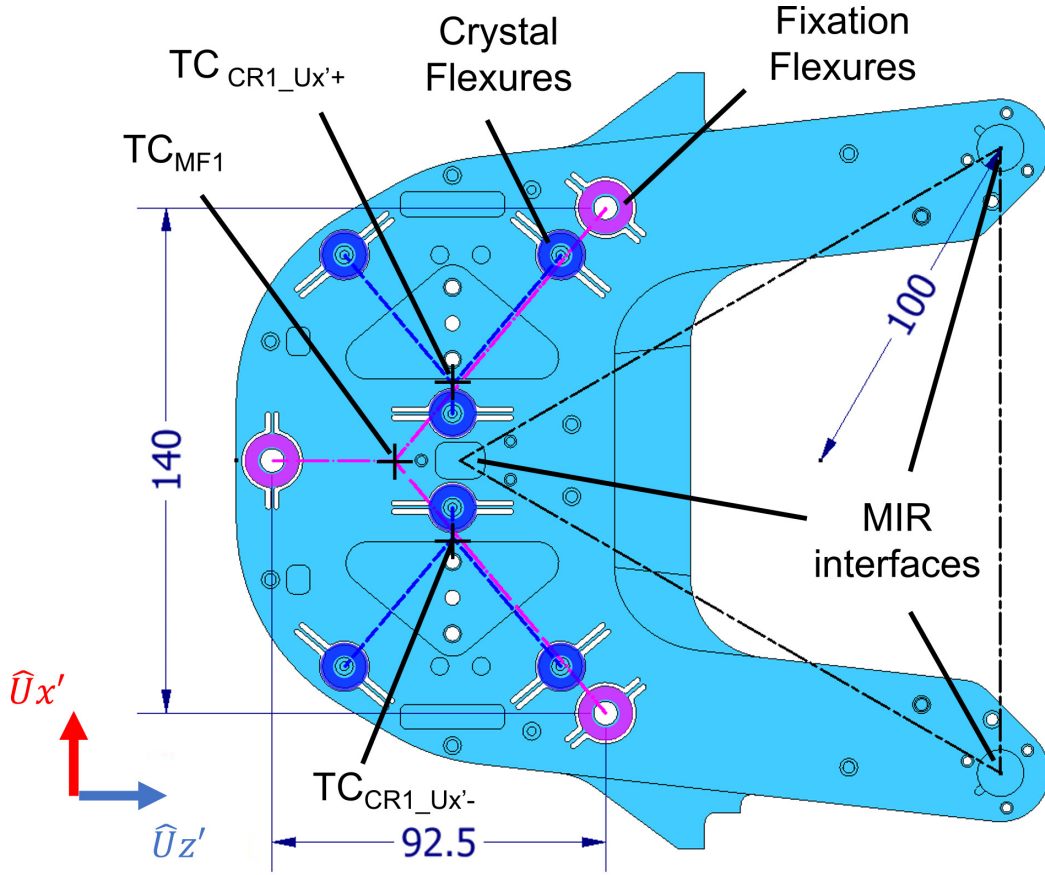
**Figure 2.10:** Mechanical design of the Module 1 in the HD-DCM. Top: Symmetrical cross-sectional view with reference dimensions given in millimeters, highlighting the main components: crystals (CR1s), shims (SH1s), metrology frame 1 (MF1), plane mirrors (MIRs), homing pins (HP1s), complementary isolation pads (CIPs), main cooling manifold (CMF), cooling manifold extension (CMX), crystal cooling blocks (CCBs), manifold mounting leafsprings (MLSs) and auxiliary frame 1 (AF1). Bottom: Partially exploded view.



**Figure 2.11:** Mechanical design of the 1<sup>st</sup> crystals (CR1s) in the Module 1 of the HD-DCM. The crystal in the negative  $Ux'$ -axis hemisphere is shown for reference, whereas the one in the positive  $Ux'$ -axis hemisphere is simply the mirrored design. Top: side view for maximum beam footprint and beam clearance at 3° and 60°, respectively, with the nominal vertical beam offset of 18 mm. Bottom: side and top views with main dimensions in millimeters and indications for the through-holes for the fixation to the metrology frame (MF1), and for clamping of the crystal cooling blocks (CCBs) and a temperature sensor.

Clamping to the MF1, through the SH1s, and between the CCBs is made by means of long bolts and stacked steel disk spring washers, so that preloading forces and thermal expansion can be properly handled.

**2.4.2.1.1.2 Metrology Frame 1 (MF1)** The C-shaped design of the MF1, shown in Figure 2.12, results from both a viable distribution for the EFSs and a convenient arrangement for the MIRs. Two sets of three flexures hold the CR1s and another set of three flexures is used for the fixation to the AF1, creating TCs for the shrinkage of the cold parts at different temperatures. The orientations of the flexures respected volume restrictions and prioritized dynamic performance over the resulting positions of the TCs, because the application is rather insensitive to small offsets in the  $Ux'Uz'$ -plane. These flexures, together with the interface stiffness in the SH1s, define the supporting stiffness  $k_{MF1,CR1}$  of Section 2.4.1.7, which is addressed in [23]. Regarding the MIRs, their distribution is basically defined by the geometry of the



**Figure 2.12:** Mechanical design of the metrology frame (MF1) in the Module 1 of the HD-DCM. The top view highlights the three sets of embedded flexural structures (EFSs) for the 1<sup>st</sup> crystals (CR1s) and the fixation to the auxiliary frame 1 (AF1), and their respective thermal centers (TCs). The positions of the interferometer target mirrors (MIRs) are at the vertices of the equilateral triangle in dash-dotted lines. The dimensions are given in millimeters.

SHS (see Section 2.4.2.1.2). The triangle over a radius of 100 mm optimizes rotational  $Rx'$  and  $Rz'$  resolutions and provides equal sensitivity to them. The region between the downstream mirrors in the  $Uz'$ -axis must be preserved for the propagation of the diffracted beam at high angles (see the top Figure 2.11).

The 40mm-thick frame is made of Invar36<sup>®</sup> because of its specific modulus (Young's modulus over mass density), to achieve sufficient dynamics, and, more importantly, because of its thermal properties. Indeed, the low coefficient of thermal expansion (CTE) and the low thermal conductivity make it a suitable material to minimize the thermal distortions with existing temperature gradients over the frame<sup>9</sup>. In fact, the particular combination of thermo-mechanical properties in Invar36<sup>®</sup> is essential to make the thermally-insulating EFSs concept feasible. Indeed, most of the temperature gradients

<sup>9</sup>CTE of Invar36<sup>®</sup> is below  $2 \times 10^{-6} \text{ K}^{-1}$  over the entire temperature range between 77 K and room temperature. Thermal conductivity is in the range of 10 to 15  $\text{W m}^{-1} \text{ K}^{-1}$ , common to stainless alloys.

between the CR1s, the MF1, and the AF1, at 80 K, 150 K and room temperature (RT), respectively, lie in the thin flexures, which may not stand large short-scale thermal deformations in many materials.

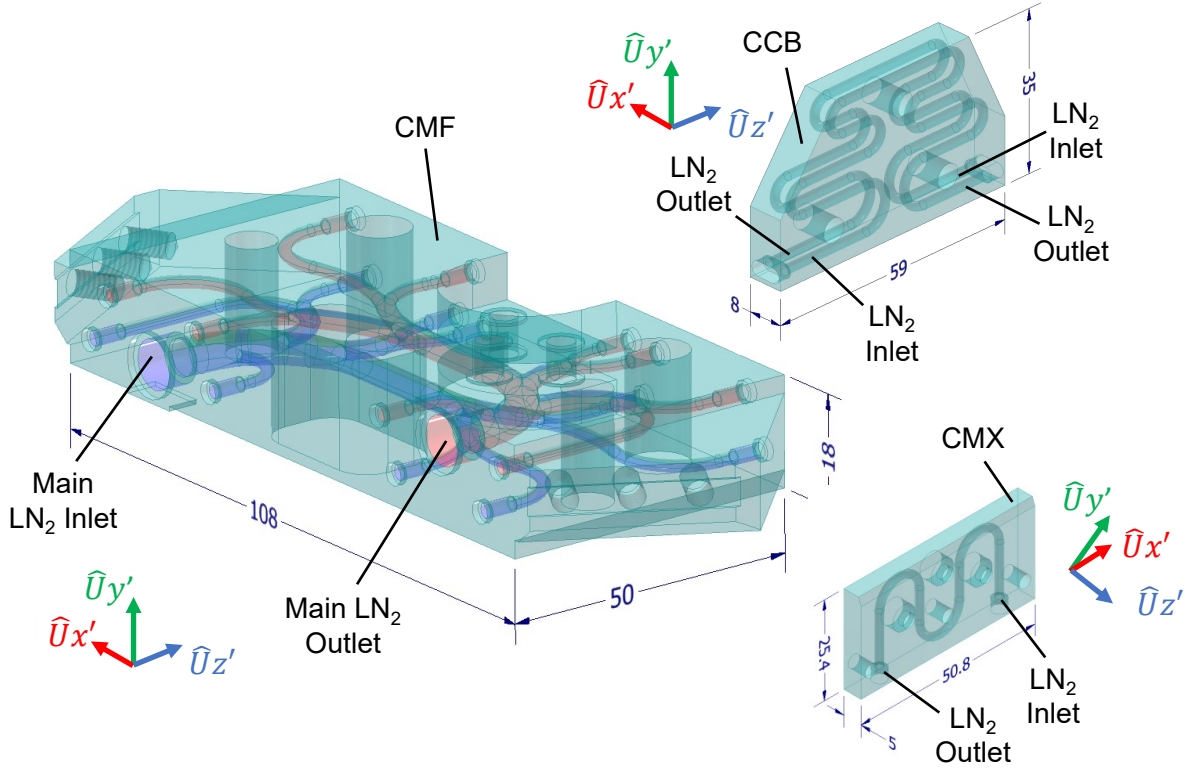
Yet, given the larger masses involving the MF1 and the parts on it, the MF1 fixation flexures reaches a practical limit in the compromise between thermal isolation and dynamic performances. So, to limit the power required for thermal management of the AF1 at RT, the CIPs made of zirconia ( $\text{ZnO}_2$ ) are implemented in series with these flexures. Taking the interfaces stiffnesses into account, they define together the supporting stiffness  $k_{Y_{MF\_MF1}}$  of Section 2.4.1.7, which is addressed in [23] as well. As done for the crystals, clamping to the AF1 is made by means of long bolts (through the MF1 and the CIPs) and stacked disk spring washers.

The HP1s work as extensions of the MF1. They are also made of Invar36<sup>®</sup> and serve an equivalent alignment purpose as the SH1s, in this case, shortening the alignment loop between metrology frames MF1 and SHS. Together with their respective counterparts in *Module 2* (see Section 2.4.2.1.2), these spacers are used as start-up and alignment references for the interferometer heads, making the parallelism between frames better than  $0.05^\circ$  (or 1 mrad), as limited by the interferometers, and working as a gap reference parameter for the crystals.

**2.4.2.1.1.3 Auxiliary Frame 1 (AF1)** In addition to simplifying manipulation of *Module 1* and its assembly to the GOF, the AF1 fulfills two important functionalities. Firstly, it holds the complex  $\text{LN}_2$  distribution system, which must be positioned with respect to the crystals and connected to them, but ideally with as low mechanical coupling as possible, to minimize FIV. Then, it defines a RT interface between the *Module 1* and the rest of the system via active temperature control. Material selection for 5083-O aluminum was based on the following characteristics: high thermal conductivity, minimizing temperature gradients; good specific modulus for dynamics; low density, for overall weight; UHV compatibility; and costs.

**2.4.2.1.1.4  $\text{LN}_2$  Distribution System** The flow of  $\text{LN}_2$  in the HD-DCM is controlled by an independent closed-circuit cryocooler commercial unit, which is capable of flow rates up 20 L/min and pressures between 2 and 10 bar for power loads up to 3 kW [33]. Unfortunately, in spite of the known detrimental flow-disturbance effects created in corrugated pipes [34], they cannot be avoided either between the cryocooler and the vacuum vessel, for positioning freedom on the bench, or inside the vessel, to comply with the large angular stroke of the core (see Section 2.4.2.1.3). In the latter section this is at least partly mitigated by minimizing the length and the number of corrugated pipes, i.e. a single pair for feed and return lines, and by using an inner metal mesh.

Within the *Module 1*, however, to minimize the FIV disturbances, a quieter circuit is created by exclusive use of smooth continuous pipes with deterministic fixed geometry, as seen in Figure 2.10. Moreover, specially tailored smooth inner channels are



**Figure 2.13:** Mechanical design of the main cooling manifold (CMF), the crystal cooling block (CCB) and the colling manifold extension (CMX) in the LN<sub>2</sub> distribution system in the Module 1 of the HD-DCM, which are made transparent to highlight the smooth inner channels to minimize flow-induced disturbances. The dimensions are given in millimeters.

designed in the CMF, CMX and CCBs cryogenic parts, as depicted in Figure 2.13. The CMF is an AISI 316L stainless steel part, made by additive manufacturing, with an arterial-based concept, such that: the main LN<sub>2</sub> flow is received from a stainless steel pipe with an inner diameter of 7 mm; then, the flow is split into nine thin stainless steel distribution pipes with inner diameters of 2 mm; finally, the returning flow is similarly collected from the thin distribution pipes into the common main outlet. One inlet-outlet pair of these distribution pipes feeds the internally-cooled CMX, an oxygen-free copper (OFC) part that works as a cold finger (or heat sink) for the copper braids that cool the CR2s. The eight remaining C-shaped pairs feed and collect LN<sub>2</sub> from the four OFC internally-cooled CCBs that are used to sandwich the two crystals (see Figure 2.10). As such, the relatively compliant link required by  $k_{CMF\_CR1}$  in Section 2.4.1.7 results from the parallel stiffness of four of these pairs per crystal, for which the tube diameter and C-shape geometry are essential. To improve temperature homogeneity and partially balance flow-induced forces, each CCB has two parallel channels running the fluid in opposite directions. As additive manufacturing for OFC was not yet readily available, the CMX and the CCBs are made of sectioned parts that are brazed together. Eventually, the tubes in the manifold assembly are either brazed

or welded to the parts, resulting in a single piece.

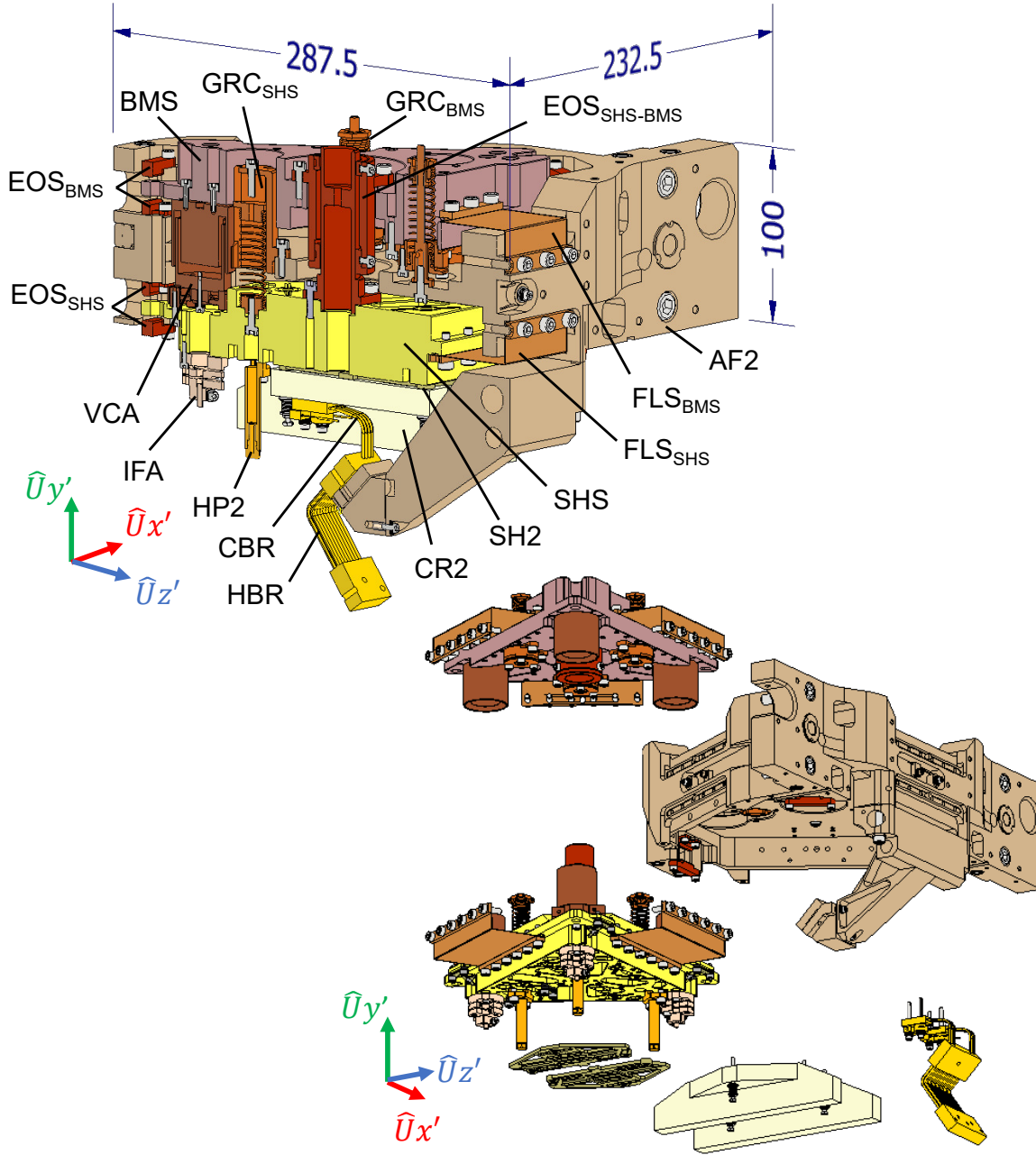
The CMF and the CMX are stiffly connected by AISI 316L stainless steel parts and this set is fixed to the AF1. To achieve sufficiently high stiffness for  $k_{AF1,CMF}$  in Section 2.4.1.7 and sufficient thermal isolation a solution equivalent to the EFSs is used. Three Grade 5 titanium sheets (with a fourth geometrically redundant sheet for the stiff inlet and outlet tubes) are arranged in a triangular geometry that assures exact constraining and defines a TC for the set. Although the CTE of titanium is six times larger than that of Invar36<sup>®</sup>, the higher thermal stresses can still be handled by its 6-fold higher strength, thus, making titanium an alternative in these thermally-decoupling solutions.

**2.4.2.1.2 Module 2** It is the sub-assembly with the 2<sup>nd</sup> crystals and the high-dynamic control capabilities. As shown in Figure 2.14, it consists of: the two crystals CR2s, their calibrated shims SH2s, and their high-conductivity and compliant cooling braids HBR and CBRs; the short-stroke frame SHS (also known as MF2), holding the crystals, three fiber interferometer assemblies IFAs, the homing pins HP2s and the coils VCCs of the three VC assemblies VCAs; the balance mass BMS, with the magnets VCMs of the VCAs; and the auxiliary frame AF2 — not shown in Figure 2.6, but actually making the interface with the long-stroke structure —, which holds the two sets of three FLSs for the SHS and the BMS, the motion end-of-strokes EOSs and the so-called gravity compensators GRCs for the SHS and the BMS, and drives the HBR.

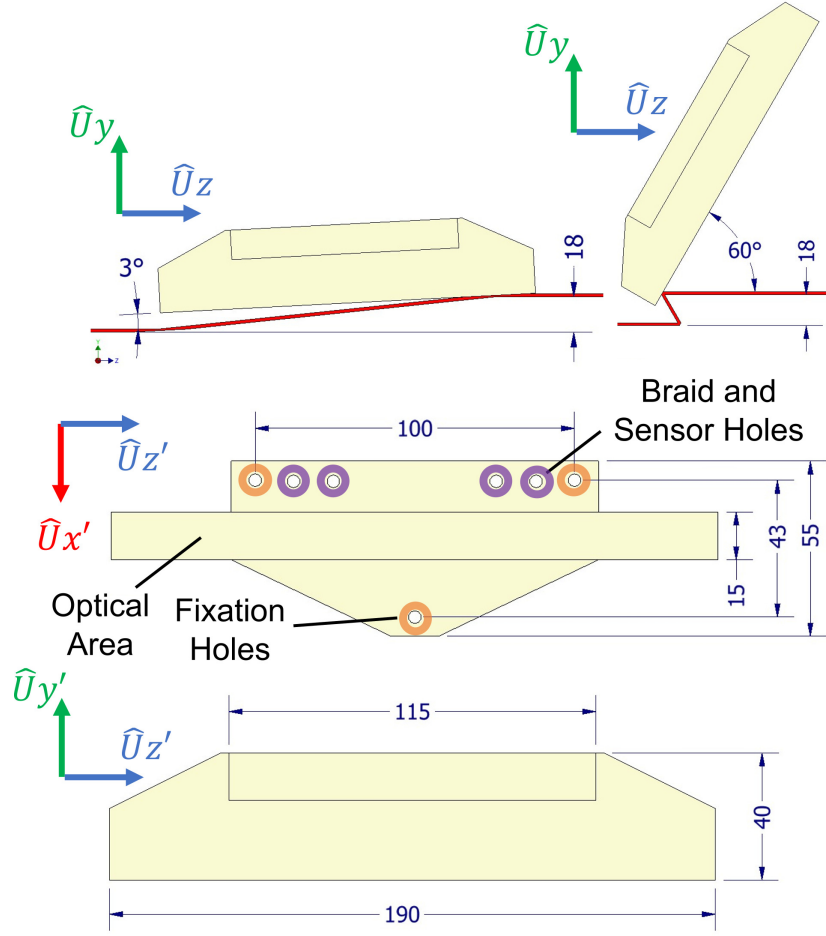
**2.4.2.1.2.1 Second Crystals (CR2s)** The design of the CR2s, also made of high-purity silicon ingots, is shown in Figure 2.15. Their length is severely impacted by the minimal-positioning-DoF approach (see Section 2.4.1.1), since it must cope with the changing beam footprint and, especially, the beam-walk over the complete main angular stroke. On the other hand, as compared with the CR1s, their height can be shorter, being defined by dynamics and the bending stiffness around the  $Ux'$ -axis. Deterministic fixation to the SHS and alignment correction is again achieved via three points through the Grade 5 titanium SH2s. As the SH1s, the SH2s also have flexural extensions with threaded holes as joint nuts, in this case, to facilitate the mechanical fixation of temperature sensors and the CBRs. Also as in the *Module 1*, clamping to the SHS is made by means of long bolts and stacked steel disk spring washers.

**2.4.2.1.2.2 Short-Stroke Frame (SHS)** The main aspects of the design of the SHS are shown in Figure 2.16. For exactly the same reasons discussed for the MF1, the SHS is also made of a 40mm-thick Invar36<sup>®</sup> block. Also as in the MF1, two sets of three flexures in the SHS hold the CR2s, taking the thermal gradient between the CR2 and the SHS — which operate at 155 K and 250 K, respectively —, and creating TCs for the shrinkage of the crystals. Again, the orientations of the flexures respected





**Figure 2.14:** Mechanical design of the Module 2 in the HD-DCM. Top: Symmetrical cross-sectional view with reference dimensions given in millimeters, highlighting the main components: crystals (CR2s), shims (SH2s), high-conductivity cooling braid (HBR), compliant cooling braids (CBRs), short-stroke frame (SHS), interferometer assemblies (IFAs), homing pins (HP2s), short-stroke folded leafsprings (FLS<sub>SHS</sub>), short-stroke gravity compensators (GRC<sub>SHS</sub>), short-stroke end-of-strokes (EOS<sub>SHS</sub>), balance mass (BMS), balance mass folded leafsprings (FLS<sub>BMS</sub>), balance mass gravity compensators (GRC<sub>BMS</sub>), balance mass end-of-strokes (EOS<sub>BMS</sub>), voice-coil assemblies (VCAs), and auxiliary frame 2 (AF2). Bottom: Partially exploded view.



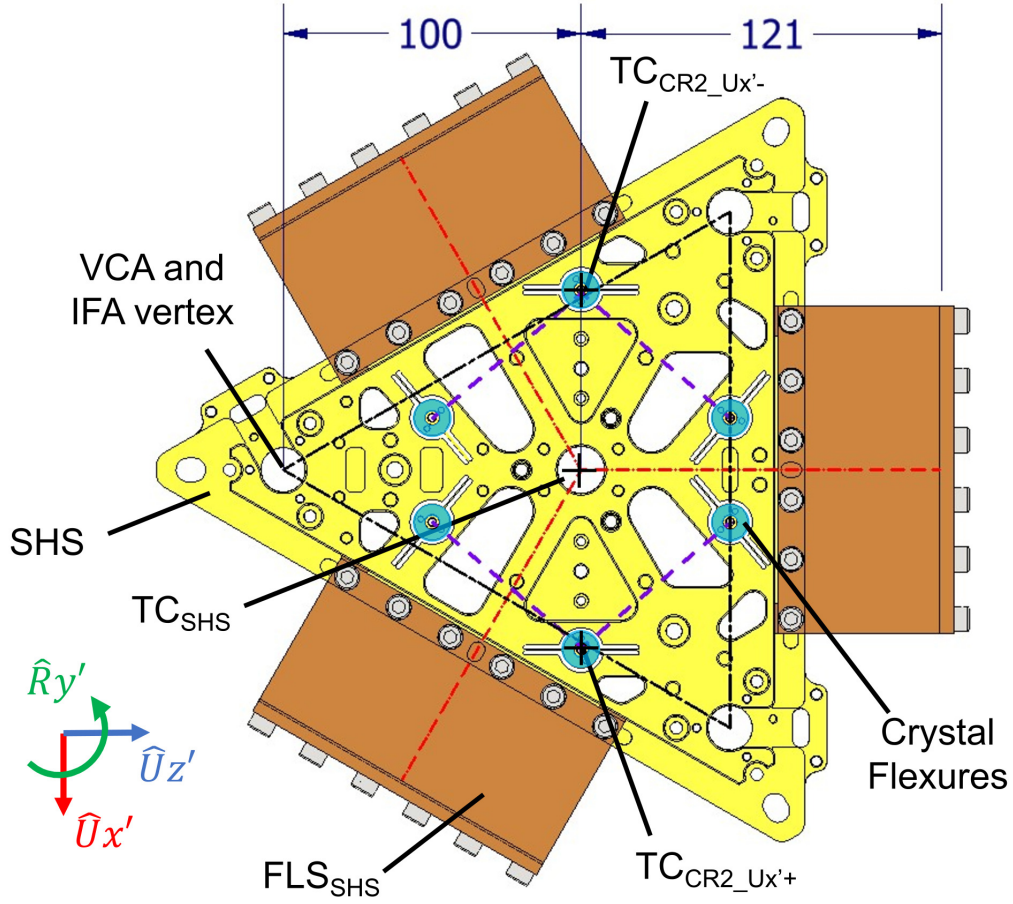
**Figure 2.15:** Mechanical design of the 2<sup>nd</sup> crystals (CR2s) in the Module 2 of the HD-DCM.

The crystal in the negative  $U_{x'}$ -axis hemisphere is shown for reference, whereas the one in the positive  $U_{x'}$ -axis hemisphere is simply the mirrored design. Top: side view for beam footprint and beam-walk at  $3^\circ$  and  $60^\circ$  with the nominal vertical beam offset of 18 mm. Middle and bottom: top and side views, respectively, with main dimensions in millimeters, and indications for the through-holes for the fixation to the short-stroke frame (SHS), and for clamping of the compliant cooling braid (CBR) and a temperature sensor.

volume restrictions and prioritized dynamic performance over the resulting positions of the TCs.

Differently from the MF1, however, with the long crystals and out of the path of the beam, a more convenient triangular symmetry can be obtained. Also, differently from the MF1, instead of having its position defined by the EFSs, the SHS is supported on the AF2 by the three  $FLS_{SHS}$ , whose stiffnesses are addressed in [23]. The triangular arrangement of the FLSs, with their folding lines on the  $U_{x'}U_{z'}$ -plane symmetrically constrain the  $U_{x'}$ ,  $U_{z'}$  and  $R_{y'}$  DoFs. With the 121 mm lever-arm, sufficient compliance and stroke capability is achieved for  $U_{y'}$ ,  $R_{x'}$  and  $R_{z'}$ , whereas the  $R_{y'}$  stiffness is increased. Using 0.25mm-thick AISI 301 stainless steel FLSs, for its Young's modulus,

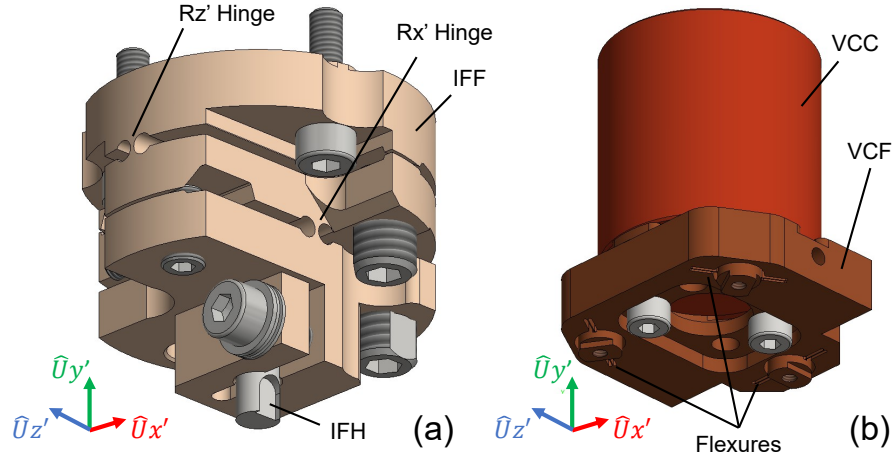




**Figure 2.16:** Mechanical design of the short-stroke frame (SHS) in the Module 2 of the HD-DCM. The top view highlights the two sets of embedded flexural structures (EFS) for the 2<sup>nd</sup> crystals (CR2s), the set of three folded leafsprings (FLS<sub>SHS</sub>), and their respective thermal centers (TCs). The positions of the interferometer assemblies (IFAs) and the coils (VCC) of the voice-coil assemblies (VCAs) are at the vertices of the equilateral triangle in dash-dotted lines. The dimensions are given in millimeters.

availability as sheet metal and high strength (as compared to 304 or 316 alloys, for instance), the SHS is capable of maximum functional strokes of  $\pm 3$  mm and  $\pm 20$  mrad, which are limited by the EOS<sub>SHS</sub> on the AF2, and EOS<sub>SHS-BMS</sub> between the SHS and the BMS. The operational ranges are eventually smaller, about  $\pm 1.5$  mm in translation, to minimize power dissipation in the VCs, and  $\pm 1$  mrad, because of the tolerances in the interferometers. The CBRs are braids with limited conductivity, but compliant enough for these ranges of motion with low forces.

The FLS<sub>SHS</sub> also create a TC for the SHS and take the gradient between the SHS and the AF2, which operates at RT. Regarding the  $Uy'$ -axis, it is important to have the plane of folding lines of the FLSs as close as possible to the center of gravity of the SHS together with its related parts, because this reduces coupling in controlling  $Uy'$ ,  $Rx'$  and  $Rz'$  DoFs. Moreover, the perpendicularity between the sections within each FLS is important for the appropriate alignment of the SHS with respect to the AF2.



**Figure 2.17:** Mechanical design of the metrology and actuation assemblies in the short-stroke frame (SHS) in the Module 2 of the HD-DMC: (a) fiber interferometer assembly (IFA), with the interferometer head (IFH) and its alignment frame (IFF), providing tip-tilt (in  $Rx'$  and  $Rz'$  axes) adjustment via flexural hinges; (b) coil (VCC) of the voice-coil assembly (VCA) and its mounting frame (VCF), which is fixed to the short-stroke frame (SHS) via a set of three embedded flexural structures (EFSs). (Arbitrary scale for clarity.)

Finally, the sharpness in the folding lines of the FLSs is a critical aspect, since it is related to how close these elements effectively are to the desired theoretical single-DoF constraint. In the  $FLS_{SHS}$ , a bending radius of 0.5 mm is specified.

Having this specific configuration and 100 mm lever-arm for the IFAs and the VCAs: nanoradian-level metrology and control can be achieved with the sub-nanometer-level resolution of the interferometers; reasonable torque can be obtained from relatively small forces; and the highly-desirable collocated control can be implemented. As detailed in Figure 2.17a, the IFAs are composed of the interferometer heads IFHs and Grade 5 titanium frames IFFs, used for fixation and manual offline alignment of the IFHs, with a range of  $\pm 20$  mrad and resolution below 0.5 mrad.

Shown in Figure 2.17b is the mounting concept of the three VCCs to the SHS via the mounting frames VCFs. The three EFSs provide convenient thermal resistance between the VCCs and the SHS, such that the SHS still works as a heat sink for the heat generated in the VCCs, but the coils are kept above 240 K, as specified by the supplier<sup>10</sup>. Naturally, the flexures also provide compliance for the relative expansion of the aluminum frame of the coil with respect to the SHS. The original material selected for the VCFs was Invar36<sup>®</sup>, but it was found to lead to non-linear negative stiffness effects within the motion range of the VCs because of stray magnetic fields in the commercial VCs. Indeed, depending on the relative position of the magnets in the BMS with respect to the coils in the SHS during operation, residual leaking fields would interact differently with the VCFs and cause inconvenient variable attraction forces,

<sup>10</sup>Initial estimates for the temperature of the SHS were 210 K. In practice, because of stronger black-body radiation effects, the SHS was found to operate at 250 K.

which would required additional control efforts. Thus, the material was changed to Inconel 625, which is another convenient non-magnetic option for EFSs with thermal isolation.

Finally, as with the HP1s, the three Invar36<sup>®</sup> HP2s work as extensions of the SHS, shortening the alignment loop between the metrology frames MF1 and SHS, and defining the reference for the offline alignment of the IFFs with respect to the MIRs in the MF1.

**2.4.2.1.2.3 Balance Mass (BMS)** The AISI 316 stainless steel frame of the BMS follows the same triangular shape of the SHS, such that, together with the magnets of the VCs (VCMs, not shown) and accessories, the sub-assembly results in mass and mass moments of inertia that are similar to those of the SHS sub-assembly (see [23]). Moreover, it is supported on the AF2 by the set of three  $FLS_{BMS}$ , which are identical to the  $FLS_{SHS}$ , reaching similar suspension frequencies between 6 to 10 Hz. Thus, reaction forces in the control of the SHS can be filtered over most of the frequency range in which dynamic effects are critical, whereas the displacement of the frame can be maintained within reasonable limits — i.e. the stiffness is sufficiently high, so that the operational forces do not lead to excessively large motion.

With the  $EOS_{BMS}$  on the AF2, the BMS stroke is also  $\pm 3$  mm, which results in maximum relative displacement between the SHS and the BMS of 6 mm, within the range of 6.5 mm of the VC<sup>11</sup>. Also the aforementioned maximum angular range of  $\pm 20$  mrad given by the  $EOS_{SHS-BMS}$  is defined by the clearance in the VCs. Finally, as the BMS works at RT, having magnets on it allow not only the SHS assembly to be as light as possible, reducing actuation forces and power dissipation, but also the cold SHS to properly drain the heat generated in the coils.

**2.4.2.1.2.4 Auxiliary Frame 2 (AF2)** Analogously to the AF1 in the *Module 1*, not only does the 5083-O aluminum AF2 simplify the manipulation of the *Module 2* and its assembly to the LOS, but it also defines a RT interface for the rest of the system via active temperature control. Moreover, in addition to the hard-stops  $EOS_{SHS}$  and  $EOS_{BMS}$  for the SHS and the BMS, the AF2 also holds the gravity compensators  $GRC_{SHS}$  and  $GRC_{BMS}$  for both sub-assemblies.

As the name suggests, GRCs are nearly-constant-force low-stiffness springs that can be adjusted to make the SHS and the BMS float around their nominal positions, minimizing gravity-related offsets and actuation efforts. In particular, the DCM geometry leads to the following effect: as the main angle increases, the  $Uy'$ -axis gravity component decreases, such that the constant force of the GRCs further pulls both the SHS and the BMS in the positive  $Uy'$ -axis direction, which happens as the gap between crystals also needs to increase (see Figure 2.5). Consequently, a natural outcome of the rotation causes the GRCs to partly compensate the gap adjustment requirements, reducing otherwise larger actuation forces of the VCs and/or displacement in the LOS.

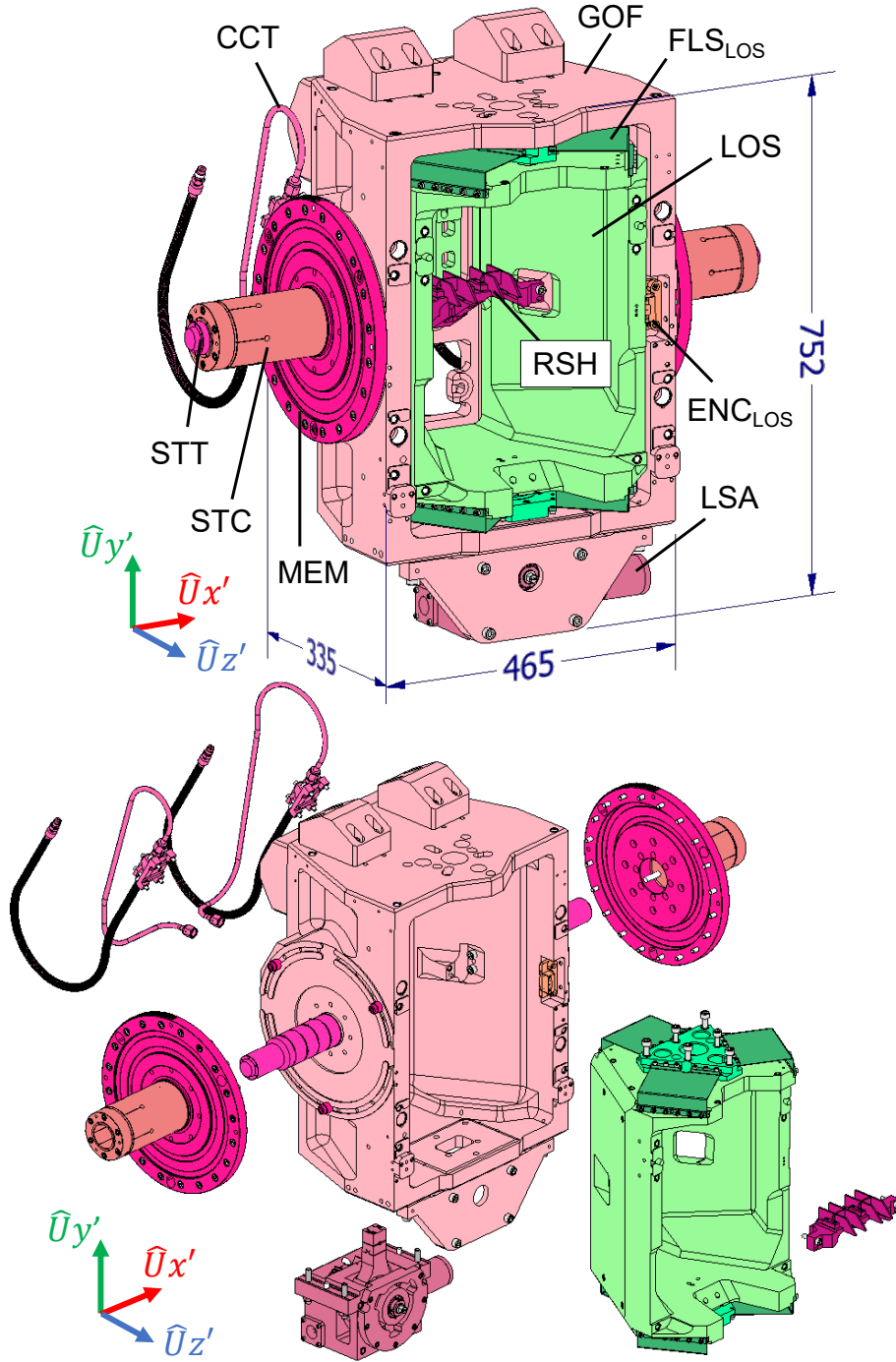
<sup>11</sup>The hardware models are detailed in [23].

The AF2 also makes the mechanical intermediate interface between the *Module 2* and the HBR cooling braid, which is connected to the CMX at its cold end. Thus, a traveling heat sink is created over the motion range of the LOS, such that the forces of this high-conductivity stiffer braid can be managed with minimum influence on the SHS and the CR2. In this interface, thermal isolation is achieved by means of embedded flexures in a Grade 5 titanium part mounted in series with a low-conductivity PEEK plastic part.

**2.4.2.1.3 LOS and GOF Modules** Shown in Figure 2.18, they are the largest structures within the core of the HD-HDM, being responsible for the long linear and rotational operational ranges, respectively. The *LOS Module* consists of the long-stroke frame LOS, the  $FLS_{LOS}$ , and the scale of the absolute linear encoder  $ENC_{LOS}$ . In turn, the *GOF Module*, is composed of: the main rotating goniometer frame GOF; the reading head of the  $ENC_{LOS}$ ; the long-stroke actuator sub-assembly LSA; coupling membranes MEMs, struts STTs and strut clamps STCs to the goniometer; a local radiation shield RSH; and the cryogenic cooling tubes CCTs.

**2.4.2.1.3.1 Long-Stroke Frame (LOS)** Made of a single 5083-O aluminum block for mechanical-tolerance budgets, the LOS is supported on the GOF by two sets — one at the bottom side and one at the top — of stronger 0.8mm-thick AISI 301 FLSs, whose stiffnesses are addressed in [23]. For them, a bending radius of 1 mm is specified due to the higher thickness. Each set of  $FLS_{LOS}$  alone has the same triangular symmetry used in the SHS and the BMS, i.e. with piston-tip-tilt free DoFs. Yet, by separating the two sets in the  $Uy'$ -axis — in this case, by a distance slightly over 0.5 m —, the free rotational DoFs become mutually constrained, such that only the piston motion remains. Technically, 5 FLSs would be sufficient to constrain the required DoFs, however, this over-constraining with 6 FLSs was intentionally made for dynamic reasons, with advantageous symmetry and stiffness results for the LOS and no detrimental influence on *Module 2*. The maximum feasible linear stroke of  $\pm 6.5$  mm in  $Uy'$ -axis is eventually reduced to an operational range of about  $\pm 3$  mm, since part of the total gap stroke of 9 mm is fulfilled by the SHS (see the discussion in the subsection about the AF2 in Section 2.4.2.1.2). This is beneficial to minimize changes in the rotational inertia of the core over the full rotation and to reduce the torque in the rotary stages.

**2.4.2.1.3.2 Long-Stroke Actuator (LSA)** The stepper-driven ball-bearing-based LSA, depicted in details in Figure 2.19, has a cam concept and lies under the GOF, acting on the LOS from below. The motor drives a worm wheel that is locked to an eccentric shaft, which, in turn, drives the plunger over a limited section of a circumference of radius of 12 mm, working as a two-bar mechanism. With microstepping and high-resolution metrology, the position of the LOS can be controlled within about 10 nm with an encoder resolution of 5 nm.



**Figure 2.18:** Mechanical design of the LOS and GOF Modules in the HD-DCM. Top: Orthographical view with reference dimensions given in millimeters, highlighting the main components: long-stroke frame (LOS), long-stroke folded leafsprings ( $FLS_{LOS}$ ), long-stroke absolute linear encoder ( $ENC_{LOS}$ ), long-stroke actuator (LSA), main rotating frame (GOF), coupling membranes (MEMs), coupling struts (STTs) and their clamps (STCs), radiation shield (RSH), and cryogenic cooling tubes (CCTs). Bottom: Partially exploded view.

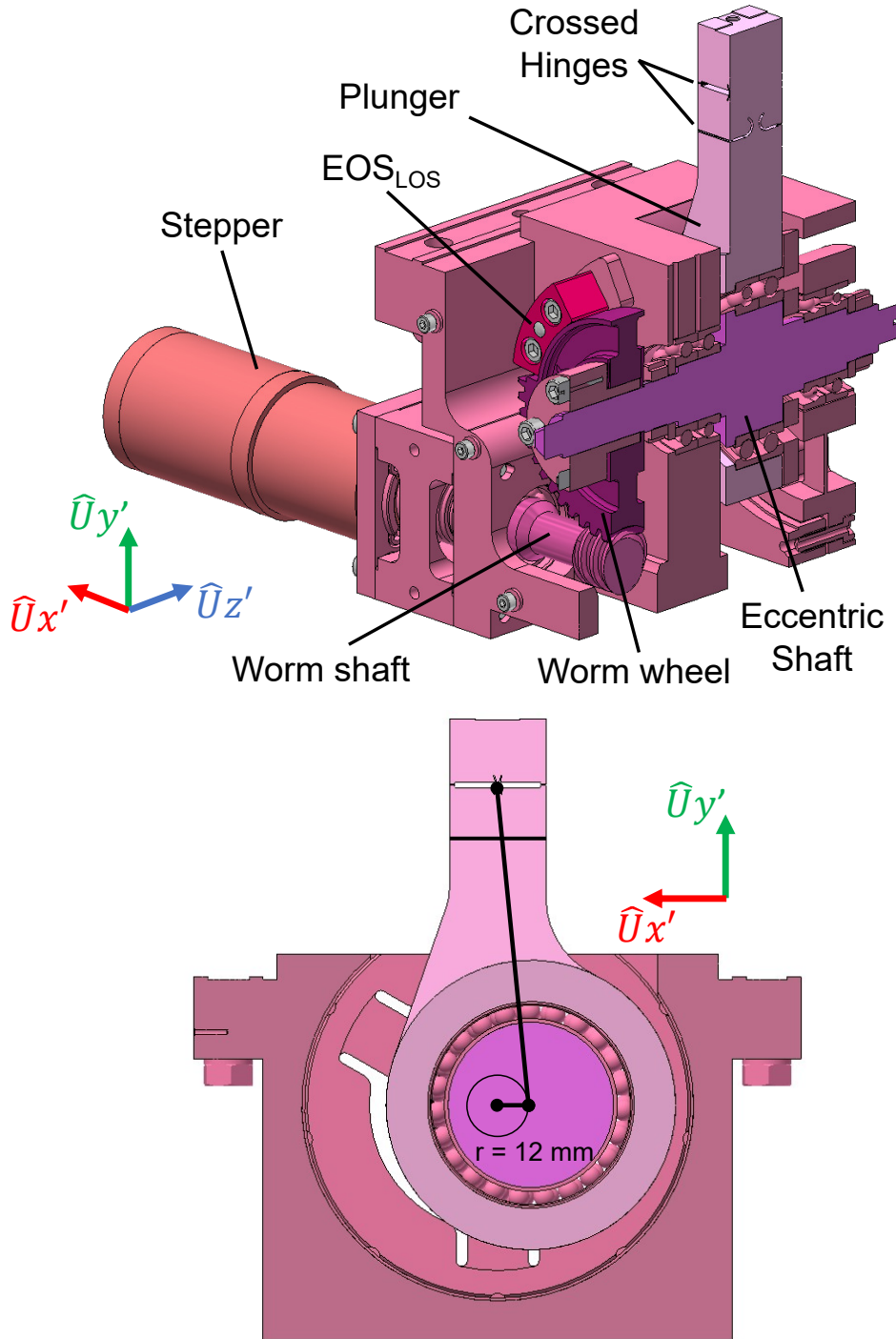
For alignment and motion, the plunger, which is made of STAVAX (stainless steel AISI 420) for high yield strength, is connected to the LOS via a set of crossed hinges with  $Rx'$  and  $Rz'$  compliance, thus creating a high-stiffness single-axis actuator. For the LOS, it is important to have the  $EOS_{LOS}$  at the worm-wheel side of the actuator, instead of directly at the load, so that excessive tension and/or compression in the crossed hinges — given by the large mechanical leverage of the actuator mechanism —, can be prevented.

**2.4.2.1.3.3 Goniometer Frame (GOF)** Also made of a single aluminum 5083-O block for mechanical-tolerance budgets (except for a complementary stiffening plate around the LSA and for a few balancing weights), the GOF is supported on the goniometer by the MEMs, STTs and STCs. As illustrated in Figure 2.20, the MEMs, made of thick 5083-O aluminum plates, are machined in a way to create a reinforced flexural membrane between their outer rings — which are connected to the GOF —, and their inner rings — fixed to the rotors of the rotary stages. Each membrane is stiff in the  $Uy'$ ,  $Uz'$  and  $Rx'$  axes, but compliant in the remaining DoFs. Indeed, since each stage individually defines a rotation axis, the MEMs prevent over-constraining in the full assembly. Therefore, the system can safely handle machining and alignment tolerances over the assembly chain, as well as wobbling and eccentricity in the stages, and thermal expansion effects. The relative distance between the MEMs mutually constrain  $Ry'$  and  $Rz'$  DoFs of GOF, just as in the *LOS Module* with the  $FLS_{LOS}$ . The  $Ux'$ -axis, however, would remain free. Once no translational free DoF is desired in the GOF, this is corrected as a final assembling step, by the AISI 316 stainless steel STTs and STCs, also shown in Figure 2.20. They work in parallel with the MEMs, between the GOF and the rotors of the goniometer with the STTs being more compliant than the MEMs in  $Uy'$ ,  $Uz'$ ,  $Rx'$ ,  $Ry'$  and  $Rz'$  axes, but axially stiff in  $Ux'$ .

The GOF anchors the inlet and outlet ways of the flexible corrugated pipes and the stiff smooth pipes of the CCTs, which is the part of cryogenic circuit between the vessel and the *Module 1*. Thermal isolation in the anchoring points is achieved once again via PEEK parts, whereas RT is maintained via local active temperature control. Finally, the GOF also holds a small assembly of 3mm-thick tungsten blades that make the shield RSH. The heavy metal covers as much solid angle as possible around the impact point of the incoming beam on the CR1s, reducing the extent of parasitic diffracted beams (glitches) and scattered X-rays within the core of the HD-DCM, which might lead to unpredicted heat loads on different parts and damage of parts and electronic components.

### 2.4.2.2 Goniometer Module

It is the interface between the *Core Module* and the *Bench Module*, being responsible for the main rotation of the instrument in the  $Rx$ -axis with respect to the incoming beam over the operational range between  $3^\circ$  and  $60^\circ$ . The maximum angular range between  $-5^\circ$  and  $65^\circ$  is mainly limited by the corrugated pipes of the CCTs, but it



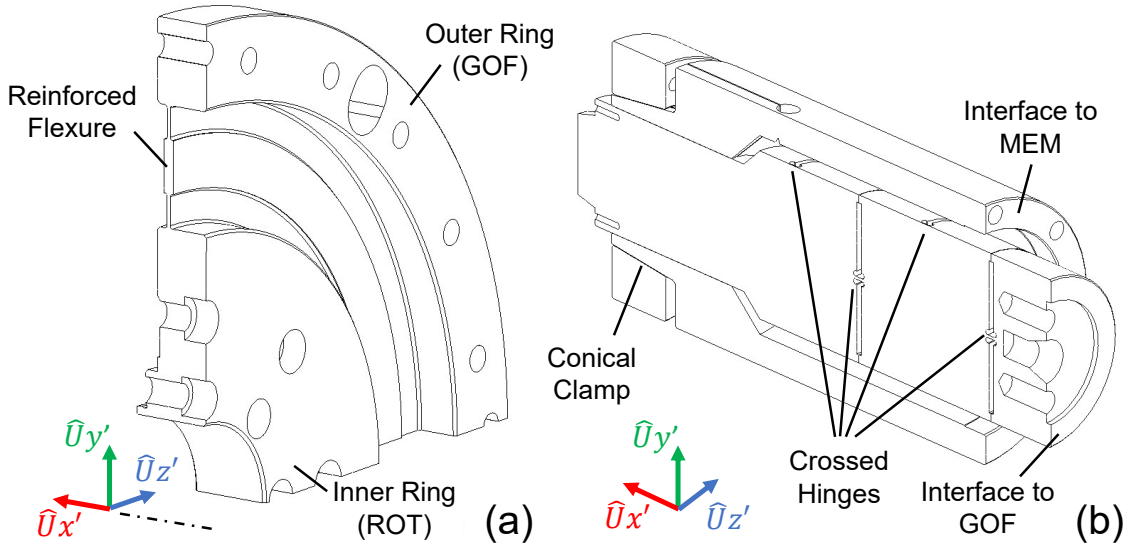
**Figure 2.19:** Mechanical design of the long-stroke actuator (LSA) in the GOF Module of the HD-DCM: Top: Orthographical cross-sectional view, highlighting the stepper motor, the worm-gear coupling, the end-of-stroke EOS<sub>LOS</sub>, the eccentric shaft on ball bearings, and the plunger with crossed hinges with  $R_{x'}$  and  $R_{z'}$  compliance. Bottom: Side cross-sectional view, with the eccentric geometry of 12 mm of radius as a two-bar mechanism. (Arbitrary scale for clarity.)



is anyhow broader than the limitations imposed by the beam and the crystals. As shown in Figure 2.21, it consists of: the rotary stages made of the stators STAs and the rotors ROTs; the supports SUPs to the base flange of the vessel VES (interfacing to the bench); and safety optical switch SSW and hard-stops  $\text{EOS}_{\text{GOF}}$ .

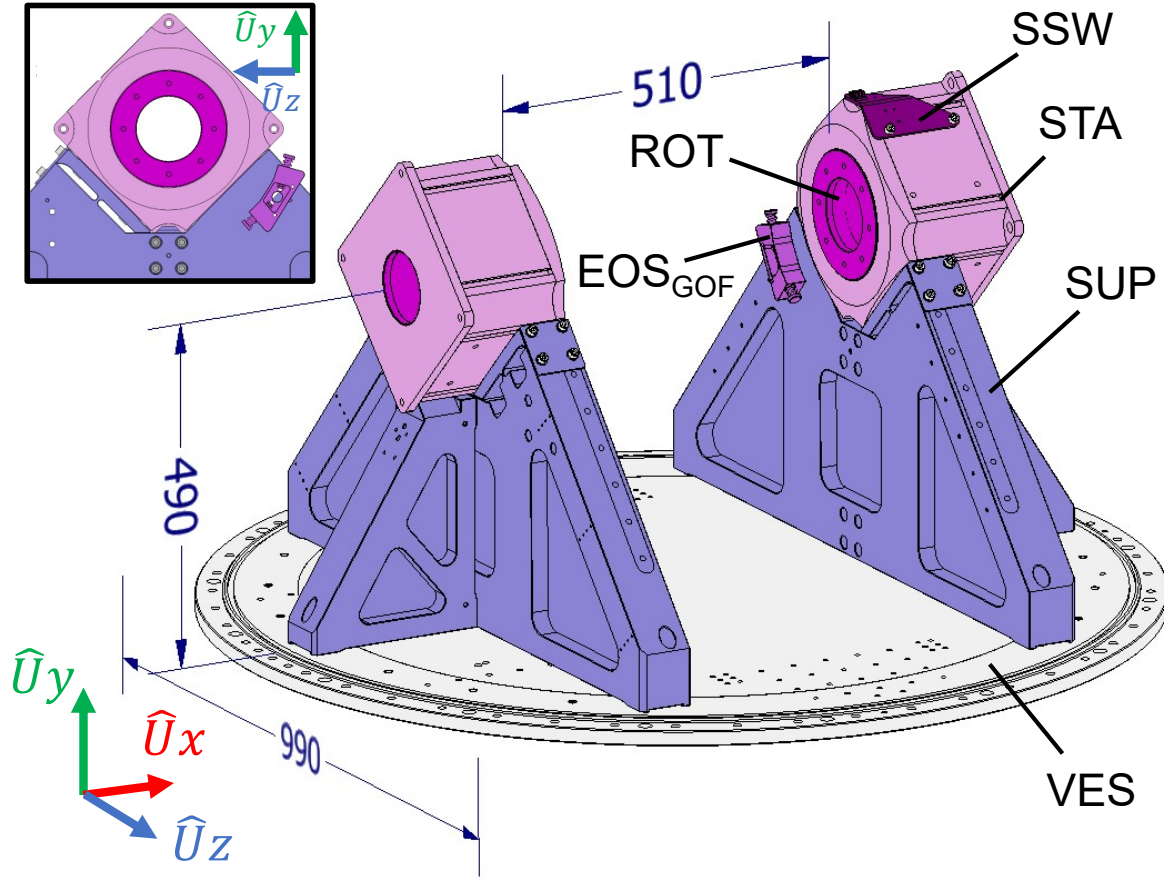
Having bearings at both sides of the core distributes the payload and balances the system, allowing for better dynamics. Commercial rotary stages have been selected to reduce initial development costs. They can be both active stages, or, as in the first units of the HD-DCM, a combination of an active stage, with a direct drive motor and an optical encoder, at one side, and a simpler passive bearing, at the other side. The current choice breaks the control symmetry and concentrates the power in a single motor, but simplifies control needs and reduces costs of additional hardware. With a high-resolution encoder and control bandwidth around 20 to 30 Hz (see [23]), typical positioning control level at stand-still has been around 25 nrad RMS.

The SUPs have been designed to fit the rotary stages with high-stiffness connections in all DoFs. They are made of 5083-O aluminum blocks with V-shaped seats for the STAs, including a flexural hinges to accommodate possible machining mismatching regarding the perpendicularity of the housings of the stages. The purpose is optimizing the local contact between the STAs and the SUPs for stiffness and reducing the risks of extra stresses on the bearings. In addition to the constraints imposed by the V-seats, a complementary connection point at the base plate of the housings improves  $U_x$ ,  $R_y$



**Figure 2.20:** Mechanical design of the membranes (MEMs), struts (STTs) and strut clamps (STCs) in the GOF Module in the HD-DCM. (a): Quarter-sectional view of the MEM, highlighting its inner ring, connected to the rotor (ROT) of the goniometer, its outer ring, connected to the goniometer frame (GOF), and the decoupling reinforced flexure in between; (b) Cross-sectional view of the STT and the STC, highlighting the four crossed hinges of the STT, the interface of the STT with the GOF, the interface of the STC with the MEM, and the conical clamp between the STT and the STC.



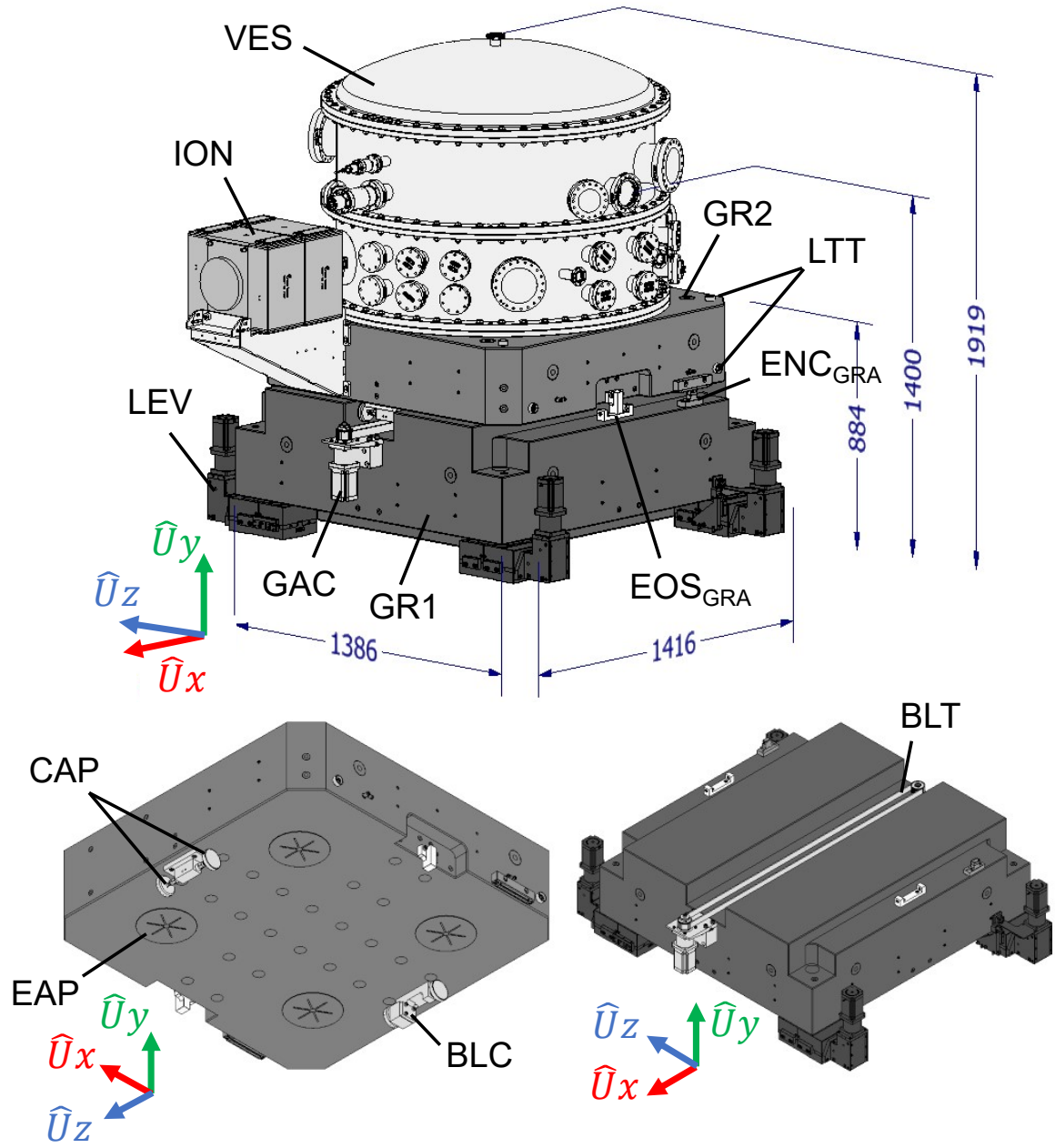


**Figure 2.21:** Mechanical design of the Goniometer Module in the HD-DMC. Orthographical view with reference dimensions given in millimeters, highlighting the main components: goniometer rotors (ROT) and stators (STAs), mounting supports (SUPs), end-of-stroke ( $\text{EOS}_{\text{GOF}}$ ), and safety optical switch (SSW). The bottom flange of the vessel (VES), to which the SUPs are connected, is also shown for a reference. The inset depicts the V-shaped seat for the rotary stages with a flexural hinge for fitting optimization.

and  $R_z$  constraints for each stage. For maximum stiffness, the SUPs are directly bolted to the bottom flange, which, in turn, is directly bolted to upper granite block of the bench.

#### 2.4.2.3 Bench Module

As depicted in Figure 2.22, the *Bench Module* includes the granite supporting structure and the vacuum infrastructure for the system. It consists of: the four levelers LEVs; the two-level granite bench GR1 and GR2; the stepper actuator GAC; embedded air-bearing pads EAPs, commercial air-bearing pads CAPs, a timing belt BLT and its clamp BLC, absolute linear encoders  $\text{ENC}_{\text{GRA}}$ , and safety hard-stops  $\text{EOS}_{\text{GRA}}$  between GR1 and GR2; laser-tracker targets LTTs for global alignment at the beamline; the vacuum vessel VES, including electric and  $\text{LN}_2$  feedthroughs, vacuum sensors, valves, safety seals and viewports; and the main ionic pump ION. The height of the system is



**Figure 2.22:** Mechanical design of the Bench Module in the HD-DCM. Top: Orthographical view with reference dimensions given in millimeters, highlighting the main components: four levelers (LEVs); granite frames (GR1 and GR2); stepper-motor-based actuator (GAC), absolute linear encoders ( $ENC_{GRA}$ ) and safety hard-stop ( $ENC_{GRA}$ ) for positioning of GR1 in  $Ux$ -axis; laser-tracker targets (LTT) for alignment procedures during the installation at the beamline; the vacuum vessel (VES), and the ionic pump (ION). Bottom: Partially exploded view, highlighting the embedded (EAP) and commercial air-bearing pads (CAP), the driving belt (BLT) at GR1 and the belt clamp (BLC) at GR2, as the mechanical solution for positioning of GR1 in  $Ux$ -axis with respect to the incoming beam at the beamline and user selection between the silicon crystal sets.

mainly resulting from the height of the beam, nominally 1.4 m above the floor, whereas the footprint is mainly dictated by the sizes of the core and the goniometer modules.

As the HD-DCM must be correlated with the beam source over tens of meters and beamline feedback is an uncertain variable, low-stiffness suspension and low-frequency decoupling of the instrument with respect to the floor may not be feasible. Thus, as a first approach, the bench is supported on four high-stiffness wedge-type LEVs, which have originally been designed in house for Sirius storage ring, with maximum stroke of  $\pm 2.5$  mm and resolution of 1  $\mu$ m. They are driven by stepper motors and linear gauges are used as feedback to measure the distance between the GR1 and the floor at the four specific locations. Together, they allow for adjustment of the MCS in  $Uy$ ,  $Rx$  and  $Rz$  axes. The four-point suspension was chosen for symmetry, load distribution and accessibility reasons, but might lead to imbalance, which are overcome with simple positioning strategies with open-loop iterative feedback.

For the main structures, granite has been selected not only due to its thermal and mechanical properties, but also its availability and costs. Indeed, given the low CTE, low thermal conductivity and large thermal inertia (given their large masses), together with the controlled environment of beamlines, drifting effects become significantly reduced. Moreover, granite has its Young's modulus comparable to that of aluminum and is mechanically extremely stable, with negligible aging effects. Equivalent performances with steel or aluminum alternative concepts would come with higher costs and/or complexity.

The GR1 and the GR2 exist as separate parts to complement the LEVs, i.e. to allow for positioning of the core with respect to the beam in  $Ux$  and  $Ry$  axes. Since all motion in the bench is part of initial setup, but not of operation of the HD-DCM with the beam, the interface between the GR1 and the GR2 is made by means of the EAPs and CAPs, which can be turned off at convenience, assuring a high-stiffness interface that is free of lubrication, wear and regular maintenance. This solution also allows for the implementation of the two DoFs through a single interface layer, which prevents additional elements and interfaces in the stiffness chain.

The EAPs consist of four air-pads sculpted in the GR2, defining deterministic lever-arms for the distribution of loads and moments. Again, three pads would be the ideal configuration to prevent four-point imbalance, however, the geometry and loads were not favorable to it. To mitigate this risk, the top block was designed to be thick enough for the distribution of forces, but simultaneously thin enough to deform and accommodate residual manufacturing lapping deviations of a few microns with the distributed load. The CAPs, in turn, are arranged in two sets of two commercial pads that are fixed to the GR2 and run in a groove at the top side of the GR1. Thus, a translational axis driven by the GAC and the BLT is created, with maximum stroke of  $\pm 50$  mm and resolution around 1  $\mu$ m, which is operated by the scientists and users for the selection of the desired set of crystals for each experiment.

By manual adjustment — or motorized adjustment with upgrade modules — of the CAP sets in the  $Uz$ -axis inside the groove, a small  $Ry$  rotation for alignment is possible.

Feedback for  $Ux$  and  $Ry$  are obtained by means of combinations of the readings of the two ENC<sub>GRA</sub>, positioned upstream and downstream, with the scales fixed to the GR1 and the heads to the GR2. As the  $Ry$  adjustment is small, it stays within the yaw angular alignment tolerances of the encoders of  $\pm 12$  mrad. The EOS<sub>GRA</sub> are present upstream and downstream between the GR1 and the GR2 to prevent excessively large displacements of the GR2, which might result in critical vacuum and/or mechanical accidents.

## 2.5 Conclusions and Discussions

Standard X-ray DCM designs have gradually evolved over four decades on the basis of high-stiffness mechanical architectures, which may have reached insurmountable limitations regarding positioning errors and scanning capabilities as required for the new challenges of 4th-generation synchrotron light source beamlines. Without doubt, the critical limitation is keeping the angular stability between crystals within about 10 nrad RMS over frequency ranges of up to 1 or 2 kHz for compatibility with fast detectors. Indeed, not only do DCMs suffer from design challenges in making large rotations of typically several tens of degrees in the core, together with relative translations in the crystals by several millimeters, but they also respond to several disturbance agents, including flow-induced vibrations. While typical stand-still fixed-energy angular stability currently spans from 50 to several hundreds of nrad RMS in different vertical-bounce DCMS, as motion disturbances act on traditional systems during fly-scans the errors often exceed several  $\mu$ rad RMS.

The HD-DCM is the first beamline vertical-bounce DCM to achieve the range of 10 nrad RMS up to 2.5 kHz, not only in stand-still condition, but even during fly-scans — which is only possible due to its decoupled mechatronic architecture, that is capable of reaching a closed-loop control bandwidth around 250 Hz for sufficient noise suppression and trajectory-following capabilities. Compared to state-of-the-art standard DCMs, it shows improvements of even a hundred fold (or more), allowing for increased quality of existing experiments and processes, and eventually enabling new science opportunities.

These “first-time-right” achievements from scratch would not have been possible without the systems approach incorporating the Dynamic Error Budgeting workflow that is presented in [23]. Here, the engineering requirements, the overall architecture and the mechanical design of the several modules that build the HD-DCM are presented in sufficient detail to share with the community the principles and insights that are aligned with the required predictive design methodology. In addition to the innovative control-based architecture, the original design concepts include minimal positioning DoFs, long-stroke and short-stroke arrangement, smooth motion guiding and actuation, inter-crystal metrology, crystal mounting, and decoupled cooling, which are deep paradigm changes within this class of instruments.

To conclude, this is only the first DCM of its kind, such that there are still many of

opportunities for upgrades and customizations in the years to come. This is important because, as an instrument in the core of a research environment, science opportunities will be continuously pushing. Thus, even though the basic original specifications have been met, investigations including alternative control strategies, optimizations in the core, and changes in the long-stroke actuator, in the goniometer and in the bench are currently ongoing. With the HD-DCM-Lite project, many of these aspects will already be covered in the near future.

## Acknowledgements

The authors would like to acknowledge the fundamental contribution of the LNLS staff, including leaders, engineers, designers and technicians of different groups, and the essential roles of Theo Ruijl and Ronald Schneider, together with the rest of the team at MI-Partners, in the development of this collaborative project. This work is part of a PhD project carried out with the CST group at TU/e, being supported by the Brazilian Center for Research in Energy and Materials (CNPEM) under contract with the Brazilian Ministry of Science, Technology and Innovation (MCTI).

## 2.A List of Abbreviations

AF1	Auxiliary frame 1
AF2	Auxiliary frame 2
BCS	Beam coordinate system
BLC	Timing belt clamp
BLT	Timing belt
BMS	Balance mass
BPM	Beam position monitor
CAP	Commercial air-bearing pad
CBR	Compliant cooling braid
CCB	Crystal cooling block
CCG	Crystal cage
CCT	Cryogenic cooling tube
CIP	Complementary isolation pads
CMF	Cooling manifold
CMX	Cooling manifold extension
CNPEM	Brazilian Center for Res. Energy and Materials
CR1	1st crystal
CR2	2nd crystal
CS	Coordinate system
CTE	Coefficient of thermal expansion
DCM	Double-Crystal Monochromator
DEB	Dynamic Error Budgeting

---

DoF	Degree of freedom
EAP	Embedded air-bearing pad
EFS	Embedded flexural structure
ENC	Encoder
EOS	End of stroke
ESRF	European Synchrotron Radiation Facility
EUV	Extreme ultraviolet
FE	Finite element
FLS	Folded leaf-spring
FIV	Flow-induced vibrations
GAC	Granite actuator
GOF	Goniometer frame
GND	Ground/floor
GR1	Bottom granite block
GR2	Top granite block
GRC	Gravity compensator
HBR	High-conductivity cooling braid
HD-DCM	High-Dynamic Double-Crystal Monochromator
HP1	Homing pin 1
HP2	Homing pin 2
IFA	Fiber interferometer assembly
IFF	Fiber interferometer frame
IFH	Fiber interferometer head
ION	Ionic pump
LINAC	Linear Accelerator
LEV	Leveler
LN2	Liquid nitrogen
LNLS	Brazilian Synchrotron Light Laboratory
LOS	Long-stroke structure
LSA	Long-stroke actuator
LTT	Laser tracker target
MCS	Main coordinate system
MEM	Coupling membrane
MF1	Metrology frame 1
MF2	Metrology frame 2
MIR	Plane mirrors
MLS	Manifold leaf-springs
OFC	Oxygen-free copper
RCS	Rotating coordinate system
RMS	Root mean square
ROT	Goniometer rotor
RSH	Radiation shield

RT	Room temperature
SH1	Calibrated shim 1
SH2	Calibrated shim 2
SHS	Short-stroke frame
SNR	Signal-to-noise ratio
SSRF	Shanghai Synchrotron Radiation Facility
SSW	Safety optical switch
STA	Goniometer stator
STC	Coupling strut clamp
STT	Coupling strut
SUP	Goniometer support
TC	Thermal center
UHV	Ultra-high vacuum
UV	Ultraviolet
VC	Voice-coil
VCA	Voice-coil assembly
VCC	Voice-coil coil
VCF	Voice-coil frame
VCM	Voice-coil magnet
VES	Vacuum vessel

## References

- [1] Eriksson M. *et al.* 2014 *J. Synchrotron Rad.* **21**(5) 837
- [2] Hettel R. 2014 *J. Synchrotron Rad.* **21**(5) 843
- [3] Liu L. *et al.* 2021 *Proc. 12th Int. Particle Acc. Conf. (IPAC'21)* (JACoW Publishing) 13–18
- [4] X. Zhang 2018 *Synchrotron Radiation Applications* (World Scientific Publishing Company)
- [5] Hastings J.B. 1977 *J. Appl. Phys.* **48**(4) 1576
- [6] Lemonnier M. *et al.* 1978 *Nucl. Instrum. Methods* **152**(1) 109
- [7] Golovchenko J.A. *et al.* 1981 *Rev. Sci. Instrum.* **52**(4) 509
- [8] Hussain Z. *et al.* 1982 *Nucl. Instrum. Methods Phys. Res.* **195**(1-2) 115
- [9] Cowan P.L. *et al.* 1983 *Nucl. Instrum. Methods Phys. Res.* **208**(1-3) 349
- [10] Kelly J. *et al.* 2013 *J. Phys. Conf. Ser.* **425**(5) 052009
- [11] Kristiansen P. *et al.* 2015 *J. Synchrotron Rad.* **22**(4) 879
- [12] Waterstradt T. *et al.* 2018 *Sub-20-nrad Stability of an LN<sub>2</sub>-Cooled Vertical-Offset Double-Crystal Monochromator*. Presented at MEDSI'18 in Paris, France, unpublished
- [13] Baker R. *et al.* 2018 *Proc. 10th Mech. Eng. Des. of Synchrotron Radiat. Equip. and Instrum. (MEDSI'18)* (JACoW Publishing) 440–444
- [14] Dolbnya I.P. *et al.* 2018 *J. Synchrotron Rad.* **26**(1) 253
- [15] Fan Y. *et al.* 2020 *Nucl. Instrum. Methods Phys. Res. A* **983** 164636
- [16] Wu J. *et al.* 2021 *Nucl. Instrum. Methods Phys. Res. A* **988** 164872

- [17] Baker R. *et al.* 2021 *ESRF Double Crystal Monochromator - Design and Working Modes*. Presented at MEDSI'20 in Chicago, USA, unpublished
- [18] European Synchrotron Radiation Facility (ESRF) 2014 *Double Crystal Monochromator Workshop* <http://www.esrf.eu/home/events/conferences/2014/double-crystal-monochromator-workshop.html>, accessed: Oct. 1st, 2021
- [19] Geraldes R.R. *et al.* 2017 *Proc. 9th Mech. Eng. Des. of Synchrotron Radiat. Equip. and Instrum. (MEDSI'16)* (JACoW Publishing) 141–146
- [20] Geraldes R.R. *et al.* 2018 *Proc. 10th Mech. Eng. Des. of Synchrotron Radiat. Equip. and Instrum. (MEDSI'18)* (JACoW Publishing) 147–152
- [21] Geraldes R.R. *et al.* 2019 *Instrument for Moving and Positioning of Optical Elements with Nanometric Mechanical Stability and Resolution in Synchrotron Light Source Beamlines*. US Patent App. 16/331,925
- [22] Jabben L. 2007 *Mechatronic Design of a Magnetically Suspended Rotating Platform* Ph.D. thesis Delft University of Technology
- [23] Geraldes R.R. *et al.* 2022 *Precision Engineering* **77** 90
- [24] Geraldes R.R. *et al.* 2023 *J. Synchrotron Rad.* **30** 90
- [25] Ashcroft N.W. 2003 *Solid State Physics* (Thomson Press (India) Ltd)
- [26] Laro D.A.H. 2009 *Mechatronic Design of an Electromagnetically Levitated Linear Positioning System using Novel Multi-DoF Actuators* Ph.D. thesis Delft University of Technology
- [27] Zhang L. *et al.* 2013 *J. Synchrotron Rad.* **20**(4) 567
- [28] Saveri Silva M. *et al.* 2017 *Proc. 9th Mech. Eng. Des. of Synchrotron Radiat. Equip. and Instrum. (MEDSI'16)* (JACoW Publishing) 194–197
- [29] Hazelton A.J. *et al.* 2002 *Wafer positioner with planar motor and mag-lev fine stage*. US Patent 6,437,463
- [30] Butler H. 2011 *IEEE Control Syst. Mag.* **31**(5) 28
- [31] Soemers H. 2011 *Design Principles for Precision Mechanisms* (T-Pointprint)
- [32] SmarAct 2020 *Picoscale Michelson Interferometer* <http://www.picoscale.com/>, accessed: Oct. 1st, 2021
- [33] Axilon 2018 *Accelerator and X-Ray Instrumentation for Laboratories, National Facilities and Industry* [http://www.axilon.de/Download/AXILON\\_Beamline-Instrumentation\\_18-04.pdf](http://www.axilon.de/Download/AXILON_Beamline-Instrumentation_18-04.pdf), accessed: Oct. 1st, 2021
- [34] Nakiboglu G. 2012 *Aeroacoustics of Corrugated Pipes* Ph.D. thesis Technical University of Eindhoven





---

## Predictive Modeling through Dynamic Error Budgeting applied to the High-Dynamic Double-Crystal Monochromator for Sirius Light Source

---

### Abstract

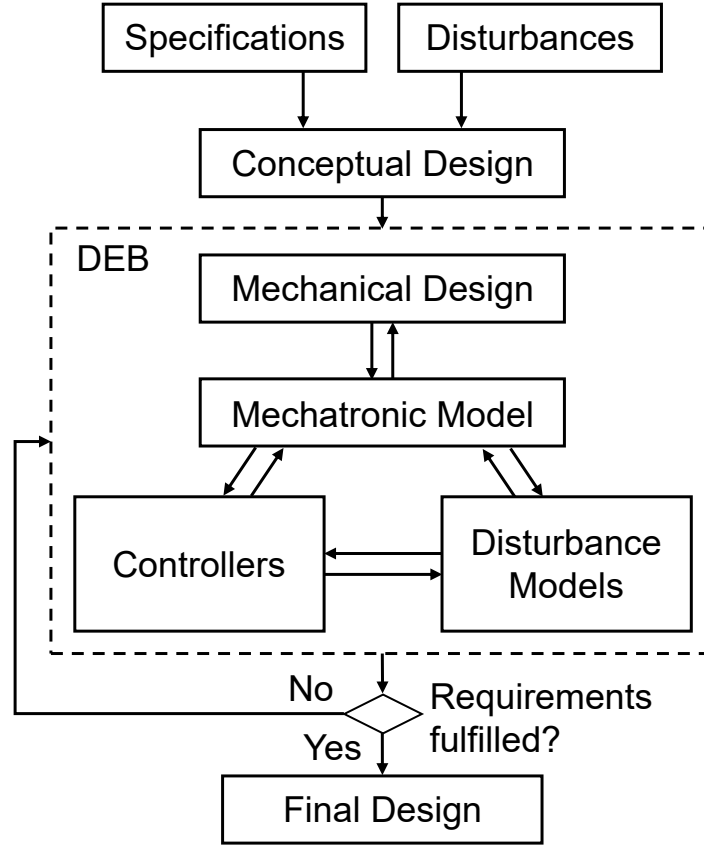
To address recent and more stringent nanometer-level requirements in positioning stability, the High-Dynamic Double-Crystal Monochromator (HD-DCM) has been in development since 2015 for X-ray beamlines of Sirius, the 4th-generation light source at the Brazilian Synchrotron Light Laboratory (LNLS). The unprecedented 10 nrad RMS (1Hz-2.5kHz) inter-crystal parallelism in fixed and scanning modes represents improvements by factors of 5 and 100 with respect to state-of-the-art DCMs, respectively — which became possible only due to its innovative isolated mechatronic architecture with high closed-loop performance, rigorous precision engineering principles, and predictive design via Dynamic Error Budgeting (DEB). This work demonstrates the DEB methodology applied to the HD-DCM via a three-dimensional-space mechatronic model based on a lumped-mass system of 11 rigid bodies. Special attention is given to the disturbance models based on measurements and to performance prediction in fixed-energy operation mode, which is finally compared with experimental results in the real system. Hence, this article presents the step-by-step predictive modeling process of the HD-DCM as a successful case study on the efficient development of innovative high-performance mechatronic machines, which could be a game changer in synchrotron beamline instrumentation.

### 3.1 Introduction

The High-Dynamic Double-Crystal Monochromator (HD-DCM) is introduced in [1], as an innovative mechatronic system that has been in development since 2015 for X-ray beamlines of Sirius, the 4th-generation light source at the Brazilian Synchrotron Light Laboratory (LNLS) at the Brazilian Center for Research in Energy and Materials (CNPEM), in Campinas, Brazil [2]. The motivation for this was overcoming core limitations in existing fixed-exit X-ray Double-Crystal Monochromators (DCMs) via deep paradigm changes, such that positioning errors could be improved in up to two orders of magnitude, as required to take the most out of the exceptional properties of this new-generation light sources [3, 4]. Indeed, with superior static and scanning performances, the HD-DCM allows for enhanced quality in existing applications and may eventually enable new science opportunities in fields ranging from biology, chemistry and medicine, to earth, energy and materials sciences, to name a few. By the end of 2020, the MANACÁ and the EMA beamlines (see [1]) were already under commissioning or in early operation at Sirius, relying on the HD-DCM as the monochromator. Next, by 2022-2023, at least two beamlines should be supplied with new members of the HD-DCM family, the so-called HD-DCM Lite, which is currently under development for slightly different specifications.

The greatest achievement of the HD-DCM is its capacity of keeping the angular stability between its energy-defining silicon crystals within about 10 nrad RMS (root mean square) in the frequency range between 1 Hz and 2.5 kHz, either at fixed wavelength or scanning modes [5, 6], whereas existing corresponding vertical-bounce DCMs would respectively perform at best from 50 nrad RMS to several microradians [7]. The key change consists in replacing the classical open-loop or low-bandwidth high-mechanical-stiffness designs by a decoupled mechatronic architecture with control-based high-bandwidth closed-loop performance. Indeed, this has proven to be an essential enabling technology for the HD-DCM to reach sufficient disturbance-suppression efficiency in handling cryogenic cooling, floor and motion disturbances, while complying with the well-known severe operational conditions that include an ultra-high vacuum (UHV) environment, high power loads and densities, and high radiation levels (see [1]).

Aiming at maximum efficiency in development time and costs, the HD-DCM project has been realized according to a predictive modeling approach relying on the Dynamic Error Budgeting (DEB) technique [8–12], as depicted in Figure 3.1. After specifications were defined and system disturbances were identified, a conceptual design was elaborated. From there, an iterative loop including the mechanical design, a mechatronic model, controller designs and disturbance models was refined until requirements were fulfilled and the final design could be obtained. In this way, the effects of the disturbances on the closed-loop dynamics of the mechatronic model of the instrument could be investigated *a priori*, allowing for countless design changes and optimizations, and building confidence towards the desired performance and the feasibility of the system, thus allowing the development of a complex and entirely new instrument “first time



**Figure 3.1:** The HD-DCM design process with the Dynamic Error Budgeting (DEB) methodology (adapted from [9, 10]).

right”.

Empowered by Dynamic Substructuring techniques [13] for the development of the plant models, the DEB methodology has been used with high-modularity advantages at various degrees of complexity. The analyses have spanned from selection of masses and stiffnesses, to investigations on bandwidth and robustness, to parasitic stiffness effects in flexural structures (due to non-linearities or misalignment), to damping and metrology alignment effects, to name a few. This work presents the DEB toolbox that has been developed over the course of this project and some of its results being compared with experimental data, demonstrating its potential not only for early predictions but also for continuous optimization.

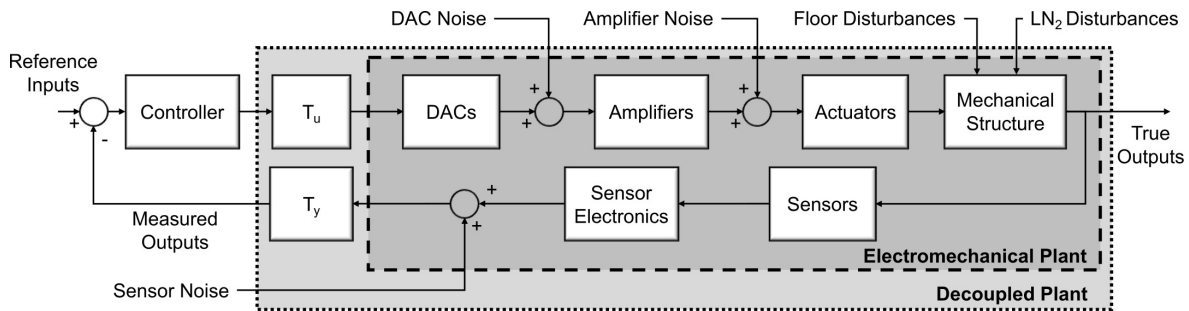
The background about DCMs at beamlines and the engineering specifications, the architecture and the detailed mechanical design of the HD-DCM can be found in [1], which serves as an introductory reference to this work, including concepts and nomenclature. Here, its modeling framework is described and DEB results are presented. Firstly, a short background and the step-by-step process concerning the creation of the models and the application of the DEB methodology are presented in Section 3.2; next, the actual mechatronic model of the HD-DCM is described in Section 3.3; after that, the DEB results for fixed-energy operation mode are shown and compared with

experimental data in the real system in Section 3.4; conclusions are elaborated in Section 3.5; lastly, a list of abbreviations is provided in Section 3.A, and design-to-model details in Section 3.B.

### 3.2 Modeling Methodology

Error budgeting is a well-known design tool in precision engineering, through which geometrical, thermal and measuring errors are explored as an attempt to predict machine performances in terms of resolution, accuracy and repeatability [14, 15]. Traditional static error budgeting, however, is not capable of evaluating the dynamic behavior of a closed-loop control system and its disturbances, which is an essential aspect in mechatronic machines with nanometer-level performance, such as the HD-DCM. To overcome this limitation – by investigating how disturbances propagate through a closed-loop system – DEB tools have been developed and successfully used over the last decade in high-end applications, particularly in the semiconductors industry [8–12]. Hence, the HD-DCM DEB modeling framework has been oriented to efficient concept validation and design assistance since the early phases of development. From preliminary versions, the models have been modularly updated and refined as desired towards higher-dimensional space and more degrees of freedom (DoFs), with higher degrees of complexity and fidelity.

Regardless its particular development stage, the HD-DCM mechatronic model can be described by the basic control loop diagram shown in Figure 3.2. It is worth noting that in addition to the *measured outputs*, a model-based design has access to the *true outputs*, i.e. the real states of the system, which in practice can never be probed —



**Figure 3.2:** Closed-loop control block diagram of the HD-DCM. In addition to the *reference inputs*, a distinction is made between the *true outputs*, as the real states of the system, and the *measured outputs*, which is a subset of these states as filtered by the sensors and contaminated by their noise. The *digital-to-analog converters* (DACs), *amplifiers*, *actuators*, *mechanical structure*, *sensors* and *sensor electronics* form the *electromechanical plant*, which can be transformed via the input and output decoupling matrices  $T_u$  and  $T_y$ , respectively, into the *decoupled plant*, as finally seen by the *controller*. The system disturbances include DAC noise, amplifier noise, sensors noise, floor disturbances and liquid nitrogen ( $LN_2$ ) disturbances.

either because of unavailability of metrology or sensor noise contamination —, but via the model may bring extended analyses possibilities, as explored in Section 3.4. The disturbance agents that impact the closed-loop performance of the mechatronic system in static operation, i.e. in the so-called *fixed-energy* mode (see [1]), are also made explicit in the figure. In the so-called *flys-scan* mode (see [1]), in turn, mechanical disturbances (from bearings, for example) and sensor errors (such as cyclic errors), as well as reference-tracking limitations, may exist and be included in the models, but these will not be addressed here for conciseness.

In the following subsections, the main DEB considerations, the choices for construction of the mechanical model, and the integration of the complete mechatronic model using Matlab® for the extraction of DEB outputs are briefly explained.

### 3.2.1 Dynamic Error Budgeting Background

As detailed descriptions of DEB can be found in [9, 10, 12], only the main concepts and assumptions are summarized here for completeness. The primary consideration is that, in many applications, mechatronic systems can be sufficiently well described as linear time-invariant (LTI) systems. Then, while the effects of deterministic disturbances can be directly evaluated in LTI systems, the DEB method allows the effects of random processes to be predicted as well.

Predictability can be achieved by considering the disturbances as stationary and ergodic random processes or signals, i.e. those that can be described by their average  $\mu$  and their variance  $\sigma^2$ , which are, by definition, not only invariant with time, but also obtainable from a sufficiently large collection of samples. The characteristics of a random process, defining the probability of a given sample falling in a certain range, is defined by its Probability Density Function (PDF), whose most frequent example is the *Gaussian* (or *normal*) *distribution*.

The reason behind the universal presence of the Gaussian distribution goes back to the *Central Limit Theorem* [16], which states that the sum of independent random variables will approach a Gaussian distribution as the number of variables increase, even if the individual distributions are not Gaussian. As in nature, and in mechatronic systems, in particular, systems generally depend on a large number of variables, they tend to approach Gaussian distributions. Next, although correlated signals can be handled if necessary, another practical assumption in the DEB is the consideration of uncorrelated signals, i.e. signals with zero covariance, so that the resulting variance  $\sigma_0^2$  of  $n$  signals becomes

$$\sigma_0^2 = \sum_{i=1}^n \sigma_i^2. \quad (3.1)$$

Moreover, as the PDF and the variance alone do not say anything about the time behavior or the spectral signature of a random signal, its power spectral density (PSD)  $S(f)$  can be considered for the analyses in the frequency domain. Then, it can be shown (see [11]) that the Cumulative Power Spectrum (CPS)  $CPS(f)$ , which is obtained by

integration of  $S(f)$  from zero up to frequency  $f$ , is related to the variance as

$$CPS(f) = \mu^2 + \sigma^2(f), \quad (3.2)$$

where  $\mu$  is the mean of the signal. In practice, for DEB purposes,  $\mu$  can be considered zero, as many of the variables and processes under analysis actually have zero mean, and occasional static error components can be eliminated by the control loop or offsets (see [10]). Furthermore, it can also be shown (see [11]) that the PSDs  $S_i(f)$  and  $S_o(f)$  of an input and an output signals, respectively, through an LTI system are related according to the given transfer function (TF)  $H(f)$  with

$$S_o(f) = |H(f)|^2 S_i(f). \quad (3.3)$$

Then, from Equation (3.1), Equation (3.2) and Equation (3.3), the contributions of several uncorrelated random disturbances to the output of a given closed-loop system mechatronic model, such as the HD-DCM in Figure 3.2, can be independently investigated over frequency via the squared Bode magnitudes of the corresponding TFs, and added to a final performance prediction. In particular, via CPS plots (see Section 3.4) the contributions can be graphically compared and the dominant frequencies can be directly identified, assisting the iterative design work in the plant and/or the controller.

### 3.2.2 Mechanical Structure Model Formulation

Referring to Figure 3.1 and Figure 3.2, it is clear that the appropriate representation of the mechanical design as part of the plant model in the closed-loop control diagram is essential in the design process and performance predictions. To this end, from the very beginning of the project until today, a lumped-mass description with rigid body assumptions has been choice for the HD-DCM mechanical models.

Arguably, this remains a viable and sufficiently accurate alternative in this application thanks to the systematic design of the mechanical parts and interfaces, as explained in [1] and further discussed in the following sections. Compared with Finite Element Analysis (FEA) alternatives, for example, the lumped-mass representation allows for the DEB workflow to run with quicker iterations and simpler parametrization even before any detailed mechanical design is available. Within this construction, the dominant characteristics of the system can be pragmatically explored with minor setting and computing efforts, whereas even internal dynamics may be addressed as specific additional lumps. Still, nothing prevents reduced FEA models or experimental modal data from being used in the future.

The lumped models are built according to the Dynamic Substructuring (DS) or Structural Dynamic Modification (SDM) techniques, which are equivalent approaches that have been used for over five decades as powerful tools in the field of structural dynamics [13,17]. Yet, here, instead its original application in combining highly-complex finite-element models, the concepts are used to create effective and versatile relatively small lumped models. Indeed, within this concept, the final dynamic models are built

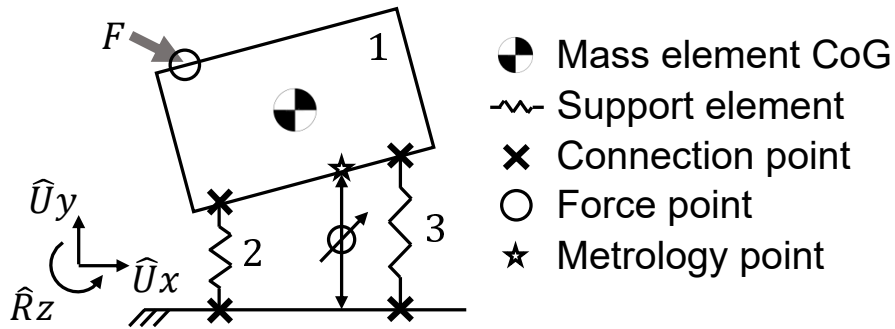
from substructures, which are discrete structures that can be described as elements (or functions) with a finite set of DoFs and coupled to each other at connection points. An example for a single rigid body with three DoFs in a two-dimensional space is illustrated in Figure 3.3.

Starting with a representation in the physical domain, the rigid bodies and supports can be simply described by block-diagonal stacked matrices for mass  $\mathbf{M}_s$ , damping  $\mathbf{D}_s$  and stiffness  $\mathbf{K}_s$ , according to a stacked vector  $\mathbf{s}$  for the DoFs. Then, by using the concepts of *Boolean*  $\mathbf{B}$  and *Boolean localization*  $\mathbf{L}$  matrices and the *primal formulation in the physical domain* (see [13]), the respective primal-assembled matrices  $\mathbf{M}$ ,  $\mathbf{D}$  and  $\mathbf{K}$  can be obtained, and  $\mathbf{s}$  can be reduced to the physical vector  $\mathbf{p}$ , containing the set of DoFs of the CoGs of the rigid bodies in a convenient basis in up to 6 DoFs (i.e.  $U_x$ ,  $U_y$ ,  $U_z$ ,  $R_x$ ,  $R_y$  and  $R_z$ ). This DS process can be summarized in the steps in Figure 3.4. Finally, including adapted damping  $\mathbf{D}_f$  and stiffness  $\mathbf{K}_f$  matrices to address the external forces that are created by displacements of the floor, the complete equation of motion of the system can be written as

$$\mathbf{M}\ddot{\mathbf{p}} + \mathbf{D}\dot{\mathbf{p}} + \mathbf{K}\mathbf{p} = \mathbf{f} + \mathbf{D}_f\dot{\mathbf{s}}_f + \mathbf{K}_f\mathbf{s}_f, \quad (3.4)$$

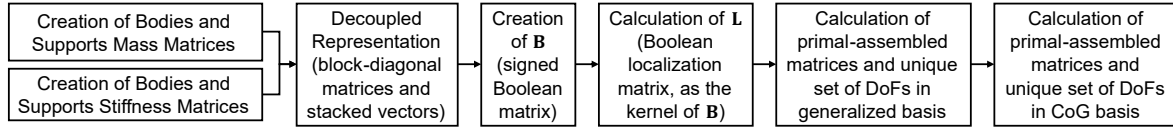
where  $\mathbf{f}$  is the force vector related to  $\mathbf{p}$ , and  $\mathbf{s}_f$  and  $\dot{\mathbf{s}}_f$  are the displacement and velocity external inputs from the floor in the corresponding floor interface DoFs of the stacked vector  $\mathbf{s}$ .

Here, to comply with the LTI requirements, the matrices must be constant. Nonetheless, the effects of known variations and non-linearities in inertia and stiffness, for example, can be investigated if desired by running complementary analyses with modified matrices. Furthermore, while the mass matrices can be easily obtained either by analytical approximations (especially for initial models) or from a CAD software, and the stiffness matrices can be — together with assumptions for contact stiffness — approximated analytically or extracted from finite element simulations, the definitions

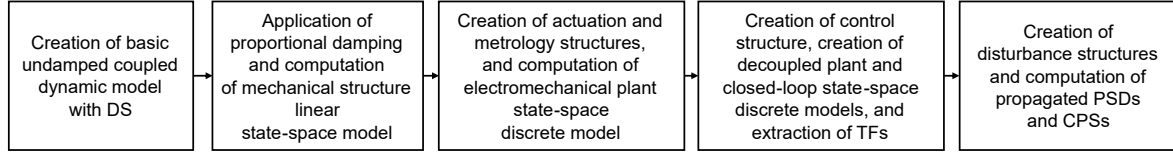


**Figure 3.3:** Lumped mass model of a single body with three degrees of freedom (DoFs) ( $U_x$ ,  $U_y$  and  $R_z$ ) in a two-dimensional space, exemplifying Dynamic Substructuring (DS) with a mass element (1) and its center of gravity (CoG), and support elements (2 and 3), coupled at connection points. Also illustrated are points of interest for force and metrology, which can be geometrically related to the CoG for disturbance points, actuators and sensors in the subsequent mechatronic model.





**Figure 3.4:** Dynamic Substructuring (DS) workflow for the HD-DCM mechanical structure models.



**Figure 3.5:** Dynamic Error Budgeting (DEB) workflow for the HD-DCM with proportional damping approximation. DS stands for Dynamic Substructuring, TF for transfer function, PSD for power spectral density and CPS for cumulative power spectrum.

for damping, on the other hand, may not be as obvious.

The HD-DCM models have been developed with proportional damping approximation, for the sake of simplicity, but also due to: 1) relatively clear decoupling strategies for different DoFs (see [1]); and 2) to separate intrinsically low-frequency dynamics with higher damping — related to the floor, bearings, meshed braids and actuators (as detailed in Section 3.3.1) — from small-damping high-frequency resonances in vacuum. As such, the undamped system can be initially fully described by  $\mathbf{M}$  and  $\mathbf{K}$  matrices, whereas damping can be more easily applied from a modal representation. In this case, the damping fractions can be estimated from experience or measured from complementary experimental setups.

Lastly, the mechanical model can be conveniently written in a linear state space form for the subsequent modeling steps. That way, points of interest out of the center of gravity (CoG), as exemplified in Figure 3.3, can be considered via the state space input vector and matrix — for forces related to mechanical disturbances and actuators — and the state space output vector and matrix — for displacements related to metrology sensors (see also [18] for an example on such transformations).

### 3.2.3 Mechatronic Model Formulation for DEB

Over the course of the development of the HD-DCM project, a toolbox for DEB based on DS has been written by the authors in Matlab<sup>®</sup>. A summary describing the process of taking user inputs and building state-space models up to the performance predictions with CPSs is given by the diagram in Figure 3.5. In the particular case of proportional damping, the undamped and unforced dynamic model is created first and animated mode shapes are used for the identification of the system modes (see Figure 3.8), such that the damping ratios can be applied individually. In the following section, the application of the described methodology to a system with nanometer-level positioning errors is given with the latest HD-DCM model.

### 3.3 HD-DCM Model

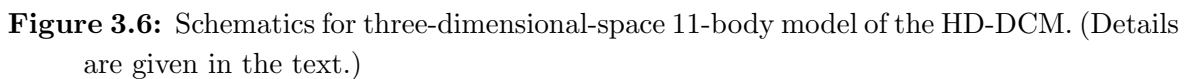
The HD-DCM modeling work started with a few bodies in one-dimensional space (i.e. in a single axis) and single-control-loop models to guide the overall design concepts [19]. In particular, the main purpose was to prove the need for a conceptual change in the fine positioning of the diffracting crystals in the so-called crystal cage (CCG), i.e. replacing the conventional high-stiffness piezo-driven DCM designs with limited control bandwidth (BW) by a low-mechanical-stiffness and high-bandwidth mechatronic architecture, with force actuators and a balance mass (see [1] for the detailed discussion).

With time and successive iterations in the DEB development loop, the models have been increased towards higher dimensions (multiple axes) — up to three-dimensional-space models including all translations and rotations, i.e.  $Ux$ ,  $Uy$ ,  $Uz$ ,  $Rx$ ,  $Ry$  and  $Rz$  axes —, more bodies and multiple control loops. In the following subsections, the latest electromechanical plant model is first described in Section 3.3.1. Then, the controller structures and decoupling matrices are discussed in Section 3.3.2. Finally, all disturbances are detailed in Section 3.3.3.

#### 3.3.1 Electromechanical Plant Model

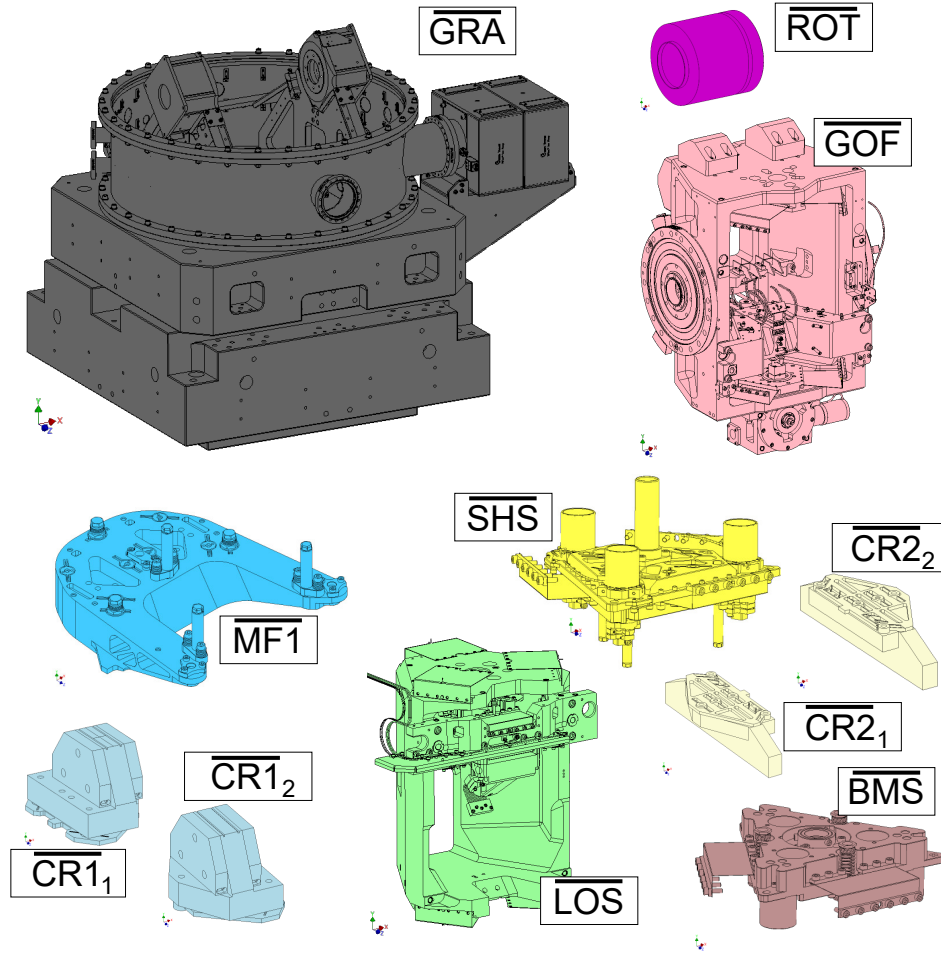
The electromechanical model is developed according to Figure 3.6, which is adapted from [1]. Here the overscore is used to differentiate the model bodies from the physical parts that are described there and mentioned in the following paragraphs for direct correlation (see Section 3.A for a complete list of abbreviations). It consists of a lumped-mass model with 11 bodies, reaching a total of 66 DoFs in the mechanical model.

One actuator and one sensor are used between the granite bench ( $\overline{\text{GRA}}$ ) and the rotor ( $\overline{\text{ROT}}$ ) as part of the Bragg control loop BRG in the  $\theta_B$ -axis (negative  $Rx$ -axis) — which is related to positioning the 1<sup>st</sup> crystals ( $\overline{\text{CR1s}}$ ) with respect to the X-ray incoming beam for energy selection (see [1]). Additionally, three actuators and three sensors are used for the three high-performance control loops in the CCG, namely: GAP, PTC and RLL, in the  $Uy$ ,  $Rx$  and  $Rz$  axes, respectively — which are related to positioning the 2<sup>nd</sup> crystals ( $\overline{\text{CR2s}}$ ) with respect to the  $\overline{\text{CR1s}}$  regarding the gap, and the pitch and roll angles (see [1]). The actuators are placed between the short-stroke frame ( $\overline{\text{SHS}}$ ) and the balance mass ( $\overline{\text{BMS}}$ ), whereas indirect metrology between the  $\overline{\text{CR1s}}$  and the  $\overline{\text{CR2s}}$  is provided by the sensors between the metrology frame ( $\overline{\text{MF1}}$ ) and the  $\overline{\text{SHS}}$ . The remaining positioning DoFs described in [1], including the actuation mechanisms for the  $\overline{\text{GRA}}$  and the long-stroke frame ( $\overline{\text{LOS}}$ ), can be statically considered as passive stiff links. The disturbances from floor vibrations are indicated in the ground ( $\overline{\text{GND}}$ ), whereas liquid nitrogen ( $\text{LN}_2$ ) flow forces are depicted in the main rotating frame ( $\overline{\text{GOF}}$ ) and in the  $\overline{\text{CR1s}}$  (see [1]).



The mechanical structure parts related to the lumped masses are shown in Figure 3.7, while the more detailed correlation between them is given in Section 3.B for completeness. With the drawings, the mass and mass moments of inertia with respect to the CoG for each body, summarized in Table 3.1, can be automatically extracted from the CAD software by the developed toolbox and used in the construction of the stacked mass matrix.

Regarding the stacked stiffness matrix, the support stiffnesses must be specified, whereas the geometric parameters are also automatically obtained from the CAD software. The supports and stiffness numbers are summarized in Table 3.2, having started



**Figure 3.7:** Parts of the mechanical structure (out of scale) related to the lumped masses for the three-dimensional-space 11-body model of the HD-DCM (see [1]).

**Table 3.1:** Mass and mass moment of inertia parameters extracted from CAD for the 6-DoF 11-body model of the HD-DCM.

Body	$m$ [kg]	$I_{xx}$ [kg.m <sup>2</sup> ]	$I_{yy}$ [kg.m <sup>2</sup> ]	$I_{zz}$ [kg.m <sup>2</sup> ]
$\overline{GRA}$	4.7e3	1.3e3	1.5e3	1.5e3
$\overline{ROT}$	2.2e1	1.2e-1	1.1e-1	1.1e-1
$\overline{GOF}$	1.9e2	1.1e1	8.0e0	1.5e1
$\overline{MF1}$	6.2e0	1.5e-2	3.1e-2	1.8e-2
$\overline{CR1}$	4.6e-1	2.6e-4	2.3e-4	1.7e-4
$\overline{LOS}$	4.5e1	1.6e0	9.0e-1	1.8e0
$\overline{SHS}$	5.9e0	1.8e-2	3.2e-2	1.8e-2
$\overline{CR2}$	4.0e-1	8.5e-4	8.4e-4	1.1e-4
$\overline{BMS}$	6.5e0	2.2e-2	4.1e-2	2.2e-2

as educated guesses and being gradually refined with FEA simulations and experimental validations. Most of the local rotational stiffnesses  $K$  are dominated by linear stiffnesses at given known distances, thus, they are mostly approximated to zero and

**Table 3.2:** Translational and rotational stiffness parameters for the creation of stacked stiffness matrix in the three-dimensional-space 11-body model of the HD-DCM:  $k_x$ ,  $k_y$  and  $k_z$  are translational stiffnesses given in main coordinate system (MCS), whereas  $k_u$ ,  $k_w$  and  $k_v$  are translational stiffnesses according to the embedded flexural structures (EFSs) or folded leaf-springs (FLSs) conventions;  $K_x$ ,  $K_y$  and  $K_z$  are rotational stiffnesses given in the MCS. See [1] for more details.

Body	Base	Support (Instances)	$k_x$ or $k_u$ [N/m]	$k_y$ or $k_w$ [N/m]	$k_z$ or $k_v$ [N/m]	$K_x$ [Nm/rad]	$K_y$ [Nm/rad]	$K_z$ [Nm/rad]
$\overline{\text{GRA}}$	$\overline{\text{GND}}$	LEV (4)	3e8	7e8 (and 2e8)	3e8	0	0	0
$\overline{\text{ROT}}$	$\overline{\text{GRA}}$	Bearing (1)	1e8	2.5e8	1.6e8	2500	2.7e5	2.7e5
$\overline{\text{GOF}}$	$\overline{\text{ROT}}$	MEM + STT (1)	3e8	1e9	8e8	1e7	0	0
$\overline{\text{GOF}}$	$\overline{\text{GRA}}$	Bearing + MEM + STT (1)	7.2e7	2.2e8	1.4e8	0	0	0
$\overline{\text{MF1}}$	$\overline{\text{GOF}}$	EFS + Interfaces (3)	2.5e7	5e7	5e7	0	0	0
$\overline{\text{CR1}}$	$\overline{\text{MF1}}$	EFS + Interfaces (3)	4e6	2.5e7	2.5e7	0	0	0
$\overline{\text{LOS}}$	$\overline{\text{GOF}}$	FLS <sub>LOS</sub> (6)	1e4	2.4e7	3e5	0	0	0
$\overline{\text{LOS}}$	$\overline{\text{GOF}}$	LSA (1)	0	1.3e8	0	0	0	0
$\overline{\text{SHS}}$	$\overline{\text{LOS}}$	FLS <sub>SHS</sub> (3)	3.2e3	2.5e7	4.8e4	0	0	0
$\overline{\text{BMS}}$	$\overline{\text{LOS}}$	FLS <sub>BMS</sub> (3)	3.2e3	2.5e7	4.8e4	0	0	0
$\overline{\text{CR2}}$	$\overline{\text{SHS}}$	EFS + Interfaces (3)	3.5e5	2.5e7	2e7	0	0	0

used only where necessary.

The  $\overline{\text{GRA}}$  is supported on the floor by four levelers (LEVs), with a lower vertical stiffness defined in one of them to emulate the inevitable partial imbalance caused by the 4-point support. The  $\overline{\text{ROT}}$  is constrained by the ball-bearing in the commercial rotary stage. The  $\overline{\text{GOF}}$  is supported both by the  $\overline{\text{ROT}}$  at one side and by the  $\overline{\text{GRA}}$  at the other — the first interface being defined by the coupling membrane (MEM) and strut (STT) (and STC), whereas the latter by the MEM and the STT, but also by the passive ball-bearing, as a dummy commercial rotary stage, in series (see [1] for details and also Section 3.A).

The  $\overline{\text{MF1}}$  is clamped to the  $\overline{\text{GOF}}$  via the embedded flexural structures (EFSs) and the complementary isolation pads (CIPs) in series (see [1]). As a matter of fact, from the first HD-DCM system that was built this interface has been found to be critical for dominant resonances in the PTC servo error in the CCG, as shown in Section 3.4. Indeed, probably due to limited contact in the interfaces, the resulting supporting stiffness of the  $\overline{\text{MF1}}$  is in practice one order of magnitude lower than the stiffness that should be determined by the flexures. This lowers the suspension frequency of the  $\overline{\text{MF1}}$  from the original target above 1 kHz to about 500 Hz, making it not only more sensitive to the energy content of the LN<sub>2</sub> flow forces at this frequency, but also inconveniently within the sensitivity peak of the PTC control loop for the operational BW (see Section 3.4.1). Hence, alternatives to improve the suspension frequency or damping (via piezo elements, as in [20]) of the  $\overline{\text{MF1}}$ , while preserving thermal management needs

(see [1]), are under investigation.

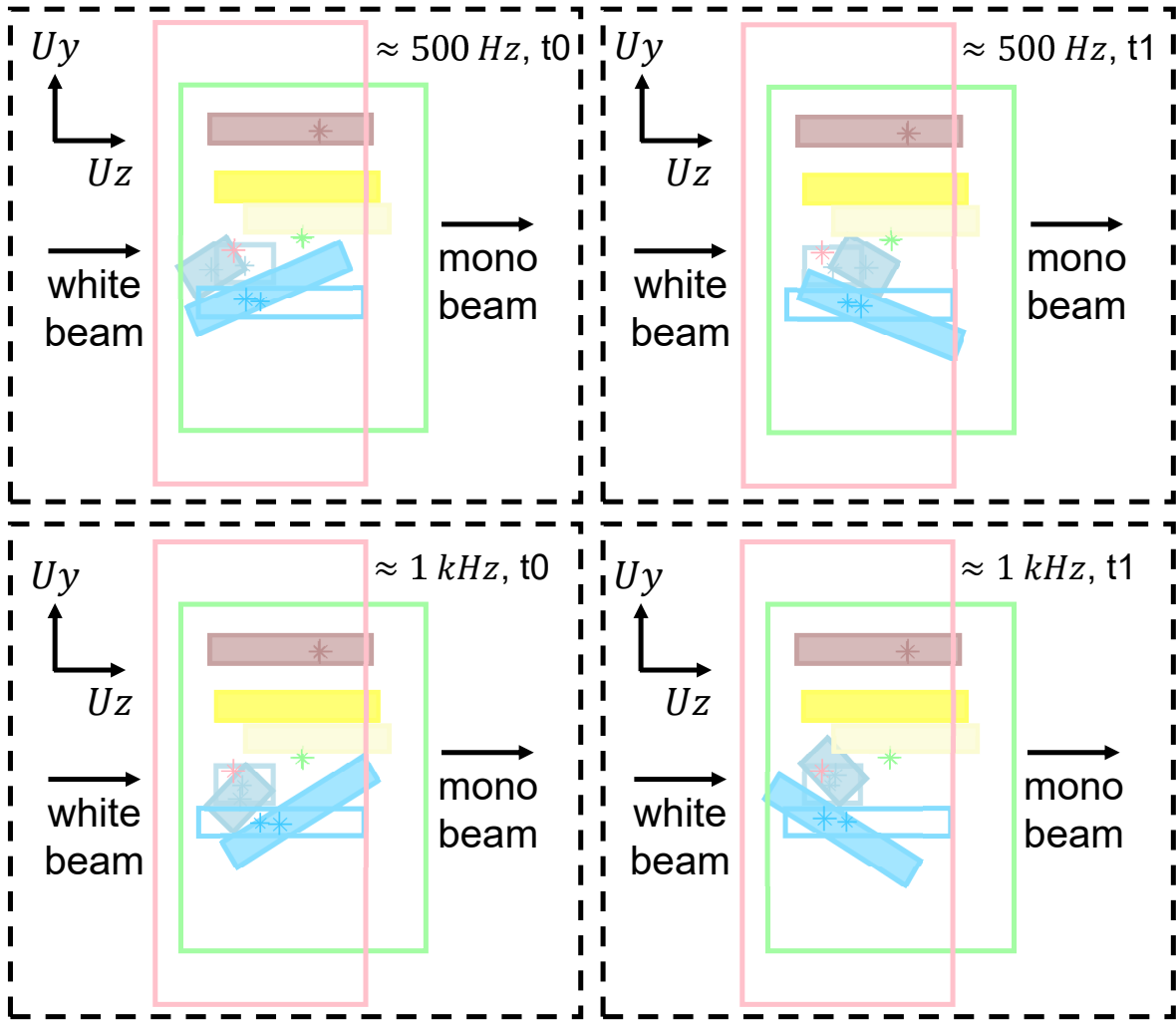
The  $\overline{\text{CR1s}}$  are clamped to the  $\overline{\text{MF1}}$  via their sets of EFS flexures and shims in series (see [1]). Although the compliance of the interfaces with the shims also reduces the originally designed stiffness from the flexures by one order of magnitude — especially because the clamping force through the crystals is limited —, the effect is less critical in terms of suspension frequencies due to the lower masses. So, here, sufficiently large suspension (above 1 kHz) to minimize the excitations by the  $\text{LN}_2$  flow forces can still be achieved. In these flexures,  $k_u$  (see [1]) is made lower to accommodate for the thermal expansion.

The suspension of the  $\overline{\text{LOS}}$  on the  $\overline{\text{GOF}}$  is made both by the set of six folded leaf-springs (FLS) and by the long-stroke actuator (LSA), in which the vertical stiffness  $k_y$  is the only relevant complementary constraint (see [1]). Both the  $\overline{\text{SHS}}$  and the  $\overline{\text{BMS}}$  are suspended on the  $\overline{\text{LOS}}$  by their identical sets of three FLSs with piston-tip-tilt free DoFs<sup>1</sup> (see [1]). Finally, the  $\overline{\text{CR2s}}$  are clamped to the  $\overline{\text{SHS}}$  via their EFSs and shims in series (see [1]), with the same remarks made for the  $\overline{\text{CR1s}}$  being applicable.

With this information and following the substructuring steps described in Figure 3.4, a modal analyses can be made and animated mode shapes can be created and investigated with the developed toolbox. An example is given in Figure 3.8 via snapshots illustrating the two critical mode shapes of the sub-assembly with the  $\overline{\text{MF1}}$  and the  $\overline{\text{CR1s}}$  on the  $\overline{\text{GOF}}$ , which currently limit the crystals pitch servo error ( $Rx$ -axis) just about the specification of 10 nrad, as discussed in Section 3.4. This step also helps verifying the consistency of the model and guiding the proportional damping definitions.

The mechanism of damping in a material or structure is, however, difficult to quantify, such that one must generally rely on empirical results [15]. Thus, replacing preliminary educated guesses based on experience, the current damping values were verified via experimental modal analyses and plant identifications (not shown). For the in-vacuum modes, the quality factor (Q) for the dominant peaks were found typically between 180 and 250, such that 0.2% damping ratio is generically applied here aiming at conservative predictions. The exceptions are: 30% in the main rotation mode of the core, resulting from the internal damping of the commercial rotary stages; and 5% in the  $\overline{\text{SHS}}$  low-frequency modes, resulting from friction in the meshed braids and eddy currents in the voice-coil (VC) actuator. Outside vacuum, 5% is used in the  $\overline{\text{GRA}}$  suspension modes, resulting from damping in the floor and friction in the levelers.

<sup>1</sup>The FLSs can be modeled via structural analyses in FEA softwares, but also predicted analytically [21]. Something that is not explicit in analytical formulations, but is important because of possibly relevant shifts in parasitic dynamics, is the loss in  $k_w$  stiffness as the FLSs operate away of their neutral line. This can be investigated with FEA simulations and plant variations in the DEB workflow. Moreover, alignment tolerances and control robustness related to the FLSs can be investigated by varying the nominal transformations of  $k_u$ ,  $k_w$  and  $k_v$  into the main coordinate system MCS. All these analyses have been made for the HD-DCM and considered during design, defining manufacturing and alignment guidelines, for example, but further diving into these details go beyond the purposes of the paper.



**Figure 3.8:** Side view screenshots of the animated mode shapes created by the DEB toolbox for the three-dimensional-space 11-body model of the HD-DCM. Two different instants ( $t_0$  and  $t_1$ ) are captured to show the resonances around 500 Hz (top) and 1 kHz (bottom). For visibility, the granite ( $\overline{\text{GRA}}$ ) and the rotor ( $\overline{\text{ROT}}$ ) bodies are not shown, and the main rotating frame ( $\overline{\text{GOF}}$ ) and the long-stroke structure ( $\overline{\text{LOS}}$ ) are depicted as wire frames. Fixed wire-frames for every body, more clearly visible for the  $\overline{\text{MFI}}$  and  $\overline{\text{CRI}}$  due to their large motions, also provide the nominal positions as references. The center of gravity (CoG) of the lumps, both for the moving parts and the reference wire-frames, are represented by stars. The color code follows Figure 3.6 and Figure 3.7.

### 3.3.1.2 Actuation and Metrology

To create a predictable and realistic model of a high-bandwidth mechatronic system based on a digital controller, some knowledge about the hardware and control sample rates is required for appropriate discretization and delay considerations. Here, as in the mechanical structure, the first models started with estimates and educated guesses, being refined with the maturity of the project and experimental characterization.

The HD-DCM runs at a sample rate of 20 kHz, i.e. with an iteration time of 50  $\mu\text{s}$  in

an NI's CompactRIO (cRIO) control platform. All actuators are controlled via the 16-bit NI-9269 DAC (digital-to-analog converter) board, with an update time below 10  $\mu$ s. The Varedan's LA-415-SA-T linear amplifier with current BW above 10 kHz is used with the Aerotech's APR260 S-240-83 rotary stage in the BRG loop, whereas Trust Automation's TA105 linear drives with current BW of 5 kHz are used with the Akribis' AVM 40-HF-6.5 VCs in the high-dynamic module of the CCG. As for the sensors, the rotary stage uses a high-resolution Renishaw's TONIC optical rotary encoder with 32768 encoder lines and additional interpolation (x1000) to deliver a quadrature signal with about 50 nrad/count at 10 MHz. The CCG, in turn, uses SmarAct's PicoScale C01 fiber-based Michelson interferometers, with 0.1 nm/count also as a quadrature signals at 10 MHz. Both quadrature signals are read by NI-9753 boards in cRIO, where the internal pulse counters that provide the actual positions are downsampled to 20 kHz in the FPGA — with averaging eventually made to reduce noise.

Since delay approximations are of particular interest for phase lag around the BW frequencies, experimental plant identifications, not shown here due to limited space, were carried out for the individual items. The results suggest that in the rotary stage chain (LA415-APR260-TONIC) the time delay is around 250  $\mu$ s, whereas in the VC chain (TA105-AVM40-PicoScale) it is below 50  $\mu$ s. Thus, the electromechanical plant model is discretized at 20 kHz using zero-order-hold (ZOH) to account for the DAC board, with 5 and 1 additional samples of delay for the BRG and three CCG loops, respectively.

### 3.3.2 Controller

Even though the HD-DCM model is a Multiple-Input-Multiple-Output (MIMO) system, it has been designed to be sufficiently decoupled in its controlled DoFs to be addressed as four independent Single-Input-Single-Output (SISO) systems, namely: BRG, GAP, PTC and RLL. This greatly simplifies the design of independent controllers, which can be done according to the *loop shaping* technique [12, 22] — with low-order controllers being manually tailored towards robustness via iterative analyses of the open-loop frequency responses and closed-loop functions. Deeper analyses for the low interaction among control loops, stability, robustness and different controllers go beyond the scope of this paper, but will be discussed in a separate article under preparation. Here, only the essential elements and control strategy for a simple and robust implementation are described for completeness.

#### 3.3.2.1 Control Decoupling Matrices

Indeed, sufficiently decoupled control loops for SISO designs are obtained with the geometry-based control matrices  $T_u$  and  $T_y$  introduced in Figure 3.2 (for a similar



analysis, see also [18]). The input matrix  $T_u$  is defined as

$$\begin{bmatrix} BRG_{a1} \\ CCG_{a1} \\ CCG_{a2} \\ CCG_{a3} \end{bmatrix} = \mathbf{T}_u \begin{bmatrix} BRG_c \\ GAP_c \\ PTC_c \\ RLL_c \end{bmatrix}, \quad (3.5)$$

$$\mathbf{T}_u = \begin{bmatrix} 1 & 0 & 0 & 0 \\ 0 & 1/3 & (2/3)r_a^{-1} & 0 \\ 0 & 1/3 & -(1/3)r_a^{-1} & (\sqrt{3}/3)r_a^{-1} \\ 0 & 1/3 & -(1/3)r_a^{-1} & -(\sqrt{3}/3)r_a^{-1} \end{bmatrix}, \quad (3.6)$$

where:  $BRG_c$ ,  $GAP_c$ ,  $PTC_c$  and  $RLL_c$  are the control efforts of each loop;  $BRG_{a1}$ ,  $CCG_{a1}$ ,  $CCG_{a2}$  and  $CCG_{a3}$  are the torque between the  $\overline{\text{ROT}}$  and the  $\overline{\text{GRA}}$ , and the forces in the three VCs between the  $\overline{\text{SHS}}$  and the  $\overline{\text{BMS}}$  in the CCG loops; and  $r_a$  is the VC radius with respect to the CoG of  $\overline{\text{SHS}}$  (see [1]).

The measurement output matrix  $T_y$ , in turn, is defined as

$$\begin{bmatrix} BRG_m \\ GAP_m \\ PTC_m \\ RLL_m \end{bmatrix} = \mathbf{T}_y \begin{bmatrix} BRG_{s1} \\ CCG_{s1} \\ CCG_{s2} \\ CCG_{s3} \end{bmatrix}, \quad (3.7)$$

$$\mathbf{T}_y = \begin{bmatrix} 1 & 0 & 0 & 0 \\ 0 & 1/3 & 1/3 & 1/3 \\ 0 & (2/3)r_s^{-1} & -(1/3)r_s^{-1} & -(1/3)r_s^{-1} \\ 0 & 0 & (\sqrt{3}/3)r_s^{-1} & -(\sqrt{3}/3)r_s^{-1} \end{bmatrix}, \quad (3.8)$$

where:  $BRG_{s1}$ ,  $CCG_{s1}$ ,  $CCG_{s2}$  and  $CCG_{s3}$  are the signals of the rotary encoder between the  $\overline{\text{ROT}}$  and the  $\overline{\text{GRA}}$ , and the interferometers between the  $\overline{\text{SHS}}$  and the  $\overline{\text{MF1}}$ ;  $BRG_m$ ,  $GAP_m$ ,  $PTC_m$  and  $RLL_m$  are the control measurements; and  $r_s$  is the inteferometer radius with respect to the CoG of the  $\overline{\text{SHS}}$ , which is equal to  $r_a$ , according to the collocated design (see [1]).

Alignment sensitivity and control robustness related to the actuators and sensors can be investigated by varying the nominal  $T_u$  and  $T_y$ . Some of these effects have also been studied during the design of the HD-DCM, but, again, will not be shown here for conciseness.

### 3.3.2.2 Controller Design

Given the fast sample rate in the digital hardware, the controllers can be designed using continuous-time techniques and later explicitly discretized as described below. With mechanically-isolated mass-based motion systems, such as the BRG and CCG subsystems in the HD-DCM, a simple generic controller based on Proportional-Integral-Derivative (PID) control can be implemented with practical rules of thumb [12]. Still,

to handle parasitic dynamics or reach specific performance targets additional filters, such as notch filters can be included.

In this work, one of the interests is justifying the innovative mechanically-isolated architecture of the HD-DCM by demonstrating the dependence of the positioning errors in the fixed-energy operation mode on the control BW, here defined as the frequency in which the open-loop TF crosses the unit gain. So, a straightforward BW analysis, discussed in Section 3.4.1, is possible with controllers written in the Laplace domain as

$$C(s) = \kappa_{BW} \cdot \frac{s + \omega_{BW}/3.5}{s + 3.5\omega_{BW}} \cdot \frac{s + \omega_{BW}/5}{s} \cdot \frac{\omega_{LP2}^2}{s^2 + 2\zeta_{LP2}\omega_{LP2}s + \omega_{LP2}^2} \cdot \frac{s^2 + 2\zeta_{N1}\omega_N s + \omega_N^2}{s^2 + 2\zeta_{N2}\omega_N s + \omega_N^2}, \quad (3.9)$$

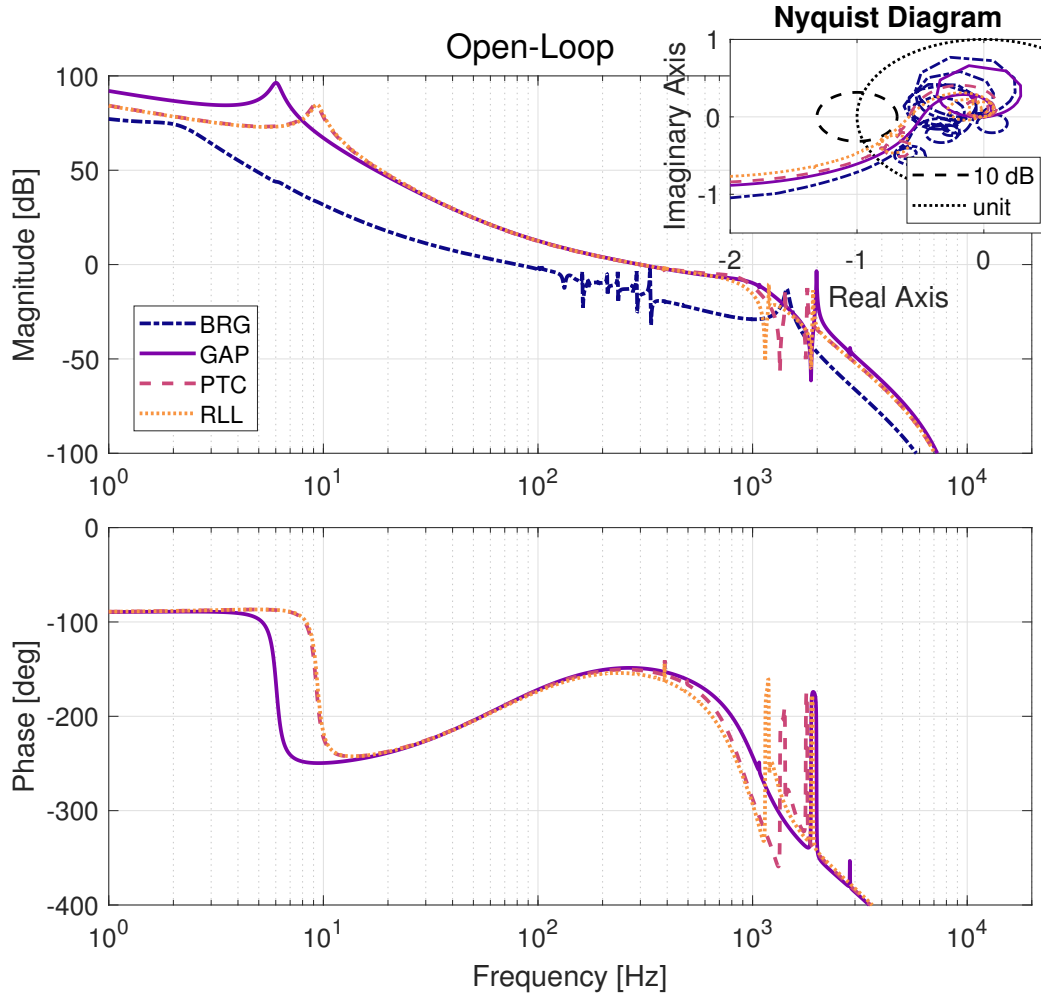
where:  $\kappa_{BW}$  is the proportional gain;  $\omega_{BW}$  is the BW frequency in rad/s;  $\omega_{LP2}$  and  $\zeta_{LP2}$  are the frequency and the damping ratio of a second-order low-pass filter, used to suppress high-frequency amplification of the dynamics and sensor noise; and  $\omega_N$ ,  $\zeta_{N1}$  and  $\zeta_{N2}$  are the frequency and damping ratios defining the width and the depth of a notch filter, used to suppress the dominant resonance in the plant dynamics. It can be seen that a lead filter with a zero at  $1/3.5$  of the BW and a pole at  $3.5$  times the BW is used for phase lead, and that an integral action with an additional zero at  $1/5$  of the BW is implemented for better tracking and disturbance rejection. The gain  $\kappa_{BW}$  is determined as a result from the desired control BW.

With this approach, BW frequencies of up 80 and 300 Hz can be obtained for the control loops of BRG and CCG, respectively, while keeping phase margins above  $25^\circ$  and robustness margins above 10 dB, as depicted in Figure 3.9 — which is considered to be sufficient for our purposes here since the small margins occur only in the extreme cases and there are further controller design possibilities. For higher BWs, phase lag and plant dynamics quickly increase the controller complexity and model-dependent risks. Once this controller form choice and BW limits are sufficient for the performance analyses in Section 3.4.1, alternative controller design approaches are left to be explored in future work.

After having the continuous controllers discretized at 20 kHz with Tustin's method — for a close discrete-time representation in the frequency domain —, the complete control loop can be connected according to Figure 3.2, and the TFs of interest for the DEB analyses can be extracted.

### 3.3.3 Disturbances

Due to fine environment control inside the beamline hutches and to the fact that most of its sensitive parts are in vacuum, the HD-DCM is relatively immune to acoustics and ambient temperature effects. Floor disturbances, on the other hand, is a permanent point of attention. Differently from isolated high-precision machines that may include vibration isolation systems, at beamlines there must be positional correlation between



**Figure 3.9:** Open-loop Bode and Nyquist plots for the three-dimensional-space 11-body model of the HD-DCM at the extreme-case bandwidth frequencies of 80 Hz for the BRG and 300 Hz for the GAP, PTC and RLL loops.

the instruments and the beam source tens of meters away (see [1]), such that decoupling becomes a more complex subject. Thus, the current supporting solution for the HD-DCM relies on high-stiffness levelers, the natural damping of the floor and the exceptional mechanical stability levels of the experimental floor shown in Section 3.3.3.1.

Regarding operational disturbances, LN<sub>2</sub> flow-induced vibrations (FIV) are among of the most detrimental influences in the HD-DCM. The high-heat-load X-ray beam itself does not act as a disturbance source within the DEB scope, because the well-decoupled thermo-mechanical design of the HD-DCM (see [1]) leads simply to isolated temperature increase in the crystals by a few degrees. This is insufficient to cause dynamical effects, resulting, for example, from changes in the plant due to variations in the Young's modulus of materials. In addition, any temperature change will be much slower than the reaction times in the active control loop. Hence, parasitic effects of the incoming beam would be related at most to slow drifts of the monochromatic beam, which would be invisible to the embedded metrology in the HD-DCM, but open

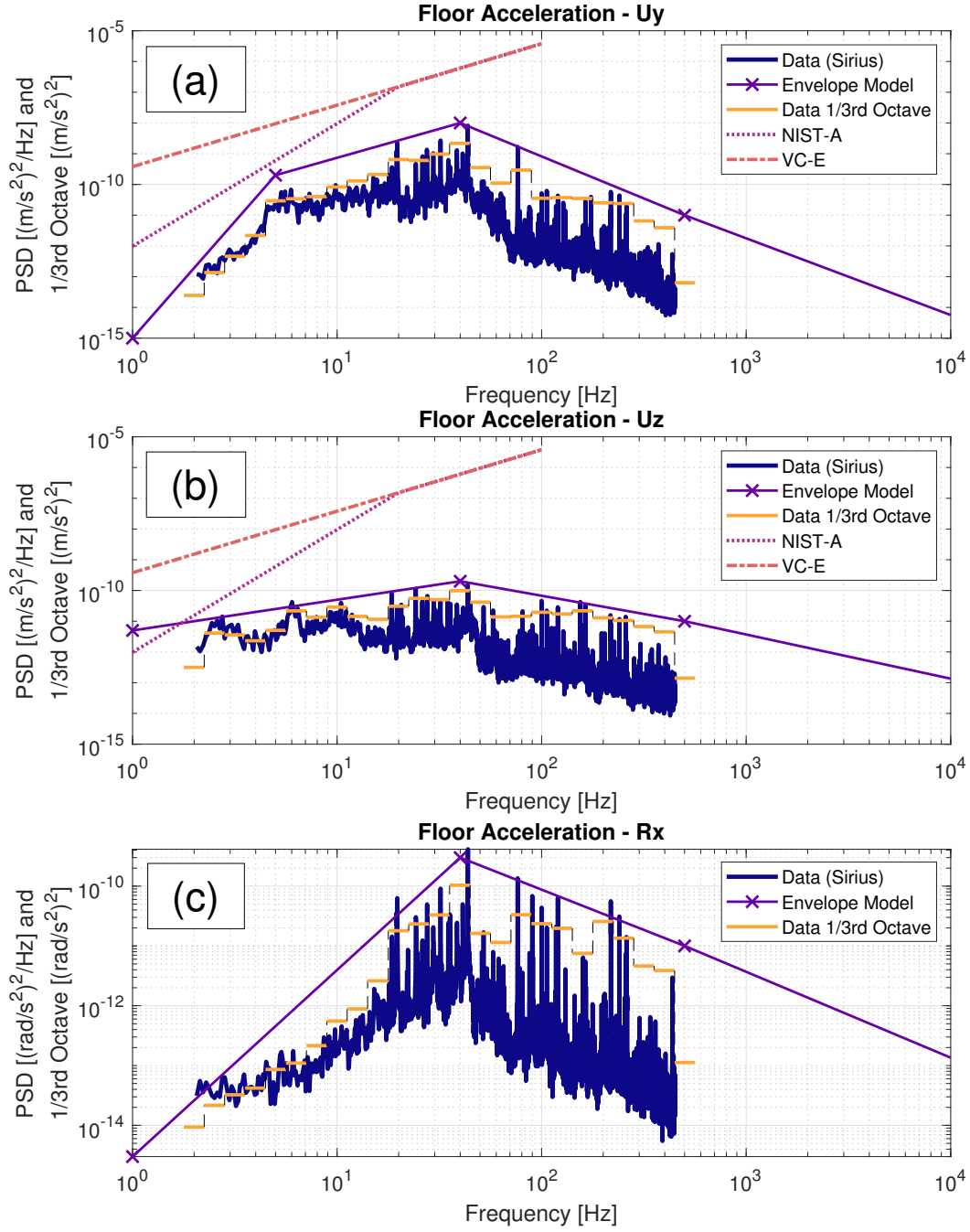
for calibration or low-bandwidth feedback correction with beamline sensors.

In addition, control and motion-related disturbances result from the choices and the quality of actuators, sensors, guiding mechanisms, controller designs and operation modes (see [1]). In the HD-DCM, in fixed-energy mode these noise sources are reduced to noise of sensors, amplifiers and DACs (see Figure 3.2). Thus, without diving into the more complex and extensive fly-scan motion disturbances, the following subsections address the components of both *mechanical* and *electronic disturbances* affecting the system in stand-still condition. Experimental data is presented and used as basis for *envelope models*, which are applied in the DEB analyses as conservative predictions.

### 3.3.3.1 Mechanical Disturbances

Although floor vibrations may have variant and invariant time components, strictly resulting in a non-stationary character, a pragmatic modeling approach for DEB consists in averaged approximations, either from basic PSD specifications or vibration measurements over representative time intervals — whereas specific system responses can be seen via time simulations [9]. Figure 3.10 shows, as examples, the floor acceleration PSDs — measured with seismometers Wilcoxon 731A and NI’s USB-4431 acquisition module at the experimental hall of Sirius —, and the derived models in  $U_y$ ,  $U_z$  and  $R_x$  axes, which are the most sensitive ones for the HD-DCM. Remarkably, it can be seen that  $U_y$  and  $U_z$  are significantly below VC-E and NIST-A standards, highlighting the excellent levels of the floor. As the floor measurements are limited in range due to instrumentation limitations, the envelope models allows for the required extrapolation to the model frequency range of interest, i.e. from 1 Hz to 10 kHz (for 20 kHz control rate). Thus, they are used as conservative inputs for DEB, contributing to it via the TFs in the mechanical structure that are related to the support of the  $\overline{\text{GRA}}$  on the floor (see Figure 3.2 and Figure 3.6).

Similarly, FIV may also have variant and invariant time components, resulting from variable pumping or flow conditions. Differently from the floor, however,  $\text{LN}_2$  FIV experimental measurements have proven to be extremely challenging — not only due to the complexity of flow effects alone, but also because of the cryogenic conditions and vacuum-compatibility requirements of the setup in the HD-DCM context. Thus, educated guestimates are still used in the models. According to preliminary experimental results [23], the FIV disturbances are modeled as a white-noise PSD with a second-order low-pass characteristic with a corner frequency of 250 Hz. For each of the four cooling blocks (CCBs) within the  $\overline{\text{CRIs}}$  an integrated RMS values of 1 mN is considered in  $U_x$ ,  $U_y$  and  $U_z$  axes, whereas 10 mN is used in the three axes for both the main manifold (CMF) and the manifold extension (CMX) within the  $\overline{\text{GOF}}$  due to higher flow speeds and derivations (see [1] and Section 3.B for details). For DEB outputs, these PSDs act on the mechanical structure via all these points through their respective TFs (see Figure 3.2 and Figure 3.6). New experimental setups and computational fluid dynamics (CFD) simulations in both acoustics and turbulence domains are ongoing research.



**Figure 3.10:** Examples of experimental and modeled power spectrum density (PSD) data of floor acceleration disturbances in the HD-DCM at Sirius/LNLS. One-third octave bands are also shown for reference. (Details are given in the text.)

### 3.3.3.2 Electronic Disturbances

Here, two groups of electronic noise may be identified, namely: actuation and metrology. The first acts on the process sensitivity TFs of the control-loop, whereas the latter on the complementary sensitivity TFs (see Figure 3.2). In early stages of the project, approximated models followed the reasoning presented in [9], with the PSDs

reflecting the contribution of different physical phenomena typically with broad-band characteristic spectra, such as *thermal noise*, *shot noise* and/or *1/f noise*. Now, at a more mature stage of the project, real data has been obtained and used.

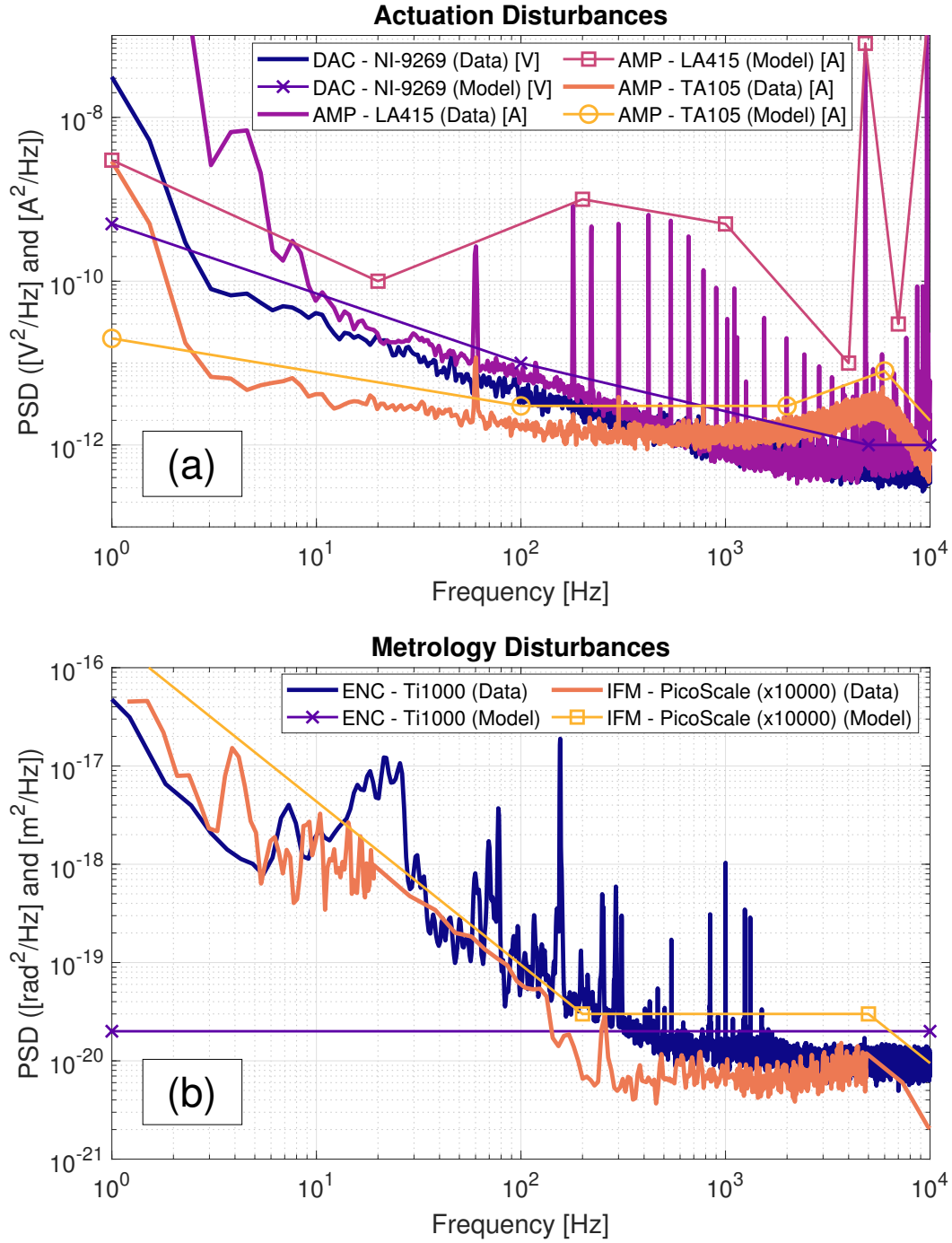
Figure 3.11a shows the measurements and the respective envelope models for the actuation group. They were realized with dedicated individual experimental setups, using NI's cRIO with NI-9239 analog-to-digital converters (ADC) at 50 kHz as the acquisition system for low noise levels. The NI-9269 DAC and the TA105 amplifier for the VCs show smooth curves, whereas the LA415 amplifier for the rotary stage shows several sharp peaks that could result from switching electronics in the hardware or pick-up noise. Actually, the TA105 amplifiers, as provided by the supplier, also showed similar peaks. The source of the problem was tracked back to its fan, and those harmonic disturbances were eliminated by switching the fan to an external power supply. Work is currently in progress to track and eliminate the Varedan's harmonic disturbances as well, since they may be significantly affecting the PTC control errors as discussed in Section 3.4.3. It should be noted that the first few points in the measured PSDs result from artifacts in data processing, such that the models follow simple extrapolation. Then, to transform the voltage and current PSD data into force and torque suitable gains are used. Constant gains have been used for simplicity, but frequency-dependent gains may also be considered. For the rotary stage, the amplifier and motor gains are 0.3 Arms/V and 7.09 Nm/Arms, respectively. For VCs, the amplifier and actuator gains are 0.05 A/V and 19.15 N/A. These PSDs enter in the DEB via the TFs from the actuation points in the model, after the transformation matrix  $T_u$  (see Figure 3.2).

Similarly, Figure 3.11b shows the experimental results and envelope models for metrology disturbances. The Ti1000 encoder data was taken already with the rotary stage in the HD-DCM assembly, such that the content up to 1.5 kHz reflects real mechanical and electronic dynamics in the system during the measurement, rather than the electronic noise of the sensor itself. Since white-noise behavior over the full range is known from previous experience with optical encoders, the model is extrapolated accordingly from the level at higher frequencies. This measurement results from the quadrature signal read by the NI-9753 cRIO board simply taken at the sample rate of 20 kHz, in which case the RMS value of the noise floor agrees with publicly available data from Renishaw, that estimates the jitter of TONIC encoders around  $0.5 \text{ nm}_{\text{RMS}}^2$ . In practice, the quadrature signal is obtained at the FPGA level at 10 MHz, such that lower noise levels can be reached with averaging to 20 kHz.

The interferometer noise, in turn, was measured in collaboration with the supplier in a dedicated static setup in air because of existing experimental limitations. Although the low frequency content (below 100 Hz) may be overestimated as compared to the real in-vacuum operation — because of refraction index effects —, the differences are expected to be well within the control BW of the CCG, so that they would be followed

---

<sup>2</sup>The calculation for a scale with radius 0.1 m follows from measurement:  $encoder_{\text{RMS}} \approx (1 \cdot 10^{-20} [\text{rad}^2/\text{Hz}]) \cdot (0.1 [\text{m}])^2 \cdot (10000 [\text{Hz}])^{1/2} = 1 \text{ nm}$ .



**Figure 3.11:** Experimental and modeled power spectrum density (PSD) data of electronic disturbances in the HD-DCM: actuation (a) and metrology (b) groups. (Details are given in the text.)

by the control loop, impacting final accuracy, but not the predicted servo error. In this case, the data results already from the maximum PicoScale acquisition rate of 10 MHz, such that this noise level already requires averaging for the 20 kHz sample rate. For both sensors, the PSDs enter in the DEB via the TFs from the sensor points, before the transformation matrix  $T_y$  (see Figure 3.2).

### 3.4 DEB Results

Given the essential role of DEB in the design process of the HD-DCM over the years, with its large flexibility and multiple analysis possibilities, only a glimpse into the extensive pool of results is offered here with a few illustrative points. Firstly, a straightforward BW analysis is made using DEB outputs. Next, the spectral aspect and superposition properties of DEB are exemplified. Finally, model predictions are compared with experimental data for the most demanding control loop PTC.

#### 3.4.1 Bandwidth Analysis

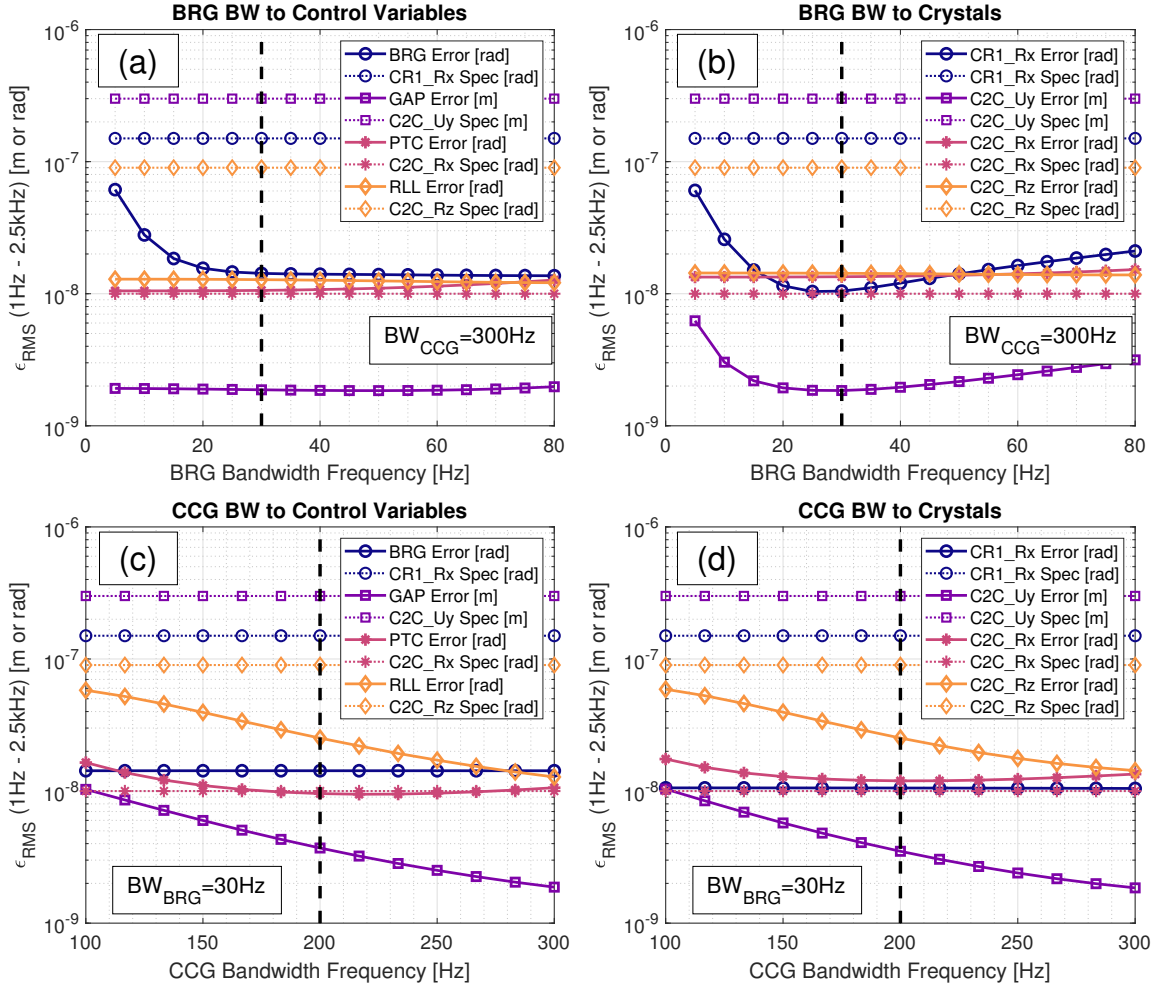
Choosing the appropriate control BW in high-performance mechatronic systems may result from a compromise between the capacity to suppress plant and actuator disturbances at one side; and, at the other, the pick-up and/or amplification of sensor noise and/or plant dynamics outside the control BW. Here, a BW analysis via DEB is made by varying the BW frequency of the control loops according to the flexibility and robustness provided by the controller form in Equation (3.9).

Along with the error in the BRG loop, between the rotor and the stator of the rotary drive, the error in the absolute incidence angle of the beam CR1\_Rx, which effectively defines the X-ray energy selection at the beamline, can also be investigated. Similarly, the effective piston, tip and tilt relative position between crystals, defined as the model variables C2C\_Uy, C2C\_Rx and C2C\_Rz, can be probed in addition to their indirect control parts GAP, PTC and RLL, respectively — which are measured between the MF1 and the SHS mounting frames. Figure 3.12 shows the system performance for both the sets, with the total DEB output of each loop or state as the RMS value in the specified range between 1 Hz and 2.5 kHz (see [1]).

Respecting the BW boundaries discussed in Section 3.3.2.2, and knowing that the BRG and CCG loops allow for very different BW ranges, the BW analysis is broken in two steps. Firstly, assuming high-BW needs in the CCG loops, GAP, PTC and RLL are kept at the maximum BW of 300 Hz while the BRG BW varies from 5 to 80 Hz. Figure 3.12a shows that the BRG performance is within specs in the full range, but it is capable of reaching a small asymptotic error value with a margin factor of 10 at about 30 Hz. The GAP and RLL errors are insensitive to the BRG BW, with large margins with respect to specs. The PTC error, on the other hand, is slightly above specs, with increasing errors as the BRG BW goes beyond 30 or 40 Hz. This is because the BRG servo captures an ever larger range of sensor, FIV and floor disturbances, which is not sufficient to change significantly the BRG error, but causes the additional control torque to leak in the nanometer level to the PTC loop. The contribution of each component becomes clearer in the CPS plots in the following subsection.

Now, checking the model states of interest in Figure 3.12b, it can be seen that 25 to 30 Hz actually happens to be an optimum BRG BW range for the beam incidence angle CR1\_Rx. Beyond 30 Hz, again, the sensor, FIV and floor disturbances are more present in the core, such that the control torque adds nanometer-level errors due to





**Figure 3.12:** Control bandwidth analysis for the three-dimensional-space 11-body model of the HD-DCM, according to the Dynamic Error Budgeting root mean square (RMS) output values in the frequency range between 1 Hz and 2.5 kHz. Along with the specifications (see [1]), the outputs display control loop performances BRG, GAP, PTC and RLL in (a) and (c), as well as states of interest in (b) and (d), namely: CR1\_Rx, C2C\_Uy, C2C\_Rx and C2C\_Rz. (Details are given in the text.)

the finite stiffness chain between the rotor and the crystal. The minimum value for CR1\_Rx is smaller than the asymptotic value of the BRG error in the first plot probably due to the relative measurement between the rotor and the stator of the rotaty stage in different bodies. The same local minimum is visible in the gap between crystals C2C\_Uy, exposing a residual cross-talk with the BRG loop that is not obvious from the GAP error. Finally, for the rotations between crystals C2C\_Rx and C2C\_Rz, the errors are slightly above those seen for PTC and RLL, also because of the finite mounting stiffness between the crystals and the metrology frames. Hence, 30 Hz for the BRG BW can be preliminarily set as a first indirect BW requirement according to the proposed control strategy, allowing for the best system performance so far.

Then, moving on to the analysis of BW in the CCG, the BRG BW is kept at 30 Hz

while the BW for the GAP, PTC and RLL loops are simultaneously varied from 100 to 300 Hz. Figure 3.12c shows that the BRG performance remains unchanged, at the level defined by the first step. Concerning the GAP error, it is reduced by a factor 5 as the BW increases, still well within specs. A similar error reduction behavior is seen in RLL, with a compliance margin increasing from 1.5 to 7.5. For PTC, on the other hand, a subtle minimum-error range is observed between 180 and 270 Hz, also where the specification between crystals is actually met. This is caused by the closed-loop control sensitivity to the mechanical resonances at 500 Hz, as mentioned in Section 3.3.1 and further discussed in the following subsections.

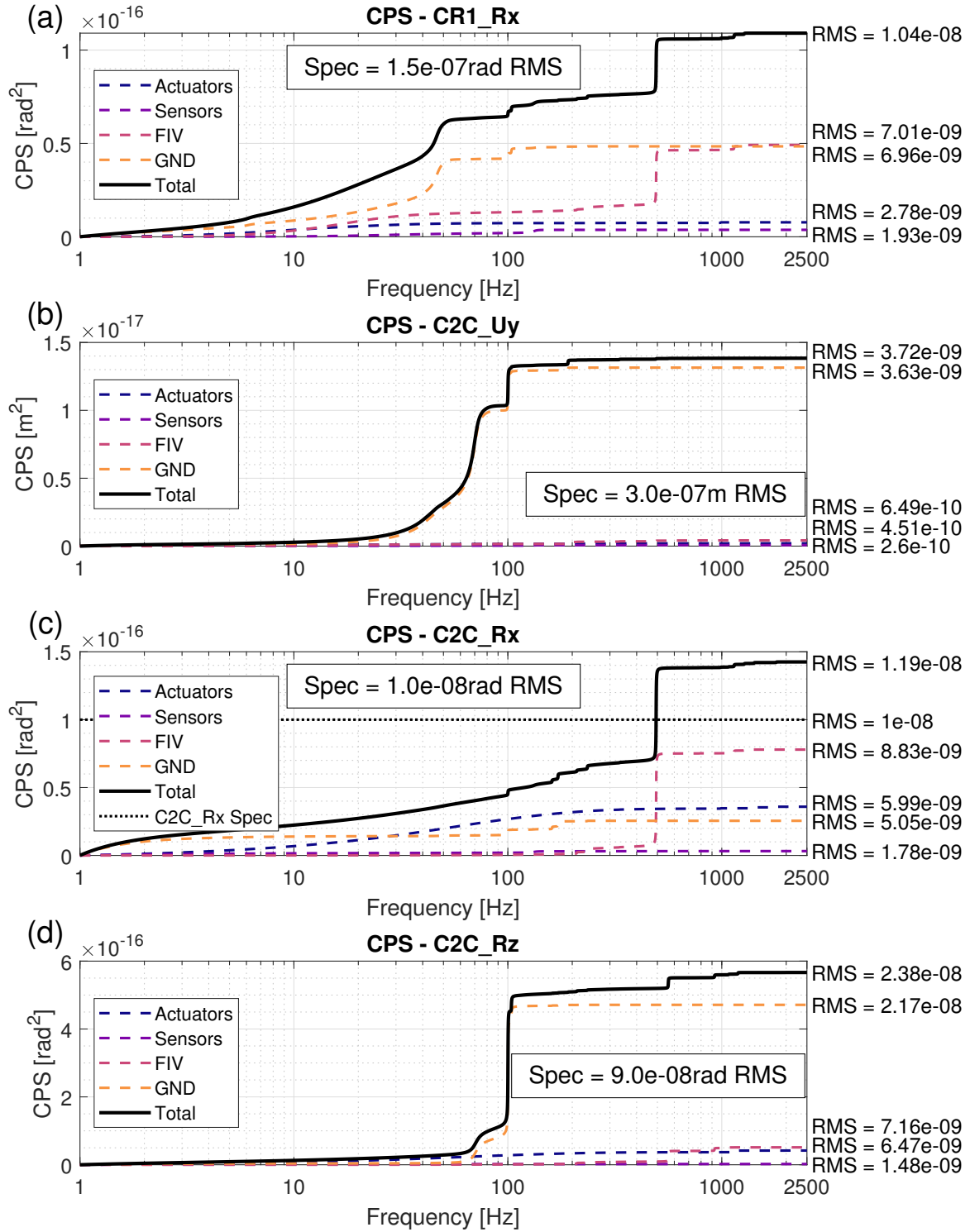
Finally, investigating the states of interest in Figure 3.12d, the remarks remain, except for the fact that the real pitch between crystals still exceeds the specs by a factor of 1.2 even at the optimum BW of 200 Hz. Indeed, C2C.Rx being larger than PTC is expected from the finite mounting stiffnesses between the crystals and their frames. Yet, although ideally smaller, this excess is not of critical concern, as elaborated in the following subsection. Therefore, for comfortable control robustness margins above 6 dB (not shown), the BW for GAP and RLL may also be set at 200 Hz, such that it can be defined as the indirect BW requirement for all CCG loops according to the proposed control strategy — with gap and roll larger margins being a natural fallout of the architecture developed for pitch.

These results support the innovative architecture of the HD-DCM and its choices for a high-bandwidth CCG for sufficient noise suppression, which include the force actuators, the balance mass as a dynamics filter, and the dynamic-oriented mechanical design (see also Figure 3.8 and Figure 3.9). They endorse the innovative embedded indirect metrology between crystals (see [1]) as well, since multiple stacked parts/stages supporting the crystals, as commonly found in the crystal cage of standard DCMs, increase the compliance between metrology and the points of interest, deteriorating the positioning performance.

### 3.4.2 Cumulative Spectra and Superposition

By construction, the contributions from every disturbance input is available to every control output or auxiliary state output in the DEB analysis. Then, by the superposition principle, these inputs may be conveniently grouped and added together over frequency in the power domain for the final DEB outputs (see Section 3.2.1). These results may be seen in PSD form, if desired, but the choice here is for the CPS representation, because it has a smoother aspect as compared with a PSD involving dynamics, such that the contributions of specific frequencies can be clearly identified and visually compared (see [11]).

Figure 3.13 shows the performances of the states of interest for the BW values derived in Section 3.4.1. The input disturbance groups, namely *floor* (GND), *FIV*, *actuators* and *sensors*, are shown together with the total CPS up to 2.5 kHz and the requirements (see [1]). Indeed, dominant disturbances and dynamics are clearly revealed, guiding analyses and the design efforts at development stage or during upgrades. The



**Figure 3.13:** Dynamic Error Budgeting (DEB) cumulative power spectra (CPS) for the states of interest of the three-dimensional-space 11-body model of the HD-DCM with BRG, GAP, PTC and RLL control bandwidths equal to 30, 200, 200 and 200 Hz, respectively. (Details are given in the text).

error in positioning the  $\overline{\text{CR1}}$ s with respect to the incoming beam in Figure 3.13a is seen to be largely dominated by the floor disturbances up to 500 Hz, where the resonance mode of  $\overline{\text{MF1}}$  shown in Figure 3.8 is excited by the FIV by a similar level. Still, the RMS error in  $\text{CR1\_Rx}$  is about a factor 14 smaller than required. In Figure 3.13b, the error in the crystals gap is completely dominated by floor disturbances, being built up between 50 and 100 Hz. Although within the GAP BW, these errors are amplified by the sensitivity peak of the BRG loop (not shown) due to the residual cross-talk between BRG and  $\text{C2C\_Uy}$  (see Figure 3.12b). Yet, the performance is still a factor 80 better than specs.

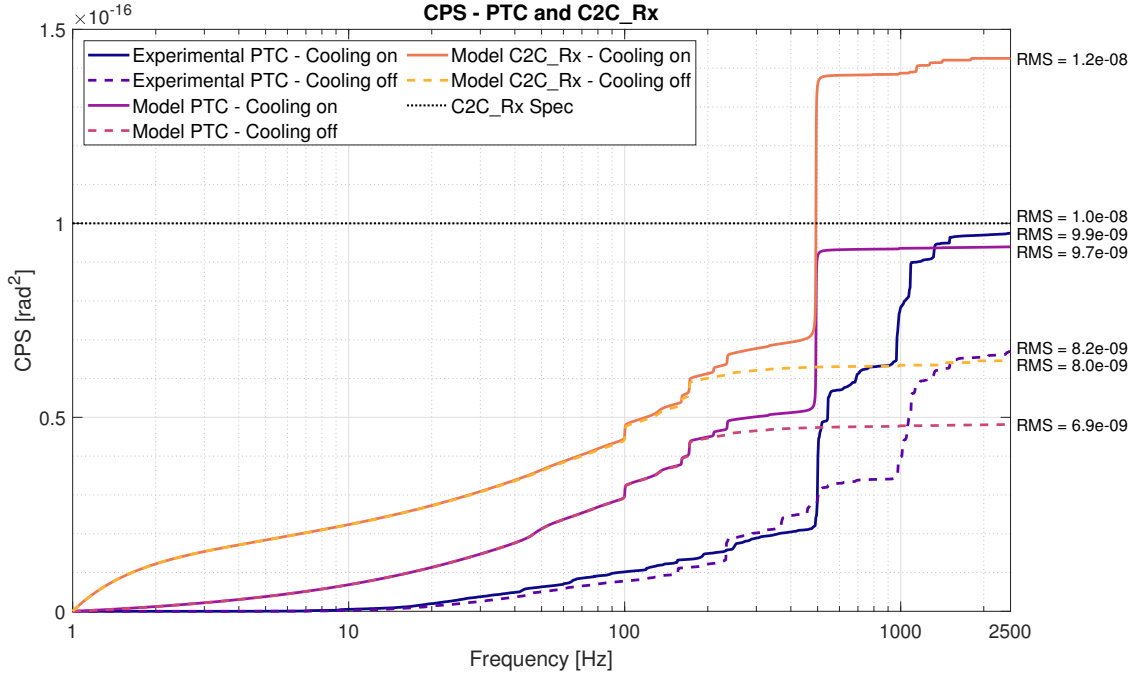
For the pitch error between crystals, Figure 3.13c shows a balanced contribution between the floor and the actuators (mostly from a residual cross-talk with the BRG loop) up to 500 Hz, where the resonance mode shown in Figure 3.8 is excited by the FIV and dominates the performance, extrapolating the specification of 10 nrad RMS by 20%. With the good agreement between model and measurements for the PTC loop discussed in Section 3.4.3, it is thus likely that the real pitch performance also marginally exceeds the nominal 10 nrad RMS. In practice, this is of no concern and some improvement for compliance with specs is possible with slightly optimized controllers. Nevertheless, without the contribution of the 500 Hz resonance and further optimized controllers,  $\text{C2C\_Rx}$  could be taken to at least 7.5 nrad RMS, which would be particularly interesting to leave margin to additional motion-related disturbances that are eventually introduced in fly-scan operation.

Finally, regarding the roll error between crystals  $\text{C2C\_Rz}$ , it is the floor that dominates performance, particularly due to an uncontrollable suspension mode of the  $\overline{\text{GOF}}$  on the bearings at 100 Hz (not shown). Nonetheless, the error is still about 3.75 times smaller than required and there is room for improvements with different controllers and higher BW.

### 3.4.3 Model Prediction and Experimental Data

Since the first HD-DCM units are already operational at the MANACÁ and the EMA beamlines at Sirius, the model-based DEB predictions can be compared with experimental data. The ideal case would be using beam-based diagnostics at the beamline to prove the HD-DCM performance. However, during this early operation phase of both the synchrotron storage ring and the beamlines, the development and validation of external diagnostics with sufficient resolution, accuracy and acquisition rate is still work in progress. Hence, results of the servo errors of the HD-DCM at MANACÁ in fixed-energy mode are taken here as a representative case.

Restraining the analysis to the most critical requirement, Figure 3.14 shows the CPS for the experimental PTC servo error, and the modeled PTC and  $\text{C2C\_Rx}$  performances in two conditions, namely: with and without  $\text{LN}_2$  flow, such that the contribution of FIV can be evaluated. For consistency, the model results follow the conditions defined in Section 3.4.1. The real hardware, in turn, was implemented with slightly different loop-shaped controllers due to historical reasons, having BRG and PTC BWs at 20



**Figure 3.14:** Cumulative power spectra (CPS) for comparison between servo errors in PTC control loop in experimental data of the HD-DCM at the MANACÁ beamline and Dynamic Error Budgeting model predictions. (Details in the text).

and 250 Hz, respectively. Still, the forms are sufficiently close for similar performance and to stress the predictive capacity and continuous optimization potential of the DEB tool. It can be seen in the model that, as it uses more conservative envelope disturbance estimates and less tailored controllers, the effects of the floor and actuators are larger when compared with the real data up to 500 Hz (see also Figure 3.13c). Yet, the detrimental contribution of the FIV disturbances at this frequency, related to the resonant mode shown in Figure 3.8, is consistent in all sets. Indeed, more specific controller designs do bring the model predictions closer to the experimental data, but this level of detail is beyond the scope here. The focus is rather showing how DEB allowed for the HD-DCM to be developed from scratch and how it can now be used for further improvement.

The most surprising element in both experimental curves is the large contribution at 1 kHz, which brings the servo error just to the requirement of 10 nrad RMS in the cryocooled operational condition. This contribution is currently credited to the excitation of a few mechanical resonances, including the second rocking mode of the  $\overline{\text{MF1}}$ , also shown in Figure 3.8. As no significant disturbance source was expected at such high frequencies and this is seen also without  $\text{LN}_2$  flow, one explanation under analysis is having some of the harmonic peaks of the Varedan amplifier shown in Figure 3.11 — which are averaged in the PSD as compared to the actual energy contents visible from FFTs (Fast Fourier Transforms) — matching these high-frequency mechanical resonances. If this is the case, some improvement can be expected with hardware mod-

ification in the amplifier. Then, design improvements in the 500 Hz mode of the MF1 may improve performance even further, such that the fixed-energy servo errors might possibly reach about 6 nrad RMS. Nonetheless, the experimental results shown here already report unmatched positioning errors in a vertical-bounce DCM in a synchrotron beamline, excelling publicly available data by a factor 5 (see [7]).

### 3.5 Conclusions

The HD-DCM brings an entirely new mechatronic architecture to the class of instruments known as X-ray DCMs in synchrotron beamlines. The profound paradigm changes were motivated by the combination of two aspects: on the one hand, the more demanding positioning errors together with high-performance fly-scan operation requirements in 4th-generation synchrotrons; and, on the other, the long-term history of efforts in the community to incrementally improve standard DCM designs. Indeed, with this single step, stand-still and fly-scan angular errors between crystals in vertical-bounce DCMs could be reduced from typical 50-200 nrad RMS and several microradian, respectively, to 10 nrad RMS up to 2.5 kHz.

The Dynamic Error Budgeting methodology has been used in high-end mechatronic systems in the semiconductor industry for more than a decade, but the HD-DCM seems to be the first beamline optical instrument to take benefit from it, using its predictive potential to develop a high-performance machine from scratch “first time right” for Sirius light source. Hence, in addition to presenting the HD-DCM model and justifying its innovative architecture by proving its performance and predictability, this work aims at sharing this powerful tool and providing a detailed and successful case study for future reference.

The next steps include cross-correlating the HD-DCM with beam-based feedback and enabling high-performance fly-scan experiments, which is expected to be realized as soon as the storage ring and the remaining beamline instruments at Sirius allow for sufficient beam stability and hardware integration.

### Acknowledgements

The authors would like to acknowledge the contributions of the LNLS staff, in particular Cassiano Bueno, Mauricio Donatti and Ricardo Caliar, for the measurements of the disturbances, and the essential roles of Theo Ruijl, Ronald Schneider and the rest of the MI-Partners team, not only in the development of this collaborative project, but also for the introduction of the DEB methodology to the LNLS team. This work is part of a PhD project carried out with the CST group at TU/e, being support by the Brazilian Center for Research in Energy and Materials (CNPEN) under contract with the Brazilian Ministry of Science and Technology and Innovation (MCTI).

### 3.A List of Abbreviations

AF1	Auxiliary frame 1
AF2	Auxiliary frame 2
BMS ( $\overline{\text{BMS}}$ )	Balance mass (model)
BRG	Bragg angle control loop
BW	Bandwidth
C2C	Crystal-to-crystal model output
CBR	Compliant cooling braid
CCB	Crystal cooling block
CCG	Crystal cage
CIP	Complementary isolation pads
CMF	Cooling manifold
CMX	Cooling manifold extension
CNPEM	Brazilian Center for Res. Energy and Materials
CoG	Center of gravity
CPS	Cumulative power spectrum
CR1 ( $\overline{\text{CR1}}$ )	1st crystal (model)
CR2 ( $\overline{\text{CR2}}$ )	2nd crystal (model)
cRIO	CompactRIO
DAC	Digital-to-analog converter
DCM	Double-Crystal Monochromator
DEB	Dynamic Error Budgeting
DoF	Degree of freedom
DS	Dynamic substructuring
EFS	Embedded flexural structure
ENC	Optical encoder
FEA	Finite element analysis
FLS	Folded leaf-spring
FIV	Flow-induced vibrations
GAP	Inter-crystal gap control loop
GOF ( $\overline{\text{GOF}}$ )	Goniometer frame (model)
GND ( $\overline{\text{GND}}$ )	Ground/floor (model)
GRA ( $\overline{\text{GRA}}$ )	Granite bench (model)
HBR	High-conductivity cooling braid
HD-DCM	High-Dynamic DCM
HP1	Homing pin 1
HP2	Homing pin 2
IFA	Fiber interferometer assembly
IFM	Fiber interferometer
LEV	Levelers
LN <sub>2</sub>	Liquid nitrogen

LNLS	Brazilian Synchrotron Light Laboratory
LOS ( $\overline{\text{LOS}}$ )	Long-stroke structure (model)
LSA	Long-stroke actuator
LEV	Leveler
LTI	Linear time-invariant
MCS	Main coordinate system
MEM	Coupling membrane
MF1 ( $\overline{\text{MF1}}$ )	Metrology frame 1 (model)
MF2	Metrology frame 2
MIMO	Multiple-input-multiple-output
MIR	Plane mirrors
PDF	Probability density function
PTC	Inter-crystal pitch control loop
PSD	Power spectrum density
RLL	Inter-crystal roll control loop
RMS	Root mean square
ROT ( $\overline{\text{ROT}}$ )	Goniometer rotor (model)
SDM	Structural dynamic modification
SH1	Calibrated shim 1
SH2	Calibrated shim 2
SHS ( $\overline{\text{SHS}}$ )	Short-stroke frame (model)
SISO	Single-input-single-output
SNR	Signal-to-noise ratio
STC	Coupling strut clamp
STT	Coupling strut
TF	Transfer function
UHV	Ultra-high vacuum
VC	Voice-coil
VCC	Voice-coil coil
VCF	Voice-coil frame
VCM	Voice-coil magnet

### 3.B Mechanical Structure to Model

For completeness, this section provides a detailed correlation between the mechanical parts of the HD-DCM described in [1] and their model equivalent (see also Section 3.A for abbreviations). The granite bench lump  $\overline{\text{GRA}}$  is built from the complete *Bench Module* plus the *Goniometer Module*, except for the active rotor (ROT), which becomes the lump  $\overline{\text{ROT}}$ ; the main rotating frame lump  $\overline{\text{GOF}}$  is made of the *GOF Module*, and the auxiliary frame AF1 and the LN<sub>2</sub> distribution system in the *Module 1* — except for the crystal cooling blocks CCBs; the metrology frame lump  $\overline{\text{MF1}}$  is made of the MF1



itself plus the homing pins HP1s and the mirrors MIRs; the 1<sup>st</sup> crystals lumps  $\overline{\text{CR1}}_1$  and  $\overline{\text{CR1}}_2$  consist of the crystals, their shims SH1s and blocks CCBs; the long-stroke lump  $\overline{\text{LOS}}$  is built from the *LOS Module*, and the auxiliary frame AF2, the cooling braids HBR and CBRs, and accessories from the *Module 2*; the short-stroke frame lump  $\overline{\text{SHS}}$  includes the SHS itself, plus the homing pins HP2s, the interferometers IFAs, the voice-coil (VC) coils VCCs and their frames VCFs, the folded leafsprings (FLSs)  $\text{FLS}_{\text{SHS}}$  and accessories; the 2<sup>nd</sup> crystals lumps  $\overline{\text{CR2}}_1$  and  $\overline{\text{CR2}}_2$  are formed by the crystals and their shims SH2s; finally, the balance-mass lump  $\overline{\text{BMS}}$  is formed by the BMS itself, the folded leafsprings  $\text{FLS}_{\text{BMS}}$  and the VC magnets VCMs.

## References

- [1] Gerald R.R. *et al.* 2022 *Precision Engineering* **77** 110
- [2] Liu L. *et al.* 2021 *Proc. 12th Int. Particle Acc. Conf. (IPAC'21)* (JACoW Publishing) 13–18
- [3] Eriksson M. *et al.* 2014 *J. Synchrotron Rad.* **21**(5) 837
- [4] Hettel R. 2014 *J. Synchrotron Rad.* **21**(5) 843
- [5] Gerald R.R. *et al.* 2018 *Proc. 10th Mech. Eng. Des. of Synchrotron Radiat. Equip. and Instrum. (MEDSI'18)* (JACoW Publishing) 147–152
- [6] Gerald R.R. *et al.* 2021 *Proc. 18th Int. Conf. on Acc. and Large Exp. Phys. Control Systems (ICALPCS'21)* (JACoW Publishing) 370–375
- [7] Kristiansen P. *et al.* 2015 *J. Synchrotron Rad.* **22**(4) 879
- [8] Monkhurst W. 2004 *Dynamic Error Budgeting: a Design Approach*
- [9] Jabben L. 2007 *Mechatronic Design of a Magnetically Suspended Rotating Platform* Ph.D. thesis Delft University of Technology
- [10] Laro D.A.H. 2009 *Mechatronic Design of an Electromagnetically Levitated Linear Positioning System using Novel Multi-DoF Actuators* Ph.D. thesis Delft University of Technology
- [11] Jabben L. and van Eijk J. 2011 *Mikroniek* **51**(2) 5
- [12] Schmidt R. *et al.* 2011 *The Design of High Performance Mechatronics: High-Tech Functionality by Multidisciplinary System Integration* 2nd edn. (IOS Press)
- [13] de Klerk D. *et al.* 2008 *AIAA Journal* **46**(5) 1169
- [14] Schellekens P. *et al.* 1998 *Cirp Annals* **47**(2) 557
- [15] Slocum A.H. 1992 *Precision Machine Design* (Society of Manufacturing Engineers)
- [16] Papoulis A. 1991 *Probability, Random Variables and Stochastic Processes* 3rd edn. (McGraw-Hill)
- [17] Avitabile P. 2003 *Sound and Vibration* **37**(1) 14
- [18] Witvoet G. *et al.* 2017 *Proc. 2017 IEEE Conf. on Control Tech. and Appl. (CCTA)* (IEEE) 726–731
- [19] Gerald R.R. *et al.* 2017 *Proc. 9th Mech. Eng. Des. of Synchrotron Radiat. Equip. and Instrum. (MEDSI'16)* (JACoW Publishing) 44–47
- [20] Ambaum N. *et al.* 2021 *Proc. 36th ASPE Annual Meeting* 89–96
- [21] Soemers H. 2011 *Design Principles for Precision Mechanisms* (T-Pointprint)
- [22] Skogestad S. and Postlethwaite I. 2007 *Multivariable Feedback Control: Analysis and Design* vol. 2 (John Wiley & Sons)

- 
- [23] Caliari R.M. *et al.* 2017 *Proc. 9th Mech. Eng. Des. of Synchrotron Radiat. Equip. and Instrum. (MEDSI'16)* (JACoW Publishing) 8–11



---

## A Review on the High-Dynamic Double-Crystal Monochromator for Sirius/LNLS

---

### Abstract

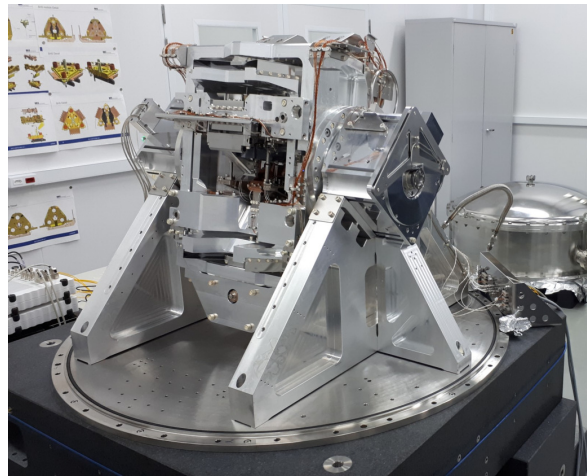
The High-Dynamic Double-Crystal Monochromator (HD-DCM) started to be developed in 2015 by the Brazilian Synchrotron Light Laboratory (LNLS) for the 4th-generation light source Sirius. The reason for the unique and innovative control-based architecture was twofold, namely: 1) reaching the unprecedented target of 10 nrad RMS (root mean square) (1Hz-2.5kHz) in crystals parallelism for a vertical-deflection DCM, to comply with the smaller new-generation source sizes; and 2) unlocking the potential of high-stability fixed-exit continuous energy scans, creating unmatched spectroscopy capabilities that benefit from the higher new beam brightness. The outcome is a machine built on essential high-precision mechatronics principles, with an integrated design for optimized dynamics, actuation, metrology, and thermal aspects. The first two units are operational at the MANACÁ (MAcromolecular micro and NAno CrystAllography) and the EMA (Extreme Methods of Analysis) undulator beamlines. This work reviews the key aspects of this new technology and presents experimental commissioning results at the beamlines, including high-quality energy continuous fly-scans up to 500 eV/s over 1 keV that demonstrate the good performance for X-ray spectroscopy by keeping inter-crystal stability below 15 nrad RMS up to 10 kHz. Preliminary EXAFS data collected at the EMA beamline at 1 keV/s is also shown. Furthermore, a discussion is held about the required beamline integration level, since the high-end experiments demand appropriate control strategies, data acquisition, triggering and performance capabilities, particularly concerning the source, the sample environment, and the detectors.

## 4.1 Introduction

The relative angular adjustment and stability between the two diffracting crystals of a Double-Crystal Monochromator (DCM) is a well-known engineering challenge at X-ray synchrotron beamlines. In the early days, these tolerances were often in the range of tens of  $\mu\text{rad}$ , being related mostly to complying with beam flux, i.e., keeping angular tuning within a fraction of the Darwin width (DW) or Rocking Curves (RC) [1,2]. Nowadays, however, the high brilliance and small source sizes provided by 4th-generation light sources bring particularly the vibration requirements to the range of tens of  $\text{nrad}$  only [3,4], otherwise increasing the effective beam size or moving the probe around the region of interest.

In 2014, at the Workshop on X-ray DCMs, held by the European Synchrotron Light Facility (ESRF), several worldwide experts in the field eventually agreed that the performances of existing DCMs might not be compatible with the latest demands. Since then, many institutes and suppliers have continued with efforts in upgrading conventional designs, reaching various success levels in improving crystal stability at fixed energies. In a parallel path – understanding that the standard mechanical architecture of DCMs might be close to practical limits in terms of angular stability at fixed conditions, and that ultimate performance in dynamic conditions, i.e., during motion, could benefit from the new sources with higher brilliance to open possibilities in terms of throughput and science opportunities –, the Brazilian Synchrotron Light Laboratory (LNLS) has developed, since 2015, in collaboration with the Dutch consultant in mechatronics MI-Partners, the High-Dynamic Double-Crystal Monochromator (HD-DCM) (see Figure 4.1) for the Sirius light source.

The HD-DCM project gathered the expertise available for DCMs in the synchrotron community and core concepts from mature technologies in the semiconductors industry – where processes are often completed in the sub-second range, positioning accuracy

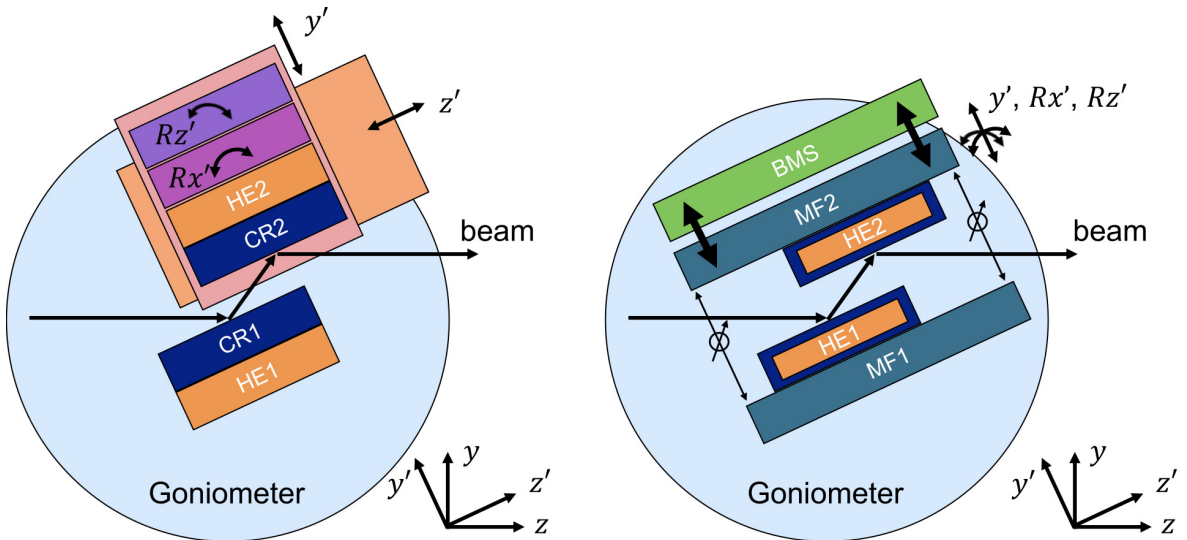


**Figure 4.1:** Photograph of the HD-DCM in a clean room at LNLS (without the vacuum vessel for visibility).

may reach the sub-nm range, and reliable operation 24/7 is required [5] – to develop an innovative high-performance mechatronic system for X-ray beamlines. Combining deterministic precision engineering principles and well-established predictive modeling tools, the instrument could be developed from scratch according to a “first-time-right” approach. Two units are currently operation at the MANACÁ (MAcromolecular micro and NAno CrystAllography) and the EMA (Extreme Methods of Analysis) undulator beamlines at Sirius, showing 10 nrad RMS (root mean square) (or better) inter-crystal stability up to 2.5 kHz, even during fly-scan spectroscopy. With Si(111) and Si(311) crystal sets, the energy range from 3 to 72 keV can be covered. Here, the main conceptual aspects of the cutting-edge HD-DCM design are discussed in Section 4.2. Then, integration and synchronization aspects with other beamline instruments, such as an undulator source and detectors, for energy fly-scan capabilities are considered in Section 4.3. Finally, performance results are demonstrated in Section 4.4 before the conclusions in Section 4.5.

## 4.2 Mechatronic Architecture

The main mechanical architecture differences between standard DCM designs and the HD-DCM can be derived from the simple schematics in Figure 4.2. In the first, despite variations regarding specific motion axes addressed by each of the crystals, a typical DCM architecture based on high-stiffness assumptions is probably recognizable. In this example, the 1st crystal CR1 is mounted to a heat exchanger HE1, which is then fixed via brackets to the goniometer, that is used to adjust the angle of the crystals with respect to the beam. Next, the 2nd crystal CR2 is fixed to its heat exchanger HE2, which is, in turn, mounted to a stack of alignment stages also fixed to the goniometer.



**Figure 4.2:** Schematic drawings of architectures of a standard DCM (left) and of the HD-DCM (right). (Description in the text.)

These stages are responsible for adjusting the pitch ( $Rx'$ ) and roll ( $Rz'$ ) angles, and for translating the crystal in the  $y'$ -axis, for the regulation of the gap, and in the  $z'$ -axis, to account for beam walk over different angles — the prime notation here represents the rotating coordinate system.

Even though this classic solution can provide high-resolution automated systems, a few remarks can be pointed in terms of stability and disturbance rejection. 1) By using the HEs as holders for the CRs, positioning and thermal management functionalities are mixed, in the sense that materials and designs that are good for thermal conductivity, may not be a good choice in terms of thermal expansion/drift or stiffness. 2) By stacking the stages for different degrees of freedom (DoFs), stiffness is lost (and in a hard-to-predict way) while mass is added, compromising the high-stiffness intention and, eventually, limiting the achieved dynamics. 3) With the  $Rx'$  as a stand-alone pitch stage, even if its performance is hypothetically made perfect, perhaps compensating disturbances via active vibration control (see [6]), there are no guarantees that the remaining of the stack or even CR1 and CR2 should be bound to small pitch angular variations. In fact, trying to actively optimize the pitch stage might increase vibrations in the rest of the system due to the control reaction forces. 4) Typically relying on stepper motors and piezo steppers, actuation is subject to step responses, which excite resonances over broad frequency ranges, increasing vibration levels and severely affecting energy fly-scan perspectives. 5) Finally, due to friction and rolling guiding elements, resolution and repeatability, including parasitic motions, are expected to reach boundaries that limit calibration possibilities.

The HD-DCM design addresses these issues via more deterministic concepts, not only replacing much of the uncertainty, but also managing disturbances. The position of the crystals CR1 and CR2 are no longer determined by the heat exchangers HE1 and HE2. Instead, the crystals are deterministically mounted to metrology frames MF1 and MF2, and the heat exchangers are mounted to the crystals via compliant links. Thus, positioning and thermal management functionalities can be decoupled and optimized. Then, instead of relying on the internal feedback of stages in a stack, which are blind to parasitic mechanical performance of the remaining items, metrology (represented by the arrows with dials) is made directly between the metrology frames, such that the DoFs between crystals, including the actual angular stability, depend on a short metrology loop. Next, only essential positioning DoFs are implemented. The 1st crystal is chosen to be fixed to goniometer, while the required DoFs for the relative positioning is concentrated in the module of the 2nd crystal. And, instead of a stack of stages, the pitch, roll and gap DoFs are implemented in parallel, by means of a convenient arrangement of folded leaf-springs that constrain the  $x'$ ,  $z'$  and  $Ry'$  DoFs and leave the piston-tip-tilt  $y'$ ,  $Rx'$  and  $Rz'$  DoFs for active control. Moreover, positioning of the 2nd metrology frame is made via force actuators (represented by the thick arrows), instead of high-stiffness actuators. This decouples it from the dynamics of the rest of the system, allowing its position to be more effectively controlled according to the metrology signals. Lastly, the reaction forces of controlling the position of the 2nd

metrology frame are directed to a so-called balance mass (BMS), which filters the forces that would otherwise be transmitted to the rest of the system and, eventually, excite resonances in the module of the 1st crystal and/or limit the active control bandwidth.

Hence, decoupling functionalities, defining deterministic interfaces, eliminating positioning stacks, choosing a short-loop metrology concept (and co-located control), using smooth mechanical guides, relying on “zero-stiffness” actuators, introducing a dynamic filter, and evaluating the noise levels of the actuators and metrology items, as well as of floor vibrations and cooling disturbances, predictive mechatronic models could be built from the early stages of the project, iteratively guiding the design towards the desired performance and saving large amounts of resources that otherwise might have been spent on faulty prototypes and rework. Indeed, building such a complex machine by trial and error seems virtually impossible. A deeper and more comprehensive description of the design and the modeling tools of the HD-DCM can be found in [7, 8].

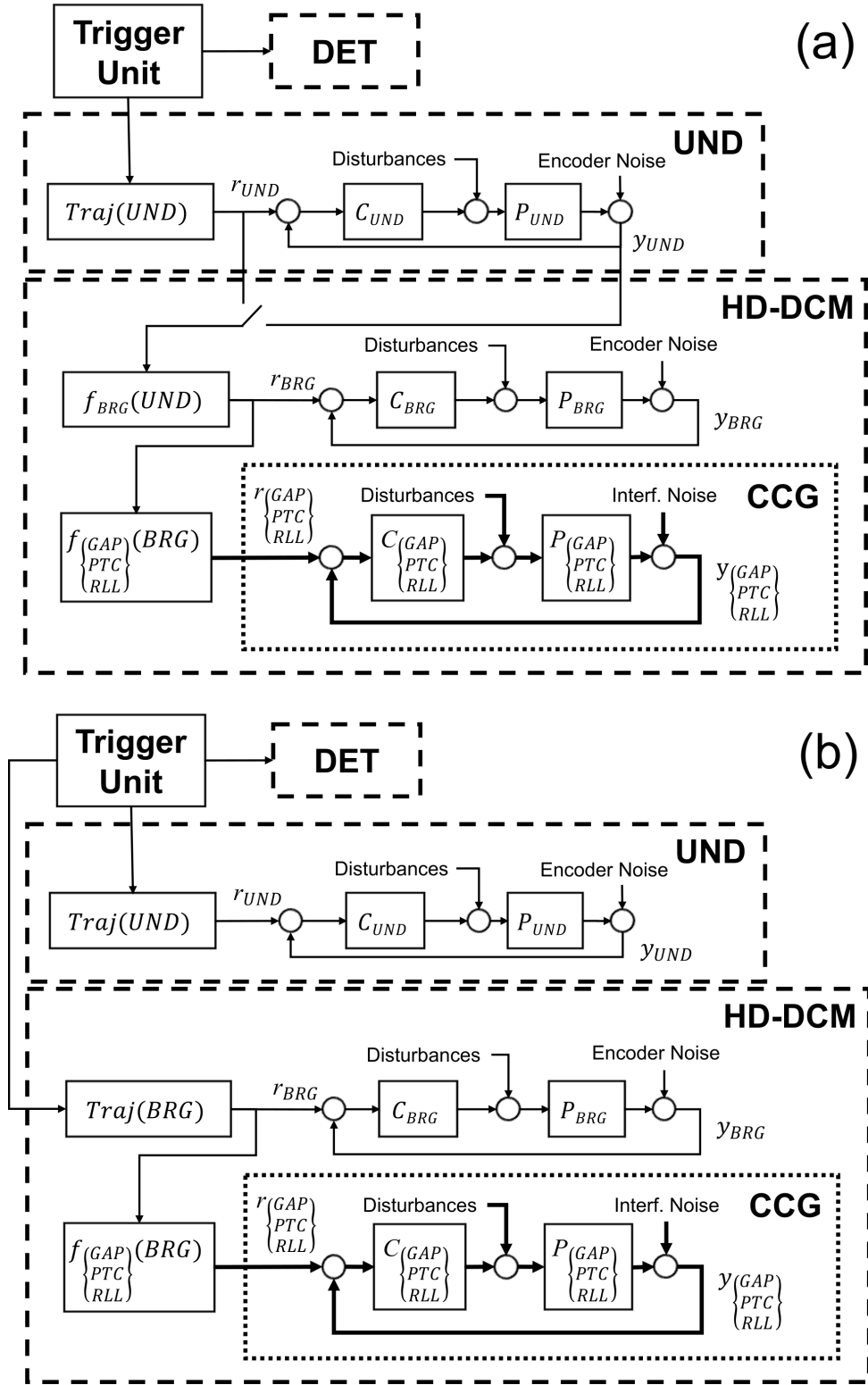
### 4.3 Integration Architecture

The HD-DCM control is implemented in NI’s CompactRIO (cRIO), partly using LabVIEW in the real-time operating system and partly using FPGA (field-programmable gate array), finally reaching a sample rate of 20 kHz. Then, for basic operation at the beamlines, it has been integrated to EPICS [9], with an IOC server that is based on the Nheengatu solution [10], a software toolbox developed in-house to integrate cRIO variables in LabVIEW into the EPICS framework. Thus, the HD-DCM can be readily operated as a stand-alone instrument, using standard beamline pieces of software and task orchestrators.

Yet, as shown in Section 4.4, the technology in the HD-DCM allows it to keep nrad level performance not only at stand-still, but also during motion, enabling high-performance energy fly-scans. Then, with scans within seconds, software and communication delays may be unacceptably large, requiring orchestration in the hardware level. At bending-magnet beamlines, it may be sufficient to synchronize and trigger the HD-DCM with detectors, but at undulator beamlines, as in MANACÁ and EMA at Sirius, the undulator becomes a key player, since parameters must be matched for energy tuning. Figure 4.3 depicts two possible integration configurations for the HD-DCM at undulator (UND) beamlines. The instruments running in closed-loop control are represented by electromechanical plants ( $P_i$ ) and controllers ( $C_i$ ), following references ( $r_i$ ) and providing measurements ( $y_i$ ). Plant disturbances and metrology noise (from encoders and interferometers) are also illustrated. The HD-DCM is separated into a Bragg angle control loop (BRG) and the crystal cage module (CCG), with the gap (GAP), pitch (PTC) and roll (RLL) independent loops. A trigger unit may be used to manage flags for motion and data acquisition in the detectors (DET).

In Figure 4.3a, the HD-DCM is a follower of the undulator, internally converting at 20 kHz the undulator phase/gap reference or its measurement signal, for example, to a





**Figure 4.3:** Schematic control diagrams with two configurations for fly-scan with the HD-DCM in undulator beamlines: (a) master-follower mode; and (b) triggered mode. (Description in the text.)

Bragg angle, according to a function ( $f_{\text{BRG}}$ ) related to the photon energy. Following the reference requires that the undulator performance (control error) is sufficient to keep the energy tuning between them within acceptable boundaries – considering motion errors and delays, for instance. Following the measurement signal, on the other hand, may include electronic noise and low-amplitude high-frequency dynamics, that may be acceptable regarding energy tuning, but still disturb the HD-DCM closed-loop performance, as shown in Section 4.4. A more detailed discussion about these tolerances will be provided in a dedicated paper under preparation.

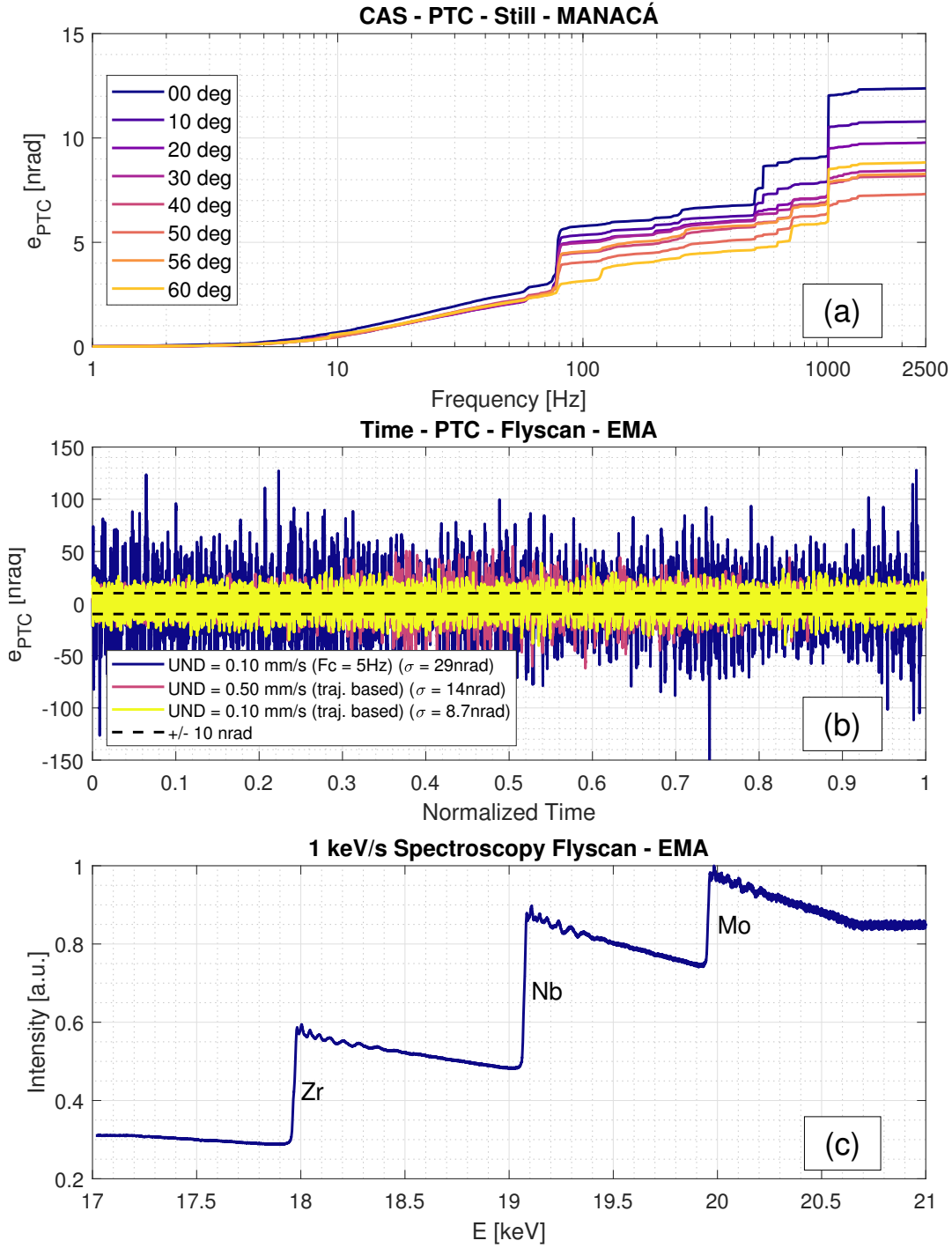
In Figure 4.3b, in turn, the HD-DCM and the undulator are linked by triggering signals only, such that their dynamics are decoupled. This is similar to the master-follower configuration with the reference connection, but the corresponding trajectories (motion setpoints) must be pre-calculated and loaded separately, requiring different electronic functionalities from the controllers. Hence, the preferred integration configuration may depend on software/hardware capacity and on the motion performance of the undulator itself. In all cases, the trajectory applied to the undulator must also consider the limits and performance impact in the HD-DCM.

## 4.4 Performance Results

The pitch performance of the HD-DCM is illustrated in Figure 4.4, via measurements taken with the two units in operation at Sirius beamlines. Figure 4.4a provides stand-still measurements of the cryocooled system at the MANACÁ beamline at a few Bragg angles over the operational angular range, namely, from 3° to 60°. The data is displayed as the cumulative amplitude spectrum (CAS), presenting the RMS value of the pitch control error as a function of frequency. The integrated RMS values up to 2.5 kHz stay between 7 and 12.5 nrad, whereas below 100 Hz fall between 3 and 6 nrad, and up to 10 Hz stay in the sub-nrad level. Still, there is some margin left for small performance improvements with further controller optimizations, if required. With a control bandwidth (defined as the cross of the unit gain in the open-loop Bode plot) of about 200 Hz, the effect of active vibration suppression in the low-frequency range is clear.

Next, Figure 4.4b provides examples with time signals collected at 20 kHz for the pitch control error during 1 keV energy fly-scans around 9 keV at the EMA beamline. Until now, in the early commissioning phase, an adjustable-phase undulator APU22 ( $K_{\text{max}}=1.4$  and  $\lambda=22$  mm) by Kyma has been used, but it will be replaced by an in-house APU20 ( $K_{\text{max}}=2.4$  and  $\lambda=20$  mm) soon. Thus, integration functionalities with the undulator are currently limited by control hardware/software and sensor resolution. Indeed, from the options discussed in the previous section, only the master-follower configuration with measurement signal integration has been available. Moreover, the temporary encoder signal is relatively coarse and there is little freedom in defining the undulator trajectory setpoint for smoothness.

So, despite using a low-pass filter with corner frequency at 5 Hz in one of the datasets



**Figure 4.4:** Experimental performance of the HD-DCM at Sirius beamlines: (a) fixed-energy cumulative amplitude spectrum (CAS) for different Bragg angles; (b) fly-scan examples at 100 and 500 eV/s; (c) absorption example at 1 keV/s. (Details in the text.)

in this example to reduce the encoder noise, a scan at about 100 eV/s (resulting from 0.1 mm/s travel speed for this undulator at this energy and the given harmonic) is seen to disturb the HD-DCM performance – although still keeping the pitch error within 30 nrad RMS, which has been a challenge for most standard DCMs even at stand-still.

Then, by using more adequate free-of-noise 3rd-order trajectories (i.e. with control over acceleration and jerk levels) simulating an optimized undulator motion as the master for the HD-DCM, two other datasets show scans at 100 eV/s (0.1 mm/s) and 500 eV/s (0.5 mm/s), in which the first can remarkably keep performance below 10 nrad RMS, whereas the latter starts to suffer from additional motion disturbances, but remains below 15 nrad RMS. Nevertheless, improvements can still be expected for the future, via further optimized trajectories and controllers.

Finally, Figure 4.4c has a case with a dummy sample consisting of a stack of Zr, Nb and Mo foils to demonstrate the combined absorption spectrum in a fly-scan at 1 keV/s and taking only 4 seconds. This is a preliminary result, with additional noise due to the current limitations given by the undulator, but it showcases the capabilities of this monochromator. Indeed, with the HD-DCM scanning times can potentially take only a few seconds (with 2, 4 and 10 seconds, in these examples) as opposed to several minutes (sometimes up more than an hour), as commonly seen in step-scan experiments, with large impact in throughput and scientific opportunities.

To conclude, the high-performance of the HD-DCM indicated by the embedded metrology could not yet be directly correlated with synchronized measurements of the photon beam up to these high frequencies (10 to 20 kHz). This is because there are remaining instabilities in the electron beam (before the fast orbit feedback becomes available at Sirius) and ongoing integration efforts with the trigger units and the detectors at the beamlines. Still, no surprises are expected since the interferometers directly probe the metrology frames, and the crystals follow deterministic mounting concepts. As a matter of fact, the predictive models estimate that the actual crystal-to-crystal pitch variations would be only up to 10% or 20% higher than what is measured in the PTC loop (see [8]). Ultimate experimental conditions are expected with the installation of the final undulators and the maturing of the integration work.

## 4.5 Conclusions

The HD-DCM mechatronic architecture provides an alternative to the struggle that standard DCMs based on high-stiffness concept have been facing regarding inter-crystal pitch vibrations. Indeed, not only does it allow sufficient noise suppression in stand-still conditions for fixed-energy experiments, but it also enables high-performance fly-scans for spectroscopy. Consequently, it may open scientific opportunities with faster experiments, as well as increase throughput.

Furthermore, it serves as a concrete example of how beamline instrumentation may benefit more from mature technology available in industry, regardless the many idiosyncrasies of the synchrotron environment. In particular, it has become a successful case of how complex and multidisciplinary instruments may be still assertively developed from scratch, according to methodical and predictable engineering approaches. Many opportunities regarding control optimization are now available, and a new model, the so-called HD-DCM-Lite, is under construction for extended scanning capacity.

## Acknowledgements

The authors would like to gratefully acknowledge the funding by the Brazilian Ministry of Science, Technology and Innovation, and the contributions of the LNLS and the MI-Partners teams to this project. The HD-DCM is also a PhD project carried out with the CST group at TUE, with Marteen Steinbuch, Hans Vermeulen and Gert Witvoet.

## References

- [1] Hastings J.B. 1977 *J. Appl. Phys.* **48**(4) 1576
- [2] Lemonnier M. *et al.* 1978 *Nucl. Instrum. Methods* **152**(1) 109
- [3] Kristiansen P. *et al.* 2015 *J. Synchrotron Rad.* **22**(4) 879
- [4] Sergueev I. *et al.* 2016 *J. Synchrotron Rad.* **23**(5) 1097
- [5] Heertjes M.F. *et al.* 2020 *Proc. 2020 Am. Control Conf. (ACC)* (IEEE) 3686–3703
- [6] Bai Y. *et al.* 2022 *Nucl. Instrum. Methods Phys. Res. A* **1029** 166418
- [7] Geraldès R.R. *et al.* 2022 *Precision Engineering* **77** 110
- [8] Geraldès R.R. *et al.* 2022 *Precision Engineering* **77** 90
- [9] Dalesio L.R. *et al.* 1991 *EPICS architecture* Tech. Rep. No. LA-UR-91-3543; CONF-911116-9 Los Alamos National Lab., NM (United States)
- [10] Alnajjar D.A.D. *et al.* 2019 *Proc. 17th Int. Conf. on Acc. and Large Exp. Phys. Control Systems (ICALPCS'19)* (JACoW Publishing) 997–1000

---

## Fly-Scan-Oriented Motion Analyses and Beamline Integration Architecture for the High-Dynamic Double-Crystal Monochromator at Sirius/LNLS

---

### Abstract

The High-Dynamic Double-Crystal Monochromator (HD-DCM) is a mechatronic system with unique control-based architecture and deep paradigm changes as compared to traditional beamline monochromators. Aiming at unprecedented inter-crystal positioning stability in vertical-bounce DCMs in the order of 10 nrad RMS (1Hz-2.5kHz), and not only in fixed-energy, but also in fly-scan operation, it has been developed according to a “first-time right” predictive design approach for hard X-ray beamlines at Sirius, the 4th-generation light source at the Brazilian Synchrotron Light Laboratory (LNLS/CNPEM). This work explores some of the challenges that emerge with this new technology and present the latest commissioning results that demonstrate the unparallel performances of the HD-DCM at the undulator-based EMA (Extreme Methods of Analysis) beamline at Sirius. With the enabled fast spectroscopy fly-scan possibilities, a new energy-tuning evaluation method, based on wave-propagation simulations, becomes part of a motion-oriented analysis that is carried out to derive the multi-axis non-linear positioning problem, covering not only energy selection and fixed-exit in the HD-DCM, but also the emission spectrum of an adjustable-phase undulator (APU). The HD-DCM control scheme and its flexible operation modes are described in detail as well. Furthermore, a new integration topology between the HD-DCM and EMA’s APU, coming already close to ultimate motion levels, is described and validated.

## 5.1 Introduction

At synchrotron light sources, hard X-ray monochromatic beams are often provided by monochromators that are implemented as a non-dispersive parallel arrangement of two identical monocrystalline structures. Constructively, this arrangement can be implemented in two basic ways, namely: 1) a single crystal with a groove, a design concept known as channel-cut; and 2) two independent crystals, generally referred to as Double-Crystal Monochromator (DCM). This work is focused on DCMs, whose key conceptual advantage over channel-cuts is the ability to keep a fixed-exit beam independently of the rotation of the crystals for energy selection, which can be important for beamline alignment purposes and relative motion of the beam with respect to the sample under analysis.

The first DCMs were developed in the late 1970s and early 1980s [1–5], since when incremental upgrades have been gradually implemented to adapt to ever more stringent requirements over time [6–11]. This evolutionary approach has generally persisted even after the Workshop on X-ray DCMs, held in 2014 by the European Synchrotron Radiation Facility (ESRF) in Grenoble [12], in which it was recognized by a great number of worldwide experts in the field that no existing DCM was able to meet some of the requirements of the new-generation beamlines. Indeed, starting in the 2010s, the new 4th-generation storage rings push the X-ray brightness and coherence fraction to unprecedented levels, opening unique science opportunities in terms of temporal and spatial resolutions [13, 14], but require that the beamline instrumentation performs accordingly. Still, after so many years of development, the main recurrent challenge in the DCMs is found as keeping the inter-crystal parallelism, so that variations in flux and beam position are kept within acceptable levels, while handling multiple moving axes, high power loads, radiation and in-vacuum operation.

Aiming at improved fixed-energy stability and unlocking high-performance fly-scan perspectives with the inter-crystal parallelism target of 10 nrad RMS (1 Hz to 2.5 kHz), the Brazilian Synchrotron Light Laboratory (LNLS/CNPEN) has developed the High-Dynamic Double-Crystal Monochromator (HD-DCM) for the 4th-generation light source Sirius [15], the first DCM to implement a high-performance control-based isolated mechatronic architecture. Herein, *fixed-energy* or *stand-still* is understood as all motion axes in position during data acquisition, which can also be related to traditional *step-scan* operation, whereas *fly-scan* refers to continuous synchronous motion of axes with simultaneous data acquisition. The first HD-DCM unit has been operational at the MANACÁ (MAcromolecular micro and NAno CrystAllography) beamline since 2020, mostly working on fixed-energy experiments, whereas the second unit at the EMA (Extreme Methods of Analysis) beamline since 2021, where the scanning perspectives started to be explored.

To advocate in favor of its powerful technology and the applied development method-

ologies, and allay insecurities in the community, a lot has been shared over the years in topical conferences: the basic conceptual design, mechatronic principles and thermal management were described in [16], [17] and [18]; the first results of in-air validation of the core, together with system identification and control techniques in the prototyping hardware were shown in [19] and [20]; the offline performance of the full in-vacuum cryocooled system, including energy fly-scan, were demonstrated in [21]; the dynamic modeling work, updated control design and NI LabVIEW FPGA implementation in the final NI's CompactRIO (cRIO) were addressed in [22], [23] and [24]; calibration and commissioning procedures, together with the first experimental results with beam were shown in [25]; and, finally, integration aspects with undulator sources started to be discussed in [26]. More recently, the detailed mechanical design and mechatronic architecture of the HD-DCM has been thoroughly described in [27] and [28]; whereas, together with updated commissioning results, a didactic discussion on the fundamental conceptual differences between the HD-DCM and standard DCM mechanical architectures has been provided in [29].

This work mainly focuses in detailing and experimentally validating the positioning problem formulations for both the HD-DCM and its current adjustable-phase undulator (APU) source from an energy fly-scan (or spectroscopy) perspective. Indeed, although basic geometrical and physical equations can be found elsewhere [30], to the best of the authors' knowledge, a mechatronic approach concerning ranges, velocities, acceleration levels, forces and torques has not been covered in literature yet — perhaps due to step-based actuation technologies and dominant fly-scan limitations related to motion errors in standard DCMs. With the HD-DCM, however, this understanding is essential to realize the full potential of the instrument, allowing for high-stability fixed-exit spectroscopy experiments to reach the order of 1 s, i.e. a time reduction of up to two or three orders of magnitude with respect to standard step-scans — which might drastically increase experimental throughput and/or even create new scientific perspectives. To that end, a partly tutorial approach is chosen here, such that the well-known geometrical and physical properties within a DCM scope can be revisited from the necessary mechatronic approach, from where practical limits, tuning tolerances, calibration strategies and advanced beamline integration needs can be derived.

This paper is organized as follows. Firstly, in Section 5.2, the energy selection and fixed-exit concepts of a DCM, both in nominal geometry and including crystal miscut, are used to derive the non-linear characteristics of a DCM and its implications in fly-scans. Then, in Section 5.3, the relevant aspects of APUs regarding their integration with the HD-DCM, particularly focusing in tuning tolerances and fly-scan positioning demands, are developed. Next, Section 5.4 describes the generic and flexible beamline integration architecture developed for the HD-DCM, as well as its operation modes, and the latest communication topology with its APU source, which finally enabled practical high-performance fly-scan spectroscopy. After that, Section 5.5 summarizes some experimental results at EMA, including: 1) stand-still inter-crystal stability measurements via rocking curve edges and knife-edge; 2) fly-scan motion performance evalua-



tion according to the new integration architecture between the HD-DCM and APU; and 3) a long-term scientific high-pressure commissioning experiment via step and fly-scan spectroscopy. Conclusions and further considerations are given in section Section 5.6. Finally, a list of abbreviations is provided for general reference in Section 5.A.

## 5.2 DCM Positioning Problem Formulation

The main geometrical concepts of a DCM are illustrated in Figure 5.1, which is thoroughly explored in the following subsections to first describe a nominal geometry, then elaborate on crystal asymmetry effects, and finally derive the main time-dependent fly-scan aspects, with highly non-linear motion characteristics that pose challenging requirements in terms of actuation, metrology, control and integration.

### 5.2.1 Nominal Case

The energy selection in a DCM results from the Bragg's law of diffraction [32], which describes that only photons of a given fundamental energy  $E$  and its harmonics are diffracted for a given incidence Bragg angle  $\theta_B$ , i.e.

$$2d \sin(\theta_B) = n \frac{hc}{E}, \quad (5.1)$$

where  $d$  is the crystal lattice parameter, also known as d-spacing,  $n$  a positive integer that defines the diffraction order,  $h$  Planck's constant and  $c$  the speed of light. Thus, different energies can be selected by adjusting  $\theta_B$ . Yet, in reality, the Bragg angle and the energy are not discrete values, but narrow distributions defined by intrinsic crystallographic properties, the so-called *Darwin width* [33], such that the monochromatic beam results from a convolution of the diffraction in both crystals.

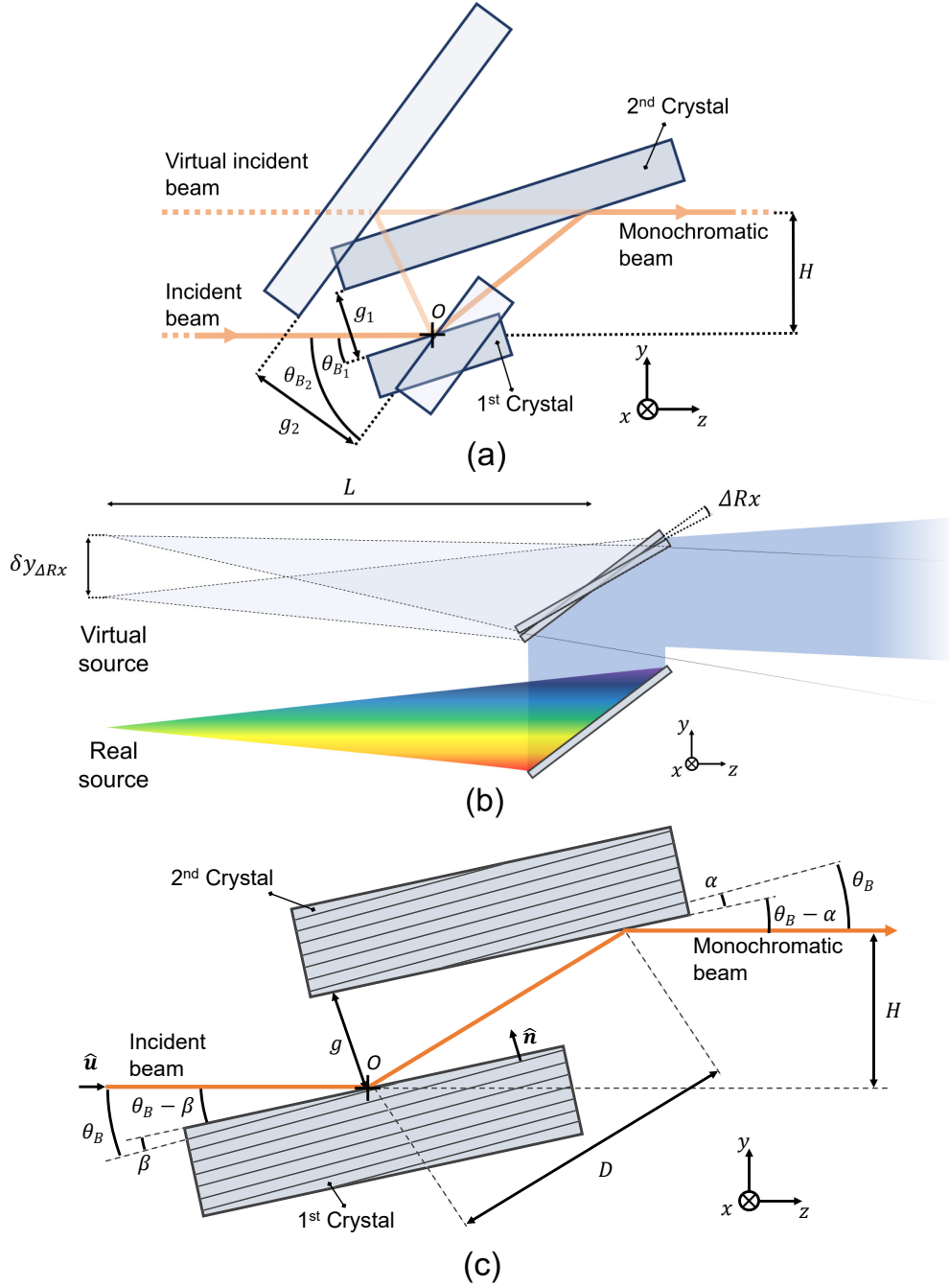
Hence, for two crystals with identical  $d$ , an ideal monochromatic beam, i.e. parallel to the incoming beam and with fixed exit, is nominally achieved by having parallel crystals and adjusting the gap  $g$  between them, such that a constant offset  $H$  is obtained according to

$$g = H \frac{\sin(\theta_B)}{\sin(2\theta_B)} = \frac{H}{2 \cos(\theta_B)}. \quad (5.2)$$

This is illustrated for two arbitrary angles in the side-view schematic of Figure 5.1a, which also follows the specific geometrical architecture chosen for the HD-DCM, namely: with the center of rotation of the crystals set on the surface of the 1<sup>st</sup> crystal; and with a long 2<sup>nd</sup> crystal to comply with the beam walk for the different energies — i.e. preventing a complementary motion stage that otherwise would be needed to longitudinally move a short 2<sup>nd</sup> crystal according to the different downstream positions of the beam after the diffraction in the first crystal.

Partially differentiating Equation (5.1) with respect to  $E$  and  $d$  individually, and applying simple manipulation, it can be shown that

$$\frac{\partial E}{E} = \frac{\partial d}{d} = -\cot(\theta_B) \partial \theta_B, \quad (5.3)$$



**Figure 5.1:** (a) DCM geometry according to the fixed beam impact point at the rotation axis  $O$ , showing Bragg angles  $\theta_{B_1}$  and  $\theta_{B_2}$  and the corresponding gaps  $g_1$  and  $g_2$ , keeping constant offset  $H$  between the monochromatic and incident beams. (b) Effect of DCM inter-crystal parallelism variation  $\Delta Rx$  in the position of the virtual source  $\delta y_{\Delta Rx}$ . (c) DCM geometry including  $\alpha$  and  $\beta$  miscut angles in asymmetric crystals, where  $\hat{u}$  represents the unit vector of the incident beam,  $\hat{n}$  the unit vector normal to the diffraction planes, which is made parallel to the gap  $g$  that defines the offset  $H$ , and  $D$  is the distance travelled by beam between crystals (adapted from [31]).

from where a few aspects can be highlighted. Firstly, it can be seen that the sensitivity to variations in  $\theta_B$  in the energy selection starts from zero at the upper limit of  $\theta_B = \pi/2$  and tends to infinity as the Bragg angle moves towards  $\theta_B = 0$ . Secondly, a given percentage of change in d-spacing is one-to-one related to the percentage of change in energy. Thus, if different d-spacings are found in the two crystals, an ideal energy matching for maximum flux would be related to slightly different  $\theta_B$  in the crystals, such that the monochromatic beam would no longer be exactly parallel to the incoming beam, and the magnitude of the deviation would be variable over the operational energy range.

In practice, even for nominally identical crystals, d-spacing variations may result from crystal imperfections or clamping distortions, but they are most noticeably related to thermal effects. Indeed, d-spacing variations due to thermal expansion, together with local curvature in the crystal lattice, are well-known issues in DCMs (and other types of monochromators) due to the local heat loads deposited in the 1<sup>st</sup> crystal, which may reach hundreds of W/mm<sup>2</sup> [34]. This effect tends to be highly non-linear in energy, since it may depend on: 1) the power variation as function of energy for undulators; 2) the particular crystal heat extraction capacity; and 3) the power load distribution over the beam footprint  $b$ , which can be written as a function of  $\theta_B$  and the beam size  $a$  as

$$b = \frac{a}{\sin(\theta_B)}. \quad (5.4)$$

Clearly, this is in contrast with the concept of an ideal DCM, requiring some kind of compromise or compensation strategy regarding flux, beam parallelism and/or beam position at a given point of interest, as elaborated next.

Figure 5.1b illustrates how a small angle  $\Delta Rx$  between crystals is related to a shift  $\delta y_{\Delta Rx}$  of the virtual source according to

$$\delta y_{\Delta Rx} = 2L\Delta Rx, \quad (5.5)$$

where  $L$  is the distance between the DCM and the source. Then, considering that variations of the virtual source are often proportionally related to shifts of the beam at the sample through the beamline optics, a common requirement is having them small as compared to the source size. With X-ray source sizes of about 5  $\mu\text{m}$  and  $L$  commonly in the order of 30 m for modern beamlines, a typical budget of 10% pushes  $\Delta Rx$  to the range of 10 nrad only. This immediately reveals the stringent dynamical angular stability requirements for state-of-the-art DCMs, as well as suggests that within an experiment there would be virtually no margin for intentional variations of  $\Delta Rx$ , for thermal effects compensation, for instance.

Yet, recalling Equation (5.2), it can be seen that displacements in the virtual source related to  $\Delta Rx$  may be at least partly compensated by energy-dependent beam offset corrections via gap adjustments. Again using partial derivatives,  $\delta y_H$  can be written as

$$\delta y_{H_g} = \partial H_g = \frac{\sin(2\theta_B)}{\sin(\theta_B)} \partial g = 2 \cos(\theta_B) \partial g. \quad (5.6)$$

Moreover, although not practically useful for intentional offset compensation because of its correlation with energy, it should be noticed that the offset is also sensitive to variations in  $\theta_B$  according to

$$\delta y_{H_{\theta_B}} = \partial H_{\theta_B} = -2g \sin(\theta_B) \partial \theta_B = -H \tan(\theta_B) \partial \theta_B. \quad (5.7)$$

Indeed, in addition to compensations with  $\delta y_{H_g}$ , these equations can be directly used for motion error specifications (see also [27]). It can be seen (refer also to Figure 5.2 in Section 5.2.2) that at low energies (high angles) the offset is sensitive to changes in  $\theta_B$  but quite insensitive to the gap  $g$ , and vice-versa. This is unfortunate, since the higher chances of corrections related to thermal effects occur precisely at low energies, where higher power densities occur due to smaller footprints (see Equation (5.4)). Thus, acceptable boundaries may need to be identified for each experiment individually. Ultimately, the target would be to have the effective virtual source variation  $\delta y = \delta y_{\Delta Rx} + \delta y_{H_g} + \delta y_{H_{\theta_B}}$  in an experiment within a fraction of the source size, i.e. typically about  $0.5 \mu\text{m}$ , or the corresponding behavior at the sample position.

The angular boundaries for  $\Delta Rx$  around an ideal energy tuning, which might be already out of perfect parallelism due to d-spacing variations, can be derived as a fraction of the angular bandwidth  $\Delta \theta_{DW}$  of the Darwin width of the crystals. This can be used, for example, to evaluate acceptable flux losses in trying to keep the incoming and outgoing beam parallel despite thermal effects. It turns out that  $\Delta \theta_{DW}$  can be described to a good approximation by a “rearrangement” of Equation (5.3)

$$\Delta \theta_{DW} = \frac{\Delta E}{E} \tan(\theta_B), \quad (5.8)$$

where  $\Delta E/E$  becomes the intrinsic energy resolution of the crystal, a constant dimensionless physical quantity that is typically in the range between  $10^{-3}$  and  $10^{-5}$ . With typical orientations of silicon crystals, such as Si(111) and Si(311), which are used in the HD-DCM,  $\Delta \theta_{DW}$  varies from hundreds of  $\mu\text{rad}$  at large  $\theta_B$  to sub- $\mu\text{rad}$  at small  $\theta_B$  (see also Section 5.5.2.1). As a side note, detuning of crystals also often finds practical use in harmonic rejection strategies.

### 5.2.2 Asymmetric crystals

One last factual aspect to be considered is the inevitable existence of deviations between the actual crystal surface and its diffraction planes. Although many times asymmetric-cut crystals reaching several degrees are intentionally designed for different purposes, including beam compression or expansion (see, for example, [1]), here ideally symmetric-cut crystals with only manufacturing miscut limitations are considered. This is depicted in Figure 5.1c, which is adapted from the discussion recently carried out by [31] on how miscuts affect the gap in DCMs, where it can be seen that, for parallel diffraction planes in the 1<sup>st</sup> and 2<sup>nd</sup> crystals, the distance between their surfaces vary over the propagation of the beam as a function of the small miscut angles  $\beta$  and  $\alpha$ , respectively.

Considering here the gap value to be taken perpendicularly to the diffraction plane of the crystals and aligned with the rotation axis, a derivation equivalent to that described in [31] shows that Equation (5.2) becomes

$$g_m = \frac{H}{\cos(\alpha)} \frac{\sin(\theta_B + \alpha)}{\sin(2\theta_B)}, \quad (5.9)$$

from where it can be seen that, in addition to the gain  $1/\cos(\alpha)$ , which is very close to unity for small  $\alpha$ , the larger deviations from Equation (5.2) occur for small  $\theta_B$ . Then, updating Equation (5.6) and Equation (5.7) yields

$$\begin{aligned} \partial H_{g,m} &= \cos(\alpha) \frac{\sin(2\theta_B)}{\sin(\theta_B + \alpha)} \partial g_m, \text{ and} \\ \partial H_{\theta_B,m} &= -H[\cot(\theta + \alpha) - 2\cot(2\theta_B)]\partial\theta_B. \end{aligned} \quad (5.10)$$

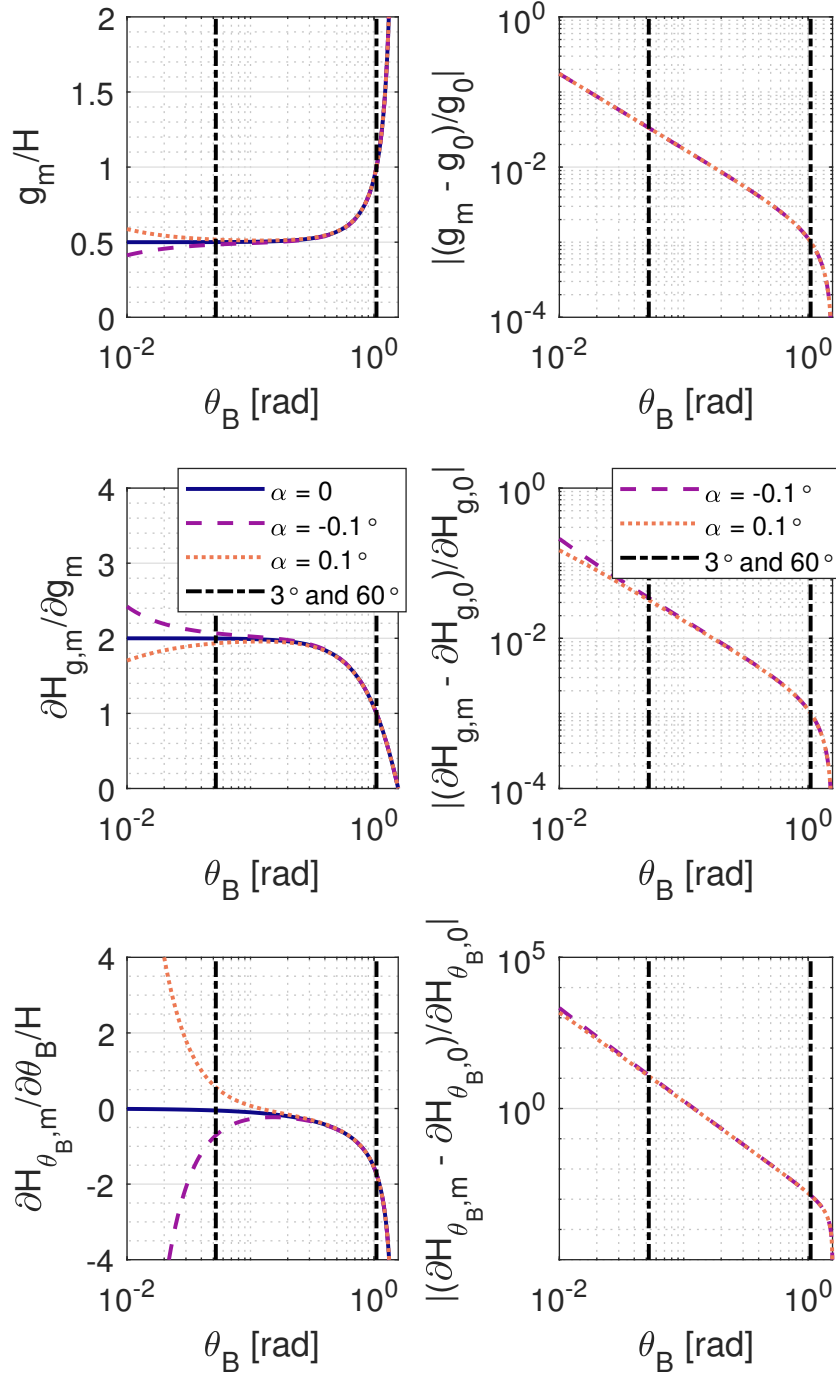
One may notice that  $\beta$  does not appear explicitly in any of these equations. This is because no beam walk is assumed in the 1<sup>st</sup> crystal. In practice, with imperfect alignment of the crystal surface together with the incidence beam on the axis of rotation, parasitic beam walk will occur, resulting in some contribution from  $\beta$  to the gap. Nonetheless, in this geometry, this contribution will be negligible as compared to that of  $\alpha$ .

Figure 5.2 shows plots comparing these quantities for  $\alpha = 0$ , i.e. the nominal case with no miscut, and two miscut cases, with  $\alpha = \pm 0.1^\circ$  to represent reasonable manufacturing limitations. The angular range from  $0.01 \text{ rad} \approx 0.57^\circ$  to  $\pi/2 \text{ rad} = 90^\circ$  is shown in logarithmic scale for clarity, and the angular limits of the HD-DCM are represented by the vertical dash-dotted lines at  $3^\circ$  and  $60^\circ$  for a reference. The dimensionless quantities are shown in the left side, whereas the relative ratio with respect to the nominal case in the right. In the upper plots, it can be seen that the gap no longer tends to an asymptotic value as  $\theta_B$  gets smaller for higher energies. Similarly, the remaining plots demonstrate the increased sensitivity in the offset position to both the gap and  $\theta_B$ , the latter in particular increasing by several orders of magnitude, when miscuts are considered.

This indicates that in reality the gap motion range may need to be larger by a few percent than nominally expected, that sensitivities at low angles may vary by more than one order of magnitude, that calibrations for fixed exit may require more than the simpler trigonometric relation of Equation (5.2) (see also [31]), and that the required velocities and accelerations related to fly-scan are in practice different from nominal ones.

### 5.2.3 Fly-scan

To conclude, the previous equations can be further discussed in terms of their implications in fly-scan spectroscopy. Firstly, for  $\theta_B$ ,  $E$  from Equation (5.1) can be substituted



**Figure 5.2:** Gap  $g$  and offset  $H$  dependences on the Bragg angle  $\theta_B$  for the DCM geometry of Fig. 5.1, including representative miscut manufacturing limitations, i.e. crystals with small asymmetric-cut angles  $\alpha$ . The quantities of interest are shown in the left and the relative ratio with respect to the nominal case in the right. The  $\theta_B$  axis is shown in logarithmic scale to highlight the contribution of the miscut at lower angles (higher energies). The HD-DCM angular limits are represented by the vertical dash-dotted lines at  $3^\circ$  and  $60^\circ$ .

in Equation (5.3), and the result taken with respect to time, such that

$$\begin{aligned} \frac{\partial E}{\partial t} &= -\frac{nhc \cos(\theta_B)}{2d \sin^2(\theta_B)} \frac{\partial \theta_B}{\partial t} \text{ or} \\ \frac{\partial \theta_B}{\partial t} &= -\frac{2d \sin^2(\theta_B)}{nhc \cos(\theta_B)} \frac{\partial E}{\partial t} = -\eta_0(\theta_B) \frac{2d}{nhc} \frac{\partial E}{\partial t}. \end{aligned} \quad (5.11)$$

Then, for the gap, Equation (5.9) can be derived for a constant offset with respect to time, yielding

$$\begin{aligned} \frac{\partial g}{\partial t} &= \eta_1(\theta_B) \frac{H}{\cos(\alpha)} \frac{\partial \theta_B}{\partial t}, \text{ where} \\ \eta_1(\theta_B) &= \frac{\cos(\theta_B + \alpha) \sin(2\theta_B) - 2 \sin(\theta_B + \alpha) \cos(2\theta_B)}{\sin^2(2\theta_B)}, \end{aligned} \quad (5.12)$$

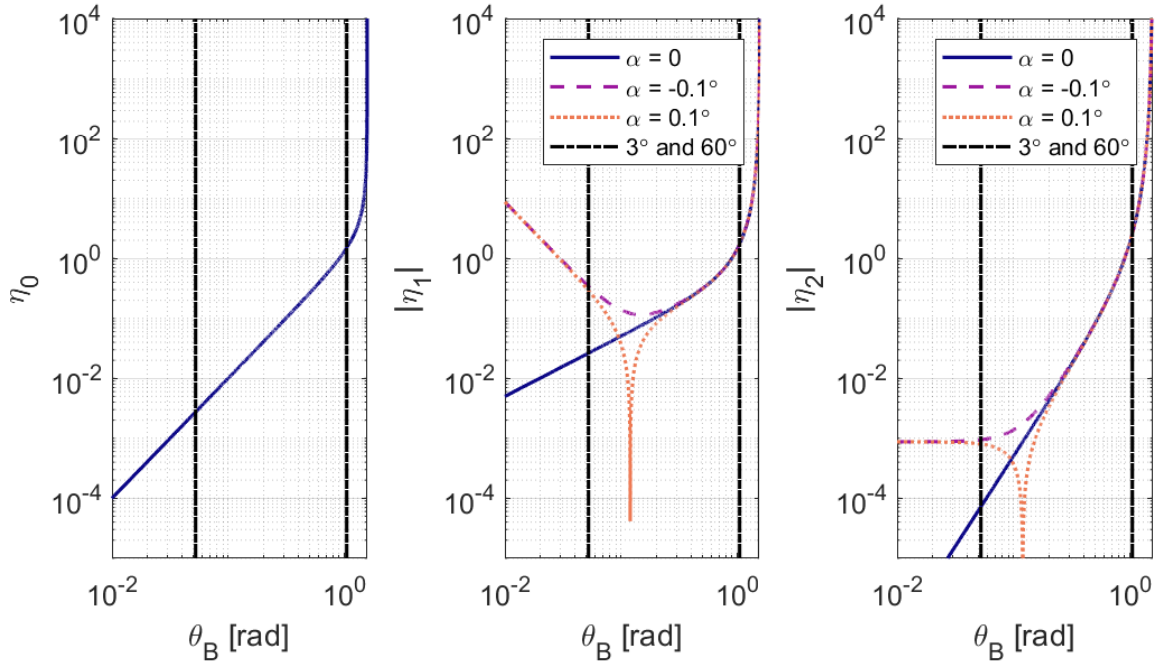
which, in terms of the energy rate, using Equation (5.11), becomes

$$\begin{aligned} \frac{\partial g}{\partial t} &= -\eta_2(\theta_B) \frac{2d}{nhc \cos(\alpha)} \frac{\partial E}{\partial t}, \text{ where} \\ \eta_2(\theta_B) &= \frac{\cos(\theta_B + \alpha) \sin(2\theta_B) - 2 \sin(\theta_B + \alpha) \cos(2\theta_B)}{4 \cos^3(\theta_B)}. \end{aligned} \quad (5.13)$$

Naturally, here  $\theta_B$  in the trigonometric arguments are actually related to  $E$  via Equation (5.1), but replacing it with the inverse trigonometric function does not add to clarity.

The functions  $\eta_0$ ,  $\eta_1$  and  $\eta_2$  are introduced in Equation (5.11), Equation (5.12) and Equation (5.13) to simplify the notation of these equations by capturing the complex trigonometric dependences on  $\theta_B$ . Indeed, from Figure 5.3, the strong non-linear relationships in following desired energy variation rates in fly-scans become evident. From  $\eta_0$ , the exponential increase in the required Bragg velocity for higher angles (lower energies) is clearly visible, changing by nearly three orders of magnitude within the operational range of the HD-DCM. From  $\eta_1$  and  $\eta_2$ , although with different slopes, similar exponential behavior occur for the gap with the nominal geometry with  $\alpha = 0$ . With miscuts, however, deviations occur in the low-angle (high-energy) range, as also seen in Figure 5.2. In particular, because  $\eta_2$  — representing the variation of  $g$  with respect to  $E$  — is the product between  $\eta_0$  and  $\eta_1$ , it actually asymptotically converges to a small constant value, either for positive or negative  $\alpha$ . Hence, differences of three to four orders of magnitude occur for the gap velocity for a given energy variation rate within the operational range of the HD-DCM.

For a control-based instrument as the HD-DCM, these aspects place demanding specifications on metrology and acquisition hardware, since very high resolution and low noise is required for the lower angular (higher energy) range, whereas high rates are necessary at opposite limit. For example, while the angular resolution in the Bragg angle quadrature encoder is 50 nrad (or about  $3 \mu^\circ$ ) for high angular resolution and small control errors, from Equation (5.11) it can be found that for an energy scan of



**Figure 5.3:** Trigonometric functions related to the variation of: the Bragg angle  $\theta_B$  with respect to energy  $E$ , as  $\eta_0$ ; and the gap  $g$  with respect to  $\theta_B$  and  $E$ , as  $\eta_1$  and  $\eta_2$  (shown in absolute values for readability in the logarithmic scale), respectively. They follow Equation (5.11), Equation (5.12) and Equation (5.13) for the DCM geometry of Figure 5.1, including representative miscut manufacturing limitations, i.e. crystals with small asymmetric-cut angles  $\alpha$ . The HD-DCM angular limits are represented by the vertical dash-dotted lines at  $3^\circ$  and  $60^\circ$ .

1 keV/s the Si(111) crystal angular speed requirements would be around  $0.1^\circ/\text{s}$  at the high energy range and as much as  $40^\circ/\text{s}$  at the low energy limit. In the latter case, the counting rates would have to be higher than the current electronics capacity of 10 MHz. Similarly for the gap, with a resolution of 0.1 nm from the quadrature laser interferometers for the nanometer-level control performance, an equivalent energy rate scan speed with Si(111) crystals without a miscut would translate via Equation (5.13) to about  $0.8 \mu\text{m}/\text{s}$  and  $20 \text{ mm}/\text{s}$  at the high and low energy limits, respectively. In the latter case, counting rates would need to reach 200 MHz.

Moreover, reaching such high speeds in a reasonable traveling range may be associated with significant acceleration levels, since the main rotation mass moment of inertia and the gap stage mass are close to, respectively,  $14 \text{ kg m}^2$  and  $6 \text{ kg}$  (see also [28]). Indeed, taking the derivatives of Equation (5.11), Equation (5.12) and Equation (5.13) with respect to time, the acceleration levels might span over even higher ranges than those of velocity, stressing the demands on the actuators, amplifiers and converters, again with very high resolution and low noise for the lower angular range, but higher forces and torques at the opposite limit. Furthermore, even considering the control-based and disturbance-oriented design of the HD-DCM, the higher speeds and accelerations at higher angles inevitably increase mechanical and setpoint-related disturbances.



The performance of the HD-DCM under these challenges and the ongoing research are discussed via results in Section 5.5, but, before that, the following section elaborates a corresponding analysis for an APU source, showing how it impacts energy fly-scans with the HD-DCM.

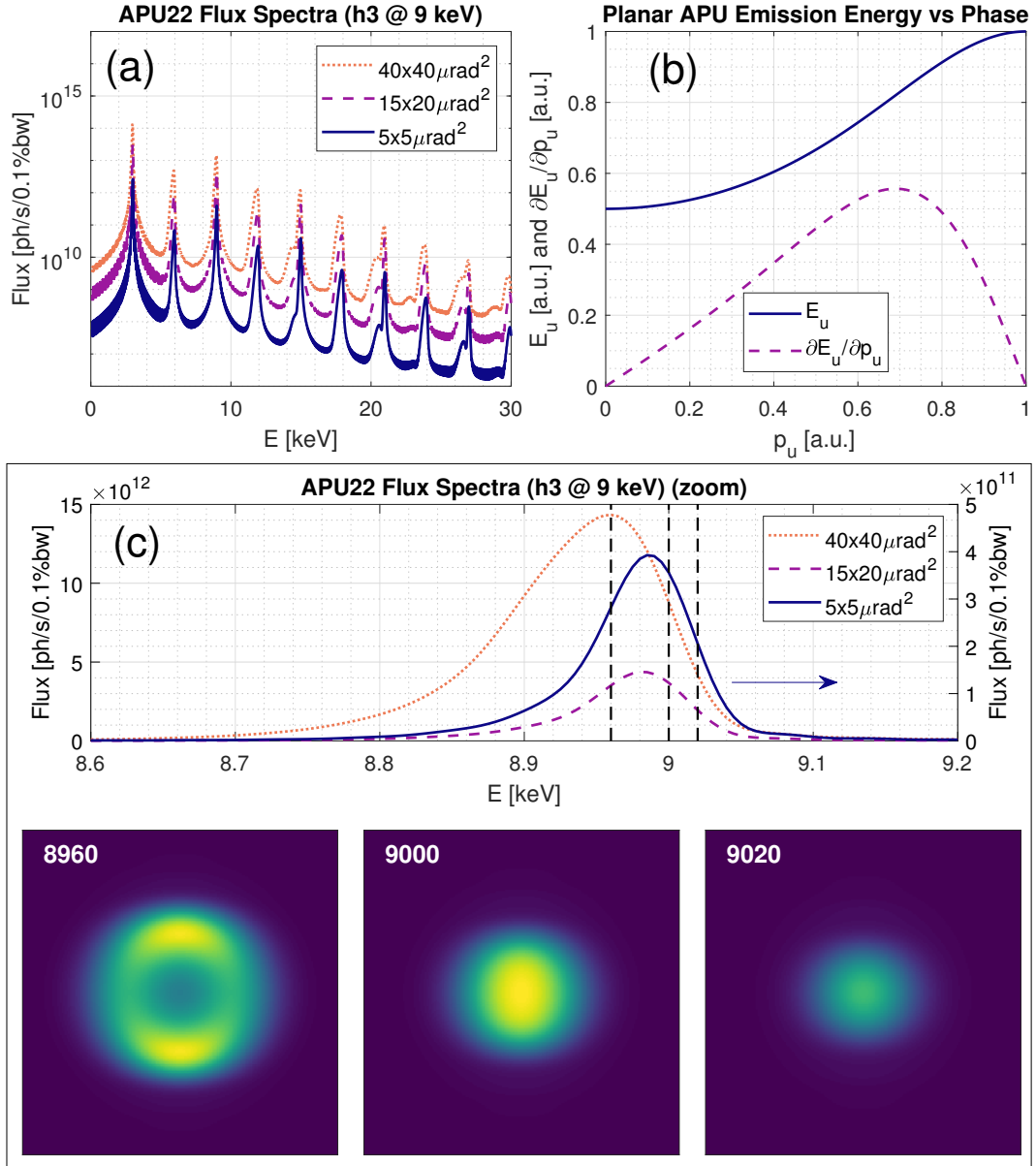
### 5.3 Undulator Properties and Positioning Analyses

So far, Sirius beamlines have been designed with 2 types of sources, namely: bending magnets, from the 3.2T permanent-magnet dipoles that are part of its five-bend achromat lattice (5BA) [15]; and undulators. The first provides a continuous and broad-band spectrum (with critical energy at 19 keV), that can be used in a number of beamlines, for different characterization methods, and is transparent with respect to a DCM operation (aside from power density variations due to the footprint dependence on  $\theta_B$ , as seen in Equation (5.4)). The latter, on the other hand, has an adjustable photon emission spectrum, justifying the specification of a particular device for each beamline individually, depending on the scientific research area, and requiring energy tuning with the monochromator. Therefore, key undulator characteristics and positioning tolerances for energy fly-scan with the HD-DCM at Sirius are investigated next. The analyses will be restricted to the case of APUs, which is the first type to be integrated with the HD-DCMs at Sirius beamlines, but, naturally, equivalent analyses can be done for different types of undulators.

#### 5.3.1 Undulator Emission Properties

Indeed, as illustrated in Figure 5.4a, the flux in an undulator spectrum is characterized by relatively narrow emission bands, which are harmonics of a fundamental energy and depend on physical constants and parameters both of the storage ring and of the particular device. Then, by online adjustment of the so-called undulator deflection parameter  $K_u$  — that is a function of its magnetic period  $\lambda_u$  and magnetic field  $B_u$ , which may have components in both axes transversal to the propagation of the electron beam —, the energy spectrum and possibly the polarization of the photon beam can be selected accordingly by the user. The plot covers the first nine harmonics of the APU22 undulator that is currently installed at both EMA and MANACÁ beamlines, in an arbitrary configuration with the 3<sup>rd</sup> harmonic tuned to 9 keV for a given  $K_u$ . It clearly illustrates the gradual reduction in flux over several orders of magnitude as the harmonic order increases towards higher energies, and also that the peak energy width and the flux depend on the angular acceptance window at the beamline.

In APUs,  $K_u$  can be varied from a maximum value to virtually zero by relatively shifting one of its magnetic cassettes with respect to the other, defining a variable generally referred to as the undulator phase  $p_u$ , which has a typical stroke in the order of 10 mm. Without diving into the development of the equations and into the physical parameters, which can be found in details in [35], it can be shown that a emission flux



**Figure 5.4:** (a) Example of the emission flux spectra of the planar adjustable-phase undulators APU22 installed at EMA and MANACÁ at Sirius, with the 3<sup>rd</sup> harmonic tuned at 9 keV. The first nine harmonics are shown for a given deflection parameter  $K_u$  and three different beamline angular acceptance windows ( $v \times h$ ) illustrate its effect in peak energy width and flux. (b) Arbitrarily scaled energy value  $E_u$  for a given emission harmonic  $n_u$  and its derivative with respect to phase, for a normalized undulator phase  $p_u$  in a planar APU, according to Equation (5.14). (c) Top: zoomed spectral flux plot of the example emission of (a), highlighting the broadening of the peak and its shift to lower energies for larger angular acceptances; bottom: “slitless” wave-propagation simulations showing the beam profile for perfectly monochromatic energies at and around the 9 keV resonance (black vertical dashed lines in the plot).

peak for a given energy  $E_u$  can be nominally written in terms of  $p_u$  as

$$E_u = \frac{n_u c_1}{c_2 \cos^2[c_3(p_u + c_4)] + c_5}, \quad (5.14)$$

where  $n_u$  is the emission harmonic and  $c_i$ , with  $i = 1, \dots, 5$ , are the constants resulting from physical constants and parameters of the storage ring and of the device. Thus, the peak emission energy dependence on  $p_u$  for such an APU has a generic shape as depicted for normalized phase values in Figure 5.4b, i.e. ranging from a minimum to a maximum value for each harmonic. In most cases, the harmonics overlap, meaning that the same energy may be reached in two or more harmonics/phases, only with different fluxes (see also Figure 5.5 in Section 5.3.2). This is especially useful for energy scans realized around the overlapping regions, such that full scans can be executed without commanding the undulator over discontinuous trajectories, which would be actually impractical in fly-scans. In other cases, energy gaps may exist, meaning that peak emissions do not occur for a given energy range with the particular combination of parameters and would not be available to the user, being a design choice.

Consequently, for DCMs operating at undulator beamlines,  $\theta_B$  must be tuned with  $p_u$  for the desired output energy. This aspect is illustrated in Figure 5.4c. Firstly, a zoomed spectral flux plot of the emission around the 3<sup>rd</sup> harmonic at 9 keV is shown to illustrate in more details in linear scale (and with the smaller acceptance in the right axis for readability) the broadening of the peak and its shift towards lower energies as the angular acceptance is increased for higher fluxes. Then, wave-propagation simulations using the *Synchrotron Radiation Workshop* (SRW, [36]) show the beam profile for perfectly monochromatic energies at and around the 9 keV resonances without any slit acceptance restrictions, from where it can be seen that, if the DCM and the APU are detuned beyond given energy-dependent margins, either the downstream flux is rapidly reduced to one side, or the ideal Gaussian beam profile is distorted to ring-like structures to the other.

Therefore, for energy fly-scans at undulator beamlines the traditional stand-still tuning between  $\theta_B$  and  $p_u$  becomes dependent on the motion capabilities of the undulator and synchronism as well. As done in the previous sections, Equation (5.14) can also be derived as a function of time, resulting in

$$\frac{\partial E_u}{\partial t} = \frac{n_u c_1 c_2 c_3 \sin[2c_3(p_u + c_4)]}{\{c_2 \cos^2[c_3(p_u + c_4)] + c_5\}^2} \frac{\partial p_u}{\partial t}, \quad (5.15)$$

which can be used in Equation (5.11) and Equation (5.13) to find the required motion correlation between all the axes of interest for an energy scan with an APU and a DCM. This correlation between the variation of  $E_u$  and  $p_u$  is also qualitatively shown in Figure 5.4b, from where both the sensitivity in the emission spectrum due to motion errors in the undulator, for instance, as well as the effectiveness in realizing scans can be observed.

For a desired energy variation rate, large speeds would be required from the undulator motion at the phase limits. In addition, as for the DCM, linear energy scans

require non-linear undulator trajectories, via an exotic function as compared to industrial standards, which may not be directly available for undulator controllers. So, it becomes clear that ideal and “simple” user settings for constant energy scanning rates, in practice must be translated according to highly non-linear functions, often tending either to zero, or infinity, as shown next for the APU22 at Sirius.

Therefore, particularly considering fly-scans, the integrated beamline control architecture requires additional attention, actuator and sensor limits must be carefully analyzed, and synchronism delays and motion-related disturbances obtain central roles. In the following section, the integration of the HD-DCM at Sirius beamlines is presented.

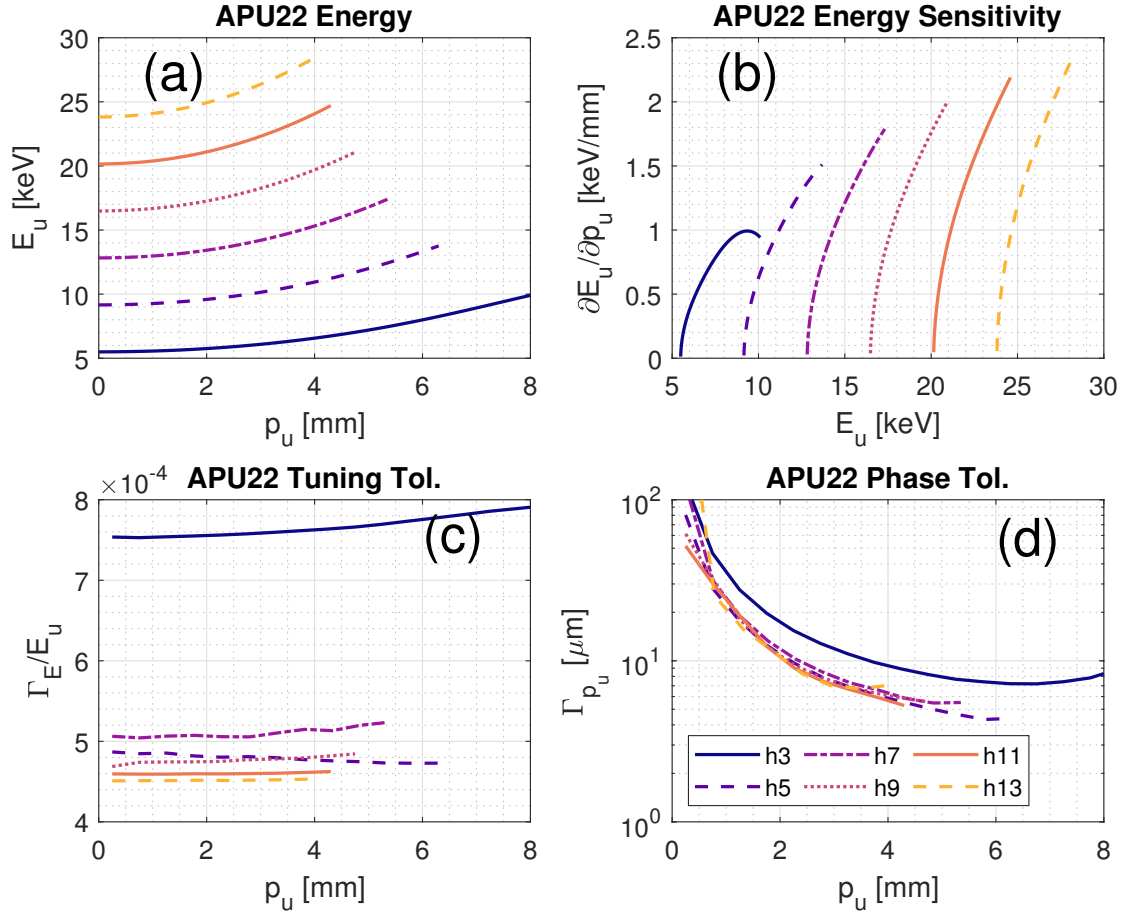
### 5.3.2 The APU22 Source

The two operational units of the HD-DCM are at the EMA and the MANACÁ beamlines at Sirius, which currently operate in a commissioning configuration with an APU22 undulator source by Kyma:  $\lambda_u = 22$  mm, length of 1.12 m and  $K_{u,max} = 1.44$ . By 2024, final configurations are expected, with two of the APU22 units in series for MANACÁ, and a new IVU18.5 (in-vacuum undulator) for EMA:  $\lambda_u = 18.5$  mm, length of 2 m and  $K_{u,max} = 2.1$ .

Hence, in this early stage both beamlines are working with lower fluxes, not only because the storage ring current is still limited to 100 mA, while expected to reach 350 mA, but also because of the shorter undulator. Besides that, EMA is working with a more limited energy range, due to an existing energy gap between 3.7 and 5.7 keV, occurring between h1 and h3, i.e. the 1<sup>st</sup> and 3<sup>rd</sup> harmonics (once even harmonics do not provide adequate sources) of the APU22. Moreover, due to a initial perspective of short-time replacement (or upgrade) of the sources, only basic features have been originally specified for the APU22 Beckhoff’s control system. This has eventually posed integration limitations with respect to the HD-DCM in the early operation phase, motivating the development of alternative solutions, as discussed in the next sections.

Following the generic shape anticipated in Figure 5.4b, Figure 5.5a shows the harmonic emission peaks between h3 and h13 as a function of phase, thus covering the energy range that has been explored so far at EMA and MANACÁ. Indeed, the useful range of h1 by the HD-DCM, i.e. between 2.3 and 3.7 keV, has a sharp flux reduction in this range (not shown) and would drastically suffer from attenuation from air and windows in the setups currently available at both beamlines. Higher energies, in turn, have prohibitively low fluxes with the APU22 and anyhow face reflectivity limitations from downstream mirrors. In the plot, the harmonics are truncated after an arbitrary overlap of 1 keV due to flux gains.

Then, Figure 5.5b illustrates the variation correlation between the energy and the phase, but as a function of the energy for the various harmonics, instead of a function of the phase as in Figure 5.4b. This can be directly used as a guide to evaluate how desired rates in keV/s are translated to mm/s in the undulator. For example, energy rates of 1 keV/s can be achieved with reasonable phase speeds in the range of 1 mm/s



**Figure 5.5:** APU22 characteristics for the different harmonics in the energy range between 5.7 and 28 keV at the EMA and the MANACÁ beamlines at Sirius: (a) peak emission energy  $E_u$  as a function of the phase  $p_u$ ; (b) variation correlation between  $E_u$  and  $p_u$  as a function of  $E_u$ ; (c) energy tuning tolerance ratio as a function of  $p_u$ ; and (d) phase error tolerance  $\Gamma_{p_u}$  as a function of  $p_u$ .

depending on the desired energy range, whereas it would require “infinite” speed around energies close to  $p_u = 0$ . Before fast orbit feedback (FOFB) and feedforward systems, that should be capable of compensating possibly higher orbit distortions caused by the fast motion of the undulators, become available at Sirius’ storage ring, an upper limit velocity of 3 mm/s has been specified to the APU22. Yet, due to the current flux limitations, at EMA the APU22 has been operated in practice well below 1 mm/s in fly-scans, reaching only a few tens of eV/s in this initial stage. Hence, ultimate fly-scan spectroscopy velocities are expected to be achieved later, with the final sources and with the storage ring systems fully implemented.

Next, to define synchronism and motion performance requirements for the APU22, a tuning tolerance method using wave-propagation simulations as those in Figure 5.4c has been developed. It consists of analyzing a finite number of energies in each harmonic, and, for each of them, mapping an energy tuning tolerance  $\Gamma_E$  corresponding to a variation of 10% of the full width at half maximum (FWHM) of the beam with respect

to the ideal “Gaussian-like” profile. The ratio between the tolerances and the central (nominal) energies are shown in Figure 5.5c, in which it can be seen that there is a higher forgiveness, around 0.075%, in h3 (and even higher for h1, around 0.18%, not shown), but similar ratios for h5 to h13, around 0.045% to 0.05%. This is because h1 and h3 are related to lower energies in which the X-ray source size and divergence are larger due to diffraction limits (not shown), whereas beyond h5 these parameters reach asymptotic values. Occasional residual inaccuracies in the estimation of  $\Gamma_E$  seem insufficient to hinder any conclusions.

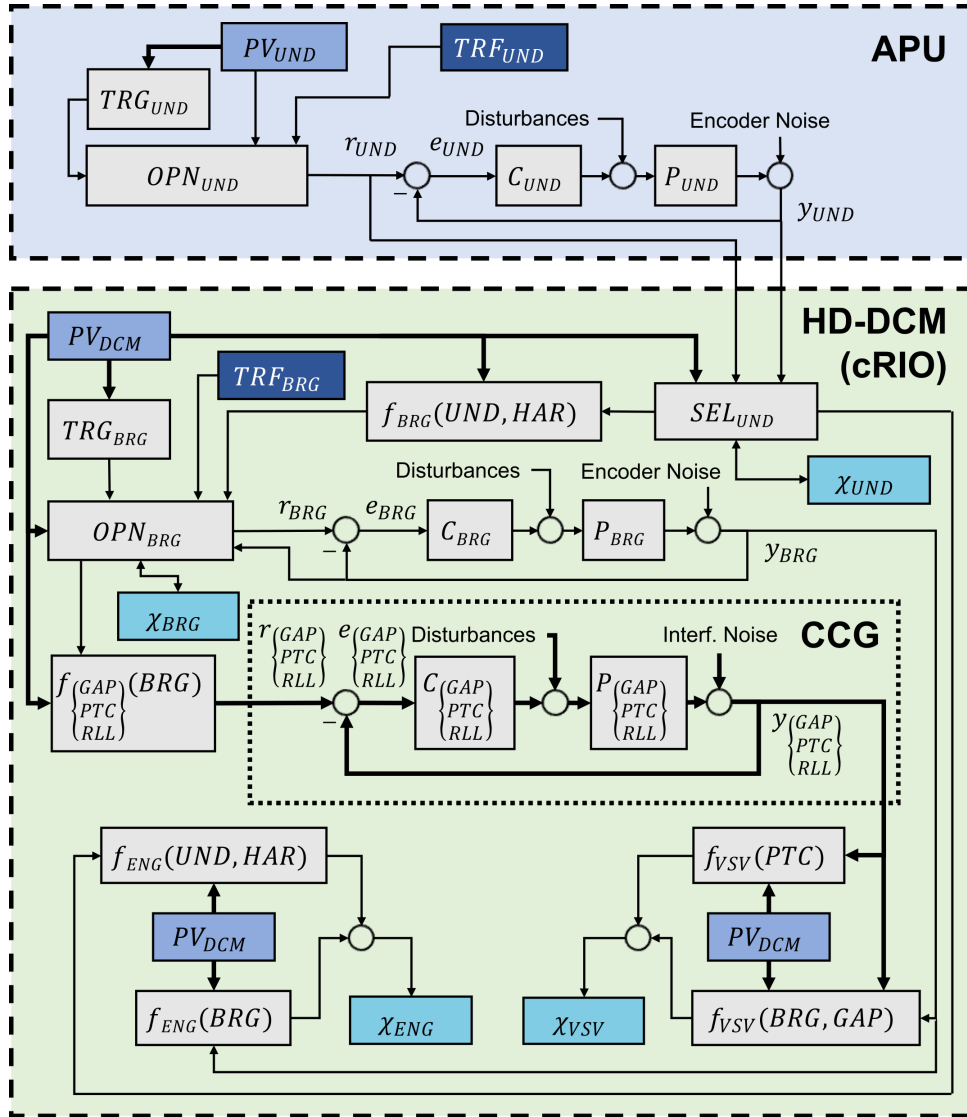
Finally, the dependence from Figure 5.5b can be combined with the tolerances from Figure 5.5c to determine phase tolerances  $\Gamma_{p_u}$  for the undulators. This is shown in Figure 5.5d, from where it can be seen that at the lower phase limit ( $< 2$  mm), related to higher velocities for given energy rates, the error tolerances exceed 10  $\mu\text{m}$ , whereas only 4 to 7  $\mu\text{m}$  are required as the most stringent values. At this point, it is worth noting that, using Equation (5.3), the same energy tolerances from Figure 5.5c can be taken to derive angular tolerances for the Bragg angle with respect to an ideal energy setpoint. It turns out that, within this energy range, these calculated tolerances remain above 30 and 60  $\mu\text{rad}$  for Si(111) and Si(311), respectively, which are much larger than the typical motion errors observed in the HD-DCM, as shown in Section 5.5.3.1. Indeed, the obtained energy tolerances varied between 4 and 16 eV, whereas spectroscopy resolutions in this energy range generally aim at sub-eV targets, such that the Bragg angle performance should be truly at least one order of magnitude better than that.

Consequently, in practice the mapped tolerance budget does remain entirely for the undulator, but must include metrology accuracy, motion control errors, and delay effects, which might possibly lead to integration-related limitations beyond the performance of each instrument individually. This has been the case with the APU22 until very recently, as elaborated in [26] and [29]. And it highlights the need of a holistic approach in beamline instrumentation for increased performances and efficiency, as discussed in the following sections.

## 5.4 HD-DCM Integration and Operation Schemes

Once the essential positioning characteristics for the HD-DCM and the APU22 have been explained — including higher-level motion parameters for fly-scan spectroscopy that are now for the first time enabled with the HD-DCM —, this section summarizes how the HD-DCM can be effectively used at Sirius beamlines, including its integration schemes and operation modes. Sufficient details, also updated with respect to [26], are given to clarify the several operational possibilities within more complex integration demands, leading to different hardware and software complexity requirements.

The HD-DCM application within a flexible integration scheme with a generic APU source is illustrated in the simplified control implementation diagram of Figure 5.6. Integration with the well-known EPICS control system [37], via the so-called *process variables* (PVs) for high-level user operation, is represented in the diagram by the



**Figure 5.6:** Simplified control implementation diagram for the integration of the HD-DCM running on NI's cRIO, with four control loops for the Bragg angle (BRG) and crystal cage (CCG, with GAP, PTC and RLL) position control, and an APU source running on a third-party controller, with one control loop for the phase. Reference  $r$  and metrology  $y$  signals are represented, together with controllers  $C$ , plants  $P$ , and functions  $f$  for coordinated motion. As detailed in the text, motion setpoint updating depends on structures for input selection (SEL) and operation modes (OPN), including trajectory generation on demand (TRG), stored trajectory files (TRF) and motion estimators ( $\chi_{UND}$  and  $\chi_{BRG}$ ). Complementary real-time performance estimators can be computed for energy tuning ( $\chi_{ENG}$ ) and virtual source vertical position ( $\chi_{VSV}$ ). Integration with EPICS is represented by the process variables (PVs). Colors are given to differentiate the APU from the HD-DCM domains, and the control blocks from data blocks (related trajectories or PVs), and from the estimators.

abstracted multidimensional structures  $PV_{UND}$  and  $PV_{DCM}$ , for variables related to the undulator and the HD-DCM, respectively.

The APU is represented by a generic single control loop UND for the phase (see Figure 5.6), typically consisting of a servo-motor and a linear encoder in a third-party controller, with sample rates in the range of 1 kHz. Evidently, APUs with different embodiment or different types of undulators can be correspondingly adapted. The HD-DCM, in turn, can be defined by four main control loops (see Figure 5.6), namely: Bragg (BRG), gap (GAP), pitch (PTC) and roll (RLL), running on NI's CompactRIO (cRIO) hardware at 20 kHz sample rate (see also [26] and [28]), as detailed next.

#### 5.4.1 The HD-DCM Control Architecture

BRG is responsible for controlling the Bragg angle  $\theta_B$  in the operational range from  $3^\circ$  to  $60^\circ$ , which is done via an in-vacuum direct-drive rotary stage with a rotary encoder, in a bandwidth of 20 Hz. Then, GAP, PTC and RLL, in turn, are part of the so-called *crystal cage* (CCG), responsible for controlling the position of the 2<sup>nd</sup> crystal with respect to the 1<sup>st</sup> crystal with nanometer-level performance, which is done via voice-coil actuators and laser interferometers, in bandwidths between 150 and 250 Hz. GAP controls the parameter  $g$  from Section 5.2, whereas PTC and RLL, referring to the pitch and roll angles, control the inter-crystal parallelism. PTC is related to the crystals DW tuning and to vertical shifts in the virtual source via  $\Delta Rx$  in Equation (5.5), with the strict target of 10 nrad RMS (1 Hz to 2.5 kHz). RLL is related to lateral shifts in the virtual source, but with dependence on  $\theta_B$  and much lower sensitivity than PTC, leading, for instance, to a positioning stability target of 90 nrad RMS. The complete set of specifications of the HD-DCM can be found in [27].

Due to a careful mechatronic architecture, in practice the originally *multiple-input-multiple-output* (MIMO) system can be statically decoupled, so that the loops may be addressed independently and simpler *single-input-single-output* (SISO) controller design techniques can be used (see also [28]). Thus, in Figure 5.6 the individual plants and controllers are represented as  $P_i$  and  $C_i$ , respectively, where  $i$  refers to UND, BRG, GAP, PTC and RLL. Each loop follows a reference  $r_i$  and provides a measurement  $y_i$ , being subject to actuator and plant disturbances, as well as measurement noise from sensors (encoders and laser interferometers). Measured error signals are defined as  $e_i = r_i - y_i$ .

The reference signals for the CCG loops are defined as functions  $f_{\text{GAP}}$ ,  $f_{\text{PTC}}$  and  $f_{\text{RLL}}$  of  $\theta_B$ , which can follow nominal correlations, according to Equation (5.2) or Equation (5.9) for the gap, for instance, or result from beam-based calibrations (see [25]), that can be updated by the user via  $PV_{\text{DCM}}$ . Regarding the control-based architecture and fly-scan demands, it is useful to have these relations as continuous smooth functions, rather than arbitrary discrete look-up tables that might be used in step-scan applications, such that discontinuities are prevented and high-frequency content is minimized in the reference signals. So far, eighth order polynomials have been used as a standard.

Furthermore, because the measurement signal  $y_{\text{BRG}}$  includes the disturbances in the BRG loop and electronic noise contamination that would deteriorate the individ-



ual performances of the CCG loops, it has been found that under normal conditions the control error  $e_{\text{BRG}}$  is sufficiently small so that the reference signal  $r_{\text{BRG}}$  may be preferable as an indicator of  $\theta_B$ . Although perhaps not an usual control strategy in leading-following systems, it benefits from favorable tolerances in the HD-DCM and its reliability. Indeed, PTC and RLL have only (at most) a small and smooth dependence on BRG, resulting essentially from fine adjustment for parallelism and fixed-exit calibrations (see [25]), with virtually no effect within small  $\theta_B$  mismatching.

The GAP, in turn, as specified in [27], can afford as much as 300 nm of mismatch in the worst case scenario before its influence in the beam offset exceeds 10% of the beam size (see also Equation (5.6) and Equation (5.10)). Then, using Equation (5.2) — or, equivalently, Equation (5.9) for miscuts —, the derivative of the gap with respect to  $\theta_B$  can be written as  $dg/d\theta_B = -(H/2)(\sin(\theta_B)/\cos^2(\theta_B))$ . Hence, with  $H = 18$  mm and assuming an ideal gap motion, the corresponding BRG tracking mismatch, again for 10% of the beam sizes, should be bound to  $|e_{\text{BRG}}| \ll 10$   $\mu\text{rad}$  in the  $3^\circ$  to  $60^\circ$  working range. As in the case of the energy tuning tolerances, this is one order of magnitude larger than the tracking errors that have been observed so far in fly-scans with the HD-DCM (see Section 5.5.3.1). This means that the loops can be connected only to necessary extent, allowing for better individual performances, particularly of the PTC — which is the most sensitive degree of freedom, operating close to the specification boundaries.

A more elaborate alternative — that, however, has not proven practical need until now — to prevent sensor noise, but still take the system response into account, consists in using an estimator  $\chi_{\text{BRG}}$  of the closed-loop response via the complementary sensitivity function (T) of the BRG loop with  $\chi_{\text{BRG}} = T_{\text{BRG}} \cdot r_{\text{BRG}}$ . Whichever the case, the desired reference selection for the the CCG loops may be done in the operation mode block  $\text{OPN}_{\text{BRG}}$  via EPICS with  $\text{PV}_{\text{DCM}}$ , which is also used to define the origin of the reference  $r_{\text{BRG}}$  itself.

Indeed, it is then the definition of how  $r_{\text{BRG}}$  is updated in the HD-DCM control loop that eventually defines how the instrument can be used at the beamline. In that sense, within the architecture in Figure 5.6, three *operation modes* can be identified such that: 1) a trajectory is asynchronously calculated for  $r_{\text{BRG}}$  internally in the cRIO just before motion, being independent from other instruments; 2) a real-time conversion for  $r_{\text{BRG}}$  is made from a leading signal; and 3) a known trajectory for  $r_{\text{BRG}}$  is previously stored in a file in the cRIO and executed after a trigger for synchronism. As these mode are related to different experimental capabilities and implementation complexity concerning other instruments at the beamline, they are separately discussed in the following subsection (see also [26] for a preliminary discussion).

### 5.4.2 Operation Modes

The first operation mode is the *stand-alone* mode, in which the HD-DCM can be operated by the user in a simple way at high level via  $\text{PV}_{\text{DCM}}$ . In this case, a trajectory generator block  $\text{TRG}_{\text{BRG}}$  in cRIO uses user-defined parameters and default trajectory

options to generate a suitable trajectory on demand and, then, triggers  $r_{\text{BRG}}$  to be updated accordingly at the 20 kHz sample rate. This is a basic mode for fixed-energy or step-scan experiments, and the undulator phase must be independently adjusted by the user via  $\text{PV}_{\text{UND}}$  for the appropriate energy tuning. Although not optimum in terms of timing, this can often be handled via standard step-scan beamline pieces of software. Moreover, this would also be a straightforward option for energy fly-scans at bending-magnet beamlines, in which the source spectrum is continuous.

Next, in the *follower* mode,  $r_{\text{BRG}}$  is updated in real time as a function of a leading input signal, which might be any external reference, but here, naturally, consists of the undulator phase. Thus,  $f_{\text{BRG}}$  is defined as a function of the undulator phase and the desired harmonic (HAR), which is selected by the user as part of  $\text{PV}_{\text{DCM}}$ . It can be nominally defined via Equation (5.1) and Equation (5.14), but, in practice, due to the relatively small tuning tolerances (see Section 5.3.2), requires beam-based calibration, as discussed in [25]. Hence, by controlling the undulator alone via  $\text{PV}_{\text{UND}}$  with reasonable motion setpoints, the user should be able to obtain a well-tuned fixed-exit monochromatic beam over the whole energy range, allowing the fly-scan spectroscopy potential to be explored at undulator beamlines. Integrating the HD-DCM with different types of undulator would basically require only adapting  $f_{\text{BRG}}$  to different parameters.

Still about the *follower* mode — in a similar fashion to the reference choice of the CCG loops —, the phase signal can be also considered from three options that are managed via the selection block  $\text{SEL}_{\text{UND}}$ , according to user settings in EPICS as part of  $\text{PV}_{\text{DCM}}$ . They are: the measurement signal  $y_{\text{UND}}$ ; the reference  $r_{\text{UND}}$  from the undulator controller; or a position estimator  $\chi_{\text{UND}}$  of the closed-loop response via the complementary sensitivity function with  $\chi_{\text{UND}} = T_{\text{UND}} \cdot r_{\text{UND}}$  (as mentioned for the BRG loop). In the first, which was the original option available for the APU22, the encoder signal  $y_{\text{UND}}$  is directly derived to the cRIO — with the reading rates typically in the order of MHz for a quadrature signal, for example, being then internally downsampled to 20 kHz. However, as in the BRG case and the CCG loops, this signal includes disturbances from the UND loop and electronic noise that are propagated to  $r_{\text{BRG}}$ . Thus, some filtering inside  $\text{SEL}_{\text{UND}}$  was found to be essential already at early implementation phase. Nevertheless, as described in [25] and [29], even with the additional filters the performance degradation to the HD-DCM loops ended up being unacceptably large for the desired fly-scan spectroscopy quality (with pitch stability exceeding 30 nrad RMS and correspondingly large Bragg control errors, for instance), such that further alternatives needed to be developed, as explained below.

Indeed, the two remaining options for the *follower* mode are based on the reference signal as the undulator phase indicator. Here, again connecting the loops only to the necessary extent, the tuning tolerances in the range of a few microns between the HD-DCM and the APU (see Figure 5.5d) can be explored to leave out disturbances and noise from the undulator system, which is typically only a micrometer-level-performance machine. Naturally, both cases require a minimum level of relia-

bility/repeatability in the undulator, which must be proven by each machine, and is demonstrated for the APU22 in Section 5.5.3. With  $r_{\text{UND}}$ , the input may come via a digital signal from the undulator controller, with the advantage of being a noiseless signal, but numerical representation limitations and lower control rates may still exist, requiring additional filtering or interpolation functionalities in  $\text{SEL}_{\text{UND}}$  to prevent significant setpoint discontinuities in  $r_{\text{BRG}}$ . This is the case for the current APU22 solution, discussed in the following subsection. For  $\chi_{\text{UND}}$  option, there is the additional challenge of knowing enough about the control of the undulator, which is not always the case, particularly with third-party instruments.

The last operation mode is the *triggered* mode, in which trajectories for  $r_{\text{BRG}}$  can be directly read from a file  $\text{TRF}_{\text{BRG}}$  that is pre-generated by the user. At bending-magnet beamlines, this may open possibilities in terms of fly-scans with non-standard trajectories. At undulator beamlines, in turn, it separates the undulator and the HD-DCM from the control perspective, preventing the issues of numerical representation, sample rates or noise that were just described in the *follower* mode. In this case, the undulator controller is also required to be able to switch between modes, according to an equivalent operation block  $\text{OPN}_{\text{UND}}$ , and to store and run the setpoints from a file  $\text{TRF}_{\text{UND}}$ , which must match those of the HD-DCM for energy tuning. Then, trigger and synchronization must be handled at the hardware level or via sufficiently fast/deterministic software implementation. Here, as well, sufficient reliability is needed in the undulator. This mode is unfortunately not yet available with the APU22, since an additional board is needed in the Beckhoff's controller for external trigger capabilities. Yet, this feature is expected to be implemented and tested in the near future.

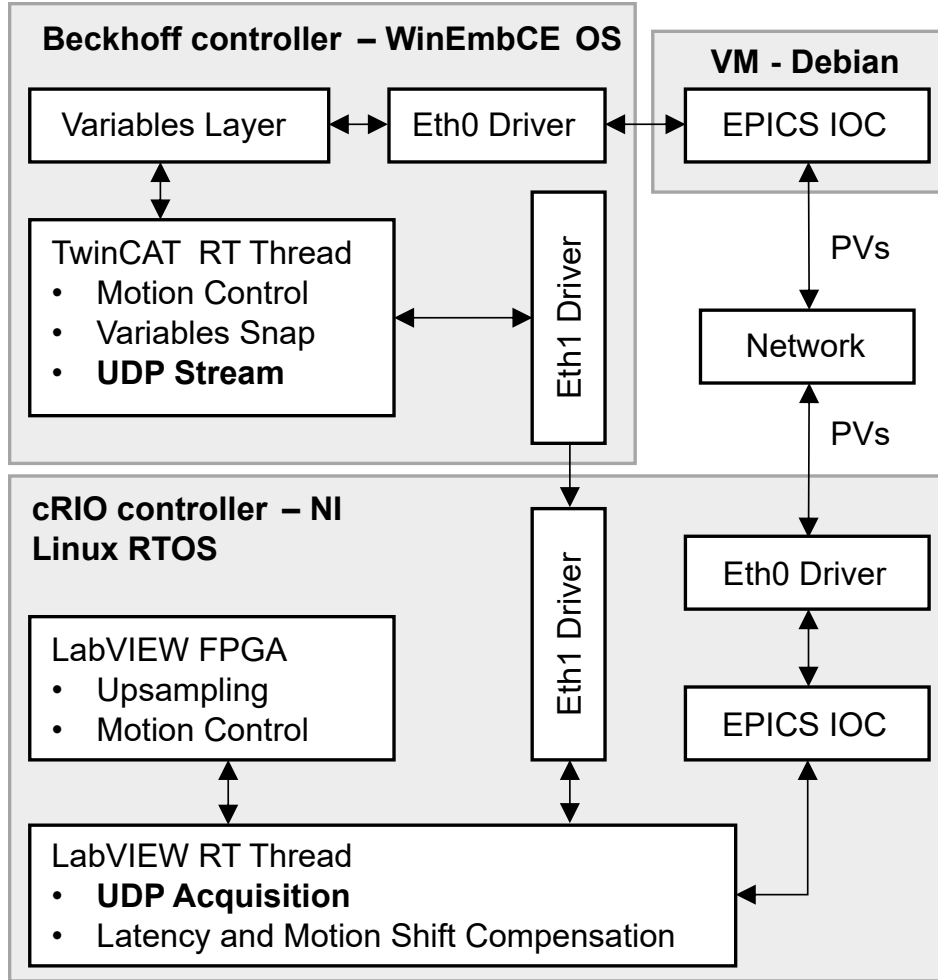
Finally, complementary performance estimators in Figure 5.6 can be optionally computed in real time to indicate compliance in the experiments. Firstly, the sensitive virtual source vertical shift  $\chi_{\text{VSV}}$ , as functions  $f_{\text{VSV}}$  of BRG, GAP and PTC, i.e.  $\theta_B$ , the  $g$  and  $\Delta Rx$ , can be calculated using Equation (5.5) and Equation (5.9), or their calibrated equivalent, and evaluated against the source size. Then, the mismatch  $\chi_{\text{ENG}}$  in the energy tuning between the source and the HD-DCM, as functions  $f_{\text{ENG}}$  of BRG, UND and HAR, i.e.  $\theta_B$  and  $p_u$  and  $n_u$ , can be computed using Equation (5.1) and Equation (5.14), or their calibrated equivalent, and compared to  $\Gamma_E$  (see Figure 5.5c). This should become common practice in the future to increase the maturity and the robustness of the experimental procedures.

### 5.4.3 Upgraded APU22-HD-DCM Integration Topology

Due to the inherent fly-scan capabilities of the HD-DCM, the known significant benefits related to fly-scan spectroscopy (elaborated in Section 5.5.3), and the inconvenient limitations found in the originally available follower operation that were mentioned in the previous subsection, integration alternatives started to be investigated. Then, while the absence of the Beckhoff's triggering board prevented fly-scan spectroscopy operation in the *triggered* mode, a solution complementing the *follower* mode operation has been developed in-house. Now, differently from the previous condition, the new

architecture allows the HD-DCM to work close to ideal scanning conditions, as shown in next section.

The upgraded topology is depicted in Figure 5.7. As before, for standard communication with the external world, the Beckhoff's controller, running a Windows Embedded CE operating system (WinEmbCE OS), exchanges variables via a python layer (Variables Layer) and an Ethernet port (Eth0 Driver) with an external virtual machine (VM-Debian), which runs an EPICS IOC server for exchanging the EPICS PVs with the Network. The cRIO controller, running a Linux real-time operating system (NI Linux RTOS), in turn, has an embedded EPICS IOC layer (Nheengatu [38]), directly communicating with the Network via an Ethernet port (Eth0 Driver).



**Figure 5.7:** Upgraded integration topology between the APU22 and the HD-DCM at EMA and MANACÁ. The APU22 uses a Beckhoff controller with a Windows Embedded CE operating systems (OS) and an external virtual machine (VM) with a Debian OS for the EPICS IOC server. The HD-DCM is based on a NI Linux real-time operating system (RTOS), with an embedded EPICS IOC server for EPICS process variables (PVs). A direct Ethernet (Eth) link using UDP (User Datagram Protocol) for setpoint streaming is now available for *follower* mode operation. Further details in the text.

Yet, now, the Beckhoff's and the cRIO controllers are also directly connected via an unidirectional Ethernet access (Eth1 Drivers), which can stream the APU22 position setpoint  $r_{UND}$  to the HD-DCM (see Figure 5.6). In the same motion control TwinCAT RT thread in the Beckhoff, motion variables (e.g. position and velocity) are calculated, sampled and streamed via UDP (User Datagram Protocol) through the dedicated Ethernet link. At the cRIO side, a LabVIEW RT code (as part of  $SEL_{UND}$  in Figure 5.6) is responsible for decoding and treating the data.

Indeed, in spite of the peer-to-peer Ethernet link and both implementations being on real-time threads, there are inherent delays, jitters and latencies in the system, which can be in principle characterized and partly compensated for in the LabVIEW RT code. One of these was the mechanical delay in the undulator response, thus allowing the HD-DCM to be closer to the real position rather than simply following an unrealistic reference setpoint. Moreover, given that the undulator control loop runs at 1 kHz only and the HD-DCM at 20 kHz, a LabVIEW FPGA code was implemented (also as part of the abstract  $SEL_{UND}$  block in Figure 5.6) to generate an upsampled position reference to the HD-DCM control algorithm.

In this configuration, the Beckhoff's controller is the one responsible for defining a suitable higher-order trajectory profile for smooth performances. Hence, obtaining deeper access and suitably defining Beckhoff's internal variables for acceleration and jerk has also been an upgrade action, as compared to the early operation phase. Yet, as typical in high-performance mechatronic systems (see [39]), a lot more can be expected to be investigated and optimized in terms of trajectories in the future, once other performance/operation bottlenecks at the beamline are eliminated. The following section demonstrates the latest progress and discusses the current operational limitations via concrete experimental examples.

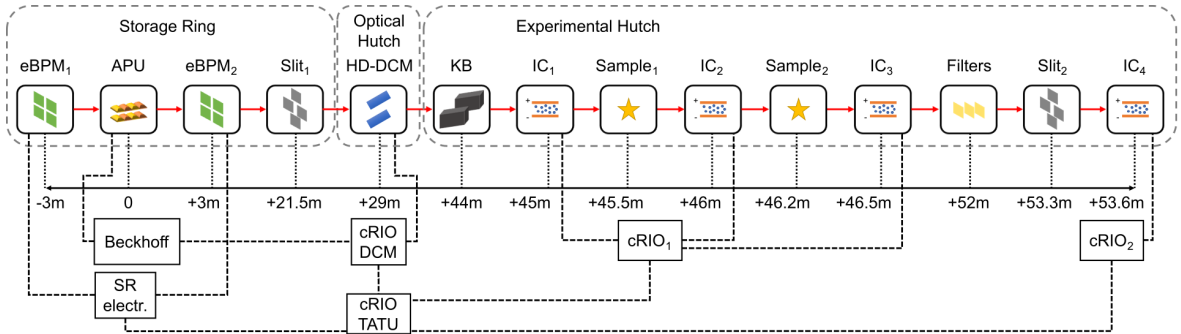
## 5.5 Experimental Results

Before becoming available to the general beamline user, the HD-DCM goes through a primary commissioning procedure that has been iteratively developed at the MANACÁ and the EMA beamlines at Sirius, according to the particularities of this new instrument and its integration system. As elaborated in [25], this includes: 1) *energy calibration* for the angular metrology of the Bragg rotary stage with respect to reference absorption edges; 2) *DCM-undulator tuning* between the Bragg angle and the undulator phase for the multiple harmonics (see also Section 5.3.2); and 3) *fixed-exit calibration* concerning the HD-DCM crystal cage (gap, pitch and roll). Then, part of these routines may be executed by the beamline crew or users via automated python scripts in a regular basis, as sanity checks or re-calibration for improved accuracy. The first commissioning results of the HD-DCMs with X-rays at MANACÁ and EMA were described in [25] and [29]. In the following subsections, updated results for stand-still and scanning performances at EMA, as well as methods developed for data analysis, are disclosed.

### 5.5.1 EMA Beamline Setup

The experimental setup layout is depicted in Figure 5.8. The APU22 source, with its Beckhoff's motion controller, is at the origin; electron beam position monitors (eBPMs) positioned 3 m upstream and downstream can provide transversal (x and y) and steering (pitch and yaw) data with sampling rates up to 572 kHz via dedicated electronics in the storage ring (SR); a set of high-heat-load slits (Slit<sub>1</sub>) is used to define the acceptance to the HD-DCM at 29 m; a set of bendable Kirkpatrick-Baez (KB) mirrors at 44 m is used to collimate or focus the downstream X-ray beam; two sample stages are present at 45.5 and 46.2 m; a set of pneumatic metal filters can be used at 52 m; a set of monochromatic slits are positioned at 53.3 m; finally, ionization chambers (IC<sub>1</sub>, IC<sub>2</sub>, IC<sub>3</sub> and IC<sub>4</sub>) are used both before and after the samples for absorption experiments, as well as after the monochromatic slits for stability measurements.

The ICs were connected to Stanford Research Instruments' SR570 low-noise current preamplifiers, whose voltages were then digitized at cRIO units (cRIO<sub>1</sub> and cRIO<sub>2</sub>) using NI's 16-bit NI-9215 analog input boards with 100 kHz sampling rate. Indeed, the cRIO has been chosen as one of the standard data acquisition hardware/controllers for Sirius beamlines, thus not only hosting the entire control of the HD-DCM, but also being used to handle digital and analog signals of a variety of devices in rates up to 10 MHz. At the higher-level user operation, the so-called Nheengatu solution has been developed by the Beamline Software Group group [38] to integrate cRIO variables in LabVIEW<sup>®</sup> into the EPICS framework. Moreover, a special software module, known as time and trigger unit (TATU) [40], has been developed in-house by the Beamline Software Group for the NI-9401 board to work as a synchronization unit



**Figure 5.8:** Simplified EMA beamline setup for the experiments with the HD-DCM, including: the APU22 source, electron beam position monitors (eBPMs); high-heat-load slits (Slit<sub>1</sub>); the HD-DCM; focusing Kirkpatrick-Baez (KB) mirrors; ionization chambers (IC<sub>1</sub>, IC<sub>2</sub>, IC<sub>3</sub> and IC<sub>4</sub>); sample stages (Sample<sub>1</sub> and Sample<sub>2</sub>); metal filters and monochromatic slits (Slit<sub>2</sub>). Connections among the Beckhoff's motion controller for the APU22, storage ring (SR) electronics for the eBPMs, and NI's cRIOs used as controller (HD-DCM), data acquisition hardware (ICs) and trigger unit (TATU) are also indicated. More details are provided in the text. The distances with respect to the undulator are provided for general reference.

in the microsecond range. This way, data from the eBPMs, the HD-DCM and the ICs can be already synchronized in the sub-millisecond domain using TTL (Transistor-Transistor Logic) trigger signals. The APU22 is expected to become part of the complete triggering framework as soon as the complementary Beckhoff's triggering board is commissioned.

### 5.5.2 Stand-still Performance

Stand-still performances of the HD-DCM with pitch levels around 10 nrad RMS up to 2.5 kHz according to its embedded metrology have been reported in [27] and [29] for the units at MANACÁ and EMA, respectively. With X-rays, however, only a preliminary stability evaluation attempt at MANACÁ was reported so far in [25]. Here, further analyses of the angular vibrations are carried out at EMA using both the rising edge of rocking curves and knife-edge methods, as described by [41], [42], and [43].

#### 5.5.2.1 Rocking Curves:

Starting with the rocking curves, the experiments were made at 25.5 keV, i.e. close to the edge of Ag. This has been about the highest energy used so far at the beamline mainly due to the weak emission of the APU22 (see Figure 5.4a) at higher energies, with the 13<sup>th</sup> harmonic being required for 25.5 keV. The selection of the highest possible energy was an attempt to maximize the sensitivity provided by narrower rocking curves (see [43]). The high-heat-load slits were set to 430  $\mu\text{m} \times 600 \mu\text{m}$  (v $\times$ h), providing an acceptance close to 15  $\mu\text{rad} \times 20 \mu\text{rad}$ , which offers a reasonable compromise between spectral purity for different diffraction orders and flux (see Figure 5.4). Both Si(333) and Si(555) reflections were used, hence with Bragg angles around 13.45° and 22.81°. The measurements were taken with the IC<sub>4</sub>, having the monochromatic slits completely open, and the sample stages and the IC<sub>2</sub> and IC<sub>3</sub> removed from the beam. The IC<sub>1</sub> was left in place to work as a filter for the lower order reflections, being sufficient for the Si(333) measurements. For the Si(555) measurements, in turn, Al filters from the filter box were added to reduce the tails in the rocking curve, as shown next. The IC<sub>1</sub> was filled with Ar95%/Kr5% and IC<sub>4</sub> with N<sub>2</sub>40%/Ar60% for efficiency at 25.5 keV. Finally, the amplifier gains for the IC<sub>4</sub> were set to 1 nA/V and 100 pA/V for the Si(333) and the Si(555) measurements, respectively.

The step-scan rocking curve measurements, with integration time of 0.1 s per point and total measurement times around one minute, are shown in Figure 5.9a. In spite of the residual tails from lower-order reflections, particularly in the Si(555) case, the agreement with the nominal simulated values [44] is remarkable, with FWHMs of about 3  $\mu\text{rad}$  and 1.12  $\mu\text{rad}$ . Furthermore, even though the total power in the HD-DCM in these conditions is only in the order of 1 W, i.e. two orders of magnitude lower than the expected final load when the storage ring is at full current and the final undulator is installed, these results prove the high quality of the crystals (manufactured at the APS (Advanced Photon Source) by Elina Kazman's team) and of the clamping and

cryogenic cooling solutions (see [27]). Next to that, as a side evaluation of fly-scan options in pitch, repeatability and long-term stability, Figure 5.9b shows a series of 13 10s-long fly-scan measurements for the Si(333), taken every 12 minutes in a total of about 2.5 h. The results find good agreement with the initial step-scan, prove the internal metrology repeatability, and demonstrate stability over a few hours, apparently with only a small drift of about 0.1  $\mu\text{rad/h}$ .

Then, with the rocking curves, conversions between intensity and inter-crystal parallelism can be made for stability analyses. Figure 5.9c shows the intensity sensitivity obtained for both step-scan measurements by taking the derivative of fitted peak functions (not shown) of the rocking curves. It is worth noting that, perhaps counter-intuitively, although the Si(555) has a steeper rising edge, the larger flux available with Si(333) made its sensitivity larger, even with a ten-fold smaller amplifier gain. Besides that, the storage ring is not yet operating in top-up mode and its current during these measurements varied from 92 to 58 mA, respectively, thus reducing the potential sensitivity with Si(555) by 42% (with respect to the 100 mA injection level).

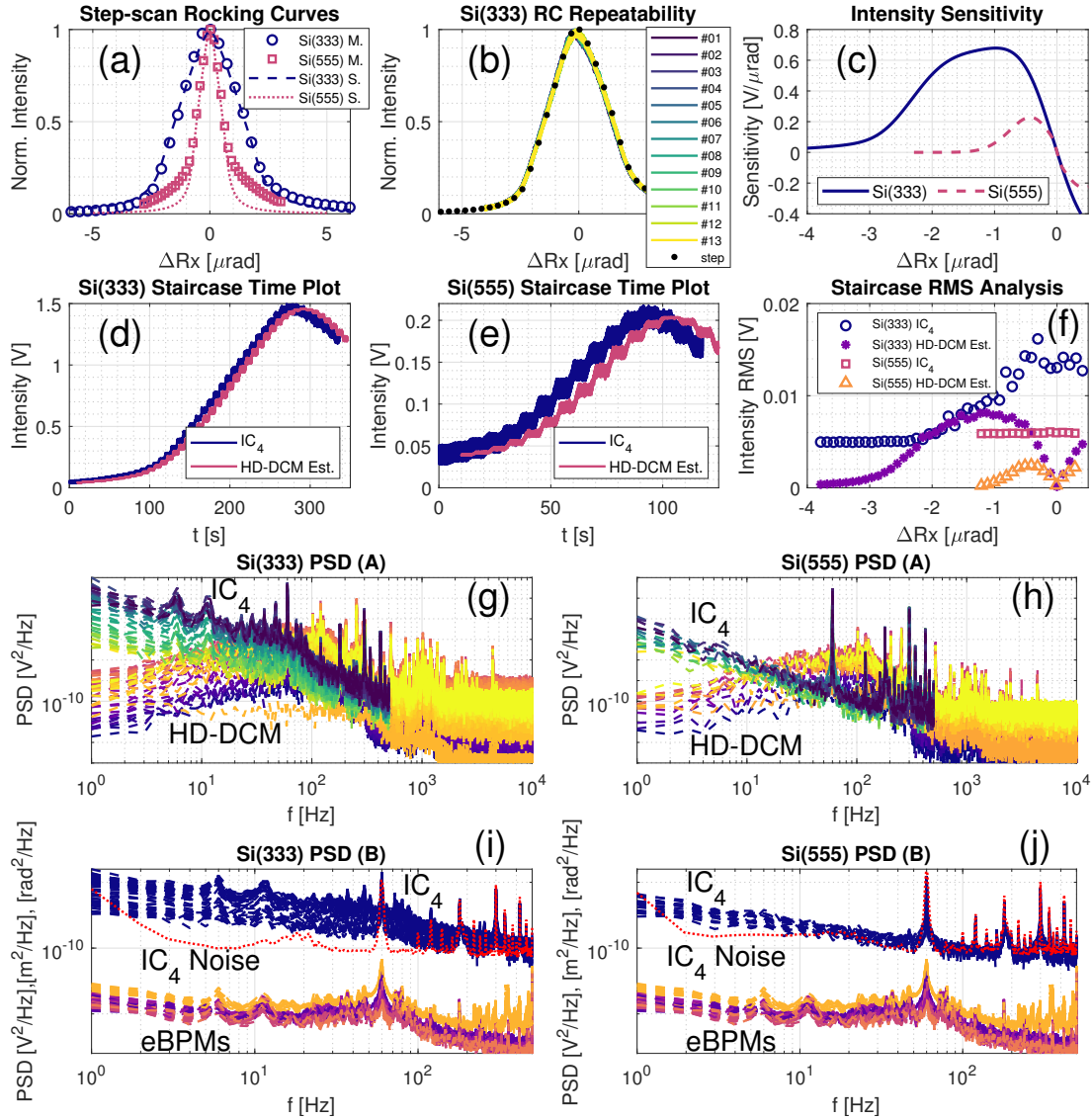
The actual stability experiments consisted in running staircase-like rocking curves, as proposed by [41]. Hence, while making continuous acquisition at sampling rates of 1 kHz for the eBPMs and the IC<sub>4</sub>, and 20 kHz for the HD-DCM, the 2<sup>nd</sup> crystal of the HD-DCM would start from a detuned condition and move over the rocking curves in a given number of steps. At every step, a dwell time of 5 s was taken for further statistical analyses. Figure 5.9d and Figure 5.9e show the time data for these scans. Together with the IC<sub>4</sub> signal, estimated intensity levels for the HD-DCM are calculated using the high-quality internal metrology — which was consistently around 11 nrad RMS at all times — and the intensity sensitivity curves.

Next, the RMS values obtained in each step are summarized in Figure 5.9f. While the HD-DCM estimates replicate the sensitivity shapes, the IC<sub>4</sub> signals shows different results. For the Si(333) measurement, it leaves a base noise floor and starts to build up close to what might be interpreted as the HD-DCM contribution, but, instead of decreasing with the HD-DCM after the sensitivity peak, it continues to rise, in a closer approximation with the absolute intensity shape. For the Si(555) measurement, in turn, the RMS value simply remains at a constant noise floor, regardless of the absolute intensity value.

To further investigate these results, Figure 5.9g and Figure 5.9h provide the Power Spectral Density (PSD) for each step in color gradients: the IC<sub>4</sub>, in the front and between 1 and 500 Hz, goes from light to dark (“viridis” colormap) as the pitch angle increases, whereas the HD-DCM, at the back and between 1 Hz and 10 kHz, goes from dark to light (“plasma” colormap). In neither case, it would be expected that the HD-DCM estimate would overtake the IC<sub>4</sub> spectra, because, by definition, the HD-DCM is only one of the contributions that might affect the intensity measurements. Moreover, the most prominent peaks in the HD-DCM estimate do not appear as the most relevant ones in the IC<sub>4</sub> spectra.

The fact is that even though the acquisition rate for the IC<sub>4</sub> was 1 kHz, the large





**Figure 5.9:** Rocking-curve-based stability assessment with the HD-DCM: (a) Si(333) and Si(555) rocking curve measurements (M) via step-scans compared with simulations (S); (b) fly-scan rocking curve repeatability test, with 13 measurements over about 2.5 h; (c) intensity sensitivity curves based on the derivative of the Si(333) and Si(555) rocking curves; (d) and (e) intensity staircase time plots of ionization chamber IC<sub>4</sub> for Si(333) and Si(555), together with intensity variation estimates from the HD-DCM internal metrology (with a time offset of 10 s for readability); (f) root mean square (RMS) values from the steps of the staircase measurements and estimates; (g) and (h) Power Spectral Density (PSD) from the steps of the staircase measurements and estimates; (i) and (j) PSD from staircase measurements together with electron beam position monitor (eBPM) data and IC<sub>4</sub> noise floors (note: eBPM data in (i) borrowed from (j) measurements due to data loss, but without any loss of applicability). Further details in the text.

gains ( $\leq 1$  nA/V) required in these measurements were associated with low bandwidths of only 15 Hz for the Si(333) and 10 Hz for the Si(555) with the SR570 amplifier (as specified by the supplier). As a matter of fact, bandwidth limitations are often the case for most current amplifiers at large gains, as a way to handle spurious noise. Yet, with the Si(333) it can be seen an increase in the  $IC_4$  spectra, with the intensity being dominated by the low frequency contribution and by peaks at 60, 180 and 300 Hz. The Si(555), in turn, barely changes with the absolute intensity, being again dominated by peaks at 60, 180 and 300 Hz. This suggests that the first is sensitive to contributions from the source, whereas the latter is already limited by the noise in the detecting elements.

This can be further confirmed by including the noise levels (floors) that had been previously measured for the ICs in the setup without the beam, and by qualitatively comparing the  $IC_4$  spectra with those of eBPM signals, as shown in Figure 5.9i and Figure 5.9j. Here, the multiple steps are represented with one same color that is associated to the different elements, namely:  $IC_4$  signal, electron beam horizontal position, electron beam vertical, electron beam yaw, electron beam pitch, and horizontal position of a dispersive eBPM (qualitatively related to the oscillation of the energy of the electrons in the storage ring, not shown in Figure 5.8). In Figure 5.9i, the  $IC_4$  PSD is mostly above the noise floor, whereas the low frequency behavior, the peaks at 6 and 12 Hz, and the “bump” between 30 and 100 Hz do correlate with features in the eBPM signals, such that it becomes clear that the beam instabilities in the storage ring, with RMS values up to  $2\text{ }\mu\text{m}$  and  $1.5\text{ }\mu\text{rad}$ , are still truly affecting the intensity stability at the beamline. In Figure 5.9j, only the very lowest range of the Si(555) signal is above the noise floor, endorsing the discussion above.

Consequently, being close to 10 nrad RMS according to its internal metrology, the pitch stability of the HD-DCM seems indeed too small to be measurable via X-ray intensity over rocking curve edges in the current conditions of EMA and Sirius storage ring. It should be emphasized, however, that the stability levels investigated with the HD-DCM are about 20 times lower than those measured in [43] and more than 50 times lower than in [41]. Still, the data analysis methodology proposed here allows for a systematic evaluation of the problem, demonstrating that the current practical measurement limitations span from instabilities in the source itself to the detecting elements, due not only to low signals (related to low fluxes with the APU22) but also to spurious electronic noise. Then, it can be used as a validation tool in following the required improvements in experimental conditions over time.

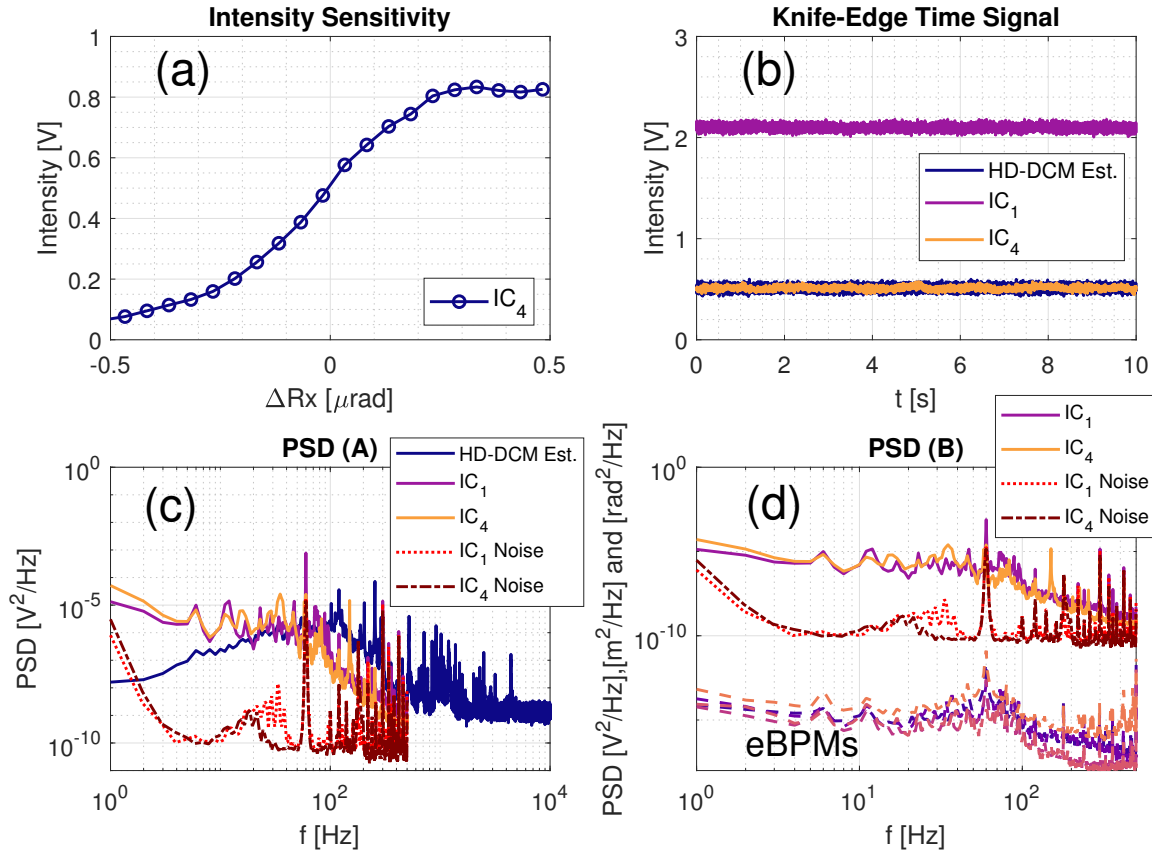
### 5.5.2.2 Knife Edge:

Next, taking advantage of the experimental setup with the Si(333) configuration, an equivalent stability analysis was carried out with a knife-edge method. Firstly, the beam was focused with the KB set to about  $7\text{ }\mu\text{m} \times 10\text{ }\mu\text{m}$  ( $v \times h$ ) at the monochromatic slits. Then, with the crystals tuned at the peak of the rocking curve, the bottom blade of the slit was scanned in front of the beam and finally centered halfway for

maximum sensitivity. Next, the 2<sup>nd</sup> crystal of the HD-DCM was step-scanned in pitch to obtain the intensity sensitivity curve shown in Figure 5.10a. Lastly, the 2<sup>nd</sup> crystal was repositioned at the tuned condition (maximum sensitivity) and continuous data was collected for 10 s.

Figure 5.10b shows the time data, with the IC<sub>4</sub> signal, the estimated intensity level for the HD-DCM (derived from its internal metrology signal and the sensitivity curve) and also the IC<sub>1</sub>, which was used as a reference signal with a gain of 5 nA/V. At the top of the rocking curve, the HD-DCM should have nearly zero impact in the IC<sub>1</sub>, which is before the knife and also takes the Si(111) background flux. Besides that, equivalently to the staircase measurements, under ideal experimental conditions the distribution of the IC<sub>4</sub> could not possibly be smaller than that of the HD-DCM.

Turning once again to the frequency domain, Figure 5.10c and Figure 5.10d show



**Figure 5.10:** Knife-edge-based stability assessment with the HD-DCM: (a) 2<sup>nd</sup> crystal pitch step-scan measurement for angle-to-intensity mapping using ionization chamber IC<sub>4</sub>; (b) intensity measurement at maximum sensitivity point, with reference ionization chamber IC<sub>1</sub>, transmitted signal IC<sub>4</sub> and intensity variation estimate from the HD-DCM internal metrology; (c) Power Spectral Density (PSD) from the knife-edge measurement, including the HD-DCM estimate and IC noise floors; and (d) PSD from knife-edge measurements with electron beam position monitor (eBPM) data and IC noise floors. Further details in the text.

the PSDs comparing all signals and including the noise floors from dark conditions. In Figure 5.10c, it can be seen that the ICs are well above the noise level for most of the frequencies. Yet, they surprisingly show very similar levels and behavior between them, from which any contributions from the HD-DCM can be hardly recognized. Only the largest peaks from the HD-DCM at 120, 204 and 255 Hz seem to find counter parts in the IC<sub>4</sub>, but with 1000-fold reduced amplitudes. Then, from Figure 5.10d, both ICs take the structures from the eBPMs spectra, as also discussed for Figure 5.9i, which again limited the investigation of the inter-crystal pitch stability of the HD-DCM with X-rays. Still, the sensitivity peak here reached 2 V/μrad (not shown), which is 2.5 times larger than what was achieved with the Si(333) rocking edge (see Figure 5.9c), making this the most sensitive and promising method available at EMA at the moment.

Unfortunately, the beamtime was over before a knife-edge measurement with Si(111) could be performed. Indeed, since this method does not rely on the sharpness of the rocking curve, working with the first diffraction order would allow fluxes one or two orders of magnitude larger (with a broader Darwin width), which could use lower gains ( $\gg 1$  nA/V) and reach bandwidths of hundreds of Hz to a few kHz, while improving the signal-to-noise ratio. In that sense, lower energies at lower harmonics should also be explored, as more than two extra orders of magnitude might be gained in flux (see Figure 5.4a). Nevertheless, as discussed in [43], one of the drawbacks of the knife-edge concept is its sensitivity to the mechanical stability of other elements in the beamline, including the mirrors and the knife itself. For example, in Figure 5.10c and Figure 5.10d the sharp peak at 150 Hz in IC<sub>4</sub> is likely related to an unmapped mechanical resonance in the optical chain. These contributions may become more relevant once the other dominant effects are eliminated.

To conclude, although the replacement date of the official undulator source — which will improve the conditions for pitch stability measurements based on rocking curve edges — remains unclear, significant improvements in overall stability are expected already in the short term. These include: 1) the implementation of the FOFB system, which will extend the electron beam control bandwidth well beyond the 1 Hz that is currently provided by the slow orbit feedback (SOFB) system [45]; 2) the top-up operation mode at the storage ring, which should minimize current-related transients; and 3) a refined grounding work to reduce electronic noise at EMA. Other than that, this commissioning round fostered the development of this systematic data analysis pipeline and a refinement in the real-time integration between several components of the storage ring and the beamline, which proved to be decisive in interpreting the experimental data and will be essential for fast experiments with sufficient statistics. A new round of beamtime for stand-still stability assessment of the HD-DCM will be realized after the identified dominant sources of beam variation and noise are solved.

### 5.5.3 Scanning Performances

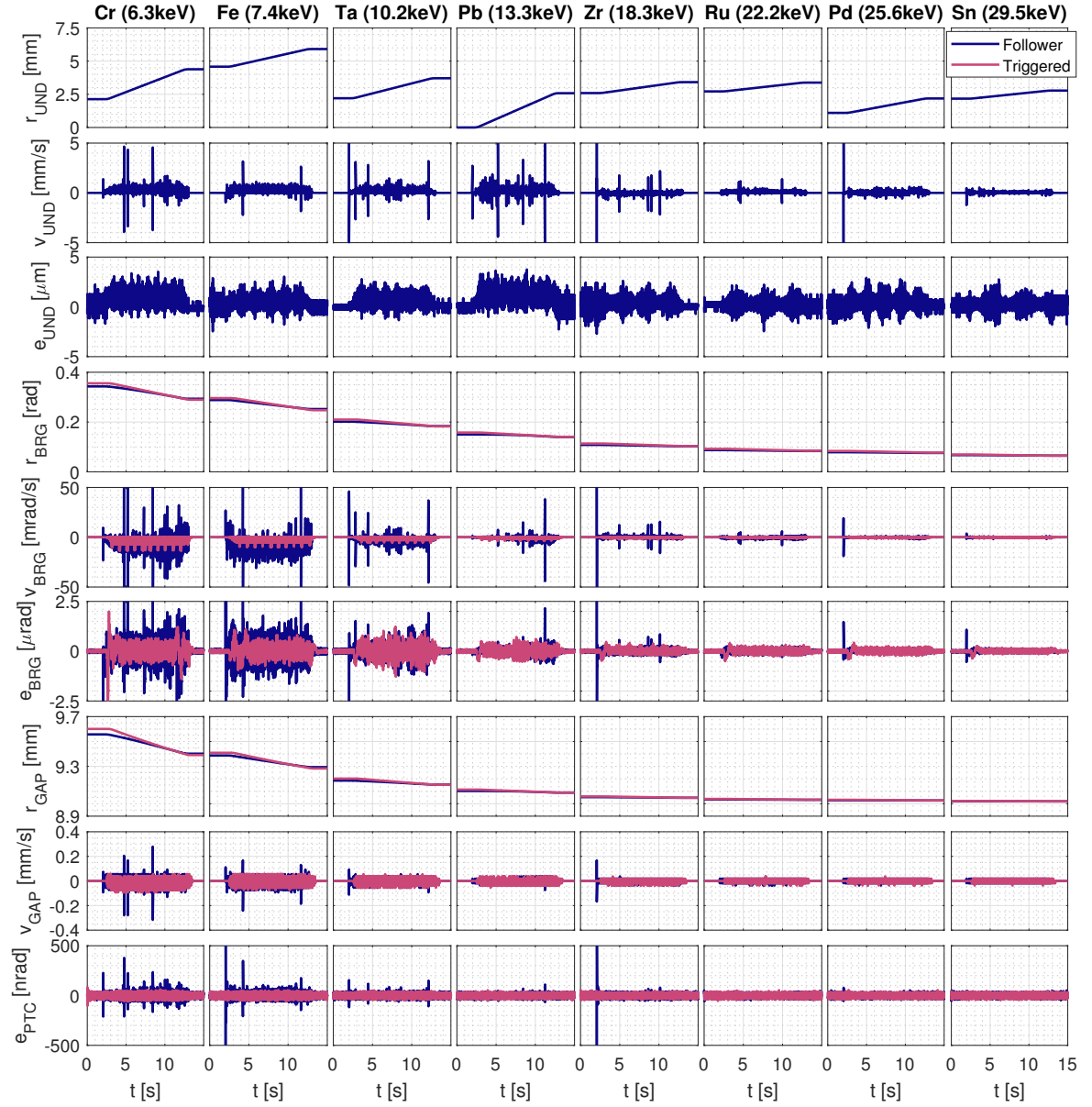
In spite of the electron beam instabilities and electronic noise levels that limited the evaluation of the HD-DCM performance in the stand-still experiments with X-rays, EMA has been perfectly able to host users from the scientific community and carry out relevant spectroscopy experiments in a regular basis. The following subsections provide results showing the remarkable motion performance and spectroscopy capabilities currently available at EMA.

#### 5.5.3.1 Fly-Scan Motion Evaluation:

The current possibilities in energy fly-scans, with the HD-DCM in the *follower* mode and the upgraded integration topology with the APU22 (see Section 5.4.3), are exemplified in Figure 5.11. Performance variables in 1-keV scans taking about 15 s with Si(111) are shown for a selection of energies for elements of interest covering the currently useful range of energies at EMA. The undulator reference signal  $r_{\text{UND}}$  entering the HD-DCM control loops is shown to cover 1 to 2 mm over different harmonics for the different energies. The undulator velocity  $v_{\text{UND}}$ , obtained by differentiating  $r_{\text{UND}}$ , is bound generally below 1 mm/s, except for larger random peaks found in most of the scans. Their cause seem related to discontinuities in the trajectory generated by the Beckhoff's controller, but this issue is still under investigation for a definitive solution. Yet, although they partly degrade the HD-DCM loops, as discussed below, this is to a far less extent than the degradation observed with the previous architecture (see [26] and [29]). Regarding the undulator tracking error  $e_{\text{UND}}$ , it shows good performance, with deviations  $\leq 3 \mu\text{m}$ , thus obeying the phase error tolerances  $\Gamma_{p_u}$  specified in Figure 5.5d.

The amplitude of the Bragg angle reference signal  $r_{\text{BRG}}$  decreases with energy, going from a stroke of 0.05 rad ( $2.85^\circ$ ) to 0.002 rad ( $0.1^\circ$ ) only. The angular velocity  $v_{\text{BRG}}$ , is generally bound to  $\leq 30 \text{ mrad/s}$  ( $1.7^\circ/\text{s}$ ), but the reaction to the peaks in the undulator velocity is clear. The control error  $e_{\text{BRG}}$ , is also significantly reduced as the photon energy increases, typically going from about 1  $\mu\text{rad}$  (in the cruising range outside the acceleration/deceleration regions) to less than 0.2  $\mu\text{rad}$  at high energies. Naturally, the influence of the undulator velocity bursts is again obvious. These angular errors can be converted to energy variations according to Equation (5.3), here falling  $< 0.1 \text{ eV}$ . Their particular impact on the experiment depend on the contributions within the integration times. More details about this will be provided in another publication under preparation.

Regarding crystal cage loops, the amplitude of the gap reference signal  $r_{\text{GAP}}$  also decreases with energy, going from a stroke of 0.15 mm to 0.001 mm only. The gap velocity  $v_{\text{GAP}}$ , is generally bound to  $\leq 0.1 \text{ mm/s}$ , mostly to dynamically correct the gap error ( $|e_{\text{GAP}}| \leq 10 \text{ nm}$ , not shown), since the gap stroke for these energies are low, except during the reactions to undulator peaks. Finally, the control error for the pitch between crystal  $e_{\text{PTC}}$ , is always within 15 nrad RMS, even at the lower energies and



**Figure 5.11:** Performance variables in 1-keV fly-scans taking about 15 s with the HD-DCM with Si(111). A selection of energies covering the current useful range at the EMA beamline and multiple harmonics in the APU22 is made. Together with the central energy of the scan, elements of interest with absorption edges within these ranges are indicated. Variables of the undulator (UND), the Bragg angle control loop (BRG), and the crystal cage loops gap (GAP) and pitch (PTC) are shown for a comprehensive motion performance evaluation. The upgraded *follower* performance can be directly compared with independent *triggered* mode as a proof of concept. The complete discussion is provided in the text.

with the disturbances of the undulator signal. In these experiments, the destination position, velocity and motion trigger were sent to the Beckhoff's controller via PVs, and the trajectories had constant speed in the undulator coordinates. For trajectories

linear in energy, pre-calculated vectors must be passed to the APU22 controller, a functionality not yet validated, but that is expected to become available soon.

Still, to remove any doubts about the undulator signal being responsible for the residual performance degradation in Figure 5.11, it also shows the Bragg and crystal cage variables for similar trajectories with the HD-DCM in the *triggered* mode, i.e. following a pre-planned trajectory and completely decoupled from the undulator. Small differences in the reference signals are because the *follower* mode used polynomials ( $f_{\text{BRG}}$  in Figure 5.6) calibrated at the beamline, whereas the *triggered* mode tests used nominal polynomials for this undulator. It can be seen that  $e_{\text{BRG}}$  and  $e_{\text{PTC}}$  are close to ideal performance, with  $\leq 0.35 \mu\text{rad}$  and  $\leq 15 \text{ nrad}$  RMS (at 20 kHz), respectively.

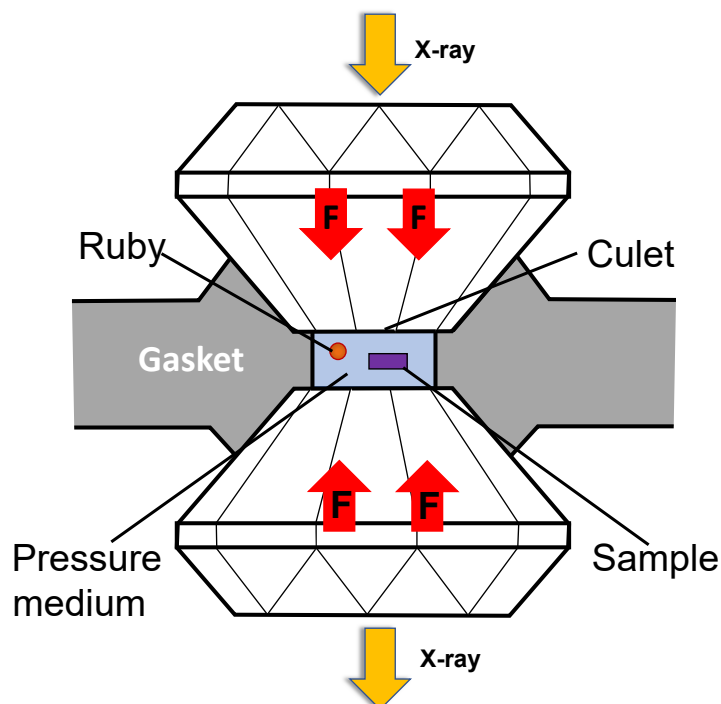
The undulator could not make part of this last proof of concept because, as mentioned above, a functional board is still missing in the Beckhoff's controller to allow for external triggers (and integration with the TATU framework). As soon as it is available, it will be possible to compare the results from the current streaming implementation with fully triggered performance for a definitive beamline operation choice. It should be noted that this high-performance synchronization effort is in agreement with what been developed in other synchrotrons [30], but here with additional subtleties related to the large sensitivity of the HD-DCM as a high-performance mechatronic system.

To conclude, the choice of scans within 15 s was arbitrary and tests at least twice as fast have achieved comparable results (not shown). Naturally, at some point, higher accelerations and faster motions on bearings, together with larger strokes required for lower energies, start to increase disturbances. These will require case-by-case analyses, particularly as the lowest energy range of the HD-DCM starts to be explored after the replacement of the APU22.

### 5.5.3.2 Spectroscopy Results:

X-ray absorption (XAS) technique is a powerful tool for studying the electronic behaviors of materials under extreme thermodynamical conditions, such as high pressure and low temperatures. In particular, the high-pressure studies are especially interesting for the 5d transition metals, whose energy levels involved at  $L_{2,3}$  edges are above 10 keV, therefore compatible with diamond anvil cells (DAC) [46]. This kind of study is among central scientific goals of the EMA beamline at Sirius.

Here, to evaluate the spectroscopy capabilities with the HD-DCM during the EMA scientific commissioning, a high-pressure XAS experiment was carried out with the Si(111) set of crystals at the Pt  $L_2$  and  $L_3$  edges ( $2p \rightarrow 5d$  transition) to probe the pressure evolution of valence band spin-orbit coupling of Pt metal. The measurements, at room temperature, were performed in transmission geometry, as illustrated in Figure 5.12, using a membrane-driven copper-beryllium DAC prepared with two full anvils, with a culet size of  $350 \mu\text{m}$  to reach pressures as high as 60 GPa. A  $5 \mu\text{m}$ -thick platinum foil was loaded in a  $60 \mu\text{m}$  hole of a rhenium gasket, together with a  $5 \mu\text{m}$  ruby sphere for in situ pressure calibration, and neon gas was used as a pressure-transmitting medium. Referring to Figure 5.8, the DAC was mounted at the Sample<sub>1</sub> position, where the



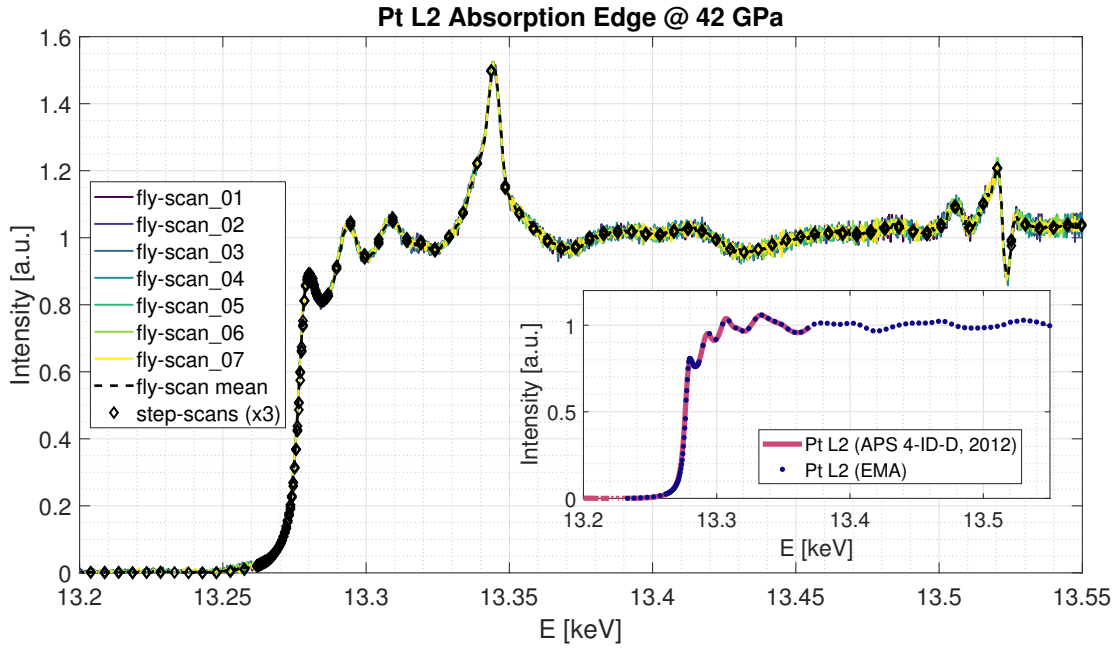
**Figure 5.12:** High-pressure setup using diamond anvil cells (DACs) to submit samples to extreme conditions. The focused X-ray beam goes through the two diamond cells that are loaded against each other through a gasket to create a closed environment with pressures reaching several tens to hundreds of GPa. A pressure medium is used to distribute the pressure and a ruby sphere is used as a pressure gauge via an optical signal. Culet sizes are typically in the order of a few hundred microns.

beam was focused to  $1\text{ }\mu\text{m} \times 2\text{ }\mu\text{m}$  ( $v \times h$ ), whereas a Pt standard foil (Exafs Materials) was placed at Sample<sub>2</sub>, while IC<sub>1</sub>, IC<sub>2</sub> and IC<sub>3</sub> were used for intensity measurements.

The experiment consisted in incrementally increasing the sample pressure in steps of roughly 5 GPa, and, in each pressure step, measuring 3 spectra in step-scan mode followed by 10 spectra in fly-scan mode, for both the L<sub>2</sub> and L<sub>3</sub> edges. The total energy range was 490 eV in all cases. For the step mode, energy step sizes of 0.5 eV were used around the edge (30 eV before and 30 eV after it) and 7 eV for the pre- and post-edge regions. The step scan integration time was 0.5 s, and the total time for each spectra was about 6 minutes, with most of it consumed by overhead from start/stop actions, as also mentioned in [30]. The fly-scans, in turn, were performed with 0.1 mm/s phase speed in the APU22 and 20 kHz sampling frequency for the HD-DCM and the ICs cRIOs (see Figure 5.8), with a measurement time of 27 s per flyscan spectra.

One representative set of data, for the L<sub>2</sub> edge at 42 GPa, is depicted in Figure 5.13. The colorful lines in the back (“viridis” colormap) are the fly-scan measurements, for which the effective sampling rate was averaged down to 40 Hz to improve signal-to-noise ratio while achieving an energy resolution of 0.5 eV; the black dashed line is their average; the diamond markers show the points of three step-scan measurements, which overlap in most cases. The accurate correspondence between the two measurement





**Figure 5.13:** X-ray absorption (XAS) spectra of a Pt foil under 42 GPa in a diamond anvil cell setup at EMA. Measurements over the Pt  $L_2$  edge were repeated 10 times in fly-scan (27 s each) (3 runs lost due to a vacuum interlock fault at the beamline) and 3 times in step-scan (6 min each), demonstrating the high-performance spectroscopy capabilities available at EMA with the HD-DCM and the APU22 source. The inset shows a simultaneous reference measurement of standard Pt sample, being compared with a previous measurement at the APS 4-ID-D beamline. Further discussion provided in the text.

methods demonstrates the reliability of the HD-DCM, the effectiveness of the upgraded *follower* mode operation, and the potential of the fly-scan method, with maximum practical speeds currently limited mostly by the APU22 flux and spurious electronic noise in the detection electronics (which is currently under improvement). Furthermore, it was found that the dispersion in the intensity signal of the fly-scan measurements is, in this case, dominated by a 12 Hz contribution (not shown in detail for conciseness), which was also observed in the stability measurements in Figure 5.9 and Figure 5.10, being likely caused by the instabilities in the electron beam. Again, these should be greatly improved with the implementation of the FOFB system.

It should be noted that the high-pressure XAS experiments using diamond anvil cells are particularly challenging because of the presence of diamond Bragg peaks in the spectra, as those around 13.34 keV and above 13.5 keV. Although these Bragg peaks, inherent to the high-pressure XAS experiments, do bring special complications to the data analysis, for our purposes they reinforce the accuracy of the fly-scan as being identical to the step-scan along the entire energy range. Moreover, in addition to the drastic time efficiency increase, it becomes clear that the fly-scans have benefits related to continuous measurements, such as the wiggle feature close to 13.52 keV,

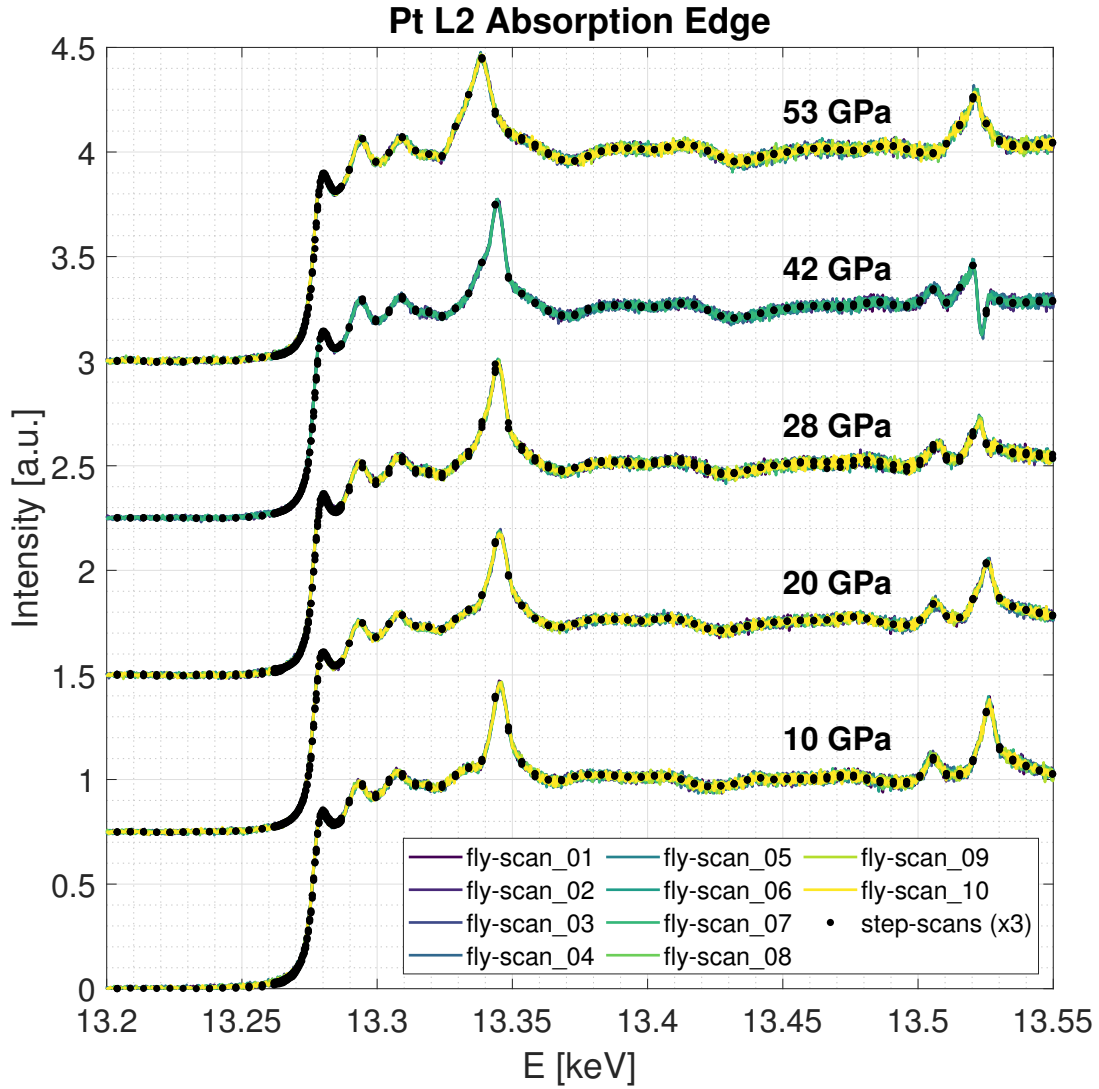
which might be misinterpreted in a step-scan with a poorer resolution. As a further validation check, the inset in Figure 5.13 compares a step-scan spectrum of the standard Pt foil in Sample<sub>2</sub> (collected simultaneously with one of the step-scan measurements in the main plot) with a standard Pt-L<sub>2</sub> XAS spectrum that had been measured at the APS 4-ID-D beamline in 2012, where the same features can be identified.

Finally, evaluating the robustness and repeatability of the experimental system, Figure 5.14 shows five sets of measurements for the L<sub>2</sub> edge from 10 to 53 GPa, with the step-scans now represented by solid black dots and vertical offset between the sets for readability. The changes in the signature of the spectra as a function of pressure can be promptly identified, but the same aspects emphasized for Figure 5.13 hold true. The whole measurement time was approximately 36 h, including injection windows, since the storage ring is still not operating in top-up mode. Without any further compensations, the variation of the peak of the L<sub>2</sub> absorption edge derivatives for all spectra (not shown), i.e. for more than 300 scans and including the current noise and electron beam stability limitations, was within  $\pm 0.75$  eV. Also considering that for each pressure step the HD-DCM would travel to the L<sub>3</sub> edge (around 11.5 keV) and back, this proves the high degree of reliability achieved at EMA.

## 5.6 Conclusions

The efforts in designing and implementing the High-Dynamic Double-Crystal Monochromator from scratch, as a high-end mechatronic machine to Sirius new-generation beamlines, have been honored with unmatched fixed-exit and fly-scan spectroscopy capabilities. Indeed, the well-known inter-crystal pitch stability performance bottleneck in standard DCMs, is in the HD-DCM solved thanks to an improvement level varying from about 5 to more than 100 fold, since 10 nrad RMS (1 Hz to 2.5 kHz) can be achieved even during fast fly-scans, which, in addition, can also reduce measurement times in at least one or two orders of magnitude.

This article has summarized, from a new perspective, engineering and operational aspects that acquire critical relevance in enabling next-level experimental possibilities with the HD-DCM. The multi-axis and highly non-linear motion control problem is stated and an energy-tuning evaluation method, based on wave-propagation simulations, is also proposed to define positioning tolerances between the HD-DCM and the APU source. Then, limitations in the originally available integration architecture with the APU — which could have been actually predicted and prevented if a dedicated analysis had been carried out during the procurement phase of the commissioning undulators —, have been overcome with a new control topology, that has been already able to provide close-to-ideal motion performance results. Furthermore, it was demonstrated how sensitive fast-acquisition experiments are to the whole beamline system, from the stability of the electron beam in the storage ring to high-bandwidth noise levels on detectors. Hence, the essential role of a holistic approach in integrating the HD-DCM to the beamlines, so as to achieve ultimate performances, higher effi-



**Figure 5.14:** X-ray absorption (XAS) spectra of a Pt foil under multiple high-pressure conditions in a diamond anvil cell setup at EMA, validating a high degree of reliability and repeatability of the HD-DCM and the beamline over hundreds of step and fly-scan repetitions in a total experimental time around 36 h. Vertical offsets introduced for readability. Further discussion provided in the text.

ciency and maximum throughput in 4th-generation-light-source beamlines, cannot be emphasized enough. Still, scientific commissioning results demonstrating operational reliability and already 10-fold faster fly-scan XAS measurements are discussed.

Technical commissioning of the HD-DCM will proceed in parallel with beamline operation, as the parameters and functional systems of the storage ring gradually reach final values, and the definitive undulators are installed at the beamlines. These will provide higher electron beam stability and higher fluxes, eventually enabling practical experiments with faster acquisition rates than today, but also affecting the HD-DCM with higher power loads. Moreover, as a next step, spectroscopy performance in *trig-*

gered mode will be compared with the current solution in *follower* mode also with X-rays. Finally, a new HD-DCM model for even faster scans, the so-called HD-DCM-Lite, is now under assembly phase for two new beamlines, and first results are expected in early 2023.

## Acknowledgements

The authors would like to acknowledge the fundamental contribution of the LNLS staff, including scientists, leaders, engineers and designers of different groups, and of the team at MI-Partners, in the development of this collaborative project. Especial thanks to Marlon Saveri Silva, Ricardo Caliari and Marcelo Moraes, who worked directly as the HD-DCM application engineers, and to Marcos Eleotério, José Claudio Corsaletti and Mauricio Donatti, who made the experimental setup at EMA possible. This work is also part of a PhD project carried out with the CST group at TU/e.

## Funding

This work is supported by the Brazilian Center for Research in Energy and Materials (CNPEM) under contract with the Brazilian Ministry of Science and Technology and Innovation (MCTI).

## 5.A List of Abbreviations

APS	Advanced Photon Source
APU	Adjustable-phase undulator
BRG	Bragg angle control loop
CCG	Crystal cage
CNPEM	Brazilian Center for Res. Energy and Materials
cRIO	CompactRIO
DAC	Diamond anvil cell
DCM	Double-Crystal Monochromator
eBPM	Electron beam position monitor
EMA	Extreme Methods of Analysis beamline
EPICS	Experimental Physics and Industrial Control System
FWHM	Full width at half maximum
ESRF	European Synchrotron Radiation Facility
FOFB	Fast orbit feedback
FPGA	Field-programmable gate array
GAP	Inter-crystal gap control loop
HAR	Undulator harmonic variable
HD-DCM	High-Dynamic DCM
IC	Ionization chamber

IOC	EPICS Input/Output Controller
IVU	In-vacuum undulator
KB	Kirkpatrick-Baez mirror configuration
LNLS	Brazilian Synchrotron Light Laboratory
MANACÁ	MAcromolecular Micro and NAno CrystAllography beamline
MIMO	Multiple-input-multiple-output
OPN	Operation mode selector
OS	Operating system
PTC	Inter-crystal pitch control loop
PSD	Power spectral density
PV	EPICS process variable
RLL	Inter-crystal roll control loop
RMS	Root mean square
RT	Real-time
SEL	Operation selector
SOFB	Slow orbit feedback
SISO	Single-input-single-output
SR	Storage ring
SRW	Synchrotron Radiation Workshop
TATU	Trigger and time unit
TRF	Trajectory file control block
TRG	Trajectory generator control block
TTL	Transistor-Transistor Logic
UDP	User Datagram Protocol
UND	Undulator control loop
VM	Virtual machine

## References

- [1] Hastings J.B. 1977 *J. Appl. Phys.* **48**(4) 1576
- [2] Lemonnier M. *et al.* 1978 *Nucl. Instrum. Methods* **152**(1) 109
- [3] Golovchenko J.A. *et al.* 1981 *Rev. Sci. Instrum.* **52**(4) 509
- [4] Hussain Z. *et al.* 1982 *Nucl. Instrum. Methods Phys. Res.* **195**(1-2) 115
- [5] Cowan P.L. *et al.* 1983 *Nucl. Instrum. Methods Phys. Res.* **208**(1-3) 349
- [6] Kelly J. *et al.* 2013 *J. Phys. Conf. Ser.* **425**(5) 052009
- [7] Kristiansen P. *et al.* 2015 *J. Synchrotron Rad.* **22**(4) 879
- [8] Waterstradt T. *et al.* 2018 *Sub-20-nrad Stability of an LN<sub>2</sub>-Cooled Vertical-Offset Double-Crystal Monochromator*. Presented at MEDSI'18 in Paris, France, unpublished
- [9] Baker R. *et al.* 2018 *Proc. 10th Mech. Eng. Des. of Synchrotron Radiat. Equip. and Instrum. (MEDSI'18)* (JACoW Publishing) 440–444
- [10] Dolbnya I.P. *et al.* 2018 *J. Synchrotron Rad.* **26**(1) 253
- [11] Fan Y. *et al.* 2020 *Nucl. Instrum. Methods Phys. Res. A* **983** 164636

- [12] European Synchrotron Radiation Facility (ESRF) 2014 *Double Crystal Monochromator Workshop* <http://www.esrf.eu/home/events/conferences/2014/double-crystal-monochromator-workshop.html>, accessed: Oct. 1st, 2021
- [13] Eriksson M. *et al.* 2014 *J. Synchrotron Rad.* **21**(5) 837
- [14] Hettel R. 2014 *J. Synchrotron Rad.* **21**(5) 843
- [15] Liu L. *et al.* 2021 *Proc. 12th Int. Particle Acc. Conf. (IPAC'21)* (JACoW Publishing) 13–18
- [16] Geraldes R.R. *et al.* 2017 *Proc. 9th Mech. Eng. Des. of Synchrotron Radiat. Equip. and Instrum. (MEDSI'16)* (JACoW Publishing) 141–146
- [17] Geraldes R.R. *et al.* 2017 *Proc. 9th Mech. Eng. Des. of Synchrotron Radiat. Equip. and Instrum. (MEDSI'16)* (JACoW Publishing) 44–47
- [18] Saveri Silva M. *et al.* 2017 *Proc. 9th Mech. Eng. Des. of Synchrotron Radiat. Equip. and Instrum. (MEDSI'16)* (JACoW Publishing) 194–197
- [19] Caliari R.M. *et al.* 2018 *Proc. 16th Int. Conf. on Acc. and Large Exp. Phys. Control Systems (ICALEPCS'17)* (JACoW Publishing) 997–1002
- [20] Moreno G.B.Z.L. *et al.* 2018 *Proc. 16th Int. Conf. on Acc. and Large Exp. Phys. Control Systems (ICALEPCS'17)* (JACoW Publishing) 1941–1946
- [21] Geraldes R.R. *et al.* 2018 *Proc. 10th Mech. Eng. Des. of Synchrotron Radiat. Equip. and Instrum. (MEDSI'18)* (JACoW Publishing) 147–152
- [22] Geraldes R.R. *et al.* 2020 *Proc. ASPE 2020 Spring – Design and Control of Precision Mechatronic Systems* 119–124
- [23] Caliari R.M. *et al.* 2020 *Proc. ASPE 2020 Spring – Design and Control of Precision Mechatronic Systems* 125–130
- [24] Moraes M.A.L. *et al.* 2020 *Proc. ASPE 2020 Spring – Design and Control of Precision Mechatronic Systems* 131–136
- [25] Geraldes R.R. *et al.* 2021 *Proc. 11th Mech. Eng. Des. of Synchrotron Radiat. Equip. and Instrum. (MEDSI'20)* (JACoW Publishing) 25–28
- [26] Geraldes R.R. *et al.* 2021 *Proc. 18th Int. Conf. on Acc. and Large Exp. Phys. Control Systems (ICALEPCS'21)* (JACoW Publishing) 370–375
- [27] Geraldes R.R. *et al.* 2022 *Precision Engineering* **77** 110
- [28] Geraldes R.R. *et al.* 2022 *Precision Engineering* **77** 90
- [29] Geraldes R.R. *et al.* 2022 *J. Phys. Conf. Ser.* vol. 2380 (IOP Publishing) 012050
- [30] Hidas D. *et al.* 2022 *Nucl. Instrum. Methods Phys. Res. A* **1031** 166505
- [31] Sterbinsky G.E. and Heald S.M. 2021 *J. Synchrotron Rad.* **28**(6) 1737
- [32] Ashcroft N.W. 2003 *Solid State Physics* (Thomson Press (India) Ltd)
- [33] Koningsberger D.C. and Prins R. 1988 *X-Ray Absorption: Principles, Applications, Techniques of EXAFS, SEXAFS and XANES* (Wiley-Interscience)
- [34] Zhang L. *et al.* 2013 *J. Synchrotron Rad.* **20**(4) 567
- [35] Onuki H. and Elleaume P. 2002 *Undulators, wigglers and their applications* (CRC Press)
- [36] Chubar O. and Elleaume P. 1998 *Proc. EPAC98 Conference* 1177–1179
- [37] EPICS 2021 *Experimental Physics and Industrial Control System.* <https://epics-controls.org/>, accessed: Nov. 1st, 2021
- [38] Alnajjar D.A.D. *et al.* 2019 *Proc. 17th Int. Conf. on Acc. and Large Exp. Phys. Control Systems (ICALEPCS'19)* (JACoW Publishing) 997–1000
- [39] Heertjes M.F. *et al.* 2020 *Proc. 2020 Am. Control Conf. (ACC)* (IEEE) 3686–3703

- [40] Piton J.R. *et al.* 2021 *Proc. 18th Int. Conf. on Acc. and Large Exp. Phys. Control Systems (ICALEPCS'21)* (JACoW Publishing) 908–911
- [41] Yamazaki H. *et al.* 2013 *J. Phys.: Conf. Ser.* **425**(052001) 1
- [42] Chumakov A.I. *et al.* 2014 *J. Synchrotron Rad.* **21**(2) 315
- [43] Sergueev I. *et al.* 2016 *J. Synchrotron Rad.* **23**(5) 1097
- [44] Sanchez del Rio M. *et al.* 2011 *J. Synchrotron Rad.* **18**(5) 708
- [45] Marques S.R. *et al.* 2022 *Proc. 13th Int. Particle Acc. Conf. (IPAC'22)* (JACoW) 226–229
- [46] Itié J.P. *et al.* 2016 *High Pressure XAS, XMCD and IXS* (John Wiley & Sons) 385–705

---

## Conclusions and Outlook

---

This thesis describes the modeling, the design, the integration and the commissioning work of a novel type of Double-Crystal Monochromator (DCM) for X-ray beamlines. In the High-Dynamic Double-Crystal Monochromator (HD-DCM), standard solutions are revisited and then an entirely new mechatronic architecture is proposed, not only to overcome the existing position-stability limitations in stand-still operation, but also to enable unprecedented high-performance fly-scan possibilities for experimental methods related to spectroscopy. Hence, a technological door is opened to start addressing some of the urges created by the rising 4th-generation synchrotron light sources.

### 6.1 Conclusions

Chapters 2 and 3, together with Appendices A and B, are dedicated to describing the HD-DCM modeling framework and design to a sufficient level of detail so as to provide a case study that can be straightforwardly used either to continue improvements in this novel sub-class of DCMs, or as a reference to other high-end mechatronic instruments, which may be required in next-generation beamlines.

The original design concepts of the HD-DCM include minimal positioning degrees of freedom (DoFs), long-stroke and short-stroke arrangement, smooth motion guiding and actuation, inter-crystal metrology, crystal mounting, and decoupled cooling. Yet, these deep changes as compared to standard DCM designs were, in fact, motivated by an emergent higher-level requirement, namely, developing an instrument that would be compatible with a high-performance control-based architecture. Indeed, the ultimate scientific needs of beams with higher position stability and faster energy scanning capabilities turned out to be related to engineering requirements of nanometer-level positioning and better motion solutions.

Fortunately, these are challenges that have been already worked out since many years by the semiconductors industry via advanced mechatronics [1, 2]. Then, in addition to particular technological solutions, many of which have been incorporated in the HD-DCM, experience in the development of high-end machines had demonstrated that beyond certain levels of complexity simpler “best-effort” or “trial-and-error” approaches are no longer applicable or sustainable. In such cases, systemic, systematic and predictive methodologies become essential tools, some of which have also been incorporated in the HD-DCM project, as demonstrated in Chapter 3 by the iterative



design approach according to the Dynamic Error Budgeting Methodology [3]. Unequivocally, it was only via pragmatic requirements engineering and a development approach with the appropriate tools — simultaneously optimizing the system in terms of interfaces, mechanics, thermal management, control and software — that the HD-DCM could be developed from scratch and meet its ambitious goals “first time right”.

Nevertheless, the HD-DCM cannot by itself unlock the full capabilities of new-generation beamlines and light sources. This is because it is still part of a complex ecosystem of interdependent instruments. Therefore, Chapters 4 and 5 are dedicated to identifying the contextualization of the HD-DCM new technology in the existing beamline environment and proposing integration solutions. On the one hand, a highly non-linear multi-axis and multi-instrument motion control problem is presented to address realistic spectroscopic scientific perspectives and map future needs. And, on the other hand, an evaluation of the global beamline control system and architecture is provided, including third-party hardware limitations, signals and communication protocols, and operation modes.

With that, regardless of partial limitations in the X-ray source and detection elements, which should be overcome in the near future, the latest topology implemented for the two beamlines relying on HD-DCM units in 4th-generation light source Sirius, at the Brazilian Synchrotron Light Source (LNLS), already allows for X-ray methods benefiting from more than 100-fold higher beam position stability and 10-fold faster spectroscopy scans. This capability is now available to the scientific and industrial communities, with potential to aid addressing many challenges faced by modern society. Yet, last but not least, the HD-DCM project has established a paradigm shift in beamline instrumentation development at the LNLS, with technological innovations being propagated to a number of other instruments, as also discussed in the next section.

## 6.2 Outlook

The content of this thesis discusses the rise of a new type of instrument in synchrotron beamlines, which not only brings promising perspectives for design improvements and future research, and also opens prospects for complementary technologies. A few topics of interest are briefly elaborated in the subsections below.

### 6.2.1 Possible Design Improvements

- **Metrology Frame 1:** As shown in Chapter 3, the resulting pitch angle suspension frequency (mechanical resonance) obtained for the metrology frame 1 (MF1) (holding the first crystals) on the auxiliary frame 1 (AF1) was significantly lower than expected by design, due to the interfaces introduced by the complementary isolation pads (CIPs) (for thermal management). So, as the pitch performance of the HD-DCM can be still improved by nearly a factor 2 by preventing its resonance from being excited by flow-induced vibrations, a design upgrade capable of

maintaining the thermal isolation but improving dynamics should be considered. One option that has been partly evaluated relied on damping solutions, which presents challenges due to the ultra-high vacuum and cryogenic conditions. Another more straightforward option is based on an alternative arrangement of embedded flexures, which shall be tested soon for the so-called HD-DCM-Lite [4, 5] — a slightly modified model of the HD-DCM for faster scanning that is about to be commissioned for two more beamlines at Sirius/LNLS.

- **Long-stroke stage:** For the sake of simplicity and initial development effort, the long-stroke stage was designed with a stepper motor and a friction-based mechanism, as described in Chapter 2. As expected, however, it negatively affects scanning performances, particularly in the lower energy range [6], for which its use is inevitable and larger gap strokes and velocities are needed, as discussed in Chapter 5. Hence, an upgraded version of the HD-DCM should definitely consider a replacement of this particular module. In preliminary brainstorming sessions about future options, concepts with negative stiffness to compensate for stiffness of the folded-leafsprings, tunable gravity compensators for the module mass, and force motors have been considered. As a remark, in the design of the HD-DCM-Lite the long-stroke module was eliminated as simpler shortcut to reduce the rotational mass moment of inertia of the core of the system (at the cost of operational energy range), so that a long-stroke upgrade for the HD-DCM design remains an open opportunity.
- **Rotary stage:** Given the load magnitude, the vacuum environment context and the motion quality required from the main rotary stage, the first version of the HD-DCM relied on a commercial model using roller bearings and a direct drive motor. So far, this choice has been sufficient for all practical purposes. However, should significantly smoother and faster scanning speeds be requested in the future, then improvements also in the rotary mechanism may be needed. In this case, in-vacuum air-bearing or magnetically-levitated concepts may be developed. On top of that, a long-stroke and short-stroke design also for the rotary mechanism might be of interest.
- **Floor isolation:** Again for the sake of simplicity and development effort in a first version of the system, the HD-DCM supporting granite bench was developed using a high-stiffness concept, as described in Chapters 2 and 3. However, as demonstrated in the Dynamic Error Budgeting analysis in Chapter 3, the floor disturbances is a significant (and often dominant) contribution to the current performance levels. Thus, if desired, further development toward an isolated suspended bench — probably an active system with the necessary level of coupling to the X-ray beam — could be considered.
- **Damping technology:** Beyond immediate benefits to the dynamics of the metrology frame 1 (MF1), further studies on damping technologies can potentially

lead to even lower positioning errors, either because of the direct attenuation of disturbance effects or possibilities in bandwidth increase for superior disturbance rejection capacity.

### 6.2.2 Control-related Topics

- **Beamline integration:** As indicated in Chapters 4 and 5, there must be a high degree of integration and performance compatibility between the HD-DCM and other beamline components — the X-ray source being the most critical one. Only the first steps have been given in this direction, with a long development work ahead before ultimate experimental performances can be achieved (see [7] for a similar discussion).
- **Thermal:** Related to beamline integration, a sensitive issue for monochromators under high power loads is the optical effect in the thermally affected area of the first crystal [8–10]. Hitherto at Sirius, the HD-DCM units have been subjected to a power load limited to only about one tenth of its maximum design power, due to the parameters of the commissioning undulator sources (APU22 in Chapter 5) and limited current in the storage ring. In the near future, thermal aspects will need to be more extensively investigated, particularly for energy scans. They may include among others: i) transient thermal effects that are invisible to the embedded metrology loop, and ii) possible scanning solutions that must include slit aperture control and/or mirror bending compensations to preserve the beamline optical design. This may lead to requirements for more sophisticated control and mechanical design in these complementary elements as well.
- **Feedforward:** Mostly due to practical priorities, the HD-DCM has been operated so far solely according to a feedback control strategy, as discussed in Chapters 3, 4 and 5. One may expect, however, that improved scanning performances could be reachable using feedforward control, particularly in the lower energy range, with longer strokes and faster motion requirements. This is an obvious thread that should be explored as soon as possible.
- **Trajectory optimization:** Together with feedforward, trajectory optimization strategies according to various criteria can be investigated. This is related to scanning routines that could be linear in energy, but not in the Bragg angle or inter-crystal gap, or vice-versa, depending on the most performance-limiting factors. To that end, the trajectory possibilities of the X-ray source for energy variation extend the boundaries of the problem beyond the HD-DCM, as discussed in Chapters 4 and 5.
- **Iterative learning control:** In line with feedforward and trajectory optimization toward scanning performance improvements for the HD-DCM, investigations

on Iterative Learning Control (ILC) strategies should be considered, since the potential for nearly perfect tracking performance has been demonstrated in the last few years for a number of mechatronic systems [11].

- **Adaptive control:** The plant model shown in Chapter 3 provides a more accurate representation of the system for the high-energy range, i.e., with Bragg angles below  $10^\circ$ . As the instrument travels to its lower-energy range, i.e., toward  $60^\circ$ , however, small plant modifications might occur due to, for example: i) more significant changes in the center of gravity of the system with respect to the main rotary axis due to the displacement of the long-stroke module; and ii) different loads and positions in the folded-leafsprings of the long-stroke and the short-stroke frames. Further examination of the plant and adaptive control strategies might offer possibilities in terms of bandwidth and performance optimization over the whole operational range of the HD-DCM.

### 6.2.3 Derived and Correlated Instruments Perspectives

- **Horizontal-offset HD-DCM:** Even though horizontal-offset DCMs historically demonstrate higher stand-still performance than their vertical-offset counterparts, the development of a horizontal-offset HD-DCM should be considered for at least two reasons: i) the typical inter-crystal pitch stability levels are still at best nearly a factor two larger than what has been proven by the HD-DCM presented in this thesis; and ii) the existing instruments suffer from the scanning limitations of standard high-stiffness designs. Indeed, horizontal-offset DCMs occupy an important niche, particularly in beamlines with vertically-polarized beams in tender X-rays, and the technology developed for the HD-DCM can be promptly adapted to a horizontal configuration by using the proper design methodology.
- **UV and soft X-rays Monochromators:** Similarly, the extrapolation of the HD-DCM architecture for lower-energy monochromator types could potentially benefit also the ultra-violet and soft X-ray research communities with higher performance systems.
- **X-ray Mirrors:** Along with monochromators, as a critical class of beamline instruments, synchrotron mirrors may greatly benefit from alternative designs. Indeed, following the HD-DCM track, the first generation of X-ray mirrors for Sirius have already incorporated not only its design methodology, but also many of its mechanical and thermal design concepts [12–14]. Nevertheless, more advanced control-based alternatives and mechanisms including mirror benders have not yet been explored.
- **End-stations:** After a few promising beamline results, including the HD-DCM itself, solutions relying on more advanced control-based options for the sample environments as well are now starting become more popular [15, 16]. At Sirius, so

far two X-rays nanoprobe have been developed with similar concepts, one being operation since 2020 and the other under assembly [17–19]. Yet, this is only the beginning of a new and promising field in synchrotron instrumentation.

## References

- [1] Butler H. 2011 *IEEE Control Syst. Mag.* **31**(5) 28
- [2] Heertjes M.F. *et al.* 2020 *Proc. 2020 Am. Control Conf. (ACC)* (IEEE) 3686–3703
- [3] Jabben L. 2007 *Mechatronic Design of a Magnetically Suspended Rotating Platform* Ph.D. thesis Delft University of Technology
- [4] Perna A.V. *et al.* 2021 *Proc. 11th Mech. Eng. Des. of Synchrotron Radiat. Equip. and Instrum. (MEDSI'20)* (JACoW Publishing) 203–206
- [5] Albuquerque G.S. *et al.* 2021 *Proc. 18th Int. Conf. on Acc. and Large Exp. Phys. Control Systems (ICALEPCS'21)* (JACoW Publishing) 619–624
- [6] Geraldès R.R. *et al.* 2018 *Proc. 10th Mech. Eng. Des. of Synchrotron Radiat. Equip. and Instrum. (MEDSI'18)* (JACoW Publishing) 147–152
- [7] Hidas D. *et al.* 2022 *Nucl. Instrum. Methods Phys. Res. A* **1031** 166505
- [8] Zhang L. *et al.* 2013 *J. Phys.: Conference Series* vol. 425 (IOP Publishing) 052008
- [9] Zhang L. *et al.* 2013 *J. Synchrotron Rad.* **20**(4) 567
- [10] Chumakov A.I. *et al.* 2014 *J. Synchrotron Rad.* **21**(2) 315
- [11] Oomen T. 2020 *Proc. 2020 IEEE 16th Int. Workshop on Adv. Motion Control (AMC)* (IEEE) 65–72
- [12] Geraldès R.R. *et al.* 2018 *Proc. 10th Mech. Eng. Des. of Synchrotron Radiat. Equip. and Instrum. (MEDSI'18)* (JACoW Publishing) 173–178
- [13] Moreno G.B.Z.L. *et al.* 2021 *Proc. 11th Mech. Eng. Des. of Synchrotron Radiat. Equip. and Instrum. (MEDSI'20)* (JACoW Publishing) 111–114
- [14] Meyer B.C. *et al.* 2021 *Synchrotron Radiat. News* **34**(6) 4
- [15] Deng J. *et al.* 2019 *Rev. Sci. Instrum.* **90**(8) 083701
- [16] Kelly J. *et al.* 2022 *Rev. Sci. Instrum.* **93**(4) 043712
- [17] Tolentino H.C.N. *et al.* 2019 *Proc. SPIE 11112, X-ray Nanoimaging: Instruments and Methods IV* vol. 11112 1111206
- [18] Geraldès R.R. *et al.* 2021 *Proc. 11th Mech. Eng. Des. of Synchrotron Radiat. Equip. and Instrum. (MEDSI'20)* (JACoW Publishing) 292–295
- [19] Geraldès R.R. *et al.* 2023 To be published *Proc. XRM2022*

# Appendices



# APPENDIX A

---

## Complementary DCM Geometrical Description

---

The most sensitive geometrical properties of a DCM were presented and discussed in detail in Chapter 2 and Chapter 5. However, a few more geometrical relations are needed for the complete set of specifications and the design choices presented therein. Hence, a complement is provided in this appendix.

### A.1 Nominal Geometry

As a brief reminder, the basic equation for the DCM geometry is the one defining the required gap  $g$  between crystals as a function of the Bragg angle  $\theta_B$ , such that a constant offset  $H$  is obtained, i.e.,

$$g(\theta_B) = \frac{H}{2 \cos(\theta_B)}. \quad (\text{A.1})$$

Next, the beam footprint  $b$  can be written as a function of  $\theta_B$  and the incoming beam size  $a$  as

$$b(\theta_B) = \frac{a}{\sin(\theta_B)}, \quad (\text{A.2})$$

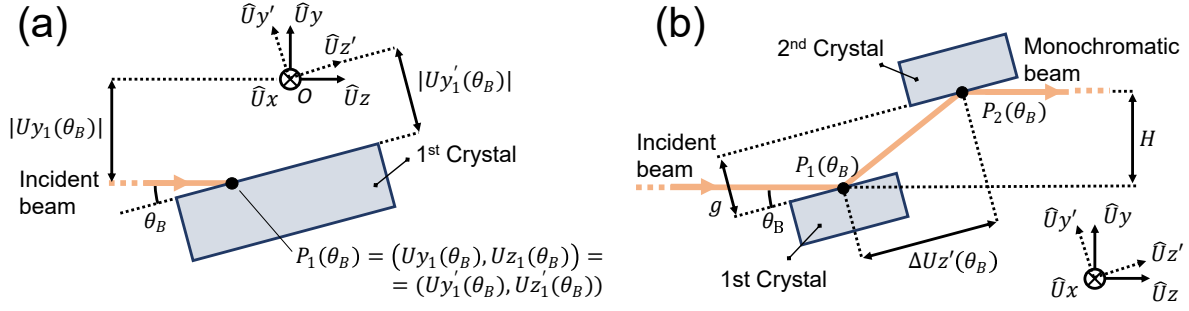
which: i) defines a minimum crystal length in which the beam is spread (taking the simple case without intentionally large asymmetric-cut crystals); and ii) is important in terms of power load distribution on the first crystal.

Then, the last two parameters that close the nominal DCM geometry are the distances from the main rotation axis  $O$  to the incident beam and to the surface of the first crystal, as represented in Figure A.1(a) by  $|Uy_1(\theta_B)|$  and  $|Uy'_1(\theta_B)|$ , respectively. Indeed, as indicated in Figure A.1(b), together with  $g$  and  $H$  they define the points of impact of the center of the beam at the first and second crystals, i.e.,  $P_1(\theta_B) = (Uy'_1(\theta_B), Uz'_1(\theta_B))$  and  $P_2(\theta_B) = (Uy'_2(\theta_B), Uz'_2(\theta_B))$ , respectively.

In the form of equations, it yields

$$\begin{aligned} Uz'_1(\theta_B) &= \frac{Uy_1(\theta_B) - Uy'_1(\theta_B) \cdot \cos(\theta_B)}{\sin(\theta_B)}, \\ Uz'_2(\theta_B) &= Uz'_1(\theta_B) + \Delta Uz'(\theta_B) = Uz'_1(\theta_B) + \frac{H}{2 \cdot \sin(\theta_B)}, \end{aligned} \quad (\text{A.3})$$





**Figure A.1:** Geometric description of the nominal beam incidence points on the first and second crystals, respectively: (a)  $P_1(\theta_B)$ , given by the inertial coordinate  $Uy_1(\theta_B)$  and the rotating coordinate  $Uy'_1(\theta_B)$  with respect to the rotation point at the origin ( $O$ ); and (b)  $P_2(\theta_B)$ , defined by  $P_1(\theta_B)$  and the downstream distance  $\Delta Uz'(\theta_B)$  (coordinate system represented out of  $O$  for readability).

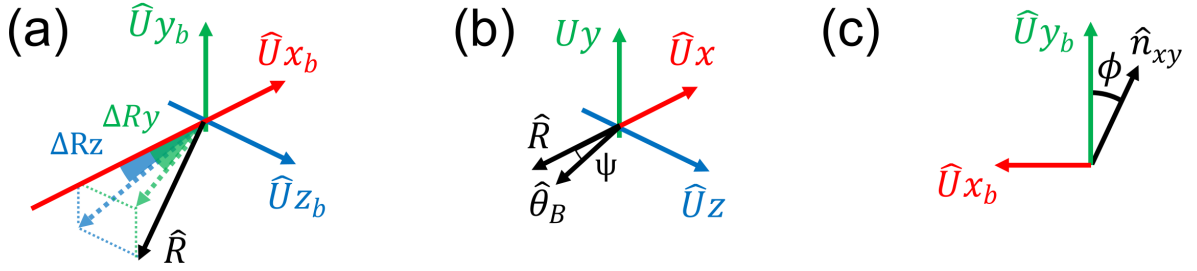
where  $\Delta Uz'(\theta_B)$  is the downstream distance between impact points in the rotated coordinate system.

Thus, it is clear that, except for  $g$  and  $\Delta Uz'$ , which have a closed dependence on  $\theta_B$  and  $H$ , the remaining geometric parameters in a DCM are relatively free to be controlled in countless motion configurations. In other words, provided that the equations for  $g$  and  $\Delta z'$  are fulfilled, in principle the rotation axis may be freely moved in the  $\hat{U}y\hat{U}z$ -plane and the crystals in the  $\hat{U}y'\hat{U}z'$ -plane at the designers best convenience. So, given the operational range of  $\theta_B$  and the desired  $H$ , equations Equation (A.1), Equation (A.2) and Equation (A.3) can be used together to determine crystal sizes and the desired motion degrees of freedom (DoFs).

In practice, these choices are eventually driven by manufacturing limitations of the crystals, convenient motion specifications, beam power effects, cooling systems boundary conditions and dynamic performance. In the HD-DCM, the choice was for  $Uy_1 = Uy'_1 = 0$ , which means having the rotation axis at the surface of the first crystal and at the height of the incoming beam. Hence, with  $Uz'_1 = 0$  and without additional motion DoFs, dynamics, metrology and cooling benefited from having the first crystal as short as possible, fixed with respect to the main rotating structure, and with the hot-spot caused by the incoming beam at a constant center symmetrically placed in the crystal. As for the second crystal, being long enough to comply with  $b$  and  $\Delta Uz'$ , a single translational DoF is required for  $Uy'_2(\theta_B) = g(\theta_B)$ .

## A.2 Alignment Effects

Once the basic geometry of a DCM is understood, the sensitivities related to parasitic alignment errors can be introduced.



**Figure A.2:** Vector representation of small misalignment angles responsible for energy selection errors and virtual source variations:  $\Delta Ry$ , the rotation angle of the DCM main rotation unit vector  $\hat{R}$  in the main coordinate system (MCS) around the  $\hat{U}y_b$ -axis in the beamline coordinate system (BCS);  $\Delta Rz$ , the rotation angle of  $\hat{R}$  around  $\hat{U}z_b$ ;  $\psi$ , the angle between the actual Bragg angle  $\hat{\theta}_B$  and  $\hat{R}$ ; and  $\phi$ , the angle between  $\hat{U}y_b$  and the projection of the crystal lattice normal vector  $\hat{n}$  in the  $\hat{U}x_b\hat{U}y_b$ -plane, i.e.,  $\hat{n}_{xy}$ .

### A.2.1 Rotation Axis

Referring to the vector representations in Figure A.2 and initially assuming the two crystals to be perfectly parallel to each other, a first set of geometry-related sensitivities and errors can be extracted from the alignment and orthogonality among (see also Chapter 2 and Chapter 5): i) the inertial beamline coordinate system (BCS), given by  $(\hat{U}x_b, \hat{U}y_b, \hat{U}z_b)$ ; ii) the DCM nominal main rotation axis  $\hat{R}$ , as negative  $\hat{U}x$  in the main coordinate system (MCS), given by  $(\hat{U}x, \hat{U}y, \hat{U}z)$ ; and iii) the  $\hat{\theta}_B$ , which is the actual Bragg axis, defined according to Bragg's equation by the beam in  $\hat{U}z_b$  and actual normal vector to the crystal lattice  $\hat{n}$ .

Within small-angle approximations, these errors can be approximately described in terms of the four small angles:  $\Delta Ry$ , the rotation angle of  $\hat{R}$  around  $\hat{U}y_b$ ;  $\Delta Rz$ , the rotation angle of  $\hat{R}$  around  $\hat{U}z_b$ ;  $\psi$ , the angle between  $\hat{\theta}_B$  and  $\hat{R}$ ; and  $\phi$ , the angle between the  $\hat{U}y_b$  and the projection of  $\hat{n}$  in the  $\hat{U}x_b\hat{U}y_b$ -plane, i.e.,  $\hat{n}_{xy}$ . The first three are primary errors, which result from alignment limitations or motion errors, whereas the last results from one or more of them. Indeed, it can be shown that  $\phi$  can be individually related to  $\Delta Ry$ ,  $\Delta Rz$  and  $\psi$  via

$$\begin{aligned}\phi_{\Delta Ry} &= \Delta Ry \cdot \tan(\theta_R), \\ \phi_{\Delta Rz} &= \frac{-\Delta Rz \cdot [1 - \cos(\theta_R)]}{\cos(\theta_R)}, \\ \phi_{\psi} &= \frac{\psi}{\cos(\theta_R)},\end{aligned}\tag{A.4}$$

where  $\theta_R$  is the nominal rotation angle around  $\hat{R}$  — which slightly differs from the actual Bragg angle  $\theta_B$  under the (inevitable) occurrence of  $\Delta Ry$ ,  $\Delta Rz$  and/or  $\psi$ . For  $\vartheta$  generically representing any of these three small angles, it can be shown that

$$\theta_B = \arcsin[(1 - \vartheta^2/2) \cdot \sin(\theta_R)].\tag{A.5}$$

Then firstly,  $\Delta\theta_R = \theta_B - \theta_R$  can be directly used to evaluate small energy selection errors and nominal gap mismatch, for instance. Next, since the projection of the offset

$H$  in the  $\hat{U}_x\hat{U}_y$ -plane actually lies along the  $\hat{n}_{xy}$ -axis, the monochromatic exit may in practice suffer from small shifts in the  $\hat{U}_x\hat{U}_y$ -plane if  $\phi \neq 0$ , hence varying the position of the virtual source over the operational energy range. Assuming that  $g$  could be nominally adjusted with respect to  $\theta_B$ , horizontal  $\delta x$  and vertical  $\delta y$  displacement components of the virtual source can be written as

$$\begin{aligned}\delta x_\phi &= H \cdot \sin(\phi), \\ \delta y_\phi &= H \cdot [1 - \cos(\phi)].\end{aligned}\tag{A.6}$$

These effects require  $\vartheta$  to be in the order of a few hundred microradians and/or further calibrations for sufficient energy and beam position accuracy.

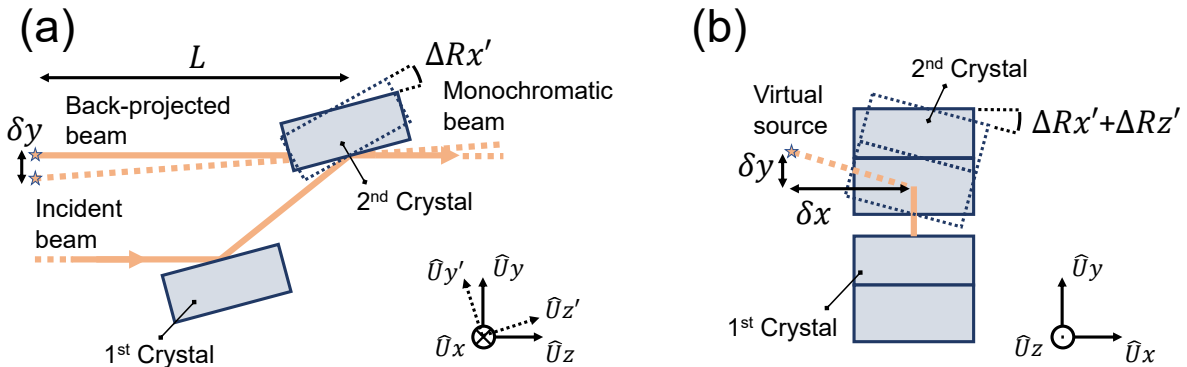
### A.2.2 Crystal-to-Crystal Parallelism

The second set of geometry-related sensitivities and errors concerns the parallelism between crystals, i.e., *pitch* for the rotation parallel to the Bragg axis ( $Rx'$ ) and *roll* for the complementary axis ( $Rz'$ ). First and foremost, they must satisfy the diffraction conditions and ideally maximize the monochromatic beam flux. For pitch this is directly derived from the Darwin width boundaries (Chapter 5), whereas for roll Equation (A.5) can be used for an equivalent analysis.

Then, in addition to that, they may be directly related to missteering of the monochromatic beam, thus varying the position of the virtual source, as depicted in Figure A.3. Without considering the rotation-axis errors discussed in the previous subsection for the sake of simplicity, it can be seen that pitch variations  $\Delta Rx'$  with respect to the first crystal would have an effect in the  $\hat{U}_x\hat{U}_z$ -plane only, whereas roll variations ( $\Delta Rz'$ ) would be related to both horizontal  $\delta x$  and vertical  $\delta y$  (though significantly smaller) components. In equations, within small-angle approximations, these shifts can be described as a function of the distance to the source  $L$  by

$$\delta y_{\Delta Rx'} = 2 \cdot \Delta Rx' \cdot L,\tag{A.7}$$

$$\begin{aligned}\delta x_{\Delta Rz'} &= 2 \cdot \Delta Rz' \cdot \sin \theta_B \cdot L, \\ \delta y_{\Delta Rz'} &= 2 \cdot (\Delta Rz')^2 \cdot \sin \theta_B \cdot \cos \theta_B \cdot L,\end{aligned}\tag{A.8}$$



**Figure A.3:** Schematic of the effect of DCM pitch  $\Delta Rx'$  and roll  $\Delta Rz'$  variations in the horizontal  $\delta x$  and vertical  $\delta y$  shift of the virtual source at a given distance  $L$ .

such that, according to typical source sizes and distances in 4th-generation synchrotron beamlines, specifications as low as  $\Delta Rx' \approx 10\text{ nrad}$  and  $\Delta Rz' \approx 100\text{ nrad}$ , or lower, may be defined to preserve beam positioning and apparent source size.

### A.2.3 Virtual Source Displacement

Therefore, it turns out that the virtual source position errors are actually given by a combination of effects, i.e.,

$$\begin{aligned}\delta x &= \delta x_H + \delta x_\phi + \delta x_{\Delta Rz'}, \\ \delta y &= \delta y_H + \delta y_\phi + \delta y_{\Delta Rx'} + \delta y_{\Delta Rz'}.\end{aligned}\tag{A.9}$$

where  $\delta x_H$  and  $\delta y_H$  represent shifts due to mismatching between the  $g$  and  $\theta_B$  (see Chapter 5).

Consequently, one option is using these equations for error separation strategies in fine alignment if necessary, whereas positioning compensation alternatives in both components can be envisioned thanks to their multiple contributions — particularly via calibrated setpoints in gap, pitch and roll, which tend to be the most sensitive parameters to  $\delta x$  and  $\delta y$ . The HD-DCM, being the first to implement embedded relative metrology between crystals and designed under high-repeatability concepts, provides ideal elements for robust calibration strategies.



# APPENDIX B

---

## Dynamic Substructuring and Modal State-Space Representation

---

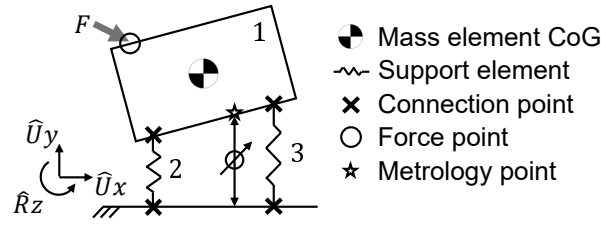
The Dynamic Error Budgeting (DEB) methodology has proven to be an essential tool in the development of the HD-DCM according to a predictive design approach. Therefore, considering that the level presented in Chapter 3 might be excessively abstract to the less experienced designer, this appendix provides a more comprehensive step-by-step summary guide about the *Dynamic Substructuring* modeling work and the chosen *modal state-space representation*. Rather than proposing new methods or solutions, the main purpose here is recapitulating and arranging known theory and concepts, with the intention that it can be more accessible and straightforwardly applicable by the interested reader.

### B.1 Dynamic Substructuring

Dynamic Substructuring and Structural Dynamic Modification techniques are equivalent approaches that allow building more complex dynamic models from substructures (or subparts). Among other points: the dynamic behavior of complex structures that, otherwise, would be impossible or too costly to be analyzed as a whole can be evaluated; local effects can be investigated and understood; and modeled and experimental components can be combined. At convenience, the systems can be represented and handled in the physical, the frequency and/or the modal domains, whereas space-state formulation may be used particularly to address damping conditions that cannot be properly handled via proportional approximations [1–3].

Substructures are discrete structures that can be described as nodes or functions with a finite set of degrees of freedom (DoFs) and coupled to each other at interfaces. In particular, the lumped-mass description with rigid body assumptions (as used in the HD-DCM mechanical models) is, perhaps, the simplest possible substructuring construction (see Figure B.1 for an illustration). Yet, in addition to the practical advantages with respect to larger FEA (finite element analysis) models, the lumped-mass representation prevents truncation issues in model reductions and difficulties related to rotational DoFs, which are two of the main issues in substructuring applications [1, 2].

As a rule, coupling between substructures must satisfy two conditions, namely: the compatibility of displacements and the equilibrium of forces in the DoFs of the



**Figure B.1:** Lumped mass model of a single body with three degrees of freedom (DoFs) ( $U_x$ ,  $U_y$  and  $R_z$ ) in a two-dimensional space, exemplifying Dynamic Substructuring (DS) with a mass element (1) and its center of gravity (CoG), and support elements (2 and 3), coupled at connection points. Also illustrated are points of interest for force and metrology, which can be geometrically related to the CoG for disturbance points, actuators and sensors in the subsequent mechatronic model.

interfaces, which are known as *compatibility* and *equilibrium* conditions, respectively. Yet, using a formalism choosing only displacements and no forces as the independent coupling DoFs, models can be made according to a so-called *primal formulation in the physical domain*, as described by de Klerk [1]. Although coupling in the physical domain is very uncommon in the experimental community, because it is impossible to experimentally obtain the full physical description of the real structures, the physical properties of the systems, particularly within the lumped-mass description, can be easily found from CAD (computer aided design) softwares.

Indeed, the substructures in the physical domain can be simply described by stacked matrices for mass  $\mathbf{M}_s$ , damping  $\mathbf{D}_s$  and stiffness  $\mathbf{K}_s$ , as stated by the equation of motion as a function of time  $t$ ,<sup>1</sup> i.e.,

$$\mathbf{M}_s \ddot{\mathbf{s}}(t) + \mathbf{D}_s \dot{\mathbf{s}}(t) + \mathbf{K}_s \mathbf{s}(t) = \mathbf{f}_s(t) + \mathbf{g}_s(t), \quad (\text{B.1})$$

where  $\mathbf{s}$  denotes the stacked (or appended) vector of DoFs in the substructures,  $\mathbf{f}_s$  is the external force vector and  $\mathbf{g}_s$  is the vector of forces connecting different parts of the substructures, i.e. the constraining forces. Here, for the sake of simplicity and compliance with the DEB assumptions, the system is assumed to be time invariant, i.e., with constant parameter, and linear, i.e., with matrices that are independent of the state of the system, but the formalism itself should be valid also for time-varying and non-linear systems. Then, handling  $n$  multiple substructures in the system may be described by block-diagonal matrices and stacked vectors as

$$\begin{aligned} \mathbf{M}_s &\triangleq \text{diag}(\mathbf{M}_1, \dots, \mathbf{M}_n); & \mathbf{D}_s &\triangleq \text{diag}(\mathbf{D}_1, \dots, \mathbf{D}_n); & \mathbf{K}_s &\triangleq \text{diag}(\mathbf{K}_1, \dots, \mathbf{K}_n); \\ \mathbf{s} &\triangleq [\mathbf{s}_1, \dots, \mathbf{s}_n]^T; & \mathbf{f}_s &\triangleq [\mathbf{f}_1, \dots, \mathbf{f}_n]^T; & \mathbf{g}_s &\triangleq [\mathbf{g}_1, \dots, \mathbf{g}_n]^T. \end{aligned} \quad (\text{B.2})$$

As a choice, bodies and mechanical interfaces can be completely separated and modeled as independent substructures. In this case, the bodies are described as stiffnessless substructures, i.e., with null stiffness matrices, and mass matrices that are

<sup>1</sup>In the remaining equations in the text the explicit time dependence is omitted for simplicity.

either approximated analytically (especially for initial models) or extracted from a CAD software. The interfaces, on the other hand, are modeled as massless springs, i.e., with null mass matrices, and linear and torsional stiffnesses that are approximated analytically or extracted from finite element simulations. Finally,  $\mathbf{s}$  includes the center of gravity (CoG) coordinates of up to 6 dimensions in space (i.e.  $U_x, U_y, U_z, R_x, R_y$  and  $R_z$ ) and interfaces coordinates with respect to the CoGs for each body.

The compatibility and equilibrium conditions can be respectively expressed by

$$\mathbf{B}\mathbf{s} = \mathbf{0} \quad \text{and} \quad \mathbf{L}^T \mathbf{g}_s = \mathbf{0}, \quad (\text{B.3})$$

where  $\mathbf{B}$  is known as the signed Boolean matrix and  $\mathbf{L}$  as the Boolean localization matrix. The Boolean reference results from the fact that these matrices are often consisting mostly of zero elements and only sparse  $-1$  and  $1$  elements connecting the DoFs. In  $\mathbf{B}$ , the non-zero elements assign pairs of DoFs that should be coincident, i.e. have the same displacement; whereas in  $\mathbf{L}$ , they assure action and reaction forces equilibrium among the substructures. Even though in many cases  $\mathbf{B}$  and  $\mathbf{L}$  are actually non-Boolean, the names remain and the discussions still hold true [1]. In the HD-DCM, for instance,  $\mathbf{B}$  and  $\mathbf{L}$  are non-Boolean due to its multibody nature and lumped-mass representation, with lever-arms taken into consideration over rigid-body geometries.

The primal formulation is finally obtained by eliminating the interface forces as unknowns and defining a *generalized unique set of displacement DoFs*  $\mathbf{q}$  with

$$\mathbf{s} = \mathbf{L}\mathbf{q}. \quad (\text{B.4})$$

Indeed, in this case  $\mathbf{L}$  represents the nullspace or the kernel of  $\mathbf{B}$  — once from Equation (B.3)  $\mathbf{B}\mathbf{s} = \mathbf{B}\mathbf{L}\mathbf{q} = \mathbf{0} \forall \mathbf{q}$  —, such that only one Boolean matrix must be created during the assembly process and the second one becomes readily available. Then, using Equation (B.3) and Equation (B.4), Equation (B.1) becomes

$$\begin{aligned} \mathbf{L}^T \mathbf{M}_s \mathbf{L} \ddot{\mathbf{q}} + \mathbf{L}^T \mathbf{D}_s \mathbf{L} \dot{\mathbf{q}} + \mathbf{L}^T \mathbf{K}_s \mathbf{L} \mathbf{q} &= \mathbf{L}^T \mathbf{f}_s + \mathbf{L}^T \mathbf{g}_s, \\ \widetilde{\mathbf{M}} \ddot{\mathbf{q}} + \widetilde{\mathbf{D}} \dot{\mathbf{q}} + \widetilde{\mathbf{K}} \mathbf{q} &= \widetilde{\mathbf{f}}. \end{aligned} \quad (\text{B.5})$$

where  $\widetilde{\mathbf{M}}$ ,  $\widetilde{\mathbf{D}}$  and  $\widetilde{\mathbf{K}}$  are known as primal-assembled matrices<sup>2</sup>, and  $\mathbf{g}$  vanishes as desired.

At this point, one may realize that, although the generalized unique set of DoFs  $\mathbf{q}$  clears the redundant DoFs existing in  $\mathbf{s}$ ,  $\mathbf{q}$  does not necessarily relate to meaningful physical coordinates. This is because it is simply the outcome from the mathematical procedure in the calculation of  $\mathbf{L}$ , according to the primal formulation constraint. In this case, a change of basis can be used via a transformation matrix  $\mathbf{A}$  to take the unique set of DoFs  $\mathbf{q}$  to a more convenient unique set of DoFs  $\mathbf{p}$  with

$$\mathbf{q} = \mathbf{A}\mathbf{p}. \quad (\text{B.6})$$

---

<sup>2</sup>As a practical remark, although  $\widetilde{\mathbf{M}}$ ,  $\widetilde{\mathbf{D}}$  and  $\widetilde{\mathbf{K}}$  are physically required to be symmetrical, numerical errors in the calculation of  $\mathbf{L}$  from the kernel of  $\mathbf{B}$  may result in asymmetric matrices. This can be approximately corrected by using a transposing average and redefining these matrices, such that  $\widetilde{\mathbf{M}} = (\widetilde{\mathbf{M}}_0 + \widetilde{\mathbf{M}}_0^T)/2$  for the mass matrix, where  $\widetilde{\mathbf{M}}_0$  refers to the initially calculated primal-assembled mass matrix, and equivalently for  $\widetilde{\mathbf{D}}$  and  $\widetilde{\mathbf{K}}$ .



Hence, the equation of motion of the coupled system in the physically-related basis becomes

$$\begin{aligned} \mathbf{A}^T \widetilde{\mathbf{M}} \mathbf{A} \ddot{\mathbf{p}} + \mathbf{A}^T \widetilde{\mathbf{D}} \mathbf{A} \dot{\mathbf{p}} + \mathbf{A}^T \widetilde{\mathbf{K}} \mathbf{A} \mathbf{p} &= \mathbf{A}^T \widetilde{\mathbf{f}}, \\ \mathbf{M} \ddot{\mathbf{p}} + \mathbf{D} \dot{\mathbf{p}} + \mathbf{K} \mathbf{p} &= \mathbf{f}. \end{aligned} \quad (\text{B.7})$$

with one remaining question regarding the choice of  $\mathbf{A}$ .

Among other options, an obvious choice for the unique set of DoFs  $\mathbf{p}$  is the coordinates of the CoG of the bodies in the model. In this case, by recalling that all these desired DoFs are already present in the stacked vector  $\mathbf{s}$ , it turns out that  $\mathbf{p}$  is simply a subset of  $\mathbf{s}$ , such that  $\mathbf{A}$  is the inverse of a subset  $\mathbf{L}_p$  of  $\mathbf{L}$ , i.e.,

$$\mathbf{s} = \mathbf{L} \mathbf{q} = \mathbf{L} \mathbf{A} \mathbf{p} \quad \text{and} \quad \mathbf{A} = \mathbf{L}_p^{-1}. \quad (\text{B.8})$$

Indeed,  $\mathbf{L}_p$  is formed by the selection of the rows of  $\mathbf{L}$  that take the unique set of DoFs  $\mathbf{q}$  to the DoFs of the CoG of the bodies in the stacked vector  $\mathbf{s}$  in Equation (B.4).

## B.2 Modal Representation of a Complete Model

Having described the procedure to integrate individual mechanical parts into a coupled mechanical model, attention must be driven towards damping assumptions and the formalization of the complete mechanical structure model. First of all, the equation of motion Equation (B.7) can be conveniently adapted to include external forces that are created by displacements of an inertial reference to which the system is attached. In the HD-DCM, this consists in displacements of the floor, such that the complete equation of motion can be written, for example, as

$$\mathbf{M} \ddot{\mathbf{p}} + \mathbf{D} \dot{\mathbf{p}} + \mathbf{K} \mathbf{p} = \mathbf{f} + \mathbf{D}_f \dot{\mathbf{s}}_f + \mathbf{K}_f \mathbf{s}_f, \quad (\text{B.9})$$

where  $\mathbf{s}_f$  and  $\dot{\mathbf{s}}_f$  are, respectively, displacement and velocity external inputs from the floor in the corresponding floor interface DoFs of the stacked vector  $\mathbf{s}$ , and  $\mathbf{D}_f$  and  $\mathbf{K}_f$  are adapted damping and stiffness matrices for the corresponding DoFs.

Next, if a proportional damping approximation can be assumed, damping can be easily applied from a modal representation. In this case, the well-known mass-normalized modal form calculated from the eigenvalue equation of the undamped and unforced system has

$$\mathbf{p} = \Phi \eta, \quad \Phi^T \mathbf{M} \Phi = \mathbf{I} \quad \text{and} \quad \Phi^T \mathbf{K} \Phi = \Omega^2, \quad (\text{B.10})$$

where  $\Phi$  is the modal matrix of mass-normalized eigenvectors,  $\eta$  is the modal vector,  $\mathbf{I}$  is the identity matrix and  $\Omega^2$  is the squared diagonal matrix of eigenvalues (i.e., the system resonance frequencies).

Then, after some manipulation, Equation (B.9) can be rewritten in the modal form as

$$\ddot{\eta} + 2\zeta \Omega \dot{\eta} + \Omega^2 \eta = \Phi^T \mathbf{f} + \Phi^T \mathbf{D}_f \dot{\mathbf{u}}_f + \Phi^T \mathbf{K}_f \mathbf{u}_f, \quad (\text{B.11})$$

where  $\zeta$  is the diagonal damping ratio matrix, with the modal damping being written as  $\Phi^T \mathbf{D} \Phi = 2\zeta \Omega$ . Consequently, damping can be applied without ever addressing the damping coefficient of the interfaces directly. Still,  $\mathbf{D}$  can be partly recovered for the creation of  $\mathbf{D}_f$ , which is still explicit in Equation (B.11).

### B.3 State-Space Representation

To conclude, the mechanical model can be written in a linear state-space form using its conventional notation

$$\begin{aligned}\dot{\mathbf{x}}_{ss} &= \mathbf{A}_{ss} \mathbf{x}_{ss} + \mathbf{B}_{ss} \mathbf{u}_{ss} \\ \mathbf{y}_{ss} &= \mathbf{C}_{ss} \mathbf{x}_{ss},\end{aligned}\tag{B.12}$$

where  $\mathbf{x}_{ss} = [\mathbf{x}_{1ss}, \mathbf{x}_{2ss}]^T$  is the state vector,  $\mathbf{u}_{ss}$  the input vector,  $\mathbf{y}_{ss}$  the output vector,  $\mathbf{A}_{ss}$  the state matrix,  $\mathbf{B}_{ss}$  the input matrix and  $\mathbf{C}_{ss}$  the output matrix.

As the state-space matrices and vectors can be defined at best convenience, a suitable choice here allows for the elimination of the explicit dependence of the floor velocity input  $\dot{\mathbf{s}}_f$  in Equation (B.11), by making it naturally derived from  $\mathbf{s}_f$ . Indeed, defining  $\mathbf{x}_{1ss} = \eta$  as part of the state vector, Equation (B.11) can be rewritten as

$$\begin{aligned}\ddot{\eta} &= (-2\zeta \Omega \dot{\eta} + \Phi^T \mathbf{D}_f \dot{\mathbf{s}}_f) + (-\Omega^2 \eta + \Phi^T \mathbf{f} + \Phi^T \mathbf{K}_f \mathbf{s}_f), \\ \text{or } \ddot{\mathbf{x}}_{1ss} &= (-2\zeta \Omega \dot{\mathbf{x}}_{1ss} + \Phi^T \mathbf{D}_f \dot{\mathbf{s}}_f) + \ddot{\mathbf{x}}_{2ss},\end{aligned}\tag{B.13}$$

such that

$$\begin{aligned}\dot{\mathbf{x}}_{1ss} &= -2\zeta \Omega \mathbf{x}_{1ss} + \mathbf{x}_{2ss} + \Phi^T \mathbf{D}_f \mathbf{s}_f, \\ \dot{\mathbf{x}}_{2ss} &= -\Omega^2 \mathbf{x}_{1ss} + \Phi^T \mathbf{f} + \Phi^T \mathbf{K}_f \mathbf{s}_f.\end{aligned}\tag{B.14}$$

Writing Equation (B.14) in matrix format,

$$\dot{\mathbf{x}}_{ss} = \begin{bmatrix} -2\zeta \Omega & \mathbf{I} \\ -\Omega^2 & \mathbf{0} \end{bmatrix} \begin{bmatrix} \mathbf{x}_{1ss} \\ \mathbf{x}_{2ss} \end{bmatrix} + \begin{bmatrix} \mathbf{0} & \Phi^T \mathbf{D}_f \\ \Phi^T & \Phi^T \mathbf{K}_f \end{bmatrix} \begin{bmatrix} \mathbf{f} \\ \mathbf{s}_f \end{bmatrix},\tag{B.15}$$

$\mathbf{A}_{ss}$  and  $\mathbf{B}_{ss}$  are directly found as

$$\mathbf{A}_{ss} = \begin{bmatrix} -2\zeta \Omega & \mathbf{I} \\ -\Omega^2 & \mathbf{0} \end{bmatrix} \text{ and } \mathbf{B}_{ss} = \begin{bmatrix} \Phi^T & \Phi^T \end{bmatrix} \begin{bmatrix} \mathbf{0} & \mathbf{D}_f \\ \mathbf{I} & \mathbf{K}_f \end{bmatrix},\tag{B.16}$$

with the input vector given by  $\mathbf{u}_{ss} = [\mathbf{f}, \mathbf{s}_f]^T$ .

Now, considering a mechatronic system such as the HD-DCM, while  $\mathbf{s}_f$  already takes into account the particular geometry of the system via  $\mathbf{D}_f$  and  $\mathbf{K}_f$ , the action and reaction forces from actuators, as well as disturbance forces, may require one additional transformation. Indeed, if these forces do not act on the CoG of the bodies,  $\mathbf{u}_{ss}$  must be expanded, such that  $\mathbf{f}$  is replaced by the general force components vector

$\mathbf{f}_n$  at the required nodes, and the appropriate linear geometrical transformation matrix  $\mathbf{N}_f$  is used in  $\mathbf{B}_{ss}$ , i.e.,

$$\mathbf{B}_{ss} = [\Phi^T \quad \Phi^T] \begin{bmatrix} \mathbf{0} & \mathbf{D}_f \\ \mathbf{N}_f & \mathbf{K}_f \end{bmatrix}, \quad (\text{B.17})$$

with  $\mathbf{u}_{ss} = [\mathbf{f}_n, \mathbf{s}_f]^T$  and  $\mathbf{f} = \mathbf{N}_f \mathbf{f}_n$ .

Lastly, the output matrix  $\mathbf{C}_{ss}$  must be defined. To address, for instance, the CoG DoFs of all bodies,

$$\mathbf{y}_{ss} = \mathbf{p} = \Phi \eta = \Phi \mathbf{x}_{1ss} = [\Phi^T \quad \mathbf{0}] \mathbf{x}_{ss}, \quad (\text{B.18})$$

such that  $\mathbf{C}_{ss}$  becomes

$$\mathbf{C}_{ss} = [\Phi^T \quad \mathbf{0}]. \quad (\text{B.19})$$

Still, equivalently to what was just described for the forces, to address the sensor nodes and extract the desired metrology architecture from the CoG states in a mechatronic system, the appropriate linear geometrical transformation matrix  $\mathbf{N}_s$  must be used. In addition to that, any complementary true state, linear combination of states, and/or particular point of interest can be extracted with an appropriate linear transformation  $\mathbf{Y}_{ss}$ , so that  $\mathbf{C}_{ss}$  can be generically written as

$$\mathbf{C}_{ss} = \begin{bmatrix} \mathbf{N}_s \\ \mathbf{Y}_{ss} \end{bmatrix} [\Phi^T \quad \mathbf{0}]. \quad (\text{B.20})$$

## References

- [1] de Klerk D. *et al.* 2008 *AIAA Journal* **46**(5) 1169
- [2] Avitabile P. 2003 *Sound and Vibration* **37**(1) 14
- [3] D'Ambrogio W. and Sestieri A. 2004 *Shock and Vibration* **11**(3–4) 295

---

## Experimental Control Implementation

---

The essential aspects of the controller design approach used in the HD-DCM were presented and discussed within the modeling scope of the Dynamic Error Budgeting framework in Chapter 3. This appendix is dedicated to partially expanding and complementing the control implementation analysis by taking further experimental aspects into account. The discussion is focused on the crystal cage loops, i.e. gap GAP, pitch PTC and roll RLL, since they are the ones requiring high bandwidth and more stringent performance.

### C.1 Position- and Machine-specific Considerations

As detailed in Chapter 3, in which a high level of agreement between model predictions and experimental data is demonstrated, the predictive model-based design framework using the Dynamic Error Budgeting tools has been essential for the assertiveness of the HD-DCM project. Nevertheless, pure models are always practically limited, either due to modeling effort, complexity or machine-specific constraints, such that the two existing units of the HD-DCM now become an experimental source for extended research.

Firstly, in motion systems position-dependent aspects may result from disturbance variations, stiffness and/or mass distribution change, and sensors and actuators alignment and gain variations, to name a few (see also [1–3]). In the HD-DCM, a dominant dependence on the Bragg angle position might be expected, since between the 3° and 60° operation range changes include: inertia variation in the plant for the rotary stage mainly due to the displacement of the long-stroke module; stiffness variation in the folded-leaf springs guiding both the long-stroke and the short-stroke modules; shifts between the coils and the magnets in the short-stroke actuators, and in the interferometer paths with respect to the 1<sup>st</sup> crystal; and disturbance injection orientation from the floor and cooling vibrations components (see Chapter 2 and Chapter 3 for design details).

Furthermore, although the units were supposed to be equal, machine-specific characteristics may result, among other factors, from: disturbance idiosyncrasies, including floor vibrations from site to site, and flow-induced vibrations from the different liquid nitrogen (LN<sub>2</sub>) cryocooling systems and circuits; production variability, including

manufacturing tolerances, motor constants, and actuators and sensors alignment; and assembly specificities, including human factors (see also [2, 4]).

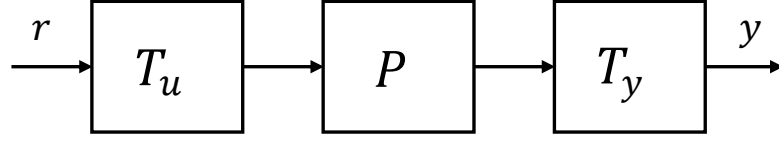
Preliminary results of the first unit of the HD-DCM under specific conditions did not take plant variations into account [5, 6], which might lead to robustness and stability issues as the full angular operation range of the machine is considered. Hence, a first step is identifying the systems in representative conditions, so that robust feedback controllers can be designed by considering the specific characteristics of each machine in various conditions. In the following section, the identification domain is expanded over the complete Bragg angular range and the two units are directly compared.

## C.2 System Identification

System identification consists of a broad field dedicated to analyzing systems, and using mathematical and statistical tools to describe their dynamic behavior [7]. And, although it is commonly used in advanced particle orbit control in synchrotron facilities since many years, its use for advanced mechatronic systems at beamlines is a more recent experience. At the LNLS, in particular, it was only within the scope of the HD-DCM project that this expertise started to be developed as an explicit technical competence. Hence, the initial work with the HD-DCM was carried out together with MI-Partners, using their extensive experience and toolboxes. Over time, the LNLS' engineering team has been independently working on developing its own set of tools and workflows, but this is still work in progress.

The first consequence of this context is that so far the system identification process for the HD-DCM is limited to its prototyping tool, namely, a Speedgoat's xPC hardware running at 10 kHz [8]. This means that hardware-related aspects, such as delay in digital/analog conversion boards, and sampling rate delay effects may differ from the final hardware implementation using NI's CompactRIO (cRIO) running at 20 kHz [9]. Another fact is that the existing system identification tools for the HD-DCM are still limited in terms of options regarding, for instance: i) white noise, multi-sine or single-sine; ii) data quality analysis for excitation gain optimization to improve signal-to-noise ratios; or iii) open-loop and closed-loop choices. Fortunately, this non-ideal condition has not been a critical factor for operation (partly because the final implementation runs at a faster sampling rate), yet it certainly limits further control optimizations in the system, so that a dedicate software toolbox for cRIO is currently under development and expected to become available soon.

Restraining here the discussion to the crystal cage loops, position-dependent and machine-specific plant variations were investigated by performing SIMO (single-input-multiple-output) system identifications, such that frequency response data (FRD) measurements were obtained by sequentially exciting each crystal cage loop with Schroeder multi-sines [10] while monitoring all three outputs. Open-loop identifications were realized according to the diagram of Figure C.1, where  $P$  is the plant, and  $T_u$  and  $T_y$  are the decoupling matrices with respect to the rigid-body center of gravity (see Chapter 3).



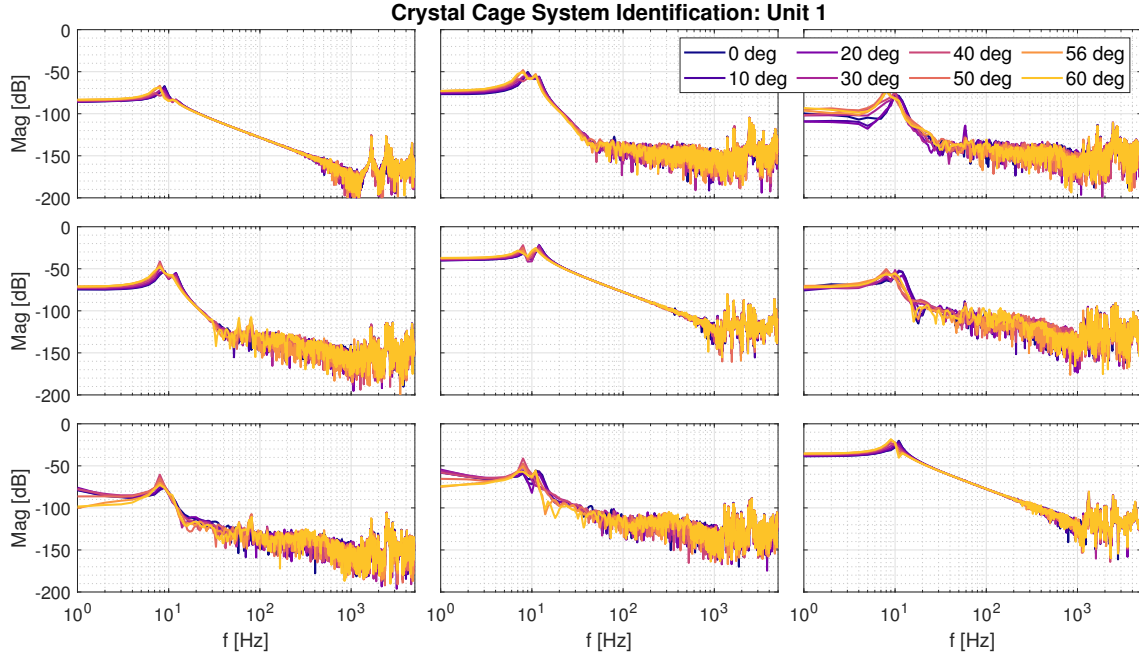
**Figure C.1:** Open-loop plant  $P$  identification diagram using decoupling matrices  $T_u$  and  $T_y$  with respect to the rigid-body center of gravity.

Differently from many motion systems that are open-loop unstable [11], this approach was only possible thanks to the open-loop stability provided by the flexure-suspended mechanical architecture (see Chapter 2). Still, previously calibrated offset values for the loops at each Bragg angle were additionally maintained to approximate the nominal gap values and keep the interferometers within angular alignment ranges (see Chapter 2). The Bragg and long-stroke control loops, in turn, were kept under closed-loop control in the cRIO hardware for the multiple angles to approximate as much as possible the real operation conditions.

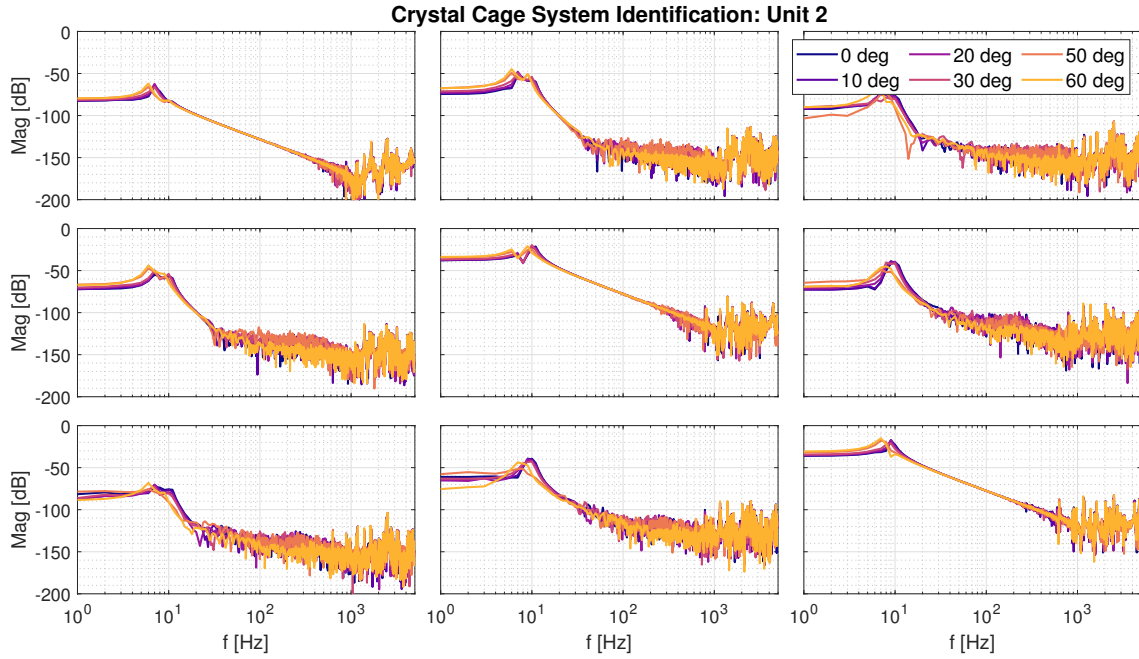
Moreover, all identifications were performed in the operational LN<sub>2</sub> cryogenic conditions, which is relevant to increasing the identification accuracy in terms of frequencies and amplitudes for at least two reasons, namely: i) thermal effects may affect alignment, preloading forces, materials mechanical and magnetic properties, and tribology, thus possibly influencing contact and suspension stiffnesses, damping factors, actuation forces and metrology; and ii) cryogenic-temperature parts have a pumping effect, improving vacuum levels by at least one order of magnitude, which also has some residual impact in damping and in the interferometric metrology. The downside of this, however, is that the LN<sub>2</sub> flow-induced vibrations add unknown disturbances to the identification procedure, reducing the signal-to-noise ratio and the overall data quality.

Figure C.2 and Figure C.3 show plant FRDs for the degrees of freedom (GAP, PTC, RLL) at multiple angles for the HD-DCM Unit 1 installed at the MANACÁ beamline and the HD-DCM Unit 2 at the EMA beamline, respectively. Next, Figure C.4 provides direct comparison between the units via a smaller set of the data showing the plants at minimum and maximum Bragg angles<sup>1</sup>. From the diagonal elements in the FRDs, no significant differences can be observed for the mass (GAP) and moments of inertia (PTC and RLL) that dominate dynamics in the range from 20 to 500 Hz, either at the different angles, or between units. Regarding the suspension stiffness  $k$  — which can be estimated as  $1/k$  from an asymptotic horizontal line in the low-frequency limit of the diagonal FRDs (roughly up to about 3 Hz) —, on the other hand, there is a consistent reduction as the Bragg angle increases (i.e., lines going up in the FRDs). Indeed, changes of up to a factor 2 occur, which is primarily associated to variations in stresses

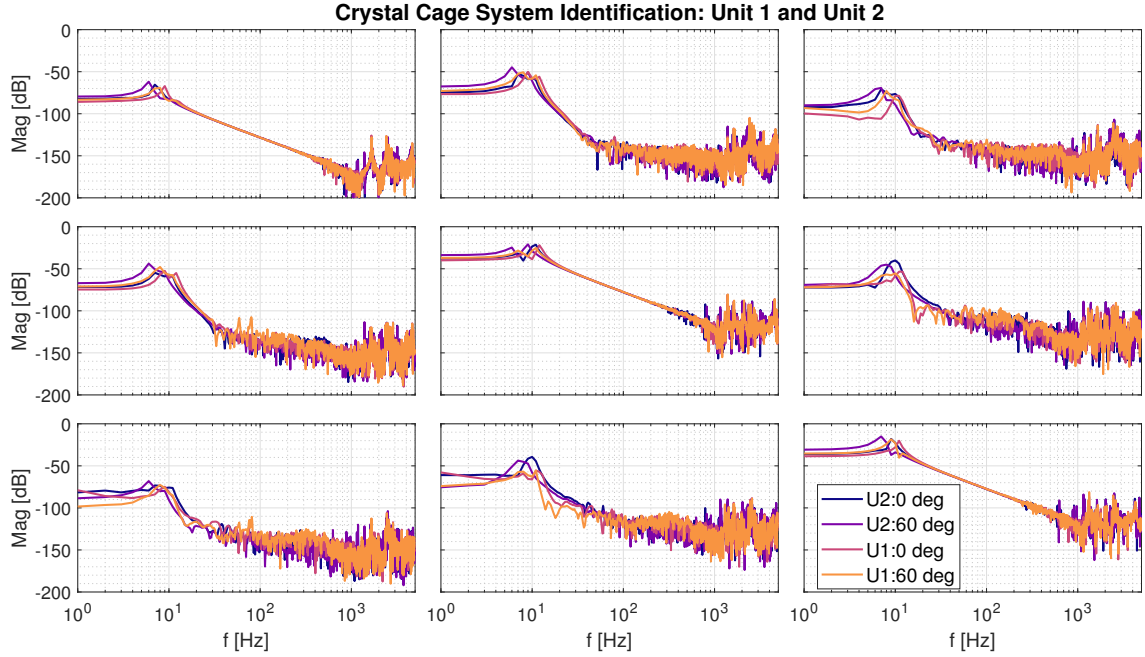
<sup>1</sup>Due to the disturbance factors acting in the plant and the currently limited functionalities in the system identification toolbox, the quality of the FRD estimates has been improved using Local Rational Method (LRM). Thanks to Paul Tacx from the CST group at TU/e for his support with LRM for this data set [10].



**Figure C.2:** Frequency response data (FRD) from multi-sine open-loop plant identifications for the HD-DCM Unit 1, installed at the MANACÁ beamline at Sirius. The crystal cage degrees of freedom (GAP,PTC,RLL) are investigated for plant variations over multiple Bragg angles.



**Figure C.3:** Frequency response data (FRD) from multi-sine open-loop plant identifications for the HD-DCM Unit 2, installed at the EMA beamline at Sirius. The crystal cage degrees of freedom (GAP,PTC,RLL) are investigated for plant variations over multiple Bragg angles.



**Figure C.4:** Frequency response data (FRD) from multi-sine open-loop plant identifications for comparison between Unit 1 (U1) and Unit 2 (U2) of the HD-DCM, installed respectively at the MANACÁ and the EMA beamlines at Sirius. The crystal cage degrees of freedom (GAP,PTC,RLL) are shown at minimum and maximum Bragg angles.

in the folded leaf-springs (see Chapter 2) caused by different loading conditions at the various angles affecting stiffness (see [12] for folded leaf-spring models). Then, between units, Unit 1 has a higher suspension stiffness, by roughly 30%, which is attributed to manufacturing tolerances.

These stiffness differences do have a small impact regarding the displacements caused by gravity compensation springs (see Chapter 2), but this can be easily compensated firstly via preliminary manual adjustment and later via the long-stroke stage. In addition, concerning dynamics and control, even though they correspondingly shift the rigid-body suspension frequencies, and may possibly ask for further variable feed-forward tuning, they are transparent to the feedback control strategy. Furthermore, the suspensions have relatively large damping, in the order of 5%, due to friction in the copper cooling braids and in residual eddy currents in the voice-coils, as discussed in Chapter 2 and Chapter 3.

The most relevant differences effectively occur at the higher frequencies, with a few poorly-damped resonances varying in position and amplitude. In particular, Unit 1 has the relevant dynamics beyond 1 kHz for all DoFs, as designed. There are only small parasitic dynamics at 370 Hz and 500 Hz in the PTC plant, due to imperfect filtering of the backward path dynamics by the balance mass, or due to residual cross-talk with respect to the remaining degrees of freedom that are constrained by the leaf-springs (see Chapter 2). Nonetheless, these occur as phase lead due to the co-located design, which can be easily handled by the controller, as shown in the next section.

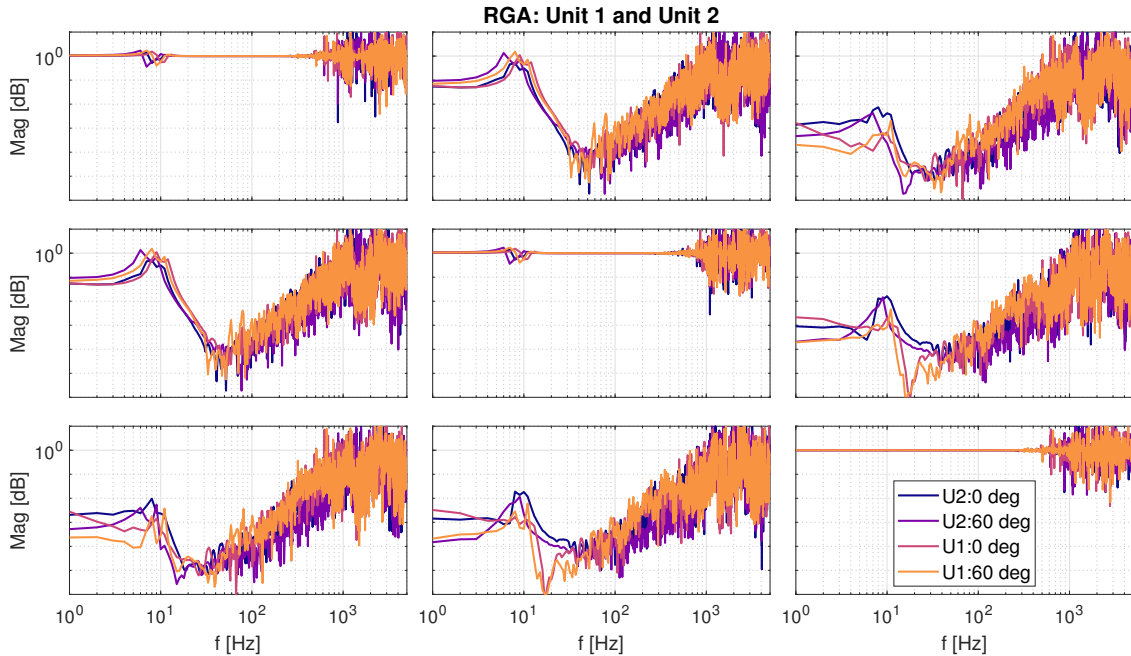


In Unit 2, however, the PTC plant has some dynamics at about 800 Hz, and the RLL plant has dynamics at around 600 and 800 Hz. This is due to a physical defect resulting from a manufacturing accident in one of the silicon crystals that is fixed to the short-stroke frame (SHS) (see Chapter 2). The required adaption in the mounting strategy eventually prevented nominal design parameters (in mounting stiffness) from being achieved. As detailed in the next section, a practical consequence of this is stricter limitations in manually achievable bandwidths via loopshaping.

Finally, the interaction in the MIMO (multiple-input-multiple-output) problem can be directly investigated via relative gain array (RGA) analyses. As presented in [13], the RGA of a non-singular square matrix  $P$  — here the  $3 \times 3$  identified plant — is a square matrix defined as

$$RGA(P) = P \times (P^{-1})^T, \quad (C.1)$$

where  $\times$  is the element-by-element multiplication (Schur product). Figure C.5 shows the results for the degrees of freedom (GAP, PTC, RLL) and the same subset (at the minimum and maximum Bragg angles) depicted in Figure C.4. It can be seen that they are close to the identity matrix in the range from 20 to 500 Hz, validating the proposed decoupling strategy. Indeed, in these conditions robust closed-loop SISO systems with bandwidth targets around 200 Hz (see Chapter 3) can be obtained by designing simpler diagonal controller structures, which is the subject of the following section.



**Figure C.5:** Relative gain array (RGA) obtained from multi-sine open-loop plant identifications comparing Unit 1 (U1) and Unit 2 (U2) of the HD-DCM, installed respectively at the MANACÁ and the EMA beamlines at Sirius. The crystal cage degrees of freedom (GAP,PTC,RLL) are shown at minimum and maximum Bragg angles.

### C.3 Controller Design

Given the fast sample rate in the digital hardware, the controllers can be designed using continuous-time techniques and later explicitly discretized (using Tustin's method and sampling rate of 20 kHz) to be embedded in the cRIO digital real-time hardware (see also [9]). Moreover, as in typical mass-based motion systems, the decoupled system of the crystal cage allows for the design of simple diagonal controllers based on PID (proportional-integral-derivative) control. As discussed in Chapter 2, in such cases the practical rules of thumb consist of [11, 14]: i) defining the desired control bandwidth (here defined as the first frequency in which the open-loop gain crosses the 0 dB); ii) introducing a lead filter around the bandwidth for phase lead; iii) implementing a low-pass above the bandwidth to suppress high-frequency amplification of the dynamics and sensor noise; iv) inserting integral action with an additional zero below the bandwidth for better tracking and disturbance rejection; and v) adding a proportional gain to achieve unit gain at the bandwidth frequency, as defined. Eventually, notch filters can be included to handle parasitic system dynamics.

Here, the controllers are designed in the frequency domain using the so-called *loop-shaping* technique (see [13, 14]) and a tool called ShapeIt, which was developed by the Control Systems Technology (CST) Group at the Eindhoven University of Technology (TU/e) [15]. This is done by manually and iteratively updating the controller parameters while checking open-loop frequency responses and closed-loop functions towards robustness.

In general terms, the controllers can be represented by a given combination of filters described in the Laplace domain. An integrator can be simply defined by its low-frequency zero  $\omega_{\text{Int}}$  (in radians), i.e.

$$C_{\text{Int}}(s) = \frac{s + \omega_{\text{Int}}}{s}. \quad (\text{C.2})$$

Next, around the bandwidth, the lead filter is defined by its lower-frequency zero  $\omega_{\text{LFz}}$  and its higher-frequency pole  $\omega_{\text{LFP}}$  as

$$C_{\text{LF}}(s) = \frac{s + \omega_{\text{LFz}}}{s + \omega_{\text{LFP}}}. \quad (\text{C.3})$$

Then, the low-pass (LP) action above the bandwidth can be implemented either as: i) a first-order filter defined by its high-frequency pole  $\omega_{\text{LP1}}$

$$C_{\text{LP1}}(s) = \frac{\omega_{\text{LP1}}}{s + \omega_{\text{LP1}}}, \quad (\text{C.4})$$

or ii) a second-order filter given by its pole  $\omega_{\text{LP2}}$  and a damping ratio  $\zeta_{\text{LP2}}$

$$C_{\text{LP2}}(s) = \frac{\omega_{\text{LP2}}^2}{s^2 + 2\zeta_{\text{LP2}}\omega_{\text{LP2}}s + \omega_{\text{LP2}}^2}. \quad (\text{C.5})$$

Finally, notches can be defined by a transfer function with imaginary zeros and poles according to the frequencies  $\omega_{\text{Nz}}$  and  $\omega_{\text{Np}}$  and damping ratios  $\zeta_{\text{Nz}}$  and  $\zeta_{\text{Np}}$

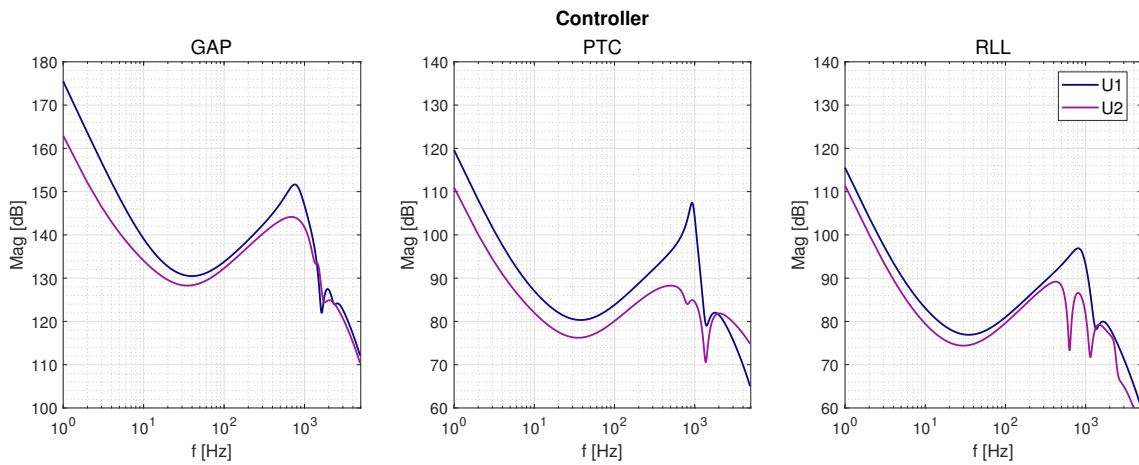
$$C_{\text{N}}(s) = \frac{s^2 + 2\zeta_{\text{Nz}}\omega_{\text{Nz}}s + \omega_{\text{Nz}}^2}{s^2 + 2\zeta_{\text{Np}}\omega_{\text{Np}}s + \omega_{\text{Np}}^2}. \quad (\text{C.6})$$

If  $\omega_{Nz} = \omega_{Np}$  and  $\zeta_{Nz} < \zeta_{Np}$ , a notch groove can be used to damp particular frequencies from the plant. Else, if  $\zeta_{Nz} = \zeta_{Np}$  and  $\omega_{Nz} \neq \omega_{Np}$ , skew notches can be used to handle magnitude or phase of the open-loop function towards stability and robustness.

In the early phases of commissioning at the metrology lab, more aggressive controllers reaching up to 250 or 300 Hz have been designed as proof of concepts (see Chapter 3). However, it was later realized that they lacked robustness (or even stability) regarding position-dependent plant variations and disturbances. Furthermore, daily operation proved that the desired 10 nrad control level for PTC could be achieved even at lower bandwidths (see Chapter 4 and Chapter 5).

Figure C.6 shows the latest controllers designed for the two HD-DCM units, such that more than 8 dB, 30°, and 6 dB of modulus, phase and gain margins, respectively, are maintained by simultaneously evaluating the multiple plants shown in Figure C.2 and Figure C.3. As a general goal, the controllers are meant to be as simple and low-order as possible and all the parameters are listed in Table C.1. As it could be expected, the achievable bandwidths in Unit 1 are larger than those in Unit 2, due to the additional mechanical resonances found in the latter. In all cases, two integrators are used to boost the low-frequency gain. The lead filters are tuned roughly between 40 and 550 Hz. The low-pass corner frequencies are tuned between 725 and 900 Hz. At least one notch (skewed or not) is necessary to handle the high-frequency dynamics of the plants, the worst case scenario being that of RLL in Unit 2, for which three notches were required to reach a bandwidth of 120 Hz.

Open-loop and sensitivity Bode plots for both units are shown in Figure C.7, Figure C.8, Figure C.9, and Figure C.10, indicating the general gain shape and bandwidths, as well as the sensitivity peaks. These figures demonstrate the high low-frequency gain and the gentle slope around the bandwidth cross frequency, as well as the well-tamed high-frequency dynamics and sensitivity. About the sensitivity plots, one may no-



**Figure C.6:** Diagonal controllers designed via the loop shaping technique using the ShapeIt tool (CST Group - TU/e) [15] for the control loops of the crystal cage of the HD-DCM: Unit 1 (U1) and Unit 2 (U2). The discretization is at 20 kHz using Tustin's method.

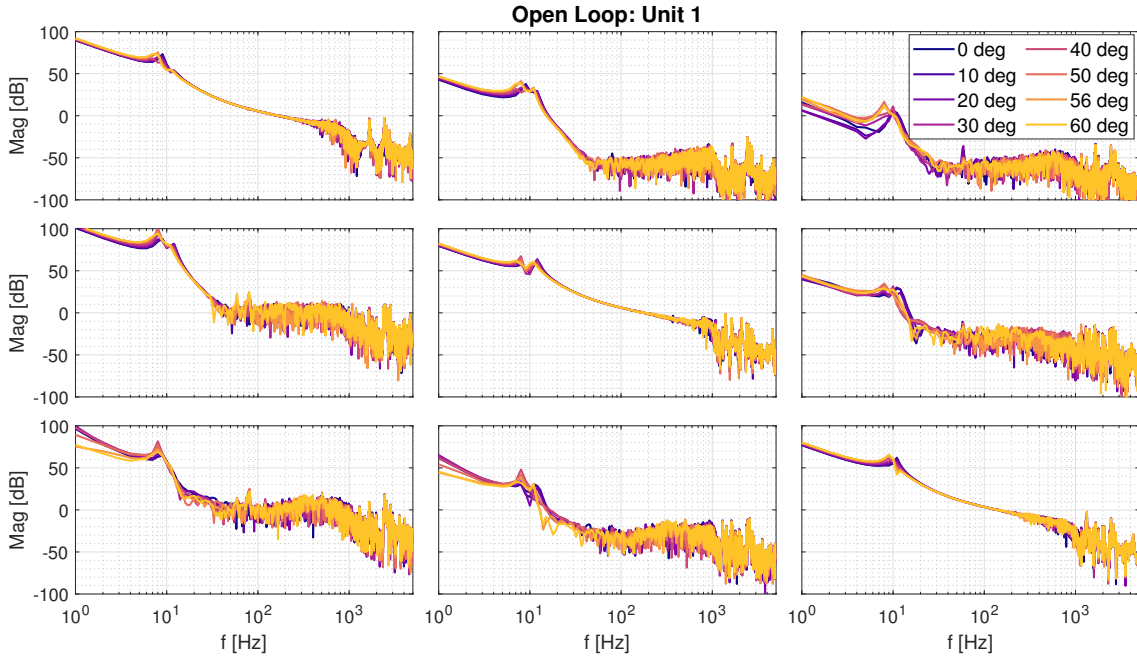
**Table C.1:** Diagonal controller parameters obtained via the loop shaping technique using the ShapeIt tool (CST Group - TU/e) [15] for the GAP, PTC and RLL control loops of the crystal cage of the HD-DCM: Unit 1 and Unit 2.

Parameter	Unit 1			Unit 2		
	GAP	PTC	RLL	GAP	PTC	RLL
BW	163	159	138	145	120	120
1st Int. Zero [Hz]	10	5	5	3	5	5
2nd Int. Zero [Hz]	30	30	30	30	30	30
Lead Zero [Hz]	45	45	40	40	40	28
Lead Pole [Hz]	570	560	470	570	500	550
F.O. LP Pole [Hz]	-	-	-	-	750	-
S.O. LP Pole [Hz]	800	950	900	900	-	725
S.O. LP Damp [-]	0.2	0.085	0.25	0.6	-	0.5
1st Notch Freq. 1 [Hz]	1660	1391	1334	1886	805	632
1st Notch Damp 1 [-]	0.05	0.085	0.1	0.1	0.1	0.03
1st Notch Freq. 2 [Hz]	1660	1391	1334	1886	805	632
1st Notch Damp 2 [-]	0.25	0.55	0.375	0.3	0.15	0.25
2nd Notch Freq. 1 [Hz]	2418	-	-	1500	1392	1154
2nd Notch Damp 1 [-]	0.1	-	-	0.1	0.05	0.05
2nd Notch Freq. 2 [Hz]	2418	-	-	1725	1392	1154
2nd Notch Damp 2 [-]	0.15	-	-	0.1	0.3	0.25
3rd Notch Freq. 1 [Hz]	-	-	-	-	-	2425
3rd Notch Damp 1 [-]	-	-	-	-	-	0.1
3rd Notch Freq. 2 [Hz]	-	-	-	-	-	2600
3rd Notch Damp 2 [-]	-	-	-	-	-	0.1

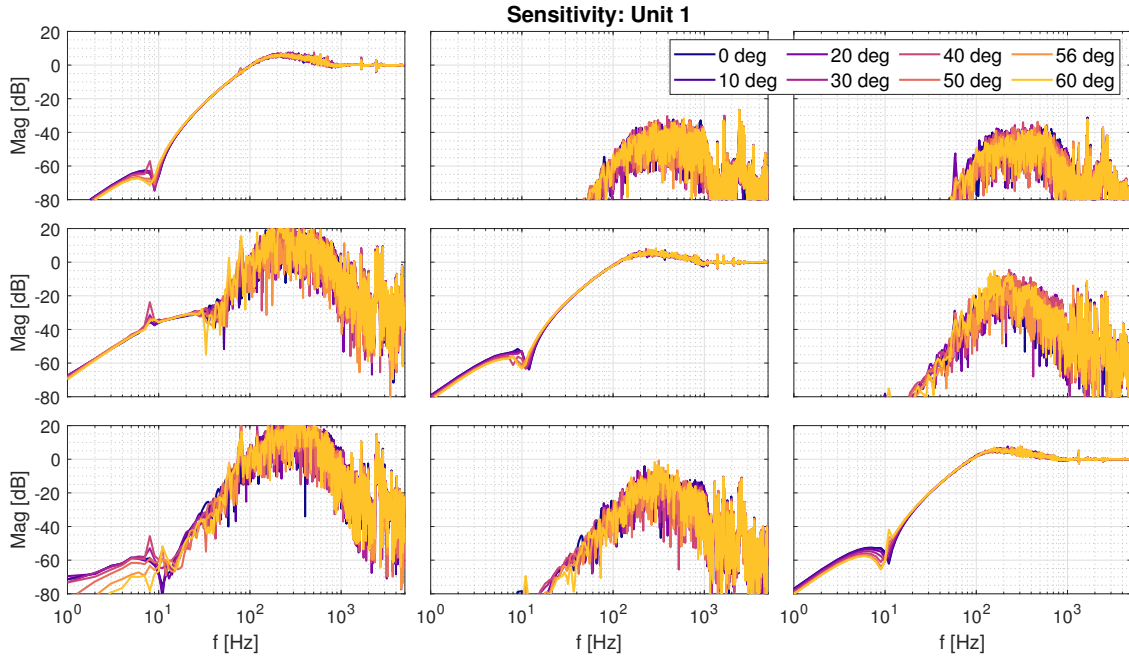
tice that the lower triangular off-diagonal terms appear to have significant amplitudes. However, since the upper triangular terms are significantly smaller, it is clear that this can be balanced using an appropriate scaling matrix — attesting for no interaction issues in the MIMO system, as also demonstrated by the RGA (see Figure C.5).

Next, stability, robustness margins and MIMO analyses can be evaluated via the Nyquist and characteristic loci plots shown in Figure C.11 and Figure C.12. Closed-loop MIMO stability is proven via the characteristic loci plots, by leaving the point  $(-1,0)$  at the left of the eigenvalues  $\lambda$  of the MIMO open-loop [13]. Then, although not strictly rigorous, the Nyquist plots of the SISO systems can provide an estimate of the robustness margins given their agreement with the MIMO eigenvalues.

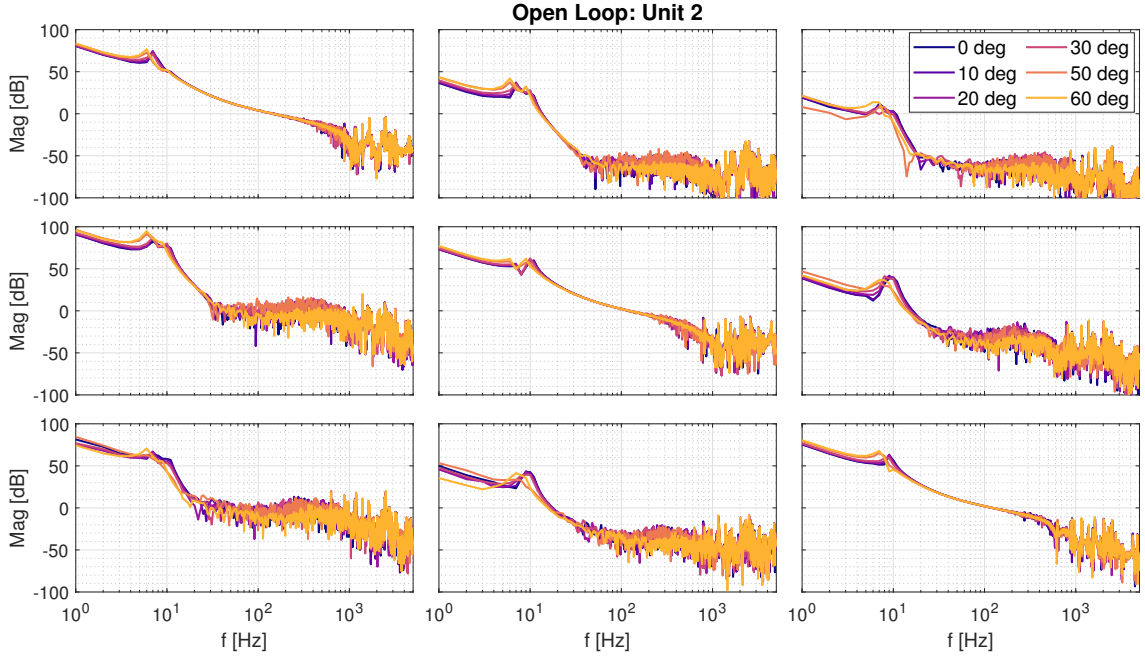
To conclude, it is worth highlighting that the conservatism in the loopshaping design work and the bandwidth values is partially due the FRD uncertainty coming from the system identification data, especially above 300 Hz — even after post-processing with local parametric methods. Indeed, the resulting uncertainty in the magnitude and phase of the plant significantly limits a more precise definition of the margins



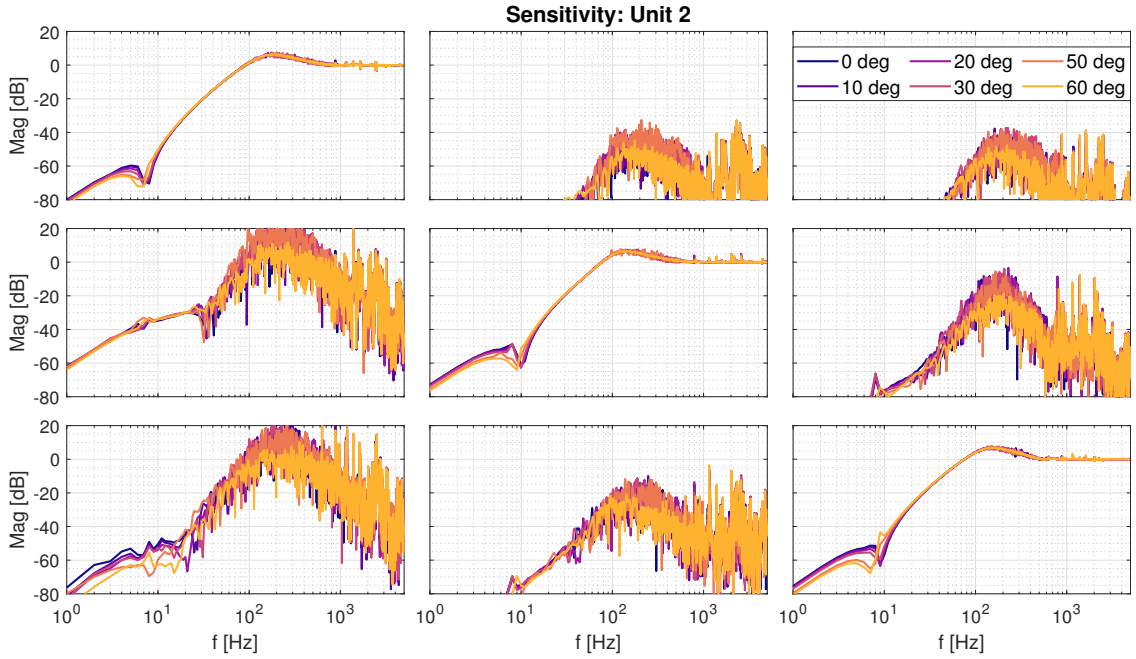
**Figure C.7:** Discrete-domain (20 kHz) open-loop Bode plot for the crystal cage of the HD-DCM Unit 1, installed at the MANACÁ beamline at Sirius. The diagonal controller design for GAP, PTC and RLL simultaneously considered plant variations over the multiple Bragg angles for robustness and stability.



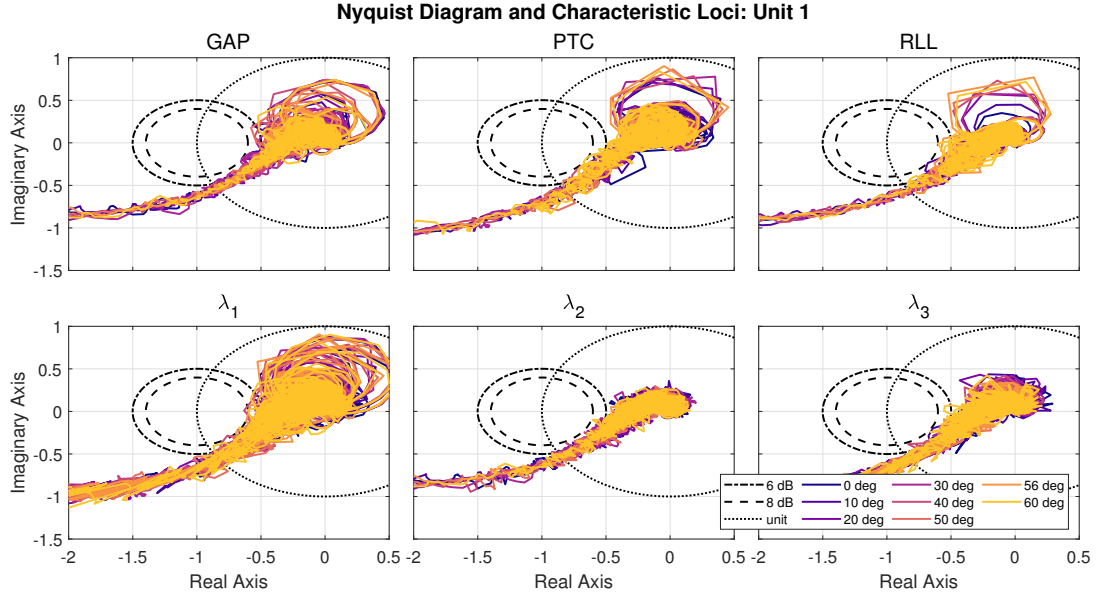
**Figure C.8:** Discrete-domain (20 kHz) sensitivity Bode plot for the crystal cage of the HD-DCM Unit 1, installed at the MANACÁ beamline at Sirius. The diagonal controller design for GAP, PTC and RLL simultaneously considered plant variations over the multiple Bragg angles for robustness and stability.



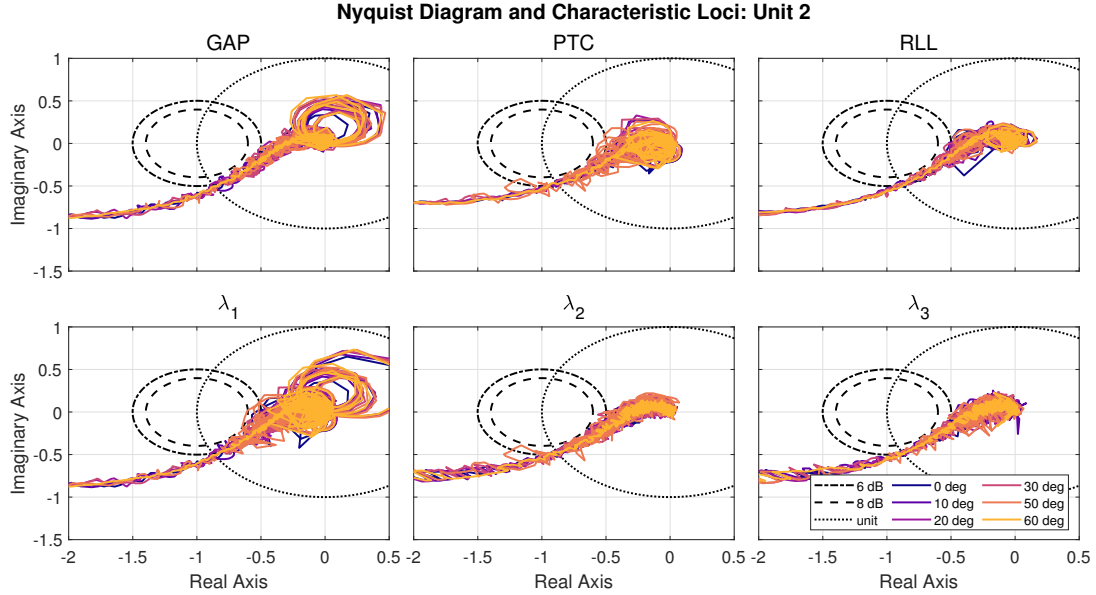
**Figure C.9:** Discrete-domain (20 kHz) open-loop Bode plot for the crystal cage of the HD-DCM Unit 2, installed at the EMA beamline at Sirius. The diagonal controller design for GAP, PTC and RLL simultaneously considered plant variations over the multiple Bragg angles for robustness and stability.



**Figure C.10:** Discrete-domain (20 kHz) sensitivity Bode plot for the crystal cage of the HD-DCM Unit 2, installed at the EMA beamline at Sirius. The diagonal controller design for GAP, PTC and RLL simultaneously considered plant variations over the multiple Bragg angles for robustness and stability.



**Figure C.11:** Nyquist diagram of the SISO systems and characteristic loci of the MIMO system for the crystal cage of the HD-DCM Unit 1 at multiple Bragg angles. The agreement between the Nyquist plot for the decoupled degrees of freedom GAP, PTC and RLL (above) and the eigenvalues of the characteristic loci (below) allows for an estimate of the robustness margins.



**Figure C.12:** Nyquist diagram of the SISO systems and characteristic loci of the MIMO system for the crystal cage of the HD-DCM Unit 2 at multiple Bragg angles. The agreement between the Nyquist plot for the decoupled degrees of freedom GAP, PTC and RLL (above) and the eigenvalues of the characteristic loci (below) allows for an estimate of the robustness margins.



(see, for instance, the modulus margin in Figure C.11 and Figure C.12), practically forcing a reduction in the bandwidth and partly compromising a finer comparison of the position-dependent variations in higher frequency range. Thus, the ongoing improvements in the system identification toolboxes at the LNLS will be indeed essential for more ambitious perspectives of with the HD-DCM in terms of control alternatives, including, for example, active damping of the high-frequency dynamics and control optimization.

## References

- [1] Oomen T. 2018 *IEEE J. Ind. Appl.* **7**(2) 127
- [2] Butler H. 2011 *IEEE Control Syst. Mag.* **31**(5) 28
- [3] Heertjes M. and Temizer B. 2012 *Proc. 2012 Am. Control Conf. (ACC)* (IEEE) 2461–2466
- [4] Heertjes M. and Van Engelen A. 2011 *Control. Eng. Pract.* **19**(12) 1423
- [5] Caliari R.M. *et al.* 2018 *Proc. 16th Int. Conf. on Acc. and Large Exp. Phys. Control Systems (ICALEPCS'17)* (JACoW Publishing) 997–1002
- [6] Caliari R.M. *et al.* 2020 *Proc. ASPE 2020 Spring – Design and Control of Precision Mechatronic Systems* 125–130
- [7] Pintelon R. and Schoukens J. 2012 *System Identification: a Frequency Domain Approach* (John Wiley & Sons)
- [8] Moreno G.B.Z.L. *et al.* 2018 *Proc. 16th Int. Conf. on Acc. and Large Exp. Phys. Control Systems (ICALEPCS'17)* (JACoW Publishing) 1941–1946
- [9] Moraes M.A.L. *et al.* 2020 *Proc. ASPE 2020 Spring – Design and Control of Precision Mechatronic Systems* 131–136
- [10] Schoukens J. *et al.* 2018 *IEEE Control Syst. Mag.* **38**(4) 49
- [11] Oomen T. and Steinbuch M. 2020 *Mechatronics and Robotics* (CRC Press) 51–80
- [12] Soemers H. 2011 *Design Principles for Precision Mechanisms* (T-Pointprint)
- [13] Skogestad S. and Postlethwaite I. 2007 *Multivariable Feedback Control: Analysis and Design* vol. 2 (John Wiley & Sons)
- [14] Schmidt R. *et al.* 2011 *The Design of High Performance Mechatronics: High-Tech Functionality by Multidisciplinary System Integration* 2nd edn. (IOS Press)
- [15] Control Systems Technology Group (CST) TU/e 2022 *ShapeIt* [https://cstwiki.wtb.tue.nl/index.php?title=Home\\_of\\_ShapeIt](https://cstwiki.wtb.tue.nl/index.php?title=Home_of_ShapeIt), accessed: May 15th, 2023





---

## Bibliography

---

- G.S. Albuquerque *et al.* (2021). ‘The Dynamic Modeling and the Control Architecture of the New High-Dynamic Double-Crystal Monochromator (HD-DCM-Lite) for Sirius/LNLS’. In ‘*Proc. 18th Int. Conf. on Acc. and Large Exp. Phys. Control Systems (ICALEPCS’21)*’, (JACoW Publishing), 619–624.
- D.A.D. Alnajjar *et al.* (2019). ‘PROJECT Nheengatu: EPICS SUPPORT FOR CompactRIO FPGA AND LabVIEW-RT’. In ‘*Proc. 17th Int. Conf. on Acc. and Large Exp. Phys. Control Systems (ICALEPCS’19)*’, (JACoW Publishing), 997–1000.
- N. Ambaum *et al.* (2021). ‘Piezoelectric Shunt Damping in Cryogenic Conditions: Application to a Flexure-based Mechanism’. In ‘*Proc. 36th ASPE Annual Meeting*’, 89–96.
- F.M. Anthony (1995). ‘High Heat Load Optics: an Historical Overview’. *Opt. Eng.* **34**(2), 313.
- N.W. Ashcroft (2003). *Solid State Physics* (Thomson Press (India) Ltd).
- P. Avitabile (2003). ‘Twenty Years of Structural Dynamic Modification-a Review’. *Sound and Vibration* **37**(1), 14.
- Axilon (2018). ‘Accelerator and X-Ray Instrumentation for Laboratories, National Facilities and Industry’. [http://www.axilon.de/Download/AXILON\\_Beamline-Instrumentation\\_18-04.pdf](http://www.axilon.de/Download/AXILON_Beamline-Instrumentation_18-04.pdf), accessed: Oct. 1st, 2021.
- Y. Bai *et al.* (2022). ‘A New Active Vibration Control Method of Double Crystal Monochromator Based on FuLMS-ADRC Hybrid Algorithm’. *Nucl. Instrum. Methods Phys. Res. A* **1029**, 166418.
- R. Baker *et al.* (2018). ‘ESRF Double Crystal Monochromator Prototype Project’. In ‘*Proc. 10th Mech. Eng. Des. of Synchrotron Radiat. Equip. and Instrum. (MEDSI’18)*’, (JACoW Publishing), 440–444.
- R. Baker *et al.* (2021). ‘ESRF Double Crystal Monochromator - Design and Working Modes’. Presented at MEDSI’20 in Chicago, USA, unpublished.
- D.H. Bilderback *et al.* (2000). ‘The Historical Development of Cryogenically Cooled Monochromators for Third-generation Synchrotron Radiation Sources’. *J. Synchrotron Rad.* **7**(2), 53.

- B. Bornmann *et al.* (2019). ‘The Quick EXAFS Setup at Beamline P64 at PETRA III for up to 200 Spectra per Second’. vol. 2054 (AIP Publishing), 040008.
- J.L. Brito Neto *et al.* (2021). ‘Temperature Control for Beamline Precision Systems of Sirius/LNLS’. In ‘*Proc. 18th Int. Conf. on Acc. and Large Exp. Phys. Control Systems (ICALEPCS’18)*’, (JACoW Publishing), 606–611.
- C.S.N.C. Bueno *et al.* (2021a). ‘Positioning Scanning Solutions at the TARUMÃ Station at the CARNAÚBA Beamline at Sirius/LNLS’. In ‘*Proc. 18th Int. Conf. on Acc. and Large Exp. Phys. Control Systems (ICALEPCS’21)*’, (JACoW Publishing), 613–618.
- C.S.N.C. Bueno *et al.* (2021b). ‘Vibration Assessment at the CARNAÚBA Beamline at Sirius/LNLS’. In ‘*Proc. 11th Mech. Eng. Des. of Synchrotron Radiat. Equip. and Instrum. (MEDSI’20)*’, (JACoW Publishing), 37–40.
- H. Butler (2011). ‘Position Control in Lithographic Equipment’. *IEEE Control Syst. Mag.* **31**(5), 28.
- F. Cacho-Nerin, J.E. Parker and P.D. Quinn (2020). ‘A Passive Hutch Cooling System for Achieving High Thermal Stability Operation at the Nanoprobe Beamline, Diamond Light Source’. *J. Synchrotron Rad.* **27**(4), 912.
- R.M. Caliori *et al.* (2017). ‘Studies on Flow-Induced Vibrations for the New High-Dynamics DCM for Sirius’. In ‘*Proc. 9th Mech. Eng. Des. of Synchrotron Radiat. Equip. and Instrum. (MEDSI’16)*’, (JACoW Publishing), 8–11.
- R.M. Caliori *et al.* (2018). ‘System Identification and Control for the Sirius High-Dynamic DCM’. In ‘*Proc. 16th Int. Conf. on Acc. and Large Exp. Phys. Control Systems (ICALEPCS’17)*’, (JACoW Publishing), 997–1002.
- R.M. Caliori *et al.* (2020). ‘Loop-Shaping Controller Design in the Development of the High-Dynamic Double-Crystal Monochromator at Sirius Light Source’. In ‘*Proc. ASPE 2020 Spring – Design and Control of Precision Mechatronic Systems*’, 125–130.
- H.F. Canova *et al.* (2017). ‘VDE - Virtual Documentation Environment’. In ‘*Proc. 11th Int. Workshop on Person. Computers and Particle Acc. Controls (PCa-PAC2016)*’, (JACoW Publishing), 53–55.
- J. Chen *et al.* (2019). ‘Ground Motion Effects on the Beam Orbit Stability at Shanghai Synchrotron Radiation Facility’. *Synchrotron Radiat. News* **32**(5), 27.
- H. Cheng, C. Chen, Z. Tsai and J. Chen (1999). ‘Utility Optimization for the Beam Orbit Stability at SRRC’. In ‘*Proc. 1999 Particle Acc. Conf.*’, vol. 2 (IEEE), 1150–1152.
- O. Chubar and P. Elleaume (1998). ‘Accurate and Efficient Computation of Synchrotron Radiation in the Near Field Region’. In ‘*Proc. EPAC98 Conference*’, 1177–1179.

- A.I. Chumakov *et al.* (2014). ‘Performance of a Silicon Monochromator under High Heat Load’. *J. Synchrotron Rad.* **21**(2), 315.
- Control Systems Technology Group (CST) TU/e (2022). ‘ShapeIt’. [https://cstwiki.wtb.tue.nl/index.php?title=Home\\_of\\_ShapeIt](https://cstwiki.wtb.tue.nl/index.php?title=Home_of_ShapeIt), accessed: May 15th, 2023.
- M. Cotte *et al.* (2019). ‘Cultural and Natural Heritage at the ESRF: Looking Back and to the Future’. *Synchrotron Radiat. News* **32**(6), 34.
- P.L. Cowan *et al.* (1983). ‘A UHV Compatible Two-crystal Monochromator for Synchrotron Radiation’. *Nucl. Instrum. Methods Phys. Res.* **208**(1-3), 349.
- L.R. Dalesio, A.J. Kozubal and M.R. Kraimer (1991). *EPICS architecture*. Tech. Rep. No. LA-UR-91-3543; CONF-911116-9, Los Alamos National Lab., NM (United States).
- W. D’Ambrogio and A. Sestieri (2004). ‘A Unified Approach to Substructuring and Structural Modification Problems’. *Shock and Vibration* **11**(3–4), 295.
- P. Denes and B. Schmitt (2014). ‘Pixel Detectors for Diffraction-limited Storage Rings’. *J. Synchrotron Rad.* **21**(5), 1006.
- J. Deng *et al.* (2019). ‘The Velociprobe: an Ultrafast Hard X-ray Nanoprobe for High-Resolution Ptychographic Imaging’. *Rev. Sci. Instrum.* **90**(8), 083701.
- I.P. Dolbnya *et al.* (2018). ‘A Water-cooled Monochromator for the B16 Test Beamline at the Diamond Light Source: Capabilities and Performance Characterization’. *J. Synchrotron Rad.* **26**(1), 253.
- EPICS (2021). ‘Experimental Physics and Industrial Control System.’ <https://epics-controls.org/>, accessed: Nov. 1st, 2021.
- M. Eriksson *et al.* (2014). ‘Diffraction-limited storage rings—a window to the science of tomorrow’. *J. Synchrotron Rad.* **21**(5), 837.
- European Synchrotron Radiation Facility (ESRF) (2014). ‘Double Crystal Monochromator Workshop’. <http://www.esrf.eu/home/events/conferences/2014/double-crystal-monochromator-workshop.html>, accessed: Oct. 1st, 2021.
- Y. Fan *et al.* (2020). ‘Angular Stability Measurement of a Cryocooled Double-Crystal Monochromator at SSRF’. *Nucl. Instrum. Methods Phys. Res. A* **983**, 164636.
- I. Faulconbridge and M. Ryan (2015). *Introduction to Systems Engineering* (Argos Press).
- D. Fearon *et al.* (2021). ‘Crystallographic Fragment Screening of SARS-CoV-2 Drug Discovery Targets’. In ‘*Acta Cryst. A*’, vol. 77. C196.
- R. Geraldès *et al.* (2016). ‘New Sensor and Non-contact Geometrical Survey for the Vibrating Wire Technique’. *Nucl. Instrum. Methods Phys. Res. A* **811**, 115.
- R.R. Geraldès *et al.* (2017a). ‘Mechatronics Concepts for the New High-Dynamics DCM for Sirius’. In ‘*Proc. 9th Mech. Eng. Des. of Synchrotron Radiat. Equip. and Instrum. (MEDSI’16)*’, (JACoW Publishing), 44–47.

- R.R. Geraldes *et al.* (2017b). ‘The New High Dynamics DCM for Sirius’. In ‘*Proc. 9th Mech. Eng. Des. of Synchrotron Radiat. Equip. and Instrum. (MEDSI’16)*’, (JACoW Publishing), 141–146.
- R.R. Geraldes *et al.* (2018a). ‘Granite Benches for Sirius X-ray Optical Systems’. In ‘*Proc. 10th Mech. Eng. Des. of Synchrotron Radiat. Equip. and Instrum. (MEDSI’18)*’, (JACoW Publishing), 361–364.
- R.R. Geraldes *et al.* (2018b). ‘The Design of Exactly-Constrained X-Ray Mirror Systems for Sirius’. In ‘*Proc. 10th Mech. Eng. Des. of Synchrotron Radiat. Equip. and Instrum. (MEDSI’18)*’, (JACoW Publishing), 173–178.
- R.R. Geraldes *et al.* (2018c). ‘The Status of the New High-Dynamic DCM for Sirius’. In ‘*Proc. 10th Mech. Eng. Des. of Synchrotron Radiat. Equip. and Instrum. (MEDSI’18)*’, (JACoW Publishing), 147–152.
- R.R. Geraldes *et al.* (2019). ‘Instrument for Moving and Positioning of Optical Elements with Nanometric Mechanical Stability and Resolution in Synchrotron Light Source Beamlines’. US Patent App. 16/331,925.
- R.R. Geraldes *et al.* (2020). ‘Dynamic Error Budgeting in the Development of the High-Dynamic Double-Crystal Monochromator at Sirius Light Source’. In ‘*Proc. ASPE 2020 Spring – Design and Control of Precision Mechatronic Systems*’, 119–124.
- R.R. Geraldes *et al.* (2021a). ‘Commissioning and Prospects of the High-Dynamic DCMs at Sirius/LNLS’. In ‘*Proc. 11th Mech. Eng. Des. of Synchrotron Radiat. Equip. and Instrum. (MEDSI’20)*’, (JACoW Publishing), 25–28.
- R.R. Geraldes *et al.* (2021b). ‘Design and Commissioning of the TARUMÃ Station at the CARNAÚBA Beamline at Sirius/LNLS’. In ‘*Proc. 11th Mech. Eng. Des. of Synchrotron Radiat. Equip. and Instrum. (MEDSI’20)*’, (JACoW Publishing), 292–295.
- R.R. Geraldes *et al.* (2021c). ‘The FPGA-based Control Architecture, EPICS Interface and Advanced Operational Modes of the High-Dynamic Double-Crystal Monochromator for Sirius/LNLS’. In ‘*Proc. 18th Int. Conf. on Acc. and Large Exp. Phys. Control Systems (ICALEPCS’21)*’, (JACoW Publishing), 370–375.
- R.R. Geraldes *et al.* (2022a). ‘A review on the High-Dynamic Double-Crystal Monochromator for Sirius/LNLS’. In ‘*J. Phys. Conf. Ser.*’, vol. 2380 (IOP Publishing), 012050.
- R.R. Geraldes *et al.* (2022b). ‘Predictive Modeling through Dynamic Error Budgeting applied to the High-Dynamic Double-Crystal Monochromator for Sirius Light Source’. *Precision Engineering* **77**, 90.
- R.R. Geraldes *et al.* (2022c). ‘The Mechatronic Architecture and Design of the High-Dynamic Double-Crystal Monochromator for Sirius Light Source’. *Precision Engineering* **77**, 110.

- R.R. Galdes *et al.* (2022d). ‘The Sample Positioning Stage for the SAPOTI Nanoprobe at the CARNAÚBA beamline at Sirius/LNLS’. In ‘*Proc. 37th ASPE Annual Meeting*’, 91–97.
- R.R. Galdes *et al.* (2023a). ‘Fly-Scan-Oriented Motion Analyses and Upgraded Beamline Integration Architecture for the High-Dynamic Double-Crystal Monochromator at Sirius/LNLS’. *J. Synchrotron Rad.* **30**, 90.
- R.R. Galdes *et al.* (2023b). ‘The High-Dynamic Cryogenic Sample Stage for SAPOTI/CARNAUBA at Sirius/LNLS’. To be published *Proc. XRM2022*.
- J.A. Golovchenko *et al.* (1981). ‘X-ray monochromator system for use with synchrotron radiation sources’. *Rev. Sci. Instrum.* **52**(4), 509.
- J.B. Hastings (1977). ‘X-ray Optics and Monochromators for Synchrotron Radiation’. *J. Appl. Phys.* **48**(4), 1576.
- T. Hatsui and H. Graafsma (2015). ‘X-ray Imaging Detectors for Synchrotron and XFEL Sources’. *IUCrJ* **2**(3), 371.
- A.J. Hazelton *et al.* (2002). ‘Wafer positioner with planar motor and mag-lev fine stage’. US Patent 6,437,463.
- M. Heertjes and B. Temizer (2012). ‘Data-based Control Tuning in Master-Slave Systems’. In ‘*Proc. 2012 Am. Control Conf. (ACC)*’, (IEEE), 2461–2466.
- M. Heertjes and A. Van Engelen (2011). ‘Minimizing Cross-talk in High-precision Motion Systems using Data-based Dynamic Decoupling’. *Control. Eng. Pract.* **19**(12), 1423.
- M.F. Heertjes *et al.* (2020). ‘Control of Wafer Scanners: Methods and Developments’. In ‘*Proc. 2020 Am. Control Conf. (ACC)*’, (IEEE), 3686–3703.
- D. Hesterberg *et al.* (2022). ‘Development of a Rhizomicrocosm for In-Vivo, 4D Imaging of Rhizosphere Processes Around an Isolated Root’. In ‘*Proc. 19th Int. Plant Nutrition Colloquium (IPNC2022)*’, 415.
- R. Hettel (2014). ‘DLSR design and plans: an international overview’. *J. Synchrotron Rad.* **21**(5), 843.
- D. Hidas *et al.* (2022). ‘High Precision Real-Time Insertion Device and Monochromator Synchronization at NSLS-II’. *Nucl. Instrum. Methods Phys. Res. A* **1031**, 166505.
- Z. Hussain *et al.* (1982). ‘Performance and Application of a Double-Crystal Monochromator in the Energy Region 800 hv 4500 eV’. *Nucl. Instrum. Methods Phys. Res.* **195**(1-2), 115.
- Y. Hwu and G. Margaritondo (2021). ‘Synchrotron Radiation and X-ray Free-electron Lasers (X-FELs) Explained to All Users, Active and Potential’. *J. Synchrotron Rad.* **28**(3), 1014.
- J.P. Itié *et al.* (2016). *High Pressure XAS, XMCD and IXS* (John Wiley & Sons), 385–705.

- L. Jabben (2007). *Mechatronic Design of a Magnetically Suspended Rotating Platform*. Ph.D. thesis, Delft University of Technology.
- L. Jabben and J. van Eijk (2011). ‘Performance Analysis’. *Mikroniek* **51**(2), 5.
- S.P. Kearney, S. Bean and J. Maser (2019). ‘Analysis of Vibration Isolated Facilities for the In-situ Nanoprobe at the Advanced Photon Source’. *Synchrotron Radiat. News* **32**(5), 13.
- J. Kelly *et al.* (2013). ‘Design, Build & Test of a Double Crystal Monochromator for Beamlines I09 & I23 at the Diamond Light Source’. *J. Phys. Conf. Ser.* **425**(5), 052009.
- J. Kelly *et al.* (2022). ‘The Delta Robot – A Long Travel Nano-positioning Stage for Scanning X-ray Microscopy’. *Rev. Sci. Instrum.* **93**(4), 043712.
- D. de Klerk *et al.* (2008). ‘General Framework for Dynamic Substructuring: History, Review and Classification of Techniques’. *AIAA Journal* **46**(5), 1169.
- D.C. Koningsberger and R. Prins (1988). *X-Ray Absorption: Principles, Applications, Techniques of EXAFS, SEXAFS and XANES* (Wiley-Interscience).
- G.F. Krebs (1997). ‘Measurement of Storage Ring Motion at the Advanced Light Source’. In ‘*Proc. 1997 Particle Acc. Conf.*’, vol. 1 (IEEE), 793–795.
- P. Kristiansen *et al.* (2015). ‘Vibration Measurements of High-heat-load Monochromators for DESY PETRA III Extension’. *J. Synchrotron Rad.* **22**(4), 879.
- P. Kristiansen *et al.* (2016). ‘Vibrational stability of a cryocooled horizontal double-crystal monochromator’. *J. Synchrotron Rad.* **23**(5), 1076.
- R. Lahlali *et al.* (2015). ‘Synchrotron-based Phase Contrast X-ray Imaging combined with FTIR Spectroscopy Reveals Structural and Biomolecular Differences in Spikelets play a Significant Role in Resistance to Fusarium in Wheat’. *BMC Plant Biol.* **15**(1), 1.
- A.J.C. Lanfredi *et al.* (2009). ‘Electron transport properties of undoped  $\text{SnO}_2$  monocrystals’. *J. Appl. Phys.* **105**(2), 023708.
- D.A.H. Laro (2009). *Mechatronic Design of an Electromagnetically Levitated Linear Positioning System using Novel Multi-DoF Actuators*. Ph.D. thesis, Delft University of Technology.
- M. Lemonnier *et al.* (1978). ‘High Vacuum Two Crystal Soft X-ray Monochromator’. *Nucl. Instrum. Methods* **152**(1), 109.
- F.R. Lena *et al.* (2021a). ‘A Cryogenic Sample Environment for the TARUMÃ Station at the CARNAÚBA Beamline at Sirius/LNLS’. In ‘*Proc. 11th Mech. Eng. Des. of Synchrotron Radiat. Equip. and Instrum. (MEDSI’20)*’, (JACoW Publishing), 306–309.
- F.R. Lena *et al.* (2021b). ‘Copper Braid Heat Conductors for Sirius Cryogenic X-ray Optics’. In ‘*Proc. 11th Mech. Eng. Des. of Synchrotron Radiat. Equip. and Instrum. (MEDSI’20)*’, (JACoW Publishing), 207–210.

- F.R. Lena *et al.* (2022). ‘Commissioning of the Cryogenic Sample Environment for the TARUMÃ Station at the CARNAÚBA beamline at Sirius/LNLS’. vol. 2380 (IOP Publishing), 012108.
- J.C. Liu *et al.* (2006). ‘Generic Radiation Safety Design for SSRL Synchrotron Radiation Beamlines’. *Rad. Meas.* **41**, S156.
- L. Liu *et al.* (2014). ‘The Sirius Project’. *J. Synchrotron Rad.* **21**(5), 904.
- L. Liu *et al.* (2021). ‘Sirius Commissioning Results and Operation Status’. In ‘*Proc. 12th Int. Particle Acc. Conf. (IPAC’21)*’, (JACoW Publishing), 13–18.
- S.R. Marques *et al.* (2022). ‘Improvements on Sirius Beam Stability’. In ‘*Proc. 13th Int. Particle Acc. Conf. (IPAC’22)*’, (JACoW), 226–229.
- B.C. Meyer *et al.* (2021). ‘Thermo-Mechanical Design Strategies for Critical Beamline Optical Components at Sirius/LNLS’. *Synchrotron Radiat. News* **34**(6), 4.
- D.M. Mills (1993). ‘High heat load synchrotron optics’. In ‘*High Heat Flux Engineering*’, vol. 1739 (SPIE), 456–463.
- L. Mino *et al.* (2018). ‘Materials Characterization by Synchrotron X-ray Microprobes and Nanoprobes’. *Rev. Mod. Phys.* **90**(2), 025007.
- T. Mochizuki *et al.* (1998). ‘Design of Compact Absorbers for High-heat-load X-ray Undulator Beamlines at SPring-8’. *J. Synchrotron Rad.* **5**(4), 1199.
- W. Monkhorst (2004). ‘Dynamic Error Budgeting: a Design Approach’.
- M.A.L. Moraes *et al.* (2018). ‘A Control Architecture Proposal for Sirius Beamlines’. In ‘*Proc. 16th Int. Conf. on Acc. and Large Exp. Phys. Control Systems (ICALEPCS’17)*’, (JACoW Publishing), 1947–1952.
- M.A.L. Moraes *et al.* (2020). ‘The FPGA Control Implementation of the High-Dynamic Double-Crystal Monochromator at Sirius Light Source’. In ‘*Proc. ASPE 2020 Spring – Design and Control of Precision Mechatronic Systems*’, 131–136.
- G.B.Z.L. Moreno *et al.* (2018a). ‘Rapid Control Prototyping Tool for the Sirius High-Dynamic DCM Control System’. In ‘*Proc. 16th Int. Conf. on Acc. and Large Exp. Phys. Control Systems (ICALEPCS’17)*’, (JACoW Publishing), 1941–1946.
- G.B.Z.L. Moreno *et al.* (2018b). ‘Synchrotron Radiation Damage in Fiber Optics Interferometers’. In ‘*EUSPEN’s 18th Int. Conf. and Exhibition*’, .
- G.B.Z.L. Moreno *et al.* (2021). ‘Exactly-constrained KB Mirrors for Sirius/LNLS Beamlines: Design and Commissioning of the TARUMÃ Station Nanofocusing Optics at CARNAÚBA Beamline’. In ‘*Proc. 11th Mech. Eng. Des. of Synchrotron Radiat. Equip. and Instrum. (MEDSI’20)*’, (JACoW Publishing), 111–114.
- G. Nakiboglu (2012). *Aeroacoustics of Corrugated Pipes*. Ph.D. thesis, Technical University of Eindhoven.
- E. Nazaretski *et al.* (2017). ‘Design and Performance of an X-ray Scanning Microscope at the Hard X-ray Nanoprobe Beamline of NSLS-II’. *J. Synchrotron Rad.* **24**(6), 1113.



- C. Nicklin, T. Arnold, J. Rawle and A. Warne (2016). ‘Diamond Beamline I07: a Beamline for Surface and Interface Diffraction’. *J. Synchrotron Rad.* **23**(5), 1245.
- H.G.P. Oliveira *et al.* (2017). ‘The LNLS Metrology Building’. In ‘*Proc. 9th Mech. Eng. Des. of Synchrotron Radiat. Equip. and Instrum. (MEDSI’16)*’, (JACoW Publishing), 17–19.
- H. Onuki and P. Elleaume (2002). *Undulators, wigglers and their applications* (CRC Press).
- T. Oomen (2018). ‘Advanced Motion Control for Precision Mechatronics: Control, Identification, and Learning of Complex Systems’. *IEEE J. Ind. Appl.* **7**(2), 127.
- T. Oomen (2020). ‘Learning for Advanced Motion Control’. In ‘*Proc. 2020 IEEE 16th Int. Workshop on Adv. Motion Control (AMC)*’, (IEEE), 65–72.
- T. Oomen and M. Steinbuch (2020). ‘Model-based Control for High-tech Mechatronic Systems’. In ‘*Mechatronics and Robotics*’, (CRC Press), 51–80.
- A. Papoulis (1991). *Probability, Random Variables and Stochastic Processes*. 3rd edn. (McGraw-Hill).
- A.V. Perna, *et al.* (2021). ‘The HD-DCM-Lite: a high-dynamic DCM with extended scanning capabilities for Sirius/LNLS beamlines’. In ‘*Proc. 11th Mech. Eng. Des. of Synchrotron Radiat. Equip. and Instrum. (MEDSI’20)*’, (JACoW Publishing), 203–206.
- R. Pintelon and J. Schoukens (2012). *System Identification: a Frequency Domain Approach* (John Wiley & Sons).
- A.C. Pinto *et al.* (2020). ‘Surface Metrology of Cylindrical Mirrors with Sagittal Curvature in Low-spatial Frequency Range’. In ‘*Proc. SPIE 11492, Adv. in Metrology for X-Ray and EUV Optics IX*’, vol. 11492 (SPIE), 57–66.
- J.R. Piton *et al.* (2021). ‘TATU: a flexible FPGA-based trigger and timer unit created on CompactRIO for the first SIRIUS beamlines’. In ‘*Proc. 18th Int. Conf. on Acc. and Large Exp. Phys. Control Systems (ICALEPCS’21)*’, (JACoW Publishing), 908–911.
- M. Sanchez del Rio *et al.* (2011). ‘SHADOW3: a New Version of the Synchrotron X-ray Optics Modelling Package’. *J. Synchrotron Rad.* **18**(5), 708.
- A.L. Robinson (2015). ‘History of Synchrotron Radiation’. *Synchrotron Rad. News* **28**(4), 4.
- F. Rodrigues *et al.* (2019). ‘Sirius Stability: from Foundation to Girders’. *Synchrotron Rad. News* **32**(5), 20.
- M. Saveri Silva *et al.* (2017). ‘Thermal Management and Crystal Clamping Concepts for the New High-Dynamics DCM for Sirius’. In ‘*Proc. 9th Mech. Eng. Des. of Synchrotron Radiat. Equip. and Instrum. (MEDSI’16)*’, (JACoW Publishing), 194–197.

- P. Schellekens *et al.* (1998). ‘Design for Precision: Current Status and Trends’. *Cirp Annals* **47**(2), 557.
- R. Schmidt *et al.* (2011). *The Design of High Performance Mechatronics: High-Tech Functionality by Multidisciplinary System Integration*. 2nd edn. (IOS Press).
- J. Schoukens, K. Godfrey and M. Schoukens (2018). ‘Nonparametric Data-driven Modeling of Linear Systems: Estimating the Frequency Response and Impulse Response Function’. *IEEE Control Syst. Mag.* **38**(4), 49.
- A. Schropp *et al.* (2020). ‘PtyNAMi: Ptychographic Nano-Analytical Microscope’. *J. Appl. Cryst.* **53**, 957.
- I. Sergueev *et al.* (2016). ‘Angular Vibrations of Cryogenically Cooled Double-Crystal Monochromators’. *J. Synchrotron Rad.* **23**(5), 1097.
- F. Siewert, J. Buchheim, T. Zeschke, M. Störmer, G. Falkenberg and R. Sankari (2014). ‘On the Characterization of Ultra-precise X-ray Optical Components: Advances and Challenges in Ex-situ Metrology’. *J. Synchrotron Rad.* **21**(5), 968.
- N. Simos (2019). ‘Synchrotron Facilities: Vibration and Stability Challenge’.
- N. Simos *et al.* (2019). ‘NSLS-II Ground Vibration Stability Studies and Design Implementation’. *Synchrotron Radit. News* **32**(5), 4.
- S. Skogestad and I. Postlethwaite (2007). *Multivariable Feedback Control: Analysis and Design*, vol. 2 (John Wiley & Sons).
- A.H. Slocum (1992). *Precision Machine Design* (Society of Manufacturing Engineers).
- SmarAct (2020). ‘Picoscale Michelson Interferometer’. <http://www.picoscale.com/>, accessed: Oct. 1st, 2021.
- H. Soemers (2011). *Design Principles for Precision Mechanisms* (T-Pointprint).
- G.E. Sterbinsky and S.M. Heald (2021). ‘A Simple Method for Mitigating Error in the Fixed-offset of a Double-Crystal Monochromator’. *J. Synchrotron Rad.* **28**(6), 1737.
- J. Susini *et al.* (2014). ‘New Challenges in Beamline Instrumentation for the ESRF Upgrade Programme Phase II’. *J. Synchrotron Rad.* **21**(5), 986.
- P.F. Tavares *et al.* (2018a). ‘Commissioning and First-year Operational Results of the MAX IV 3 GeV Ring’. *J. Synchrotron Rad.* **25**(5), 1291.
- P.F. Tavares *et al.* (2018b). ‘Future Development Plans for the MAX IV Light Source: Pushing further towards Higher Brightness and Coherence’. *J. Electron Spectros. Relat. Phenomena* **224**, 8.
- H.C.N. Tolentino *et al.* (2019a). ‘Innovative Instruments Based on Cryogenically Cooled Silicon Crystals for the CARNAÚBA Beamline at Sirius-LNLS’. *AIP Conf. Proc.* **2054**, 060026.
- H.C.N. Tolentino *et al.* (2019b). ‘TARUMÃ Station for the CARNAÚBA Beamline at Sirius/LNLS’. In ‘*Proc. SPIE 11112, X-ray Nanoimaging: Instruments and Methods IV*’, vol. 11112. 1111206.

- H.C.N. Tolentino *et al.* (2021). ‘X-ray Microscopy Developments at Sirius-LNLS: First Commissioning Experiments at the CARNAÚBA Beamline’. In ‘*Proc. SPIE 11839, X-Ray Nanoimaging: Instruments and Methods V*’, vol. 11839. 1183904.
- F. Villar *et al.* (2018). ‘Nanopositioning for the ESRF ID16A Nano-Imaging Beamline’. *Synchrotron Radiat. News* **31**(5), 9.
- L. Volpe *et al.* (2018). ‘Optimization Method Using Thermal and Mechanical Simulations for Sirius High-stability Mirrors’. In ‘*Proc. 10th Mech. Eng. Des. of Synchrotron Radiat. Equip. and Instrum. (MEDSI’18)*’, (JACoW Publishing), 273–276.
- L.M. Volpe *et al.* (2017). ‘High Heat Load Front Ends for Sirius’. In ‘*Proc. 9th Mech. Eng. Des. of Synchrotron Radiat. Equip. and Instrum. (MEDSI’16)*’, (JACoW Publishing), 324–326.
- L.M. Volpe *et al.* (2021). ‘Thermal Model Validation for the Cryogenic Mirror Systems for Sirius/LNLS’. In ‘*Proc. 11th Mech. Eng. Des. of Synchrotron Radiat. Equip. and Instrum. (MEDSI’20)*’, (JACoW Publishing), 320–323.
- T. Waterstradt *et al.* (2018). ‘Sub-20-nrad Stability of an LN2-Cooled Vertical-Offset Double-Crystal Monochromator’. Presented at MEDSI’18 in Paris, France, unpublished.
- W.H. Wilendorf *et al.* (2021). ‘Electrochemistry and Microfluidic Environments for the TARUMÃ Station at the CARNAÚBA Beamline at Sirius/LNLS’. In ‘*Proc. 11th Mech. Eng. Des. of Synchrotron Radiat. Equip. and Instrum. (MEDSI’20)*’, (JACoW Publishing), 310–313.
- P. Willmott (2019). *An Introduction to Synchrotron Radiation: Techniques and Applications* (John Wiley & Sons).
- P.J. Withers (2015). ‘Fracture Mechanics by Three-dimensional Crack-tip Synchrotron X-ray Microscopy’. *Philos. Trans. R. Soc. A* **373**(2036), 20130157.
- G. Witvoet *et al.* (2017). ‘Predictive-model-based MIMO Motion Control of an Unstable 6-DoF Hexapod Stage for Overlay Measurements’. In ‘*Proc. 2017 IEEE Conf. on Control Tech. and Appl. (CCTA)*’, (IEEE), 726–731.
- J. Wu *et al.* (2021). ‘Improvement of the performance of a cryo-cooled monochromator at SSRF. Part II: Angular stability of the exit beam’. *Nucl. Instrum. Methods Phys. Res. A* **988**, 164872.
- X. Zhang (2018). *Synchrotron Radiation Applications* (World Scientific Publishing Company).
- H. Yamazaki *et al.* (2013). ‘Improvement in Stability of SPring-8 X-ray Monochromators with Cryogenic-cooled Silicon Crystals’. *J. Phys.: Conf. Ser.* **425**(052001), 1.
- L. Zhang *et al.* (2013a). ‘Liquid Nitrogen Cooled Si Crystal Monochromator: X-ray Focusing by Controlled Heat Load’. In ‘*J. Phys.: Conference Series*’, vol. 425 (IOP Publishing), 052008.

- L. Zhang *et al.* (2013b). ‘Thermal deformation of cryogenically cooled silicon crystals under intense X-ray beams: measurement and finite-element predictions of the surface shape’. *J. Synchrotron Rad.* **20**(4), 567.
- V.B. Zilli *et al.* (2021). ‘Installation and Commissioning of the Exactly-constrained X-ray Mirror Systems for Sirius/LNLS’. In ‘*Proc. 11th Mech. Eng. Des. of Synchrotron Radiat. Equip. and Instrum. (MEDSI’20)*’, (JACoW Publishing), 33–36.



---

## List of Publications

---

- G.S. Albuquerque *et al.* (2021). ‘The Dynamic Modeling and the Control Architecture of the New High-Dynamic Double-Crystal Monochromator (HD-DCM-Lite) for Sirius/LNLS’. In ‘*Proc. 18th Int. Conf. on Acc. and Large Exp. Phys. Control Systems (ICALEPCS’21)*’, (JACoW Publishing), 619–624.
- J.L. Brito Neto *et al.* (2021). ‘Temperature Control for Beamline Precision Systems of Sirius/LNLS’. In ‘*Proc. 18th Int. Conf. on Acc. and Large Exp. Phys. Control Systems (ICALEPCS’18)*’, (JACoW Publishing), 606–611.
- C.S.N.C. Bueno *et al.* (2021a). ‘Positioning Scanning Solutions at the TARUMÃ Station at the CARNAÚBA Beamline at Sirius/LNLS’. In ‘*Proc. 18th Int. Conf. on Acc. and Large Exp. Phys. Control Systems (ICALEPCS’21)*’, (JACoW Publishing), 613–618.
- C.S.N.C. Bueno *et al.* (2021b). ‘Vibration Assessment at the CARNAÚBA Beamline at Sirius/LNLS’. In ‘*Proc. 11th Mech. Eng. Des. of Synchrotron Radiat. Equip. and Instrum. (MEDSI’20)*’, (JACoW Publishing), 37–40.
- R.M. Caliari *et al.* (2017). ‘Studies on Flow-Induced Vibrations for the New High-Dynamics DCM for Sirius’. In ‘*Proc. 9th Mech. Eng. Des. of Synchrotron Radiat. Equip. and Instrum. (MEDSI’16)*’, (JACoW Publishing), 8–11.
- R.M. Caliari *et al.* (2018). ‘System Identification and Control for the Sirius High-Dynamic DCM’. In ‘*Proc. 16th Int. Conf. on Acc. and Large Exp. Phys. Control Systems (ICALEPCS’17)*’, (JACoW Publishing), 997–1002.
- R.M. Caliari *et al.* (2020). ‘Loop-Shaping Controller Design in the Development of the High-Dynamic Double-Crystal Monochromator at Sirius Light Source’. In ‘*Proc. ASPE 2020 Spring – Design and Control of Precision Mechatronic Systems*’, 125–130.
- H.F. Canova *et al.* (2017). ‘VDE - Virtual Documentation Environment’. In ‘*Proc. 11th Int. Workshop on Person. Computers and Particle Acc. Controls (PCaPAC2016)*’, (JACoW Publishing), 53–55.
- R. Geraldès *et al.* (2016). ‘New Sensor and Non-contact Geometrical Survey for the Vibrating Wire Technique’. *Nucl. Instrum. Methods Phys. Res. A* **811**, 115.
- R.R. Geraldès *et al.* (2017a). ‘Mechatronics Concepts for the New High-Dynamics DCM for Sirius’. In ‘*Proc. 9th Mech. Eng. Des. of Synchrotron Radiat. Equip. and Instrum. (MEDSI’16)*’, (JACoW Publishing), 44–47.

- R.R. Geraldes *et al.* (2017b). ‘The New High Dynamics DCM for Sirius’. In ‘*Proc. 9th Mech. Eng. Des. of Synchrotron Radiat. Equip. and Instrum. (MEDSI’16)*’, (JACoW Publishing), 141–146.
- R.R. Geraldes *et al.* (2018a). ‘Granite Benches for Sirius X-ray Optical Systems’. In ‘*Proc. 10th Mech. Eng. Des. of Synchrotron Radiat. Equip. and Instrum. (MEDSI’18)*’, (JACoW Publishing), 361–364.
- R.R. Geraldes *et al.* (2018b). ‘The Design of Exactly-Constrained X-Ray Mirror Systems for Sirius’. In ‘*Proc. 10th Mech. Eng. Des. of Synchrotron Radiat. Equip. and Instrum. (MEDSI’18)*’, (JACoW Publishing), 173–178.
- R.R. Geraldes *et al.* (2018c). ‘The Status of the New High-Dynamic DCM for Sirius’. In ‘*Proc. 10th Mech. Eng. Des. of Synchrotron Radiat. Equip. and Instrum. (MEDSI’18)*’, (JACoW Publishing), 147–152.
- R.R. Geraldes *et al.* (2020). ‘Dynamic Error Budgeting in the Development of the High-Dynamic Double-Crystal Monochromator at Sirius Light Source’. In ‘*Proc. ASPE 2020 Spring – Design and Control of Precision Mechatronic Systems*’, 119–124.
- R.R. Geraldes *et al.* (2021a). ‘Commissioning and Prospects of the High-Dynamic DCMs at Sirius/LNLS’. In ‘*Proc. 11th Mech. Eng. Des. of Synchrotron Radiat. Equip. and Instrum. (MEDSI’20)*’, (JACoW Publishing), 25–28.
- R.R. Geraldes *et al.* (2021b). ‘Design and Commissioning of the TARUMÁ Station at the CARNAÚBA Beamline at Sirius/LNLS’. In ‘*Proc. 11th Mech. Eng. Des. of Synchrotron Radiat. Equip. and Instrum. (MEDSI’20)*’, (JACoW Publishing), 292–295.
- R.R. Geraldes *et al.* (2021c). ‘The FPGA-based Control Architecture, EPICS Interface and Advanced Operational Modes of the High-Dynamic Double-Crystal Monochromator for Sirius/LNLS’. In ‘*Proc. 18th Int. Conf. on Acc. and Large Exp. Phys. Control Systems (ICALEPCS’21)*’, (JACoW Publishing), 370–375.
- R.R. Geraldes *et al.* (2022a). ‘A review on the High-Dynamic Double-Crystal Monochromator for Sirius/LNLS’. In ‘*J. Phys. Conf. Ser.*’, vol. 2380 (IOP Publishing), 012050.
- R.R. Geraldes *et al.* (2022b). ‘Predictive Modeling through Dynamic Error Budgeting applied to the High-Dynamic Double-Crystal Monochromator for Sirius Light Source’. *Precision Engineering* **77**, 90.
- R.R. Geraldes *et al.* (2022c). ‘The Mechatronic Architecture and Design of the High-Dynamic Double-Crystal Monochromator for Sirius Light Source’. *Precision Engineering* **77**, 110.
- R.R. Geraldes *et al.* (2022d). ‘The Sample Positioning Stage for the SAPOTI Nanoprobe at the CARNAÚBA beamline at Sirius/LNLS’. In ‘*Proc. 37th ASPE Annual Meeting*’, 91–97.
- R.R. Geraldes *et al.* (2023a). ‘Fly-Scan-Oriented Motion Analyses and Upgraded Beamline Integration Architecture for the High-Dynamic Double-Crystal Monochromator at Sirius/LNLS’. *J. Synchrotron Rad.* **30**, 90.
- R.R. Geraldes *et al.* (2023b). ‘The High-Dynamic Cryogenic Sample Stage for SAPOTI/CARNAUBA at Sirius/LNLS’. To be published Proc. XRM2022.
- D. Hesterberg *et al.* (2022). ‘Development of a Rhizomicrocosm for In-Vivo, 4D Imaging of Rhizosphere Processes Around an Isolated Root’. In ‘*Proc. 19th Int. Plant Nutrition Colloquium (IPNC2022)*’, 415.
- A.J.C. Lanfredi *et al.* (2009). ‘Electron transport properties of undoped sio<sub>2</sub> monocystals’. *J. Appl. Phys.* **105**(2), 023708.

- 
- F.R. Lena *et al.* (2021a). ‘A Cryogenic Sample Environment for the TARUMÃ Station at the CARNAÚBA Beamline at Sirius/LNLS’. In ‘*Proc. 11th Mech. Eng. Des. of Synchrotron Radiat. Equip. and Instrum. (MEDSI’20)*’, (JACoW Publishing), 306–309.
- F.R. Lena *et al.* (2021b). ‘Copper Braid Heat Conductors for Sirius Cryogenic X-ray Optics’. In ‘*Proc. 11th Mech. Eng. Des. of Synchrotron Radiat. Equip. and Instrum. (MEDSI’20)*’, (JACoW Publishing), 207–210.
- F.R. Lena *et al.* (2022). ‘Commissioning of the Cryogenic Sample Environment for the TARUMÃ Station at the CARNAÚBA beamline at Sirius/LNLS’. vol. 2380 (IOP Publishing), 012108.
- B.C. Meyer *et al.* (2021). ‘Thermo-Mechanical Design Strategies for Critical Beamline Optical Components at Sirius/LNLS’. *Synchrotron Radiat. News* **34**(6), 4.
- M.A.L. Moraes *et al.* (2018). ‘A Control Architecture Proposal for Sirius Beamlines’. In ‘*Proc. 16th Int. Conf. on Acc. and Large Exp. Phys. Control Systems (ICALEPCS’17)*’, (JACoW Publishing), 1947–1952.
- M.A.L. Moraes *et al.* (2020). ‘The FPGA Control Implementation of the High-Dynamic Double-Crystal Monochromator at Sirius Light Source’. In ‘*Proc. ASPE 2020 Spring – Design and Control of Precision Mechatronic Systems*’, 131–136.
- G.B.Z.L. Moreno *et al.* (2018a). ‘Rapid Control Prototyping Tool for the Sirius High-Dynamic DCM Control System’. In ‘*Proc. 16th Int. Conf. on Acc. and Large Exp. Phys. Control Systems (ICALEPCS’17)*’, (JACoW Publishing), 1941–1946.
- G.B.Z.L. Moreno *et al.* (2018b). ‘Synchrotron Radiation Damage in Fiber Optics Interferometers’. In ‘*EUSPEN’s 18th Int. Conf. and Exhibition*’, .
- G.B.Z.L. Moreno *et al.* (2021). ‘Exactly-constrained KB Mirrors for Sirius/LNLS Beamlines: Design and Commissioning of the TARUMÃ Station Nanofocusing Optics at CARNAÚBA Beamline’. In ‘*Proc. 11th Mech. Eng. Des. of Synchrotron Radiat. Equip. and Instrum. (MEDSI’20)*’, (JACoW Publishing), 111–114.
- H.G.P. Oliveira *et al.* (2017). ‘The LNLS Metrology Building’. In ‘*Proc. 9th Mech. Eng. Des. of Synchrotron Radiat. Equip. and Instrum. (MEDSI’16)*’, (JACoW Publishing), 17–19.
- A.V. Perna, *et al.* (2021). ‘The HD-DCM-Lite: a high-dynamic DCM with extended scanning capabilities for Sirius/LNLS beamlines’. In ‘*Proc. 11th Mech. Eng. Des. of Synchrotron Radiat. Equip. and Instrum. (MEDSI’20)*’, (JACoW Publishing), 203–206.
- A.C. Pinto *et al.* (2020). ‘Surface Metrology of Cylindrical Mirrors with Sagittal Curvature in Low-spatial Frequency Range’. In ‘*Proc. SPIE 11492, Adv. in Metrology for X-Ray and EUV Optics IX*’, vol. 11492 (SPIE), 57–66.
- M. Saveri Silva *et al.* (2017). ‘Thermal Management and Crystal Clamping Concepts for the New High-Dynamics DCM for Sirius’. In ‘*Proc. 9th Mech. Eng. Des. of Synchrotron Radiat. Equip. and Instrum. (MEDSI’16)*’, (JACoW Publishing), 194–197.
- H.C.N. Tolentino *et al.* (2019a). ‘Innovative Instruments Based on Cryogenically Cooled Silicon Crystals for the CARNAÚBA Beamline at Sirius-LNLS’. *AIP Conf. Proc.* **2054**, 060026.
- H.C.N. Tolentino *et al.* (2019b). ‘TARUMÃ Station for the CARNAÚBA Beamline at Sirius/LNLS’. In ‘*Proc. SPIE 11112, X-ray Nanoimaging: Instruments and Methods IV*’, vol. 11112. 1111206.



- H.C.N. Tolentino *et al.* (2021). ‘X-ray Microscopy Developments at Sirius-LNLS: First Commissioning Experiments at the CARNAÚBA Beamline’. In ‘*Proc. SPIE 11839, X-Ray Nanoimaging: Instruments and Methods V*’, vol. 11839. 1183904.
- L. Volpe *et al.* (2018). ‘Optimization Method Using Thermal and Mechanical Simulations for Sirius High-stability Mirrors’. In ‘*Proc. 10th Mech. Eng. Des. of Synchrotron Radiat. Equip. and Instrum. (MEDSI’18)*’, (JACoW Publishing), 273–276.
- L.M. Volpe *et al.* (2021). ‘Thermal Model Validation for the Cryogenic Mirror Systems for Sirius/LNLS’. In ‘*Proc. 11th Mech. Eng. Des. of Synchrotron Radiat. Equip. and Instrum. (MEDSI’20)*’, (JACoW Publishing), 320–323.
- W.H. Wilendorf *et al.* (2021). ‘Electrochemistry and Microfluidic Environments for the TARUMÃ Station at the CARNAÚBA Beamline at Sirius/LNLS’. In ‘*Proc. 11th Mech. Eng. Des. of Synchrotron Radiat. Equip. and Instrum. (MEDSI’20)*’, (JACoW Publishing), 310–313.
- V.B. Zilli *et al.* (2021). ‘Installation and Commissioning of the Exactly-constrained X-ray Mirror Systems for Sirius/LNLS’. In ‘*Proc. 11th Mech. Eng. Des. of Synchrotron Radiat. Equip. and Instrum. (MEDSI’20)*’, (JACoW Publishing), 33–36.

---

## Acknowledgements

---

Sitting down to write this section of the thesis is a remarkable moment, not only because it is related to getting to the end of an unimaginably intense phase of my life, but also because I personally believe that gratitude is at least in the top three best feelings one can experience in life. Our history is in practice written by the planned and unplanned situations that we go through and by the people that we meet in this journey. In that sense, I am extremely fortunate, both at the personal and the professional sides. Keeping a full-time job at the Brazilian Synchrotron Light Laboratory (LNLS), sharing the responsibility of building Sirius next-generation beamlines, and carrying out this PhD, while going through the pandemic of COVID-19 *in Brazil*, was no ride in the park. Yet, it would have been impossible without a beautiful support network.

First and foremost, I thank my life partner Mayra for an inconceivable level of patience, understanding and selflessness — not for a day or a month, but for more than five years in this whole process. Mayra, I could not have done this without your love, your caring and your support. Then, I could not possibly be thankful enough to my parents Lino and Darci, who have given everything they could and done their very best in caring, providing for and educating my brother and myself. Thank you for your values, your love and support! In this context, I am also grateful to my brother Renato, to my family members and to my closest long-time friends for sharing so much, for the trust and companionship — even if often from a distance. You are many to be named and I do not want to leave any of you out, but you know who you are. Thank you!

Then, career-wise I still find it hard to believe in the number of extraordinary people that I have come across and how generous they have been to me. In order of appearance, firstly I would like to acknowledge Prof. Dr. Adenilson José Chiquito, my dear supervisor in the scientific initiation research project in nanotechnology during my Bachelor's studies in Engineering Physics. Prof. Chiquito, thank you for introducing me to the experimental physics and academic worlds, for the friendship and professionalism, and for being my first role-model in terms of technical excellence.

Next, Regis Neuenschwander had a decisive role in my life by opening the doors of the LNLS for me, providing the first opportunities of international travels and inserting me in a high-level international community. Thank you, Regis! Your creativity and

intuition are many times fascinating, and your support and confidence in me resulted in tons of life-changing personal and professional experiences. I am also extremely grateful to Prof. Dr. Antonio José Roque da Silva, Director of the Brazilian Center for Research in Energy and Materials (CNPEM), Dr. Harry Westfahl Júnior, Director of the LNLS, and Lucas Sanfelici, head of the Division of Beamline Engineering of the LNLS, a brilliant triad that (among so many others) have been doing so much for me personally and for the science in Brazil. Your optimism, intelligence, knowledge, and political and people skills are exceptional and absolutely inspiring. Thank you for your decisive roles in making Sirius possible and increasingly better, with all that it represents and brings with it, and for your continuous support and investment in me — this PhD being a concrete proof of it. Furthermore, someone else that could not be left out is Gustavo Rodrigues, my former group leader at the LNLS, who provided an essential support for me to continue over the past few years. And I would also like to honor the memory of Dr. Antonio Ricardo Droher Rodrigues, my co-promoter in my Master's degree and one of the main characters in the recent history of the Brazilian science — having idealized and built, with a handful of other national heroes, the LNLS itself and the UVX storage ring in the 80's and 90's, and more recently contributing enormously to Sirius. To him all my respect and recognition.

On my way toward precision engineering and mechatronics, I am deeply thankful to Monsier Yves Dabin, from the European Synchrotron Radiation Facility (ESRF), who, even over only a short period of time, very generously and enthusiastically has taught me so much about beamline design and many precision engineering concepts within it. Mr. Dabin, my memories from you are still an everyday inspiration in how to share knowledge with other people and whet curiosity. You were also the one that introduced MI-Partners to Regis, to the LNLS, and eventually to me, which completely changed the game. Getting in contact with the “Dutch school of engineering” and carrying out the project of the HD-DCM finally filled a long-time void in my engineer's soul, which yearned for systematic and predictive project execution.

Theo Ruijl and Ronald Schneider, you showed me that many things thought by many to be impossible may actually be a matter of good training, broad and yet deep knowledge, technical discipline and methodology, communication and management (and sufficient financial resources). It has been an unspeakable privilege to have worked with you and learned so much from you. You are technically and on the personal level amazing guys. Thank you for your availability, guidance, openness, generosity and friendship. Theo, you were the main motivator of this PhD project, it would not have happened without your push. I am also thankful to everyone else at MI-Partners who I have had the pleasure to meet, but especially to Erik Ruinemans, who taught me a lot about mechanical design as well as about life balance.

Next, I will be forever extremely grateful to my promoters Prof. Dr. Ir. Hans Vermeulen and Prof. Dr. Ir. Maarten Steinbuch, who accepted the challenge of taking me not only for a remote PhD but also in a very particular topic. Thank you so much for your support, your interest and your commitment to this project. I am honored

to have been part of the Control Systems Technology (CST) Group and of such a prestigious and relevant university as the Eindhoven University of Technology (TU/e). If I ever could wish for more, it would only have been having had more time over these years there in Eindhoven, to meet and interact more with its brilliant students, take classes, and attend the super rich technical and social events. To my co-promoter Dr. Ir. Gert Witvoet, my most sincere and profound appreciation. Gert, thanks for being there all these years. Thank you for your excellence and sharpness, your willingness, your caring, your patience and your commitment until the end. I have learned a lot from you in many aspects. Thanks for the discussions, the instructions and the reviews, for making this work and this thesis better in every interaction.

Last but not least, I would like to acknowledge my colleagues and friends from the LNLS who walked the path of the HD-DCM with me. Ricardo Caliari, thank you for the partnership in starting from scratch with me in this marvelous world of precision mechatronics. Those first years were of great curiosity and excitement, together with countless hours of work and studies. Marcelo Moraes, thank you for joining us, with your energy, passion and optimism. Thank you for joining us, developing the software of the HD-DCM, putting the HD-DCM to work at the beamlines, and helping me with the development of the Dynamic Error Budgeting toolbox for LNLS, which was mostly done in the late nights, early mornings and Sundays. My deep gratitude (and apologies) also to your families, wives and kids, who were patient and understanding enough to stand our crazy routine in making this happen. Sergio Lordano, you have a special role in this as well. Thank you for your partnership, energy, willingness and commitment. Thanks for the optical analyses, the discussions, the complementary material and the reviews. Thanks for staying up with me several times for over 24 hours during beam time for commissioning and experimental analyses. João Leandro de Brito Neto, the “hot swap” replacing Ricardo and Marcelo was no easy task. Thank you for taking the challenge and keeping the game on. Your energy and commitment have been also essential to make the HD-DCM thrive. I could not have done this without you guys!

Marlon Saveri Silva, thank you for being with us on this since the beginning as well. The HD-DCMs would not be there today without your design, analysis and management work. Thank you to Alexis Sikorski, Erik Pereira, Guilherme Sobral, Alain Perna, Cassiano Bueno, Gabriel Moreno, Telles Soares, Marcos Eleotério, Maurício Donatti, Fernando Henrique Cardoso, Henrique Canova, Fernando Henrique de Sá, Daniel Tavares and many others who contributed with design and assembly work, measurements, discussions, hardware and software. Thanks to my co-authors and the LNLS staff for all the support. Thank you to Paul Tacx for the remote support in improving our system identification data set for the analyses in the appendix. I am also grateful to all those in the synchrotron community that contributed directly or indirectly to this project.



---

## Curriculum Vitae

---

Renan Geraldles was born on 28/11/1985, in São Paulo, Brazil. He completed his High School education together with the Technical Course in Electronics at the Federal Center for Technological Education of São Paulo (CEFET-SP) in 2002. In 2006, he started studying Engineering Physics at the Federal University of São Carlos (UFSCar), during which he also carried out a three-year Scientific Initiation project entitled “The Study of Electronic Properties in Semiconductor Nanostructures”.



In 2010, he started as an intern in Mechanical Engineering at the Brazilian Synchrotron Light Laboratory (LNLS), where he remains to this date. He is currently the group leader of the Mechatronics and Precision Engineering (MEP) Group in the Division of Beamline Engineering (DEL). Since 2014, his main contributions have been in leading novel beamline instrumentation projects for the 4th-generation light source Sirius at the LNLS, including the High-Dynamic Double-Crystal Monochromator that is described in this dissertation, a family of X-ray mirror systems, and two X-ray nanoprobe.

In April 2015, he received his Master’s degree in Physics with emphasis in Scientific Instrumentation from the Brazilian Center for Research in Physics (CBPF). His thesis was entitled “The Development of a Magnetic Alignment Bench by the Vibrating-Wire Technique”. In December 2017, he started his PhD research within the Control Systems Technology (CST) Group at the department of Mechanical Engineering at the Eindhoven University of Technology (TU/e) — which was performed at Sirius/LNLS.

Over the last decade, he presented regular contributions at conferences in the synchrotron community, mainly at MEDSI, ICALEPCS and XRM. He also participated in conferences of the American Society for Precision Engineering (ASPE) and the European Society for Precision Engineering and Nanotechnology (EUSPEN), as well as attended courses in Precision Engineering and Mechatronics at the Cranfield University, in the United Kingdom, and at the High Tech Institute, in the Netherlands.